

CONNECTING GALAXY AND SUPERMASSIVE BLACK HOLE GROWTH
DURING THE LAST 8 BILLION YEARS

by
Stéphanie Juneau

A Dissertation Submitted to the Faculty of the
DEPARTMENT OF ASTRONOMY
In Partial Fulfillment of the Requirements
For the Degree of
DOCTOR OF PHILOSOPHY
In the Graduate College
THE UNIVERSITY OF ARIZONA

2011

THE UNIVERSITY OF ARIZONA
GRADUATE COLLEGE

As members of the Dissertation Committee, we certify that we have read the dissertation prepared by Stéphanie Juneau entitled "Connecting Galaxy and Super-massive Black Hole Growth During the Last 8 Billion Years" and recommend that it be accepted as fulfilling the dissertation requirement for the Degree of Doctor of Philosophy.

_____ Date: 30 August 2011
Mark Dickinson

_____ Date: 30 August 2011
Romeel Davé

_____ Date: 30 August 2011
Xiaohui Fan

_____ Date: 30 August 2011
Benjamin Weiner

_____ Date: 30 August 2011
Dennis Zaritsky

Final approval and acceptance of this dissertation is contingent upon the candidate's submission of the final copies of the dissertation to the Graduate College.

I hereby certify that I have read this dissertation prepared under my direction and recommend that it be accepted as fulfilling the dissertation requirement.

_____ Date: 30 August 2011
Dissertation Director: Mark Dickinson

_____ Date: 30 August 2011
Co-Dissertation Director: Xiaohui Fan

STATEMENT BY AUTHOR

This dissertation has been submitted in partial fulfillment of requirements for an advanced degree at The University of Arizona and is deposited in the University Library to be made available to borrowers under rules of the Library.

Brief quotations from this dissertation are allowable without special permission, provided that accurate acknowledgment of source is made. Requests for permission for extended quotation from or reproduction of this manuscript in whole or in part may be granted by the head of the major department or the Dean of the Graduate College when in his or her judgment the proposed use of the material is in the interests of scholarship. In all other instances, however, permission must be obtained from the author.

SIGNED: Stéphanie Juneau

ACKNOWLEDGMENTS

I would like to thank my colleagues and collaborators over the years for motivation, support, insightful conversations and for sharing their passion, especially my closest collaborator and thesis advisor: Mark Dickinson for guidance, professional advice, motivating discussions, and for letting me pursue my own research directions.

Among astronomers who aided my research: my collaborators David Alexander, Samir Salim, Benjamin Magnelli, Jeyhan Karteltepe, Elisabete da Cunha, John Moustakas, Shane Bussmann, Desika Narayanan, Yancy Shirley, Paul Vanden Bout, Rob Kennicutt. I would also like to thank Christy Tremonti and Michael Cooper for kindly sharing code, data catalogs and general advice during our overlap at the University of Arizona and multiple colleagues for useful and stimulating discussions: Jen Lotz, Casey Papovich, James Mullaney, Andy Gould, Frédéric Bournaud, Emanuele Daddi, Barry Madore, Pat McCarthy, Tim Heckmann, Richard Ellis, Nick Scoville, Lee Armus, Kim-Vy Tran, Guinevere Kauffmann, Vassilis Charmandaris, David Elbaz, George Helou, Lisa Kewley, Myrto Symeonidis, Almudena, George Rieke, Wiphu Rujopakarn, Anton Koekemoer, and Norman Grogin.

I would like to acknowledge the positive impact of the Women's Science Forum at several levels including scientific communication, peer review and leadership workshops, outreach opportunities, mentoring opportunities, and for providing an overall supportive and motivating environment. I am grateful to valuable teaching opportunities with Chris Impey and Richard Poss, and to indispensable help from Michelle Cournoyer, Jeff Fookson, Catalina Diaz-Silva, Susan Warner, Treva Dickerson, and Carmen Henley.

My experience would not have been the same without the current and former graduate students of Steward Observatory, especially Stephanie Cortes, Amy Stutz, Iva Momcheva, Aleks Diamond-Stanic, Jon Trump, Brandon Kelly, Kevin Flaherty, Stéphane Herbert-Fort, Amanda Ford, Greg Walth, and partner in crime Jared Gabor.

I gratefully acknowledge the following financial support: a FQRNT fellowship (Fonds Québécois de recherche sur la nature et la technologie, Québec, Canada), a University of Arizona College of Science Fellowship, a Philanthropic Educational Organization (P.E.O.) Scholar Award, and research funding through Mark Dickinson's Spitzer and Herschel grants.

Lastly, I would like to acknowledge the many members of the GOODS and AEGIS teams who obtained, reduced, and cataloged some of the data used in this thesis, Cartel Coffee Lab, and the patience and understanding of the Miville, Juneau, McGinnis and Gabor families.

DEDICATION

This thesis is dedicated to P. Juneau and A. Juneau, with love.

TABLE OF CONTENTS

LIST OF FIGURES	9
LIST OF TABLES	11
ABSTRACT	12
CHAPTER 1 INTRODUCTION	14
CHAPTER 2 ENHANCED DENSE GAS FRACTION IN ULTRA-LUMINOUS INFRARED GALAXIES	18
2.1 Introduction	18
2.2 Methods	23
2.2.1 Sample	23
2.2.2 Optical AGN Classification	27
2.2.3 Infrared Luminosity	31
2.2.4 Numerical Models	34
2.3 Results	35
2.3.1 Correlation Between Molecular Line and Infrared Luminosities	35
2.3.2 Comparison Between High- and Low-Density Molecular Tracers	43
2.3.3 Possible Causes of Higher Gas Density	48
2.4 Model Line Ratios	52
2.5 Possible Chemistry Effects	57
2.6 Conclusions	60
CHAPTER 3 A NEW DIAGNOSTIC OF ACTIVE GALACTIC NUCLEI: REVEALING HIGHLY-ABSORBED SYSTEMS AT REDSHIFT > 0.3	64
3.1 Introduction	65
3.2 Low-Redshift Galaxy Sample	69
3.3 Emission-line Diagnostic Diagrams	69
3.3.1 Calibration Using $z \sim 0.1$ SDSS Galaxies	70
3.3.2 A closer look at LINERs	78
3.3.3 A Probabilistic Approach to Galaxy Classification	81
3.4 Intermediate-Redshift Galaxy Sample	85
3.4.1 Emission Line Fluxes	88
3.4.2 Stellar Masses	90
3.4.3 X-ray Luminosity and Classification	91
3.5 Diagnostics at Redshift $0.3 - 1$	93
3.5.1 Comparison with X-ray Classification	93
3.5.2 X-ray Stacking	98

TABLE OF CONTENTS — <i>Continued</i>	
3.5.3	Demographics of X-Ray Selected AGNs 103
3.6	Compton-Thick AGN Candidates 105
3.6.1	X-Ray Absorption Versus Observed AGN Power 106
3.6.2	X-Ray Absorption Versus Intrinsic AGN Power 108
3.6.3	X-ray Stacking of Highly-Absorbed AGNs 112
3.6.4	Linking AGN Absorption and Optical Classification 115
3.7	Discussion 116
3.7.1	Comparison with existing diagnostics 118
3.7.2	A More Complete Census of AGNs 120
3.7.3	Notes on Composite Galaxies 122
3.7.4	Absorbed AGN Fractions 126
3.7.5	Possible evolutionary effects 128
3.8	Summary 130
CHAPTER 4 ON THE UBIQUITY OF ACTIVE GALACTIC NUCLEI AMONG FAR- INFRARED SELECTED GALAXIES 134	
4.1	Introduction 134
4.2	Galaxy Samples 140
4.2.1	Multiwavelength Dataset 140
4.2.2	Sample Selection 143
4.2.3	Infrared Luminosities 144
4.2.4	Mid-to-Far Infrared Color 146
4.2.5	Low-Redshift Comparison Samples 146
4.3	Multiwavelength AGN Diagnostics 149
4.3.1	X-ray Diagnostic 149
4.3.2	MEx Diagnostic 150
4.3.3	IRAC Single-Color and Two-Color Diagnostics 151
4.4	Results 158
4.4.1	AGN Fraction as a Function of Stellar Mass and SFR 159
4.4.2	Global AGN Fraction in Intermediate-Redshift Infrared Galaxies 166
4.4.3	Effect of AGN on Mid-to-Far Infrared Color 170
4.4.4	Star Formation Rates and AGN Luminosities 176
4.5	Discussion 177
4.5.1	X-ray Absorbed AGN 177
4.5.2	Physical Origin of High AGN Fractions 181
4.5.3	Caveats 184
4.6	Summary 186

TABLE OF CONTENTS — *Continued*

CHAPTER 5	CONCLUSIONS	189
5.1	Enhanced molecular gas density in nearby (U)LIRGs	189
5.2	New AGN diagnostic: Toward a more complete AGN census	190
5.3	Occurrence of AGN among intermediate-redshift FIR-selected galaxies	190
APPENDIX A	OBSERVED HCN(3-2) SPECTRA	193
APPENDIX B	COMPARING THE MEX AND CEX DIAGRAMS	196
APPENDIX C	STELLAR MASS ESTIMATION	199
APPENDIX D	COMPARISON WITH THE <i>Blue</i> DIAGRAM	202
APPENDIX E	AGN FRACTION ON THE SFR-MASS PLANE	207
REFERENCES	211

LIST OF FIGURES

2.1	BPT Emission-line diagnostic diagram.	30
2.2	FIR/IR luminosity ratio in galaxies.	33
2.3	Critical density for typical molecular gas transitions in galaxies. . .	37
2.4	Relationship between infrared luminosity and molecular line luminosities.	38
2.5	Slope of $\log(L_{IR}) - \log(L')$ as a function of molecular line critical densities.	42
2.6	Molecular line luminosity ratios as a function of infrared luminosity.	45
2.7	Values of the slopes α as a function of R_{crit}	49
2.8	Molecular line luminosity ratios as a function of infrared luminosity: Comparison between simulations and observations.	54
2.9	HCN(1 – 0)/CO(1 – 0) luminosity ratio as a function of metallicity and ionization parameter of the diffuse ISM.	58
3.1	BPT and MEx Emission line diagnostic diagrams.	71
3.2	AGN classification completeness and contamination rates.	75
3.3	Bivariate distributions of MEx-classified SDSS galaxies.	77
3.4	The [S II] BPT diagram.	80
3.5	SF and AGN fractions on the MEx and CEx diagnostic diagrams. . .	86
3.6	Application of the MEx diagnostic to galaxies at $0.3 < z < 1$	94
3.7	Application of the BPT diagram to galaxies at $z \sim 0.35$	96
3.8	Example spectra with the most obvious [Ne V] $\lambda 3425$ detections. . .	97
3.9	Compton-thickness parameter as a function of hard X-ray luminosity.	109
3.10	Compton-thickness parameter as a function of [O III] $\lambda 5007$ luminosity.	111
3.11	Compton-thickness parameter as a function of the effective photon index	114
3.12	X-ray unabsorbed and X-ray absorbed AGN on the MEx diagnostic diagram.	117
4.1	Total infrared luminosity as a function of redshift.	145
4.2	Observed 24-to-70 μm flux density ratio as a function of redshift. .	147
4.3	FIR-selected galaxies on the MEx AGN diagnostic diagram.	152
4.4	FIR-selected galaxies on IRAC color-color diagram.	155
4.5	FIR-selected galaxies on IRAC color versus redshift diagram.	157
4.6	Probability of presence of AGN as a function of SFR and stellar mass.	163
4.7	AGN fraction as a function of SFR.	164
4.8	AGN fraction as a function of L_{IR} for the FIDEL and combined galaxy samples.	167

LIST OF FIGURES — *Continued*

4.9	AGN fraction as a function of stellar mass for the FIDEL and combined galaxy samples.	168
4.10	AGN fraction of the total FIR-selected galaxy sample as a function of AGN absorption and accretion phase.	171
4.11	Combined optical/IR AGN diagnostic.	174
4.12	AGN fraction as a function of mid- to far-IR color.	175
4.13	Infrared luminosity versus [O III] $\lambda 5007$ and $H\beta$ luminosities.	178
4.14	Compton-thickness parameter as a function of total infrared luminosity.	180
A.1	HCN(3-2) spectra	193
B.1	Bivariate distributions of the SDSS galaxies on the MEx and CEx diagrams.	198
C.1	Stellar mass from SED fitting versus absolute rest-frame K -band magnitude	201
D.1	Distribution of SDSS galaxies on the blue diagram.	204
D.2	Intermediate redshift galaxy sample on the Blue diagram.	206
E.1	AGN and emission-line galaxy fractions on the SFR-Mass plane (S/N>3).	208
E.2	AGN and emission-line galaxy fractions on the SFR-Mass plane (S/N>2).	210

LIST OF TABLES

2.1	Infrared, far-infrared and molecular line luminosities for our combined sample of 34 galaxies	25
2.2	Slopes of $\log(L_{IR}) - \log(L'_{mol})$ and $\log(L_{FIR}) - \log(L'_{mol})$ for five molecular lines.	40
2.3	Slopes of $\log(L'_{HD}/L'_{LD}) - \log(L_{IR})$ and $\log(L'_{HD}/L'_{LD}) - \log(L_{FIR})$ for ten molecular line luminosity ratios.	47
3.1	Demographics of the MEx Diagram	74
3.2	X-ray Stacking of Non-Detections	102

ABSTRACT

It has become increasingly clear that a complete picture of galaxy evolution requires a better understanding of the role of Active Galactic Nuclei (AGN). In particular, they could be responsible for regulating star formation and galaxy growth via feedback processes. There are also competing views about the main modes of stellar growth and supermassive black hole growth in galaxies that need to be resolved. With high infrared luminosities (thus star formation rates) and a frequent occurrence of AGN, galaxies selected in the far-infrared wavebands form an ideal sample to search for a connection between AGN and star formation. The first part of this thesis contains a detailed analysis of the molecular gas properties of nearby infrared luminous and ultraluminous infrared galaxies (LIRGs and ULIRGs). We find that the enhanced molecular gas density in the most IR-luminous systems can be explained by major galaxy mergers, and that AGN are more likely to reside in higher-density systems. While the frequent concurrence of AGN and galaxy mergers in ULIRGs was already established, this work provides a coherent framework that explains trends observed with five molecular gas tracers with a broad range of critical densities, and a comparison with simulations that reproduce observed molecular line ratios without invoking AGN-induced chemistry. The second part of the thesis presents an analysis of the AGN content of intermediate redshift galaxies ($0.3 < z < 1$). However, identifying complete AGN samples at these redshift is challenging because it is difficult to find X-ray weak or absorbed AGN. To alleviate this problem, we developed the Mass-Excitation (MEx) diagram, which is applicable out to redshift of ~ 1 with existing optical spectra. It improves the overall AGN census by detecting AGN that are missed in even the most sensitive X-ray surveys. The new diagnostic was used to study

the concurrence of star formation and AGN in $70\ \mu\text{m}$ -selected galaxies from the Far-Infrared Deep Extragalactic Legacy survey. When multiple AGN diagnostics are combined, we find not only a high AGN fraction in FIR-selected galaxies (as high as for nearby FIR-selected galaxies), but a high incidence of X-ray absorbed AGN. These findings may have considerable implications for current views about the main mode of AGN growth.

CHAPTER 1

INTRODUCTION

Most if not all galaxies contain a supermassive black hole (SMBH) in their center (Richstone et al., 1998), which follow fundamental relations to their host galaxies (Magorrian et al., 1998; Ferrarese & Merritt, 2000). Furthermore, the accretion history of supermassive black holes follow a similar, scaled-down, trend as the cosmic star formation history (Barger et al., 2001). Taken together, these observations strongly suggest that black hole accretion and star formation may be linked phenomena. In particular, active galactic nuclei (AGN) have been invoked in galaxy evolution models as a means to control the rate of star formation in galaxies via feedback (e.g., Croton et al., 2006; Narayanan et al., 2008). While some observational evidence is provided by, e.g., high-velocity outflows in post-starburst galaxies (Tremonti et al., 2007), the full picture on the interplay between AGN and their host galaxies remains unclear.

In fact, there are now opposing views about the main mode of SMBH growth in typical (i.e., moderate-luminosity) AGN. A number of studies propose, or support, the idea that the most active phase of SMBH growth was primarily driven by major galaxy mergers (Di Matteo et al., 2005; Hopkins et al., 2006). According to the major merger scenario (Sanders et al., 1988), when gas-rich galaxies collide, gas is torqued inward creating a compact and luminous starburst. Some of the gas makes it all the way to the nucleus and efficiently feeds the growth of the central black hole. This active growth phase takes places buried inside the starburst, until the active nucleus creates feedback and injects energy back into its surrounding. As a consequence, the remaining gas is ejected revealing an X-ray bright AGN. This scenario was originally based on the Toomre & Toomre (1972)

sequence and developed by Sanders et al. (1988). In particular, it explained the similarity between the number density of bright quasars and that of ultraluminous infrared galaxies (ULIRGs, with infrared luminosity $> 10^{12} L_{\odot}$) as an evolutionary sequence of the same galaxy population. There is also direct evidence that quasars host that appear to be normal elliptical galaxies have signs of past strong gravitational interactions when more sensitive images are taken, revealing low surface brightness tidal tails and/or shells (Canalizo et al., 2007; Bennert et al., 2008).

However, recent studies of X-ray selected AGN claim that SMBH growth is largely secular and independent of major mergers and of the star formation rate in galaxies. This alternative scenario is supported by the observations that a large fraction of X-ray selected AGN reside in disk galaxies, which would not have survived a major merger (Gabor et al., 2009; Cisternas et al., 2011; Schawinski et al., 2011) and the lack of evidence for an excess of merger signatures in Hubble Space telescope imaging of high-redshift AGN hosts relative to non-AGN hosts (Grogin et al., 2005; Kocevski et al., 2011). Furthermore, the AGN hosts have star formation rates typical of normal star-forming galaxies given their stellar mass (i.e., not enhanced as expected in galaxies undergoing a major merger; Mullaney et al., 2011b). Some authors claim hybrid models where the high-luminosity end (quasar regime, with $L_{AGN} > 10^{44} \text{ erg s}^{-1}$) is dictated by major galaxy mergers while the lower-luminosity AGN follow a secular evolution (e.g., Shao et al., 2010; Lutz et al., 2010).

There are considerable observational difficulties, however. The conclusions derived from X-ray selected AGN samples are biased toward less obscured sources and hence suffer from an incomplete view of SMBHs. Identifying various AGN phases require multiple diagnostics given that each method has its own limita-

tions. In this thesis, we aim to shed light on the regime(s) of AGN growth by gathering a more complete sample of AGN including unobscured and obscured systems. With a better census of AGN, we will establish more accurate trends with their host galaxies. We are interested in moderate-luminosity AGN (with bolometric luminosity $10^{42.5} < L_{bol} < 10^{45} \text{ erg s}^{-1}$), which grow the central SMBH more slowly than quasars ($L_{bol} > 10^{45} \text{ erg s}^{-1}$) but which may be physically distinct from a yet weaker phase of accretion with $L_{bol} < 0.01 \times L_{Edd}$ (Ho, 2008; Trump et al., 2011). The latter may instead have a radiatively inefficient accretion flow (RIAF) and lack the broad line region and obscuring torus invoked in AGN unified models. Moderate-luminosity AGN are also much more numerous than quasars and live in galaxies that are more representative than quasar hosts. We will focus our work in that intermediate range.

It was shown that infrared-luminous galaxies were contributing more significantly to the cosmic star formation history at earlier epochs (Le Flocc'h et al., 2005; Magnelli et al., 2009), with a dominant contribution by luminous infrared galaxies (LIRGs, with $L_{IR} > 10^{11} L_{\odot}$) around $z \sim 1$. Is there a relation with the growth of the central SMBH? What fraction of these actively star forming galaxies also host an active galactic nucleus? To address these questions, we select infrared luminous galaxies (i.e., highly star-forming systems) in two different regimes: low-redshift LIRGs and ULIRGs (rare luminous objects at that epoch), and intermediate-redshift LIRGs (more common objects when approaching $z \sim 1$), and we study the presence of AGN in context with the host galaxy properties.

This thesis is organized as follows. In Chapter 2, we probe the molecular gas density profile in nearby LIRGS and ULIRGs by combining five molecular gas tracers spanning a broad range in critical density. We search for merger-

driven density effects with a comparison to radiative transfer models applied to simulations of isolated galaxies and galaxy major mergers. Combining our findings with results from the literature, we build a coherent picture where enhanced molecular gas density (which we attribute to be merger-driven) can cause both a starburst and SMBH accretion. The results from Chapter 2 are also published in Juneau et al. (2009). We then move on to study infrared-selected galaxies at intermediate redshift ($0.3 < z < 1$). Because traditional nebular line diagnostics become unavailable in optical spectra at $z > 0.4$, the first step is the design of a new AGN diagnostic diagram that is applicable to higher redshift. The Mass-Excitation (MEx) diagnostic is introduced in Chapter 3 and published in Juneau et al. (2011). Taking advantage of the very sensitive X-ray surveys conducted with the *Chandra* Space Observatory, we compare the MEx diagnostic AGN selection to standard X-ray selection methods. We present evidence that the MEx diagram not only recovers the majority of X-ray selected AGN, but it also finds additional AGN which are either absorbed or weak in their X-ray emission. Lastly, we apply multi-wavelength AGN diagnostics to FIR-selected galaxies in order to quantify the incidence of AGN including both unobscured and obscured cases (Chapter 4). We combine AGN selections from the MEx diagnostic diagram, the X-ray method based on luminosity in the hard band (2 – 10 keV) and on the hardness ratio, and two diagnostics based on IRAC colors, which probe AGN-heated dust emission. Once combined, these methods allow us to differentiate between X-ray unabsorbed AGN, X-ray absorbed AGN, and X-ray weak AGN. Possible implications for the mode of SMBH growth and the connection with host galaxies are discussed.

CHAPTER 2

ENHANCED DENSE GAS FRACTION IN ULTRA-LUMINOUS INFRARED GALAXIES

We present a detailed analysis of the relation between infrared luminosity and molecular line luminosity, for a variety of molecular transitions, using a sample of 34 nearby galaxies spanning a broad range of infrared luminosities ($10^{10} < L_{IR} < 10^{12.5} L_{\odot}$). We show that the power-law index of the relation is sensitive to the critical density of the molecular gas tracer used, and that the dominant driver in observed molecular line ratios in galaxies is the gas density. As most nearby ultra-luminous infrared galaxies (ULIRGs) exhibit strong signatures of active galactic nuclei (AGN) in their center, we revisit previous claims questioning the reliability of HCN as a probe of the dense gas responsible for star formation in the presence of AGN. We find that the enhanced HCN(1-0)/CO(1-0) luminosity ratio observed in ULIRGs can be successfully reproduced using numerical models with fixed chemical abundances and without AGN-induced chemistry effects. We extend this analysis to a total of ten molecular line ratios by combining the following transitions: CO(1 – 0), HCO⁺(1 – 0), HCO⁺(3 – 2), HCN(1 – 0), and HCN(3 – 2). Our results suggest that AGNs reside in systems with higher dense gas fraction, and that chemistry or other effects associated with their hard radiation field may not dominate (NGC 1068 is one exception). Galaxy merger could be the underlying cause of increased dense gas fraction and the evolutionary stage of such mergers may be another determinant of the HCN/CO luminosity ratio.

2.1 Introduction

Over the past 50 years, there have been a number of studies relating galaxy star formation rate (SFR) and the amount of molecular gas available. Schmidt (1959)

proposed a power-law relationship between star formation rate volume density and molecular gas volume density. Kennicutt (1998) (also see Kennicutt, 1989) framed the problem in terms of surface densities, yielding the Kennicutt-Schmidt relation: $\Sigma_{SFR} \propto \Sigma_{gas}^{1.4 \pm 0.15}$.

While a power-law index around 1.4 or 1.5 holds for the molecular gas traced by CO(1 – 0), a power-law index of unity was found when relating SFR to the molecular gas traced by HCN(1 – 0) (Solomon et al., 1992; Gao & Solomon, 2004b, hereafter GS04b). This difference in index is interpreted as a consequence of the different critical densities¹ of the molecular tracers used. Having a lower critical density, CO(1 – 0) traces the global molecular gas content, some of which may not be involved in the star formation process, whereas HCN(1 – 0) traces denser molecular gas ($n > 10^4 \text{ cm}^{-3}$) more closely linked to star formation. Since the Solomon et al. (1992) and Gao & Solomon (2004a, hereafter GS04a) observations, several interpretations regarding the linear L_{IR} -HCN(1 – 0) relation in galaxies have been put forth by both observational arguments and numerical models.

For example, by extending the linear relationship between the total infrared luminosity, $L_{IR} [\equiv L(8-1100\mu\text{m})]$, and HCN(1 – 0) to Galactic cloud cores, Wu et al. (2005) added to the original GS04b interpretation by framing the relationship in terms of individual star-forming dense-gas “units”. As one increases the number of dense star-forming clumps in a galaxy, L_{IR} and HCN(1 – 0) both increase in lock-step. In this view, the only difference between an extreme starburst galaxy and Galactic star-forming region is the number of dense star-forming units emitting HCN and infrared emission.

Recent observations may challenge the existence of the tight, linear correla-

¹ $n_{crit} \equiv A_{ul}/\Gamma_{ul}$, where A_{ul} is the Einstein A coefficient and Γ_{ul} is the collision rate for a transition from upper (u) to lower (l) energy level.

tion between L_{IR} and HCN(1 – 0) luminosity² reported by GS04b. For instance, Graciá-Carpio et al. (2008, hereafter GC08) obtained new HCN and HCO⁺ measurements for 17 luminous and ultra-luminous infrared galaxies (LIRGs: $10^{11} < L_{\text{IR}} < 10^{12} L_{\odot}$ and ULIRGs: $L_{\text{IR}} > 10^{12} L_{\odot}$). They found conflicting HCN(1 – 0) measurements for several galaxies that overlap with the Solomon et al. (1992) sample. They attribute the differences to calibration errors in the older survey, and proceed to compare their revised $L_{\text{IR}}-L'_{\text{HCN}}$ relation with the original one. They find a larger and more significant increase of $L_{\text{IR}}-L'_{\text{HCN}}$ with L_{IR} , meaning that the $L_{\text{IR}}-L'_{\text{HCN}}$ power-law would be steeper than an index of unity. These authors interpreted the higher $L_{\text{IR}}/L'_{\text{HCN}}$ ratio as an enhanced star formation efficiency in ULIRGs.

A large fraction of nearby LIRGs and ULIRGs appear to be mergers of gas-rich progenitor galaxies and therefore have a high concentration of dense molecular gas in their center which feeds strong starburst and AGN activity (see Sanders & Mirabel, 1996, and references therein). It has been noted that sources with brighter IR luminosities are both more likely to host an AGN (e.g. Veilleux et al., 1995; Lutz et al., 1998; Veilleux et al., 1999), as well as show higher HCN(1 – 0)/CO(1 – 0) molecular line luminosity ratios (GS04b, Graciá-Carpio et al., 2006). It is tempting to associate the increased HCN(1 – 0)/CO(1 – 0) luminosity ratio with the presence of AGN. Indeed, Graciá-Carpio et al. (2008) report evidence for an enhanced abundance of HCN in ULIRGs, and caution that care must be taken when converting HCN line luminosities into dense gas masses.

Moreover, some theoretical work suggests that AGN-induced processes could potentially increase the abundance of HCN (e.g. Lintott & Viti, 2006), causing the observed $L_{\text{IR}}-L'_{\text{HCN}}$ relation to have a shallower slope than the $L_{\text{IR}}-L'_{\text{CO}}$ rela-

²We use the notation L' for molecular line luminosities as they are expressed in $\text{K km s}^{-1} \text{pc}^2$, whereas other luminosities are expressed in L_{\odot} .

tion. In this picture, X-ray emission resulting from AGN buried in ULIRGs may enhance the abundance of HCN molecules via an increased availability of free electrons that facilitates combination with ions (e.g., $\text{HCNH}^+ + e^- \rightarrow \text{HCN} + \text{H}$). Some high-resolution HCN observations of nearby galaxies have shown stronger emission of $\text{HCN}(1-0)$ relative to $\text{CO}(1-0)$ in the center of a few LIRGs and ULIRGs known to host an AGN (e.g. Graciá-Carpio et al., 2006; Krips, 2007). These authors have interpreted this higher molecular line ratio in terms of an increased abundance of HCN. Others interpret high molecular line ratios in terms of the mid-plane pressure, in the sense that larger ambient pressure could trap or maintain dense gas (Levine et al., 2008; Blitz & Rosolowsky, 2006).

In recent years, new theoretical models suggest a different physical explanation for the observed L_{IR} -molecular line luminosity relationships. Specifically, models that couple non-local thermodynamic equilibrium (LTE) radiative transfer calculations with models of star-forming giant molecular clouds (GMCs) (Krumholz & Thompson, 2007) and hydrodynamic simulations of disk galaxies and galaxy mergers (Narayanan et al., 2008b) find that the driving force controlling the $\text{SFR}-L_{\text{mol}}$ relation in galaxies is the fraction of thermalized molecular gas at a given molecular transition. In the Krumholz & Thompson (2007) and Narayanan et al. (2008b) picture, the SFR is controlled by the relation $\text{SFR} \propto n^{1.5}$, where n is the number density of molecular hydrogen. When the observed molecular line traces the bulk of the molecular gas in the galaxy (e.g. $\text{CO}(1-0)$), the $\text{SFR}-L_{\text{mol}}$ power-law index (hereafter “slope” as this relationship is typically considered in log-log space) is equivalent to the Kennicutt-Schmidt index (i.e. close to 1.5). On the other hand, higher critical density molecular line tracers (e.g. $\text{HCN}(1-0)$) trace an increasingly smaller fraction of the gas in a galaxy, and so the index in the observed $\text{SFR}-L_{\text{mol}}$ power-law relation decreases. These theo-

ries were tested by Bussmann et al. (2008), who observed HCN(3 – 2) — a higher critical density tracer than HCN(1 – 0)— in the GS04a,b sample of galaxies, and found a SFR-HCN(3 – 2) index less than unity (0.72 ± 0.08).

In this paper, we expand on the Bussmann et al. work by studying the relationship between five molecular line tracers and infrared luminosity. In particular, we emphasize the importance of considering the critical density of each molecular line tracer. We present support that HCN(1 – 0) is a valid probe of dense molecular gas and we revisit the interpretation of the enhanced HCN(1 – 0)/CO(1 – 0) luminosity ratio in high IR luminosity systems. Our results suggest that this feature is primarily driven by the increased dense gas fraction in galaxies undergoing a merger and/or a strong episode of starburst activity; we do not require X-ray driven chemical abundance effects to explain the observed molecular line ratios. Overall, we build a coherent picture where the governing parameter is the density distribution of the molecular gas.

We describe our sample of 34 galaxies in §2.2, along with the measurements that we use. Section 2.3 contains our results regarding power-law relationships between infrared luminosity and various molecular line luminosities (§2.3.1), as well as the study of molecular line ratios as a function of infrared luminosity (§2.3.2). The interpretation is partially based on the theoretical models of Narayanan et al. (2008b), which we apply to this study in §2.4. We include a brief discussion of chemistry effects in §2.5 and present our conclusions in §2.6. Throughout this paper we assume a flat Λ CDM cosmological model with $(\Omega_M, \Omega_\Lambda, H_0) = (0.3, 0.7, 70 \text{ km s}^{-1} \text{ Mpc}^{-1})$.

2.2 Methods

2.2.1 Sample

Our primary sample consists of 29 nearby galaxies with HCN(1 – 0) observations (Gao & Solomon, 2004b) as well as integrated optical spectroscopy (Moustakas & Kennicutt, 2006, hereafter MK06). We obtained follow-up HCN(3 – 2) observations for 22 of these 29 galaxies (10 detections and 12 upper limits) using the 10 m Heinrich Hertz Submillimeter Telescope (see Bussmann et al., 2008, hereafter B08 for more detail on the HCN(3 – 2) observations). In order to expand our sample and include additional transitions spanning a range of critical densities and excitation states, we incorporate the sample from Graciá-Carpio et al. (2008, hereafter GC08). These authors include observations of the HCN(1 – 0), HCN(3 – 2), HCO⁺(1 – 0), HCO⁺(3 – 2) transitions for 17 galaxies, of which 12 overlap with our original sample. Thus, the combined sample comprises 34 galaxies. We note a distinction between our primary sample and that of GC08. While the GC08 sample spans the high infrared luminosities ($L_{IR} = 10^{11.3} - 10^{12.5} L_{\odot}$), our sample extends the range down to $L_{IR} \sim 10^{10} L_{\odot}$.

Molecular line and (far-)infrared luminosities are tabulated in Table 2.2.1. When combining our primary sample and GC08 sample, we convert all the luminosities to common cosmological parameters and luminosity distances. The CO(1 – 0) and HCN(1 – 0) measurements were taken from GS04a,b. When available, we substitute updated HCN(1 – 0) luminosities from GC08. These authors published new HCN(1 – 0) luminosities for their 17 galaxies and found significantly different values for galaxies overlapping with the Solomon et al. (1992) subsample. These galaxies were also included in the GS04b compilation and the new values from GC08 are approximately a factor of two lower in several cases. GC08 attributed these discrepancies to observational errors, namely the calibration of the

receiver used on the 30-m IRAM telescope during the earlier observations.

$L'_{\text{HCN}(3-2)}$ values were obtained from B08 (see Appendix A) and GC08. Among eight galaxies in common, five have consistent values within the uncertainty, in which case we use the average (or the maximum upper limit in the case of two upper limits). We adopt the GC08 measurements for two non-detections in B08 (Mrk 231 & IRAS 17208-0014), as well as for NGC 6240, which had a discrepant measurement. This galaxy has a very broad HCN(3 – 2) emission line, so in this case we prefer to use the data from GC08 because of their significantly wider bandwidth.

We use the $L'_{\text{HCO}^+(1-0)}$ and $L'_{\text{HCO}^+(3-2)}$ measurements published in GC08 with a conversion for the luminosity distances adopted here. On average, this distance conversion changes molecular line luminosities by 0.055 dex (min=-0.073 and max=0.16), which is less than the average uncertainty on these quantities.

Observing different molecular transitions with a variety of telescopes leads to varying beam sizes. Since most sources in the samples we use in this study have not been mapped, it is important to consider aperture effects associated with the use of varying beam sizes. First, two galaxies have a lower limit in HCN(1 – 0) because they were not mapped even though they are nearby (NGC 660 and NGC 2903, see GS04a). For the HCN(3-2) observations in B08, the beam size of 30'' is sufficient to cover the central kpc for galaxies beyond 7 Mpc. We expect to detect most of the HCN(3-2) emission in these cases since it is the dense nuclear regions of galaxies that are responsible for the majority of the emission from molecular transitions with high critical densities for excitation. Meanwhile, targets selected for study in GC08 all lie at distances >60 Mpc and therefore we are assured of sampling the full extent of the high density molecular emission.

Table 2.1. Infrared, far-infrared and molecular line luminosities for our combined sample of 34 galaxies

Source	D_L (Mpc)	L_{IR} $\log(L_\odot)$	L_{FIR} $\log(L_\odot)$	$L'_{CO(1-0)}$ $\log(L')$	^a $L'_{HCN(1-0)}$ $\log(L')$	^a $L'_{HCN(3-2)}$ $\log(L')$	$L'_{HCO+(1-0)}$ $\log(L')$	$L'_{HCO+(3-2)}$ $\log(L')$	Class
IC 1623	84 ± 6	11.64 ± 0.07	11.48 ± 0.07	10.14 ± 0.10	8.95 ± 0.10	SF
NGC 520	37 ± 3	11.04 ± 0.09	10.93 ± 0.09	9.38 ± 0.10	7.97 ± 0.10	7.15 ± 0.09	SF/AGN
NGC 660	13 ± 1	10.50 ± 0.11	10.37 ± 0.11	8.80 ± 0.10	> 7.35	6.60 ± 0.11	SF/AGN
NGC 695	135 ± 7	11.62 ± 0.05	11.48 ± 0.05	9.98 ± 0.10	8.29 ± 0.09	< 7.75	8.44 ± 0.06	< 7.84	SF
NGC 1068	16 ± 1	11.41 ± 0.10	11.04 ± 0.10	9.31 ± 0.10	8.55 ± 0.10	7.58 ± 0.09	AGN
NGC 1144	119 ± 7	11.39 ± 0.06	11.27 ± 0.06	10.06 ± 0.10	8.45 ± 0.10	SF
NGC 1614	67 ± 5	11.60 ± 0.08	11.40 ± 0.08	9.45 ± 0.10	8.15 ± 0.10	< 7.36	SF/AGN
05189-2524 ^b	180 ± 7	12.08 ± 0.04	11.84 ± 0.04	9.87 ± 0.10	8.84 ± 0.10	AGN
NGC 2146	17 ± 2	11.08 ± 0.10	10.93 ± 0.10	9.24 ± 0.10	8.12 ± 0.10	6.41 ± 0.10	SF/AGN
Arp 55	170 ± 7	11.66 ± 0.04	11.56 ± 0.04	10.14 ± 0.10	8.69 ± 0.04	< 8.17	8.65 ± 0.06	8.11 ± 0.12	SF
NGC 2903	8 ± 1	10.23 ± 0.18	10.08 ± 0.18	8.68 ± 0.10	> 7.27	5.95 ± 0.10	SF
UGC 05101	170 ± 7	11.93 ± 0.04	11.84 ± 0.04	9.76 ± 0.10	8.98 ± 0.04	< 7.87	8.70 ± 0.07	8.45 ± 0.04	AGN

Table 2.1—Continued

Source	D_L (Mpc)	L_{IR} $\log(L_\odot)$	L_{FIR} $\log(L_\odot)$	$L'_{CO(1-0)}$ $\log(L')$	^a $L'_{HCN(1-0)}$ $\log(L')$	^a $L'_{HCN(3-2)}$ $\log(L')$	$L'_{HCO+(1-0)}$ $\log(L')$	$L'_{HCO+(3-2)}$ $\log(L')$	Class
NGC 3079	19 ± 1	10.76 ± 0.09	10.65 ± 0.09	9.54 ± 0.10	8.16 ± 0.10	7.20 ± 0.08	SF/AGN
NGC 3628	11 ± 1	10.36 ± 0.09	10.24 ± 0.09	9.24 ± 0.10	7.77 ± 0.10	6.56 ± 0.10	SF
NGC 3893	15 ± 1	10.14 ± 0.09	10.00 ± 0.09	8.71 ± 0.10	7.46 ± 0.10	< 6.00	SF
NGC 4414	17 ± 0	10.54 ± 0.02	10.40 ± 0.02	9.22 ± 0.10	7.76 ± 0.10	< 5.70	SF
Arp 193	106 ± 7	11.64 ± 0.06	11.55 ± 0.06	9.72 ± 0.10	8.49 ± 0.03	7.88 ± 0.04	8.70 ± 0.03	8.23 ± 0.03	AGN
NGC 5194	8 ± 1	10.33 ± 0.13	10.20 ± 0.13	9.13 ± 0.10	7.54 ± 0.10	SF
UGC 08696	165 ± 7	12.09 ± 0.04	11.98 ± 0.04	9.89 ± 0.10	8.87 ± 0.05	8.56 ± 0.09	8.88 ± 0.05	8.53 ± 0.04	AGN
Arp 220	85 ± 6	12.16 ± 0.07	12.08 ± 0.07	10.01 ± 0.10	9.23 ± 0.01	8.82 ± 0.02	8.89 ± 0.02	8.23 ± 0.02	AGN
NGC 6240	111 ± 7	11.84 ± 0.06	11.69 ± 0.06	10.01 ± 0.10	8.89 ± 0.04	8.78 ± 0.04	9.15 ± 0.02	8.45 ± 0.06	AGN
17208-0014 ^b	187 ± 7	12.32 ± 0.04	12.25 ± 0.04	10.24 ± 0.10	9.27 ± 0.03	8.87 ± 0.04	9.10 ± 0.04	8.67 ± 0.05	SF
NGC 6701	61 ± 5	11.07 ± 0.08	10.94 ± 0.08	9.59 ± 0.10	8.20 ± 0.10	7.43 ± 0.13	SF/AGN
NGC 7130	71 ± 6	11.35 ± 0.07	11.22 ± 0.07	9.73 ± 0.10	8.59 ± 0.10	SF/AGN

2.2.2 Optical AGN Classification

The nature of the powering source of galaxies in our sample (star formation, AGN, or hybrid i.e. hosting both star formation and AGN activity) is determined using the optical diagnostic diagram known as the *BPT diagram* (Baldwin et al., 1981; Veilleux & Osterbrock, 1987; Osterbrock, 1989). The optical emission-line ratios used in this diagram ($[\text{O III}] \lambda 5007/\text{H}\beta$ and $[\text{N II}] \lambda 6584/\text{H}\alpha$) probe a combination of the oxygen abundance and ionization parameter of the interstellar medium (ISM) present in these galaxies. This provides us with an indirect signature of the source of ionizing radiation (young stars versus AGN). As shown in Figure 2.1, the Sloan Digital Sky Survey (SDSS, York et al., 2000) galaxies (gray area and contours) show a tight excitation sequence of star-forming galaxies (below the solid line from Kauffmann et al. (2003)), as well as a plume of galaxies that are either hybrid (between the solid and dashed lines) or AGN (above the dashed line adapted from Kewley et al. (2001b)). The SDSS emission-line measurements are taken from the MPA/JHU SDSS team website³ (Brinchmann et al., 2004; Tremonti et al., 2004) based on observations of galaxies contained in the SDSS data release 7 (DR7; Abazajian et al., 2009).

Galaxies from our combined sample are overlaid with colored symbols. Among 34 galaxies, 13 are classified as star-forming (SF, red circles), 10 galaxies are classified as hybrid (SF/AGN, green squares) and 11 galaxies show a strong signature of AGN (blue triangles). These numbers include five galaxies which are classified but not shown on the diagram. Two galaxies (Mrk 231 and NGC 7469) have obvious broad emission lines in their optical spectrum indicating a Type 1 (broad-line) AGN, and therefore need not be classified using this narrow-line diagnostic. IRAS 23365+3604 fails the signal-to-noise cut for the $[\text{N II}] \lambda 6584$ line but occupies

³<http://www.mpa-garching.mpg.de/SDSS/DR7>

Table 2.1—Continued

Source	D_L (Mpc)	L_{IR} $\log(L_\odot)$	L_{FIR} $\log(L_\odot)$	$L'_{CO(1-0)}$ $\log(L')$	^a $L'_{HCN(1-0)}$ $\log(L')$	^a $L'_{HCN(3-2)}$ $\log(L')$	$L'_{HCO^+(1-0)}$ $\log(L')$	$L'_{HCO^+(3-2)}$ $\log(L')$	Class
IC 5179	50 ± 4	11.18 ± 0.08	11.05 ± 0.08	9.49 ± 0.10	8.61 ± 0.10	SF
NGC 7469	69 ± 2	11.59 ± 0.04	11.39 ± 0.04	9.59 ± 0.10	8.43 ± 0.02	7.87 ± 0.05	8.59 ± 0.01	7.79 ± 0.09	AGN
23365+3604 ^b	269 ± 6	12.12 ± 0.02	11.97 ± 0.02	9.94 ± 0.10	8.78 ± 0.08	< 8.47	8.61 ± 0.10	...	AGN
NGC 7771	60 ± 5	11.35 ± 0.08	11.23 ± 0.08	9.96 ± 0.10	8.63 ± 0.01	7.85 ± 0.03	8.62 ± 0.03	7.67 ± 0.08	SF
Mrk 331	77 ± 6	11.42 ± 0.07	11.28 ± 0.07	9.75 ± 0.10	8.41 ± 0.02	7.66 ± 0.10	8.50 ± 0.02	7.94 ± 0.07	SF/AGN
Mrk 231 ^c	188	12.51 ± 0.07	12.26 ± 0.07	10.00 ± 0.10	9.09 ± 0.03	8.49 ± 0.05	9.07 ± 0.04	8.50 ± 0.06	AGN
12112+0305 ^{b,c}	335	12.31 ± 0.07	12.19 ± 0.07	...	9.22 ± 0.09	< 8.90	8.99 ± 0.11	...	AGN
VII Zw 31 ^c	241	11.96 ± 0.07	11.83 ± 0.07	10.16 ± 0.10	8.84 ± 0.07	< 8.57	8.90 ± 0.06	8.44 ± 0.10	SF
Arp 299A ^c	50 ± 4	11.67 ± 0.07	11.48 ± 0.07	...	8.21 ± 0.02	7.45 ± 0.11	8.48 ± 0.02	7.93 ± 0.04	SF/AGN
Arp 299B ^c	50 ± 4	11.56 ± 0.07	11.29 ± 0.07	...	8.02 ± 0.03	< 7.19	8.22 ± 0.03	7.55 ± 0.07	SF/AGN

The optical classification is included in the last column.

a: When no formal uncertainties are available for published CO(1-0) or HCN(1-0) line luminosities, we estimate the calibration error to be 0.1 dex (20–25%).

b: Full galaxy name starts with *IRAS*.

c: These five galaxies are not part of our primary sample. L_{IR} and L_{FIR} were obtained from GC08 after converting their luminosity distance to our assumed cosmology ($\{\Omega_M, \Omega_\Lambda, H_0\} = \{0.3, 0.7, 70 \text{ km s}^{-1} \text{ Mpc}^{-1}\}$). Because GC08 do not provide errors on L_{IR} and L_{FIR} , we use the mean error for the rest of our sample (≈ 0.07 dex).

the AGN portion of the [O I] $\lambda 6300/\text{H}\alpha$ diagram. Finally, Arp 299A & Arp 299B are both classified as SF/AGN based on the classification of the Arp 299 system. With the exception of IRAS 12112+0305 and VII Zw 31, spectra were obtained with a long-slit drift-scanning technique in order to integrate the light spatially (MK06). Spectroscopic measurements for IRAS 12112+0305 and VII Zw 31 were obtained from Veilleux et al. (1999) and from Wu et al. (1998), respectively.

We note that dust obscuration can challenge the identification of an AGN in the optical spectral range. Sufficient optically thick material with a large covering fraction surrounding the nuclear region could potentially mask all AGN signatures at these wavelengths. However, we identify an AGN in all but one of the most IR-bright galaxies (IRAS 17208-0014). The latter is the only optically-obscured, potentially MIR-obscured, AGN candidate sometimes referred to as *buried* AGN (Imanishi, 2009). We also note that although this diagnostic indicates the presence of an AGN, it does not allow to quantify its strength and its relative contribution to the total infrared light of its host galaxy. For example, the well-known ULIRG Arp 220 is thought to be mainly powered by star formation (Lutz et al., 1996) even though it is known to host a Seyfert nucleus (Rieke et al., 1985). Furthermore, there has been accumulating evidence that most LIRGs and ULIRGs are mainly powered by starbursts (Lutz et al., 1998; Genzel et al., 1998; Farrah et al., 2003; Vega et al., 2008; Nardini et al., 2008), except for a few notable cases such as Mrk 231 (Condon et al., 1991; Spoon et al., 2007), IRAS 05189-2524 (Spoon et al., 2007; Armus et al., 2007), and NGC 1068 (Le Floch et al., 2001). These three examples stand out from the rest of our sample as they exhibit the largest mid-IR excesses (they correspond to the three blue triangles below the dotted line in Figure 2.2).

Among others, (Nardini et al., 2008) report that the AGN contribution may

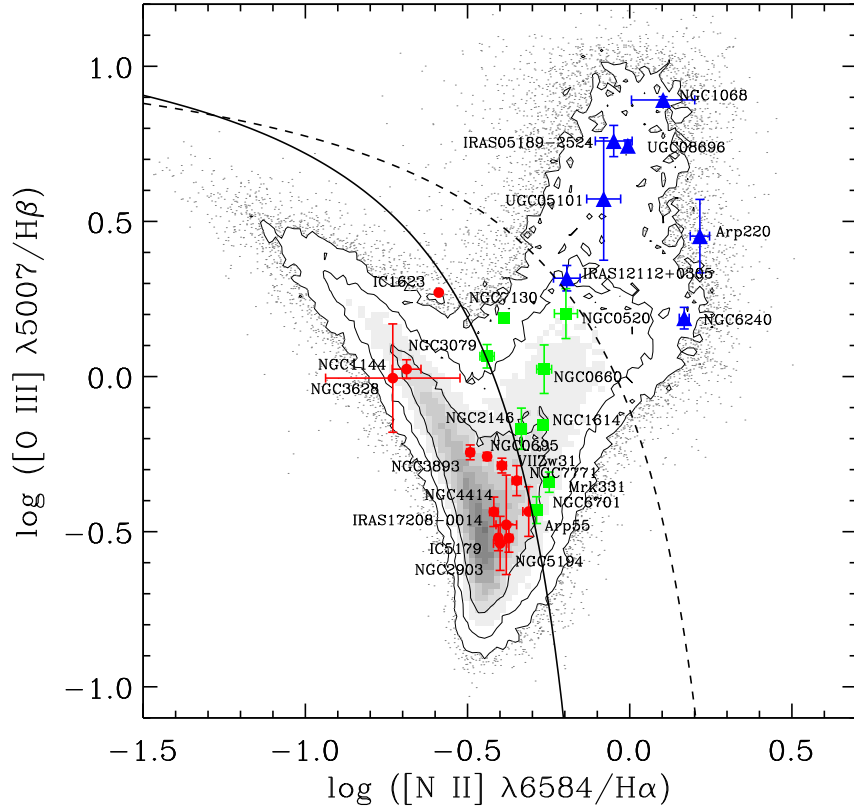


Figure 2.1 Emission-line diagnostic diagram indicating the position of normal star-forming galaxies (*below and to the left of the solid curve*), AGNs (*above and to the right of the dashed curve*), and galaxies with an admixture of star formation and AGN activity (*between the solid and dashed curves*). The individual galaxies in our sample are labeled and plotted using color symbols with error bars, with the exception of five galaxies mentioned in the text. The different symbols represent the optical spectral type: star-forming (SF) (*red circles*); AGN (*blue triangles*); and SF/AGN (*green squares*). For reference, the gray-scale and contours (enclosing 52%, 84%, and 97% of the points) show the locus of emission-line galaxies in the SDSS. The solid and dashed curves are adapted from Kauffmann et al. (2003) and Kewley et al. (2001b), respectively.

dominate in the mid-IR range while remaining a small fraction of the total infrared light, typically less than 25%. Recent work suggests a correlation between the optical spectral classification and the AGN contribution to the bolometric luminosity of ULIRGs. Using a sample of 74 ULIRGs, Veilleux et al. (2009) find that the AGN contribution ranges from $\sim 15\%$ – 35% among purely star-forming (SF) and LINER ULIRGs to ~ 50 and 75% among Seyfert 2 and Seyfert 1 ULIRGs, respectively. Individual galaxies may deviate from this trend as their sample includes a Seyfert 2 ULIRG with as little as 20% AGN contribution and SF-classified ULIRGs with roughly 50% AGN contribution. Thus, we stress that although the optical classification used here indicates the presence of an AGN, it does not allow us to quantify its contribution at infrared wavelengths on a galaxy-by-galaxy basis. Indeed, several systems classified as AGN are also undergoing major episodes of star formation.

2.2.3 Infrared Luminosity

We estimate far-infrared [$L_{FIR} \equiv L(40 - 500 \mu\text{m})$] and total infrared [$L_{IR} \equiv L(8 - 1100 \mu\text{m})$] luminosities of the galaxies in our sample using IRAS observations at 12, 25, 60, and 100 μm (Sanders et al., 2003). Following Moustakas et al. (2006), we model the infrared spectral energy distribution of each object longward of 100 micron using a modified blackbody with dust emissivity proportional to λ^{-1} and dust temperature given by the observed $S_\nu(60 \mu\text{m})/S_\nu(100 \mu\text{m})$ flux ratio (Gordon et al., 2000; Bell, 2003). We then integrate numerically over the appropriate wavelength range to derive L_{FIR} and L_{IR} .

When interpreting galaxy infrared luminosity, one has to take into account potential contributions of recent or ongoing star formation, older stellar populations, and AGN. In the case of LIRGs and ULIRGs, the infrared emission from dust heated by powerful starbursts dominates over that contributed by old stars,

so we ignore the older stellar population component. It has been suggested that because the typical AGN IR SED peaks in the mid-infrared range (around $\lambda = 10 - 20 \mu\text{m}$, e.g. Elvis et al., 1994), the far-infrared portion of the SED roughly corresponds to the star-forming component. We compare the total IR and FIR emission in Figure 2.2 and find a similar ratio ($L_{IR}/L_{FIR} = 1.38$) to that reported in the literature (1.3, GC08). Most of the galaxies in our sample lie within one sigma of the mean value obtained for a control sample of galaxies (MK06, small plotting symbols in Figure 2.2). There are a few outliers, the most striking example being the prototype Seyfert 2 galaxy NGC 1068, which has the largest MIR-excess and lies 4.5σ from the mean. Interestingly, even when the fractional AGN contribution to the mid-IR light dominates over the starburst contribution, it still appears to be the case that the AGN total IR contribution is mostly less than 25-30% (Nardini et al., 2008).

The larger spread in L_{IR}/L_{FIR} ratios observed in brighter galaxies may be related to a combination of varying extinction and AGN contribution. For instance, Veilleux et al. (2009) suggest an evolutionary sequence with three AGN classes for nearby ULIRGs. The first class is characterized by small extinctions and large PAH equivalent widths. ULIRGs in this class are highly starburst-dominated. The second class includes galaxies with large extinctions but that are still likely dominated by starburst; while galaxies belonging in the third class show both small extinctions and PAH equivalent widths and have a significant AGN contribution (at least as important as the starburst). A detailed analysis is beyond the scope of this paper, but we refer the reader to published analyses utilizing mid-infrared spectroscopy (Lutz et al., 1998; Genzel et al., 1998; Spoon et al., 2007; Armus et al., 2007; Farrah et al., 2007, e.g.). Here, we simply identify the presence of an AGN using optical emission lines (§2.2.2) and we do not attempt to quantify

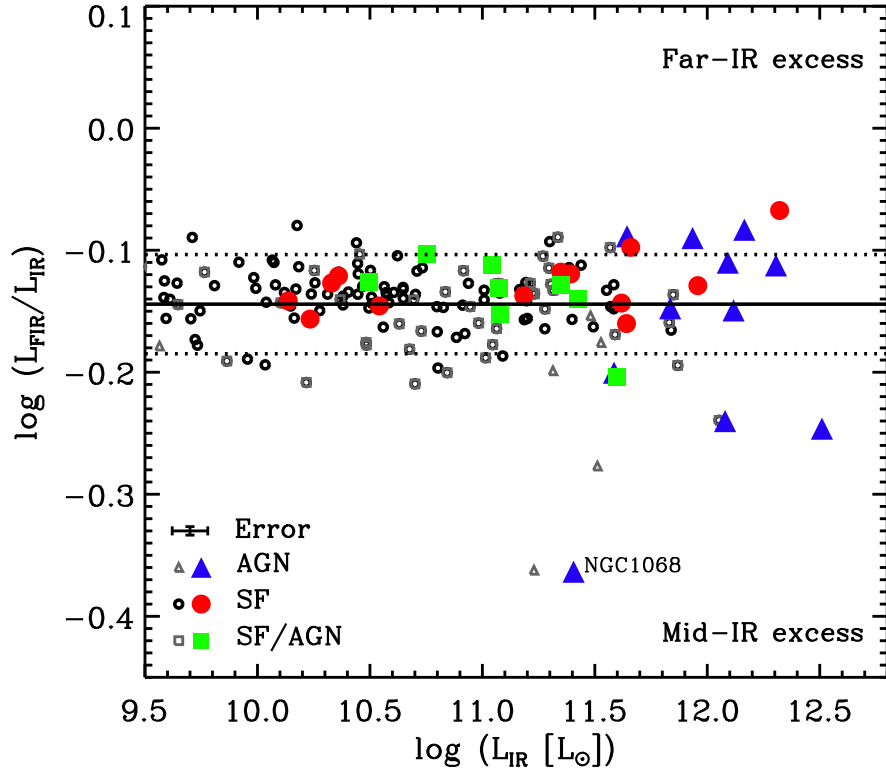


Figure 2.2 FIR/IR luminosity ratio for the MK06 sample of galaxies (gray and black open symbols) and for our combined sample of galaxies (filled colored symbols as in Figure 2.1, also see legend). We find an average value of $\log(L_{FIR}/L_{IR}) = -0.14$ (corresponding to $L_{IR}/L_{FIR} = 1.38$, which is close to the value of 1.3 used in GC08). Although most of the galaxies in our sample are fairly close to that value, there are some noticeable outliers, the most striking one being NGC 1068. We stress that our results remain unchanged (within the uncertainties) if we adopt FIR instead of total IR luminosities in our analysis.

its contribution, given the large uncertainties in doing so.

Because we do not interpret L_{IR} strictly as a SFR, we choose to plot the total infrared luminosity throughout this paper. We repeated our analysis using FIR instead of IR luminosity. This change has a negligible effect on our results (the differences are all well within the uncertainties, see Tables 2.2 & 2.3).

2.2.4 Numerical Models

We utilize the numerical models of Narayanan et al. (2008b) as a comparison for our observations. We refer the reader to this work for details on the models, though we summarize the aspects most relevant to the present study.

In an effort to model the observed SFR- L_{mol} relations in galaxies, Narayanan et al. (2008b) coupled 3D non-LTE radiative transfer calculations with smoothed particle hydrodynamics (SPH) simulations of galaxies in evolution. The SPH simulations were calculated utilizing a modified version of the publicly available code GADGET-2 (Springel, 2005), including prescriptions for a multi-phase ISM, supernovae pressurization of the ISM, and star-formation following a generalized (3D) version of the Kennicutt-Schmidt law (Springel & Hernquist, 2003). Here, we set the index of the Kennicutt-Schmidt relation to 1.5, which has important consequences in driving the simulated SFR- L_{mol} relations (Narayanan et al., 2008b). We additionally include energy feedback from accreting AGN (Springel et al., 2005), though note that it has negligible impact on the simulated SFR- L_{mol} relations.

The molecular line emission properties of the model galaxies were extracted using the 3D non-LTE radiative transfer code, *Turtlebeach* (Narayanan et al., 2006). *Turtlebeach* considers both collisional and radiative (de-)excitation in determining the level populations of a given molecule, and utilizes Monte Carlo methods for sampling the spatial and frequency domains. Because the hydrodynamic simu-

lations typically have a coarser physical resolution than the scale of GMCs, sub-grid prescriptions for including GMCs as singular isothermal spheres following a Galactic mass spectrum and mass-radius relation have been implemented (for details, please see Narayanan et al., 2006, 2008a).

The SPH simulations consist of ~ 100 galaxies comprised of isolated disks as well as gas-rich, binary, 1:1 galaxy mergers. The structure of the galaxies were initialized following the Mo et al. (1998) formalism. In order to probe a relatively large dynamic range of galaxies, the galaxies were initialized with gas fractions $f_g[0.2, 0.4, 0.8]$ and total (halo) mass ranging from $\sim 1 \times 10^{12} M_\odot$ to $\sim 4 \times 10^{13} M_\odot$ spaced in 4 mass bins. The galaxy mergers were run at a single initial gas fraction and mass ($f_g=0.4$ and $M_{\text{DM}}=1 \times 10^{12} M_\odot$). A key feature of these simulations is that they include constant Galactic abundances for HCN and CO, i.e. no chemistry is modeled. These simulations were shown to accurately recover the observed $L_{\text{IR}}\text{-HCN}(1-0)$, $L_{\text{IR}}\text{-CO}(1-0)$ and $L_{\text{IR}}\text{-CO}(3-2)$ relations. Furthermore, they predicted a sub-linear $L_{\text{IR}}\text{-HCN}(3-2)$ relation, which was subsequently observed by B08.

The HCN and CO simulations were taken from the study of (Narayanan et al., 2008b), while HCO^+ simulations of gas-rich galaxy mergers were run specifically for this work.

2.3 Results

2.3.1 Correlation Between Molecular Line and Infrared Luminosities

The molecular gas tracers used in this work span a broad range of critical densities ($n_{\text{crit}} \equiv A_{ul}/\Gamma_{ul}$) varying between $\sim 10^{3.3} \text{ cm}^{-3}$ for $\text{CO}(1-0)$ and $\sim 10^{7.7} \text{ cm}^{-3}$ for $\text{HCN}(3-2)$ (Figure 2.3). Although the critical density of $\text{HCN}(1-0)$ is an order of magnitude larger than that of $\text{HCO}^+(1-0)$ it is almost a perfect match to

the critical density of $\text{HCO}^+(3-2)$. In what follows, we consider the values of n_{crit} at an assumed temperature of 30 K, noting that they are roughly constant over a broad range of temperatures (20 – 100 K, see Figure 2.3). Even though we use n_{crit} to guide some of our interpretations, we caution that molecular gas emission can be observed in gas with densities less than critical (Evans, 1999). Substituting critical densities with effective densities as defined in Evans (1999) does not alter our main conclusions.

Assuming that L_{IR} (or L_{FIR}) provides a good estimate of SFR and that the molecular line luminosity traces the mass of molecular gas above a certain density, $L_{IR} - L'_{mol}$ relations (or their surface density equivalent) are commonly interpreted and/or used to derive universal SFR prescriptions. In this section, we present relationships between galaxy infrared luminosity and the luminosity of various molecular lines. We compute the slope (β) between $\log(L_{IR})$ and molecular line luminosity of $\text{CO}(1-0)$, $\text{HCO}^+(1-0)$, $\text{HCO}^+(3-2)$, $\text{HCN}(1-0)$ and $\text{HCN}(3-2)$ (Figure 2.4). When available, we compute the slope for the combined sample (solid lines). However, observations for the $\text{HCO}^+(1-0)$ and $\text{HCO}^+(3-2)$ transitions are only available for the GC08 sample (open symbols). The latter sample comprises fewer galaxies and is biased towards higher infrared luminosities, resulting in derived slopes (dashed lines) with much larger uncertainties. Galaxies hosting an AGN (blue triangles) occupy the bright end of L_{IR} but appear to follow the same relationship as the rest of the sample. Molecular line non-detections are shown with arrows but are not included when computing the slope (β) or the Pearson correlation coefficient (r).

All slopes are computed using the LINMIX IDL routines from Kelly (2007). In these routines, the distributions of independent variables are modeled as a mixture of Gaussian functions, which allows for greater flexibility when comput-

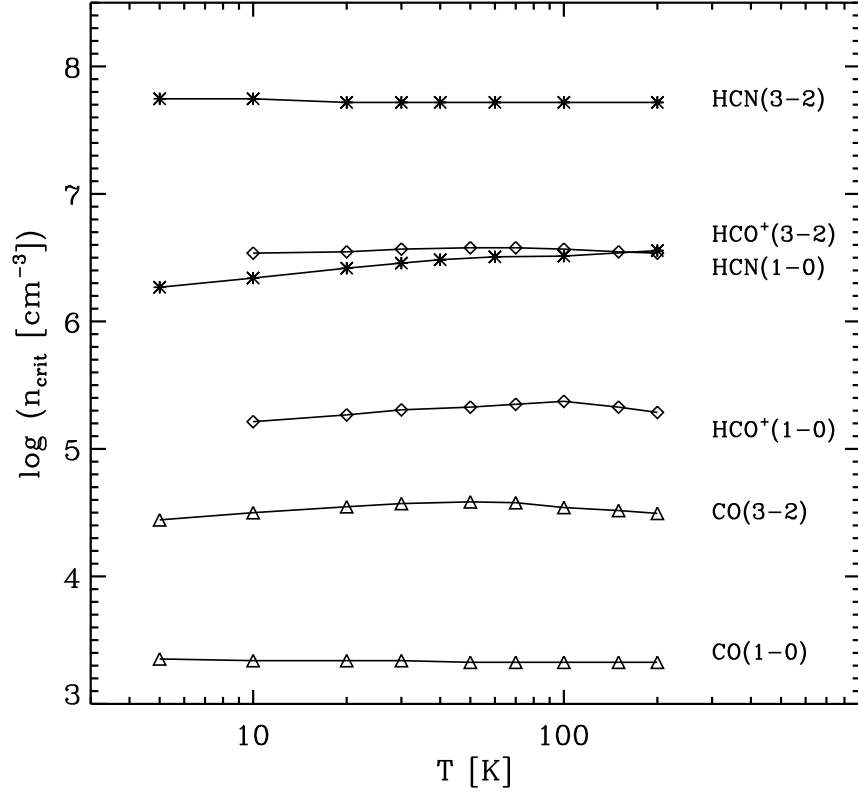


Figure 2.3 Critical density, $n_{crit} \equiv A_{ul}/\Gamma_{ul}$, for typical molecular transitions used to trace molecular gas in galaxies. The critical density is fairly insensitive to temperature over a wide range. Note that the HCN(1-0) and HCO⁺(3-2) transitions have a remarkably close value of critical density, whereas the critical density of HCO⁺(1-0) is over one order of magnitude smaller than that of HCN(1-0). Molecular data come from the Leiden Atomic and Molecular Database (Schöier et al., 2005).

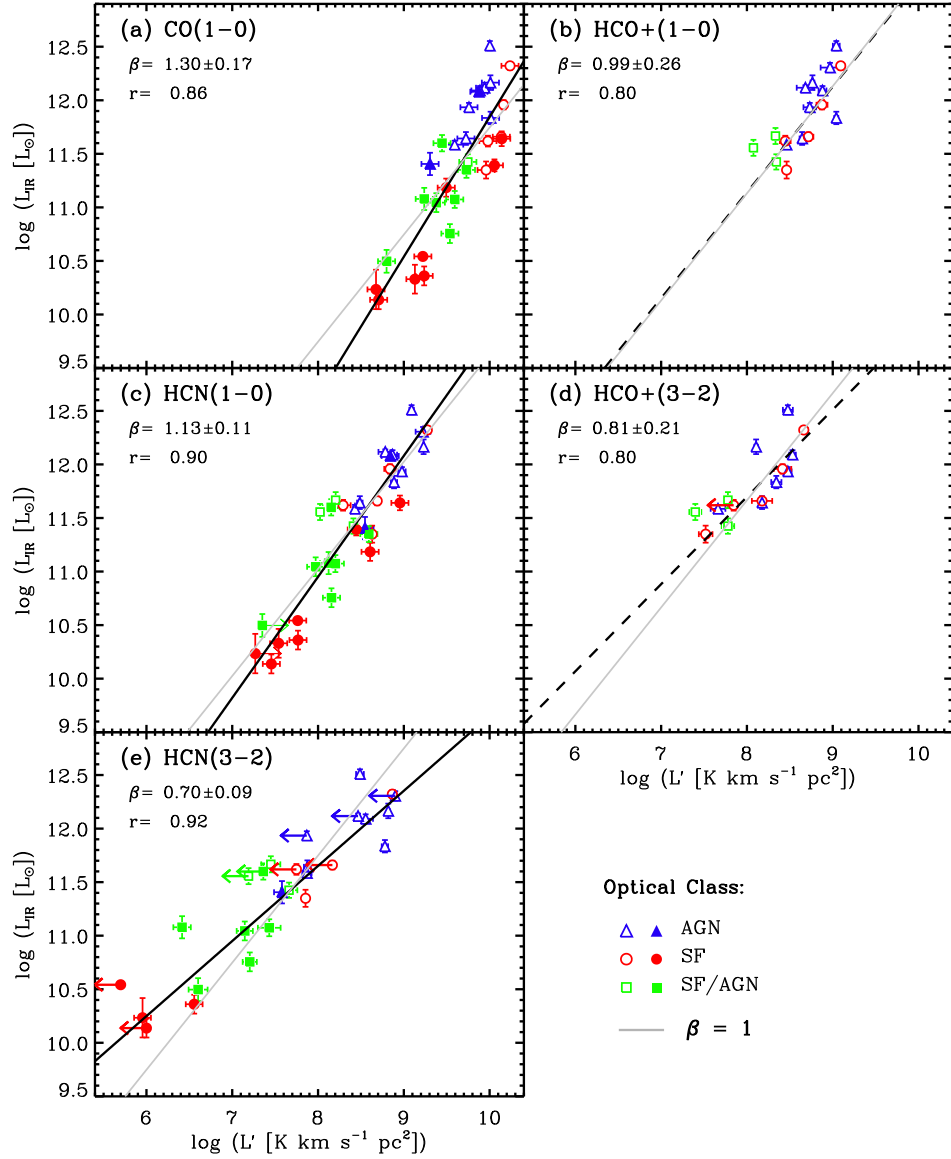


Figure 2.4 Relationship between infrared luminosity and CO(1 – 0) (a), HCO⁺(1 – 0) (b), HCN(1 – 0) (c), HCO⁺(3 – 2) (d), and HCN(3 – 2) (e), molecular line luminosities. We show galaxies from our primary sample (filled symbols) as well as from the GC08 sample (open symbols). Panels are ordered by increasing molecular line critical density. Our optical AGN classification is shown using the same color scheme as in Figure 1 (also see legend).

Figure 2.4 *continued*. Each panel is labeled with the mean and standard deviation of the corresponding slope (β) distribution and with the linear correlation coefficient r . The gray lines have a slope of unity and are included for visualization purposes.

ing the true distributions of these variables (i.e. without measurement errors) given the observations. Using a Bayesian statistical approach, the likelihood distribution function is computed and then integrated over the entire data set. This method offers several advantages compared to other algorithms. Namely, it provides likelihood distributions for the values of slopes and intercepts while allowing for intrinsic scatter (i.e. scatter present in the absence of measurement errors). Most relevant for this work, this method is successful at recovering linear regressions when measurement errors dominate the scatter and when there is a non-negligible number of non-detections in the sample. We note that the value of the slope found using a simple linear least-squares fitting routine available in IDL (LINFIT) is always included within one-sigma of the mean of the distribution of slopes derived by LINMIX. The mean values of the distribution of slopes are shown in Figure 2.4. We also report the slopes obtained by substituting L_{IR} by L_{FIR} (Table 2). The FIR slopes are slightly higher on average, but consistent within 1σ . Our results agree with previous work in that $\beta_{CO(1-0)} > 1$ (2σ) and that $\beta_{HCN(3-2)} < 1$ (3σ). The derived slopes for $HCO^+(1-0)$, $HCN(1-0)$ and $HCO^+(3-2)$ are statistically consistent with each other (and with a slope of unity), given the large uncertainties.

Figure 2.4 suggests that the proportionality between infrared luminosity $\log(L_{IR})$ and molecular line luminosity $\log(L')$ varies as a function of critical density. We compile the mean and standard deviation of slope distributions ($\beta \pm \sigma$) obtained

Table 2.2. Slopes of $\log(L_{IR}) - \log(L'_{mol})$ and $\log(L_{FIR}) - \log(L'_{mol})$ for five molecular lines.

Transition	$\log(n_{crit}[cm^{-3}])$	β_{IR}	β_{FIR}	$\beta_{FIR}-\beta_{IR}$	Sample
CO($J = 1 - 0$)	3.3	1.30 ± 0.17	1.34 ± 0.16	0.04	combined
HCO ⁺ ($J = 1 - 0$)	5.3	0.99 ± 0.26	1.07 ± 0.26	0.08	GC08
HCN($J = 1 - 0$)	6.5	1.13 ± 0.11	1.14 ± 0.10	0.01	combined
HCO ⁺ ($J = 3 - 2$)	6.6	0.81 ± 0.21	0.90 ± 0.19	0.09	GC08
HCN($J = 3 - 2$)	7.7	0.70 ± 0.09	0.71 ± 0.08	0.01	combined

The transitions are ordered in increasing critical density (n_{crit}). For each transition, we report the difference between the two values of slopes ($\beta_{FIR}-\beta_{IR}$) and we identify the sample used for the calculations.

previously and show them as a function of the critical density of the corresponding molecular transition (Figure 2.5). We find evidence for a shallower $\log(L_{IR}) - \log(L')$ slope with increasing molecular line critical density. We supplement our results with published relations between $\log(L_{IR})$ and $\log(L'_{mol})$ for the following transitions: CO(1 – 0) and HCN(1 – 0) from GS04 (open squares), CO(3 – 2) from Narayanan et al. (2005, filled circle) and, in order of increasing critical density, CO(1 – 0), CO(2 – 1), HCO⁺(1 – 0), CS(3 – 2) and HCN(1 – 0) from Baan et al. (2008, asterisk symbols). Baan et al. (2008) published slopes for the inverse relation [$\log(L'_{mol}) - \log(L_{IR})$]. Thus, the asterisks symbols are not truly calculated slopes, but rather the inverse of the published numbers. These points are included for visual reference, but should be considered more uncertain than the associated error bars. All transitions are labeled at the top of the figure. Points corresponding to HCN(1 – 0) and HCO⁺(3-2) are very close given their near-identical critical densities. We added small offsets in critical density for clarity of the plotting symbols around $\log(n_{crit}) \sim 3.3$ and 6.5.

Similar results have been found by Iono et al. (2009). These authors looked at the reciprocal relation but find a slope that varies with critical density in the same sense (i.e. the inverse of their slope decreases with n_{crit} , reaching close to unity for their higher density tracers). While they only considered CO(1 – 0), CO(3 – 2) and HCN(1 – 0), here we extend the trend to a larger number of molecular line transitions and, more importantly, to a transition with a higher critical density probing the regime where the $\log(L_{IR}) - \log(L')$ slope is less than unity [HCN(3 – 2)].

In their coupling of non-LTE radiative transfer calculations with hydrodynamic galaxy evolution simulations, Narayanan et al. (2008b) predicted the SFR- L_{mol} relations in local galaxies as a function of increasing molecular transition

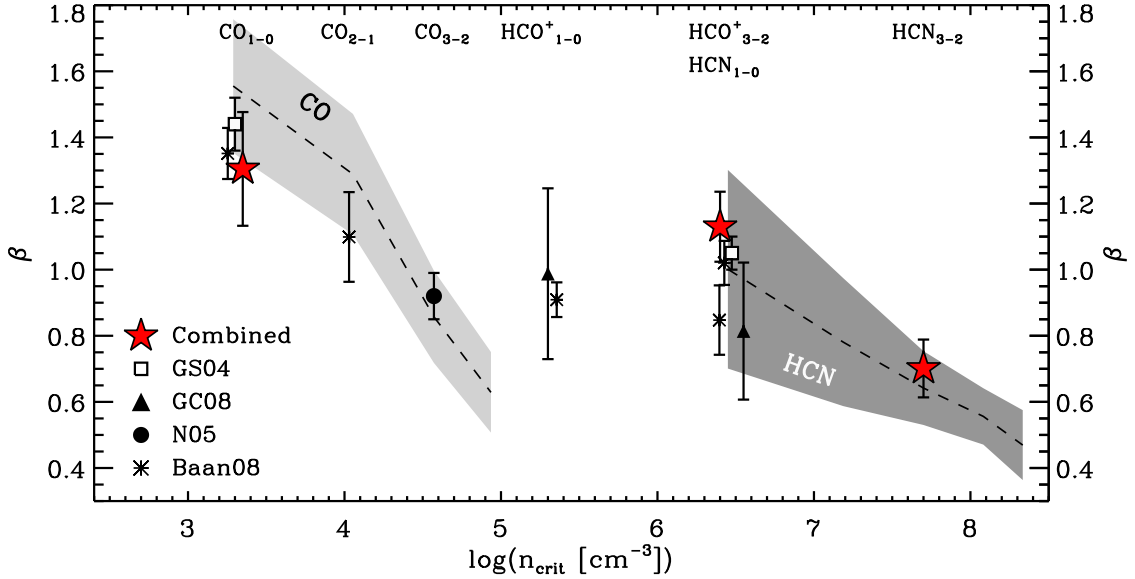


Figure 2.5 Slope of $\log(L_{IR}) - \log(L')$ versus molecular line critical densities for the GC08 sample (triangles) and our combined sample (stars). Individual slopes are shown in the previous figure. We add values from the literature: CO(1 – 0) and HCN(1 – 0) from GS04 (open squares), CO(3 – 2) from Narayanan et al. (2005, filled circle) and, in order of increasing critical density, CO(1 – 0), CO(2 – 1), HCO⁺(1 – 0), CS(3 – 2) and HCN(1 – 0) from Baan et al. (2008, asterisk symbols). The corresponding molecular line transitions are labeled at the top of the figure. Some of the points around $\log(n_{crit}) \sim 3.3$ and 6.5 were offset slightly in critical density for clarity of the plotting symbols. The shaded regions show the predictions of N08 models for CO (pale gray) and HCN (dark gray) rotational transitions from $J = 1 - 0$ to $J = 5 - 4$. See text for more detail.

which serve as a natural comparison for the observations compiled here. We compare the observations with the numerical simulations of Narayanan et al. in Figure 2.5 by over-plotting their model predictions as the gray shaded regions⁴. The predicted slopes were calculated by randomly sampling 25 of the ~ 100 model galaxies in the Narayanan et al. sample, and calculating the slope for the subset of galaxies. The shaded region is the 1σ dispersion in slopes, and the dashed line is the mean. The model SFR- L_{mol} slope decreases as a function of increasing critical density owing to the arguments described in §1. Because higher J-level molecular line transitions trace a smaller fraction of the galaxy’s molecular content, the SFR- L_{mol} slope decreases from the assumed Kennicutt-Schmidt index of 1.5. We find good agreement between the compiled molecular line observations and the theoretical predictions for CO and HCN.

2.3.2 Comparison Between High- and Low-Density Molecular Tracers

In this section, we study the possibility that the enhanced HCN(1 – 0)/CO(1 – 0) luminosity ratio actually corresponds to an enhanced dense gas fraction. The five transitions studied in this work allow us to examine ten molecular line luminosity ratios as a function of IR luminosity. This set includes published line ratios for which the lines involved probe different densities. We introduce a new line ratio, $L'_{\text{HCO}^+(3-2)}/L'_{\text{HCN}(1-0)}$, for which both molecular transitions have nearly the same critical density (see Figure 2.3).

When comparing two tracers, we adopt the convention of dividing the higher-density (HD) tracer by the lower-density (LD) tracer. We quantify the contrast of their critical densities as follows: $R_{\text{crit}} \equiv \log(n_{\text{crit}}^{\text{HD}}/n_{\text{crit}}^{\text{LD}})$. Our set of line ratios spans 4 orders of magnitude in critical density contrast $0.1 < R_{\text{crit}} < 4.4$. We

⁴We note that Narayanan et al. (2008b) only published the model SFR- L_{mol} slopes for CO and HCN.

quantify the IR luminosity dependence of each molecular line ratio by a power-law (see Figure 2.6). Whenever possible, we fit for our combined sample (open and filled symbols, solid lines). Otherwise, we fit to the GC08 sample only (open symbols, dashed lines). We report the mean and standard deviation on the distribution of possible slopes (α) in the top of each panel. We also include the critical density contrast (R_{crit}) and the Pearson linear correlation coefficient (r) in each case.

Our results are summarized in Table 2.3 and indicate an enhancement in molecular luminosity ratio of high- to low-density tracer (L'_{HD}/L'_{LD}) with increasing IR luminosity. This trend is observed, with varying degree of significance, for all ratios with $R_{crit} > 1$. In contrast, $L'_{\text{HCO}^+(3-2)}/L'_{\text{HCN}(1-0)}$ — the only ratio of lines with nearly equal critical densities ($R_{crit} \sim 0$) — remains flat even at high infrared luminosities. The same trend is observed when substituting L_{IR} by L_{FIR} (see Table 2.3).

The relations are better constrained ($> 3\sigma$) for transitions for which it is possible to use our combined sample as it increases the dynamic range in IR luminosity by one order of magnitude. Cases where only the GC08 observations are available are subject to more uncertainty, and would benefit from additional measurements at lower IR luminosities to confirm the trend observed here. Nevertheless, we find a compelling case for interpreting the variations in line luminosity ratios in terms of the molecular gas density distribution.

In Figure 2.7, we present a compilation of the values of α shown in Figure 2.6. We identify the points that originate from our combined sample (red stars) and those that correspond to the GC08 sample (black circles). Although we expect other variables such as molecular gas temperature and excitation to add to the scatter around each value of α , the existence of a significant positive correlation

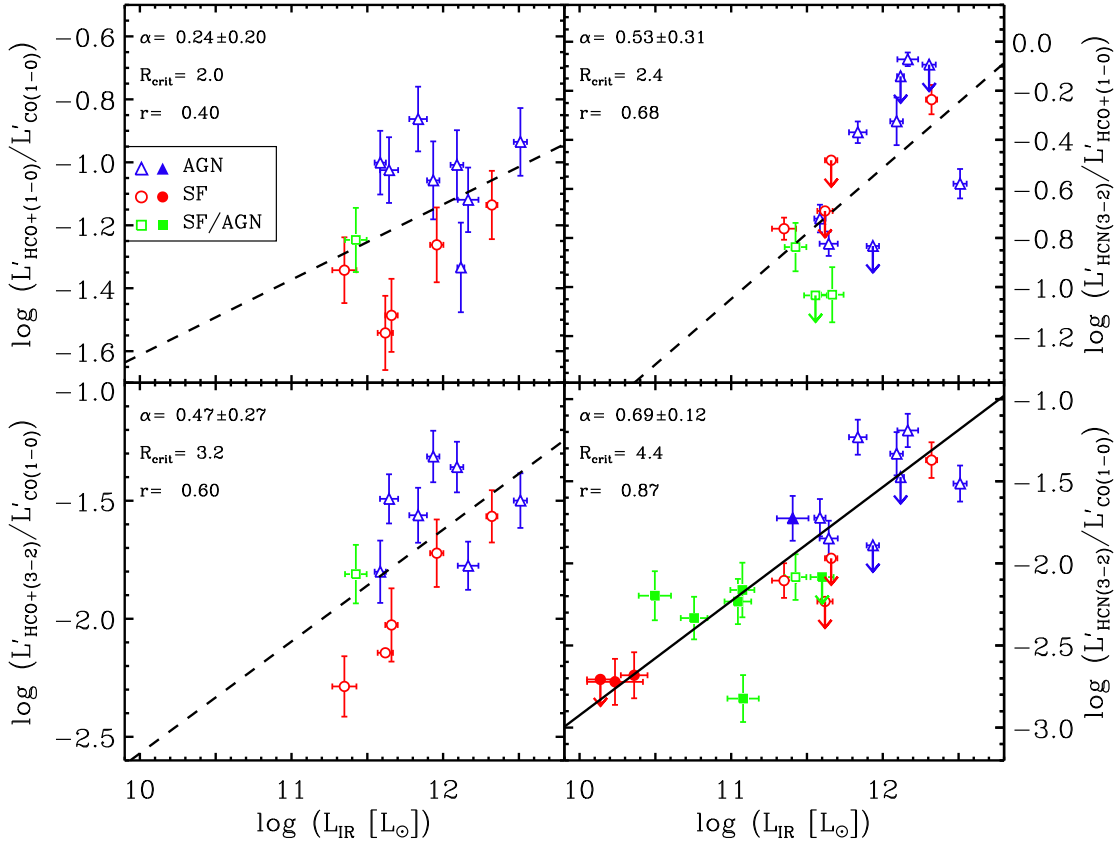


Figure 2.6 Molecular line luminosity ratios as a function of infrared luminosity. We compare high- and low-critical density molecular lines, $\log(L'_{HD}/L'_{LD})$, and label each panel with the best-fit slope (α), the ratio of the critical densities ($R_{crit} \equiv \log(n_{crit}^{HD}/n_{crit}^{LD})$) and the linear correlation coefficient (r). The slope is computed for our combined sample when available (solid lines) and otherwise for the GC08 sample only (dashed lines). The line ratios used are: *Top left*: $\text{HCO}^+_{J=1-0}/\text{CO}_{J=1-0}$, *Top right*: $\text{HCN}_{J=3-2}/\text{HCO}^+_{J=1-0}$, *Bottom left*: $\text{HCO}^+_{J=3-2}/\text{CO}_{J=1-0}$, *Bottom right*: $\text{HCN}_{J=3-2}/\text{CO}_{J=1-0}$. The different symbols represent the optical spectral type: star-forming (SF) (red circles); AGN (blue triangles); and SF/AGN (green squares). Open symbols denote galaxies from the GC08 sample, whereas filled symbols are used for galaxies in our primary sample only.

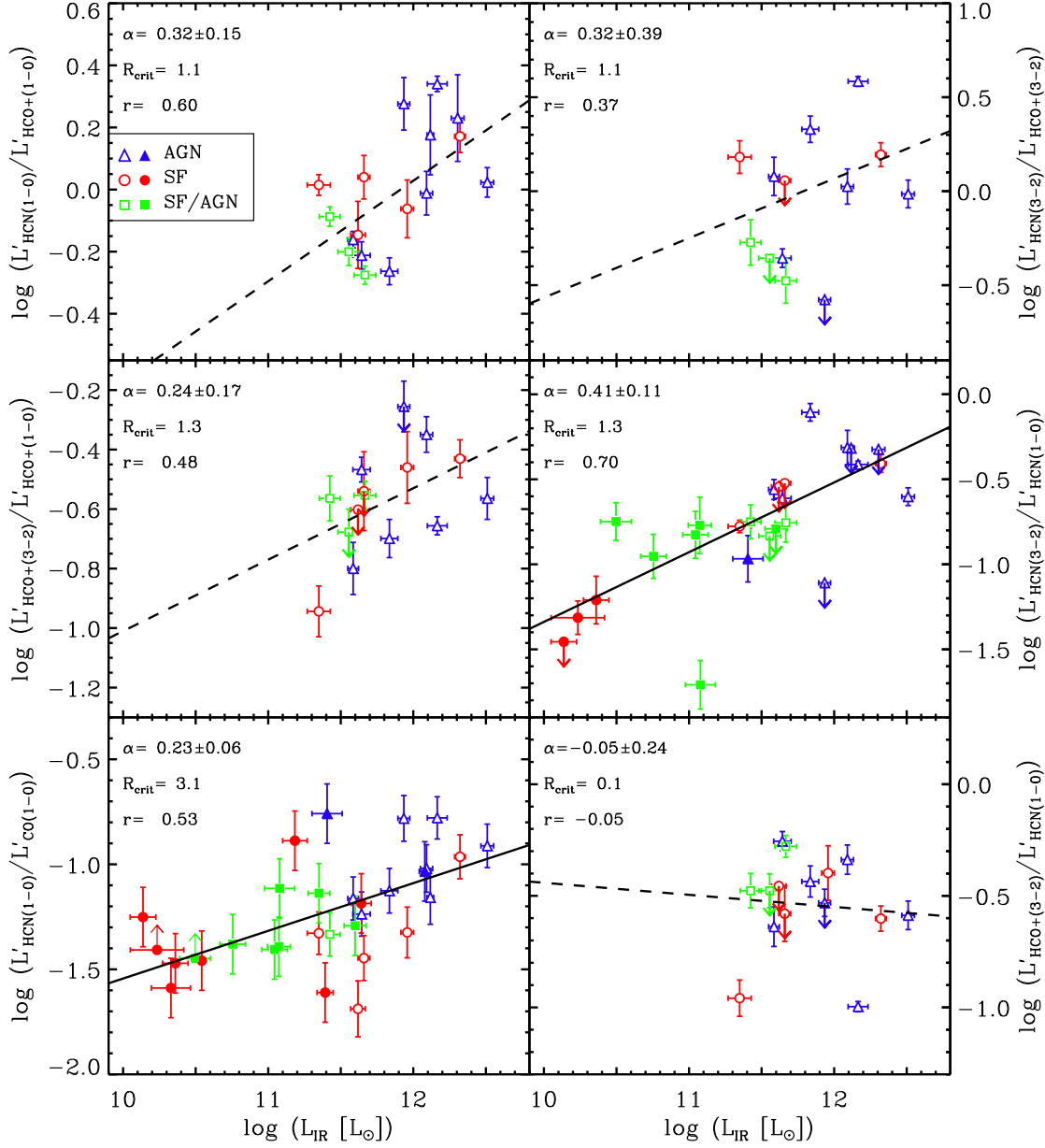


Figure 2.6 continued. Ratios shown here are: *Top left*: $\text{HCN}_{J=1-0}/\text{HCO}_{J=1-0}^+$, *Top right*: $\text{HCN}_{J=3-2}/\text{HCO}_{J=3-2}^+$, *Middle left*: $\text{HCO}_{J=3-2}^+/\text{HCO}_{J=1-0}^+$, *Middle right*: $\text{HCN}_{J=3-2}/\text{HCN}_{J=1-0}$, *Bottom left*: $\text{HCN}_{J=1-0}/\text{CO}_{J=1-0}$, *Bottom right*: $\text{HCO}_{J=3-2}^+/\text{HCN}_{J=1-0}$.

Table 2.3. Slopes of $\log(L'_{HD}/L'_{LD}) - \log(L_{IR})$ and $\log(L'_{HD}/L'_{LD}) - \log(L_{FIR})$ for ten molecular line luminosity ratios.

Line Ratio	R_{crit}	α_{IR}	α_{FIR}	r_{IR}	r_{FIR}
$\text{HCO}_{3-2}^+/\text{HCN}_{1-0}$	0.1	-0.054 ± 0.24	-0.068 ± 0.22	-0.05	-0.08
$\text{HCN}_{1-0}/\text{HCO}_{1-0}^+$	1.1	0.32 ± 0.15	0.36 ± 0.13	0.60	0.66
$\text{HCN}_{3-2}/\text{HCO}_{3-2}^+$	1.2	0.32 ± 0.39	0.38 ± 0.38	0.37	0.42
$\text{HCO}_{3-2}^+/\text{HCO}_{1-0}^+$	1.3	0.24 ± 0.17	0.26 ± 0.15	0.48	0.53
$\text{HCN}_{3-2}/\text{HCN}_{1-0}$	1.3	0.41 ± 0.11	0.41 ± 0.12	0.70	0.72
$\text{HCO}_{1-0}^+/\text{CO}_{1-0}$	2.0	0.24 ± 0.20	0.22 ± 0.19	0.40	0.28
$\text{HCN}_{3-2}/\text{HCO}_{1-0}^+$	2.4	0.53 ± 0.31	0.62 ± 0.30	0.68	0.75
$\text{HCN}_{1-0}/\text{CO}_{1-0}$	3.1	0.23 ± 0.064	0.22 ± 0.065	0.53	0.49
$\text{HCO}_{3-2}^+/\text{CO}_{1-0}$	3.2	0.48 ± 0.27	0.48 ± 0.26	0.60	0.60
$\text{HCN}_{3-2}/\text{CO}_{1-0}$	4.4	0.70 ± 0.12	0.68 ± 0.11	0.87	0.87

For each line ratio, we report the contrast in critical density (R_{crit}), the mean and standard deviations of the slope distributions (α_{IR} & α_{FIR}), and the linear correlation coefficients (r_{IR} & r_{FIR}).

in Figure 2.7 suggests that the molecular gas density distribution may be the primary physical mechanism driving the observed molecular line luminosity ratios in LIRGs and ULIRGs.

This result is consistent with the analysis of Iono et al. (2009) who find that the CO(3–2) source size is more compact than the CO(1–0) size for ULIRGs suggesting that their high FIR (IR) luminosity is linked with them having a large amount of dense molecular gas concentrated within their central region. Furthermore, there is evidence suggesting that the ISM ambient density in ULIRGs is higher by a factor of 100 compared to normal star-forming galaxies (Solomon et al., 1997). A number of other studies support the presence of warm and dense molecular gas in these IR-bright galaxies (e.g. Lahuus et al., 2007; Armus et al., 2007).

Our findings are also in agreement with the Arp 220 and NGC 6240 case studies of Greve et al. (2009), who report an increased dense gas fraction in these two prototypical ULIRGs. Using measurements of a large number of dense molecular tracers, these authors infer that, for these two ULIRGs, most of the molecular gas is in a dense phase and that the GMCs mass-size power-law is steeper than in normal star-forming galaxies, indicating that HCN emission traces denser and more compact GMCs compared to HCO⁺ transitions between the same J levels.

2.3.3 Possible Causes of Higher Gas Density

Assuming that variations in temperature and excitation are smaller than the effect of varying density, a positive relation between α and R_{crit} would imply that more IR-luminous galaxies have a larger fraction of dense gas than galaxies with smaller IR luminosities (see §2.4 for comparison to radiative transfer models). Several mechanisms could create such a situation (which translates to a larger average density of the molecular gas). For example, superwinds capable of expelling interstellar material have been observed in IR-bright starburst galaxies

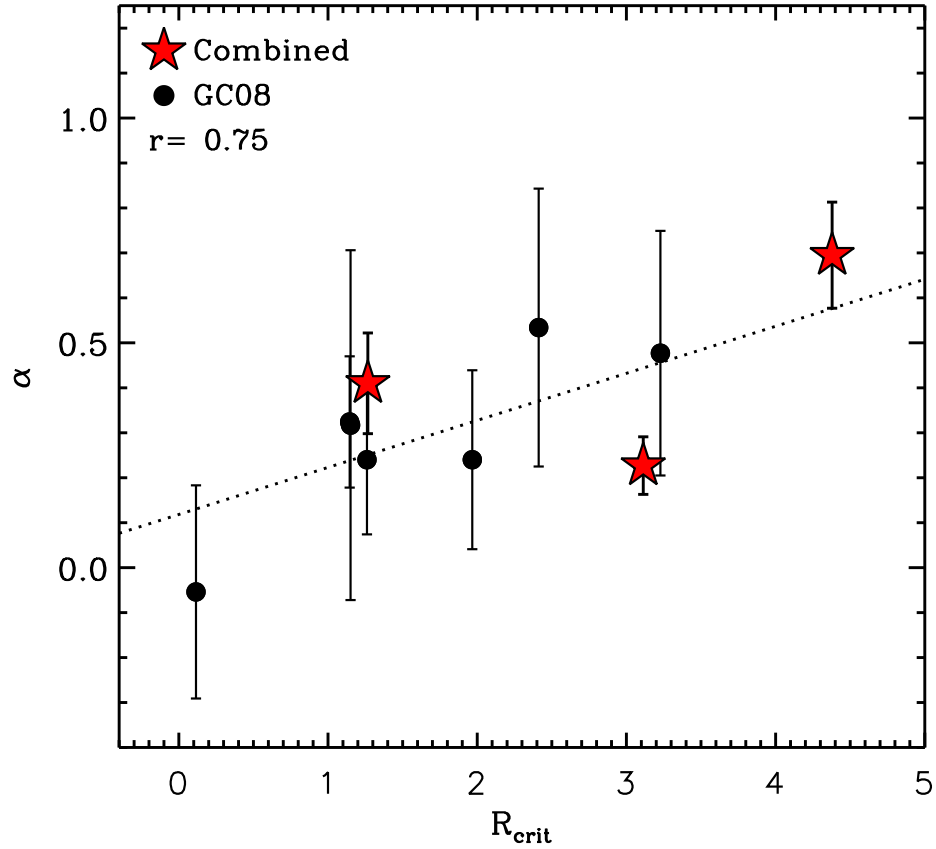


Figure 2.7 Values of α as a function of R_{crit} , the logarithm of the ratio of critical densities of the lines. The index α characterizes the L_{IR} -dependence of the molecular line luminosity ratios shown in Figure 2.6 (i.e. $(L'_{HD}/L'_{LD}) \propto (L_{IR})^\alpha$). Most line ratios included in this figure have $R_{crit} > 1$. Correspondingly, these ratios show a positive index indicating an increase toward high L_{IR} . On the other hand, HCN(1 – 0) and HCO⁺(3 – 2) have a similar critical density (their R_{crit} is close to zero), and their luminosity ratio is consistent with being constant with infrared luminosity ($\alpha = 0$). The slope distribution of the points in this figure has a mean and standard deviation of 0.10 ± 0.07 (1.5σ away from zero, dotted line).

(Heckman et al., 2000). AGN-driven outflows have been modeled and are predicted to be capable of expelling molecular gas from galaxies (Narayanan et al., 2006, 2008a).

Although signatures of atomic gas outflows have been reported in a large number of studies (e.g. Heckman et al., 1990; Veilleux et al., 1995; Rupke et al., 2005; Martin, 2006; Spoon & Holt, 2009, for a review, see Veilleux et al. (2005)), observational evidence for large-scale outflows of molecular gas is scarce and very recent. Based on their observations of CO(3-2), HCO⁺(3-2), HCO⁺(4-3), Sakamoto et al. (2009) find P-cygni profiles indicating outflows of molecular gas around the two merging nuclei of Arp 220. They also report that the HCO⁺ emission is more concentrated around the nuclei relative to the CO emission, in agreement with the picture presented here, where this difference would reflect an enhanced molecular gas density in these regions. In addition, molecular gas outflows have recently been identified for the S0 galaxy NGC 1266 (Alatalo et al., in prep). In this case, the outflow may be associated with the high-density enshrouded nucleus (Mouri et al., 1998), but the powering source (AGN or stellar) remains unclear. Future searches for molecular outflows in galaxies would be useful to understand their energy and gas content balance.

The gas density distribution could be affected if, for example, low-density gas is depleted more easily than denser gas during such outflows. In support of this scenario, lower-density medium is expected to occupy a larger volume and would acquire larger outflow velocity by conservation of momentum. In addition, the evidence that outflow velocities increase with IR luminosity (Martin, 2005; Rupke et al., 2005) is consistent, at least qualitatively, with an increase in dense gas fraction in more IR-luminous galaxies as they can more easily deplete less dense gas. On the other hand, gas accretion and inflows could counteract

this effect to a certain extent and help replenish the gas content.

Alternatively, one could posit that galaxies with a larger reservoir of dense gas (and/or higher dense gas fraction) can sustain higher IR luminosity by allowing for more powerful starbursts and AGN activity. Mergers of gas-rich galaxies can trigger and fuel both starburst and AGN activity and consequently appear as ULIRGs. Indeed, most if not all of the ULIRGs in this sample are undergoing a galaxy merger. The important change in the dynamics of these systems, and in particular, of their molecular gas content might be the underlying cause of the different gas density distributions and consequently, enhanced HD/LD line luminosity ratios.

Direct comparisons between high- and low-density molecular gas tracers to interpret the physical conditions of the molecular ISM in infrared luminous galaxies were also used in Baan et al. (2008). These authors propose that the gas density distribution reflects the evolutionary stage of a nuclear outburst in (U)LIRGs. In their picture, the denser gas is depleted more rapidly than the lower density gas as the nuclear starburst progresses, and the molecular line ratios provide clues about a shift in the dominant heating source (UV versus X-ray photons).

Baan et al. (2008) modeled some of the key molecular line ratios presented in Baan et al. (2008) and found that mechanical feedback heating is a crucial process to explain the low HNC(1-0)/HCN(1-0) ratio observed in some systems. They provide additional support for a time-dependent model of the physical conditions in the nuclear regions of luminous infrared galaxies, according to which the molecular ISM switches from a high-density ($\sim 10^5 \text{ cm}^{-3}$) phase, dominated by stellar heating, to a lower-density ($\sim 10^{4.5} \text{ cm}^{-3}$) phase, dominated by mechanical heating.

We explore a varying HD/LD line luminosity ratio further in the next section,

where we present simulations of individual disk galaxies as well as mergers of gas-rich galaxies.

2.4 Model Line Ratios

In order to investigate whether X-ray induced chemistry is necessary to drive the observed trends of line ratio with infrared luminosity (e.g. Graciá-Carpio et al., 2006), we compare observed molecular line ratios with fixed-abundance numerical simulations (Narayanan et al., 2008b).

In the left column of Figure 2.8, we show the model predictions, and compare them directly to the observations in the right column. The HCN and CO simulations were taken from the study of (Narayanan et al., 2008b), while HCO⁺ simulations of gas-rich galaxy mergers were run specifically for this work. When available, the isolated disk galaxies include a large dynamic range of gas fractions and masses (see § 2.2.1). The two galaxy merger simulations are identical in all ways except for their feedback implementation. The thick gray curve represents a galaxy merger in which 0.5% of the accreted mass energy onto the central black hole is re-injected into the surrounding ISM as thermal energy input, while the merger shown by the thin yellow curve does not include AGN feedback. Each time step of $5 h^{-1}$ Myr is shown with a filled triangle (circle) for the model with(without) black-hole feedback. During their peak burst (when the galaxy may be most visible as a ULIRG), AGN winds can vary both the star formation history and gas density profiles in the galaxies (e.g. Springel et al., 2005). Hence, these two models effectively serve as two different galaxies probing different line ratio- L_{IR} relations. The infrared luminosity of the simulated galaxies is estimated from their known SFR. We use the Kennicutt (1998) conversion $L_{FIR} = (5.5 \times 10^9) \times SFR$ and our observed relation $L_{IR} = 1.38 \times L_{FIR}$ found

in Figure 2.2.

The molecular line luminosity ratios considered here are $\text{HCN}(1-0)/\text{CO}(1-0)$, $\text{HCN}(3-2)/\text{CO}(1-0)$, $\text{HCO}^+(3-2)/\text{HCO}^+(1-0)$ and $\text{HCN}(3-2)/\text{HCN}(1-0)$. As before, we show the galaxies overlapping with the GC08 sample with open symbols, whereas filled symbols are for observations from our primary data set only. Because galaxies with HCO^+ observations strictly belong to the GC08 sample, they occupy the brighter end of the L_{IR} range, which is well-sampled by the merger models. The isolated gas-rich galaxies (open circles) cover the low-end of the infrared luminosity, with the exception of two cases at $L_{IR} \sim 10^{11.5} - 10^{12} L_{\odot}$, which were designed to explore extreme conditions that are physically unrealistic at low-redshift (e.g. the most massive $M_{\text{DM}} \sim 10^{13} M_{\odot}$ galaxies).

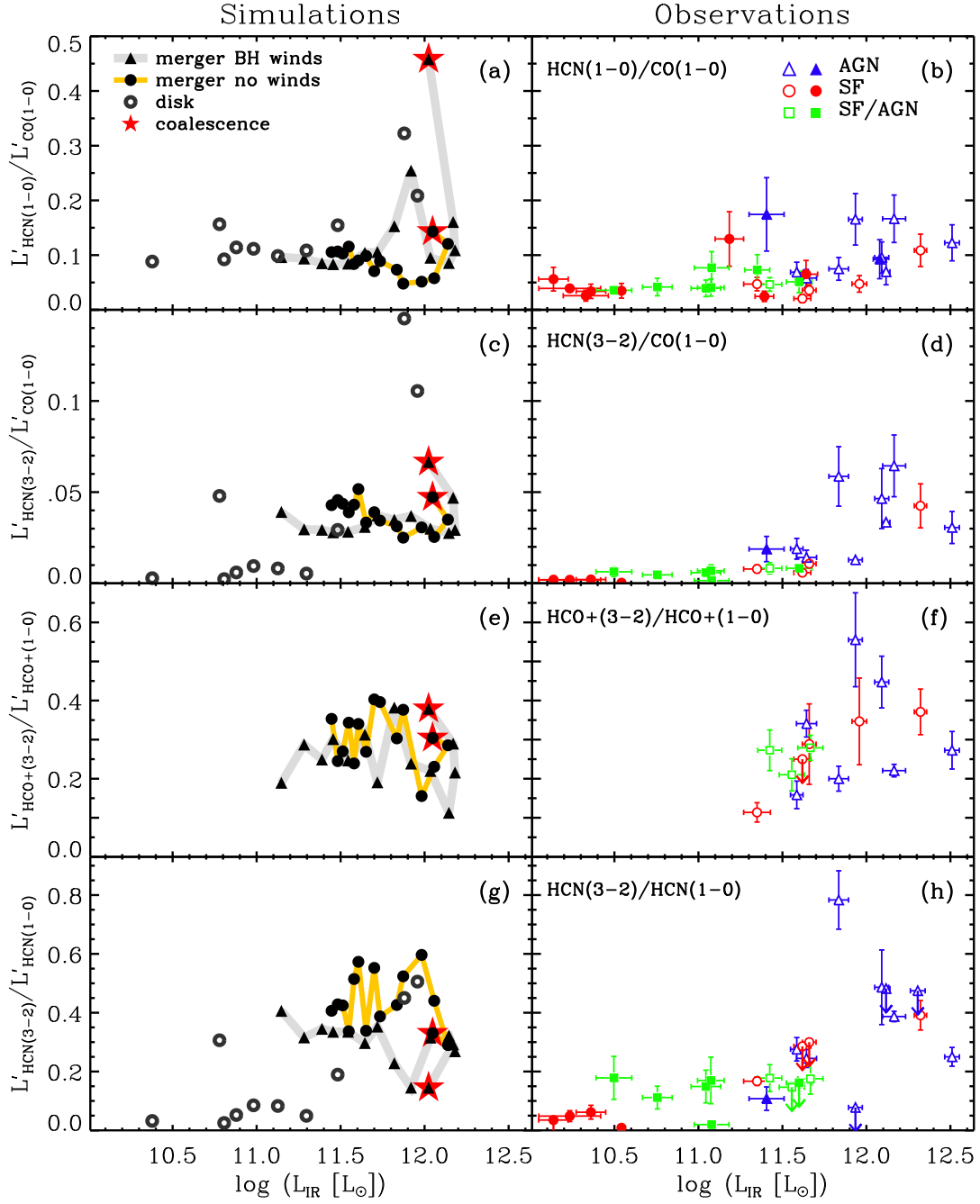


Figure 2.8

Figure 2.8 Several molecular line luminosity ratios as a function of infrared luminosity. The simulation results are shown in the left-hand column while the observations for the corresponding ratio are shown on the right. From top to bottom, the luminosity ratios are: $\text{HCN}(1-0)/\text{CO}(1-0)$ (*a,b*), $\text{HCN}(3-2)/\text{CO}(1-0)$ (*c,d*), $\text{HCO}^+(3-2)/\text{HCO}^+(1-0)$ (*e,f*), and $\text{HCN}(3-2)/\text{HCN}(1-0)$ (*g,h*). This figure shows evolutionary tracks of equal-mass merger simulations with (gray line) and without (yellow line) SMBH feedback combined with simulations of individual gas-rich disk galaxies (open circles). The tracks start at black-hole coalescence (large star symbol), and each time step is marked with a black symbol. Although their dynamical range differs slightly, the models successfully reproduce the spread observed in the data. Plotting symbols for the observations are as follows: star-forming galaxies (SF) (*red circles*); AGN (*blue triangles*); and SF/AGN (*green squares*). We use open symbols for galaxies that belong to the GC08 sample and filled symbols otherwise.

Generally speaking, there is an excellent correspondence between the range of the observations and models in their molecular line ratios. At large infrared luminosities (SFRs), the line ratios tend to increase. This effect is simply a manifestation of the fact that the galaxies at the high infrared luminosity range are undergoing a starburst event. When the fraction of dense gas in a galaxy increases (for example, owing to a merger) so does the rate at which stars form. Large amounts of dense gas also imply that starbursting galaxies are more easily able to excite high critical density tracers (such as various transitions of HCN or HCO^+), thus increasing the observed HD/LD line ratios. Because the simulations include constant, Galactic-based abundances without chemistry-driven variations, the agreement between model and data demonstrate that chemistry-driven abundance variations are not necessary to produce the observed line ratios.

We note that generally the dynamic range of the modeled line ratios seems to match the observations reasonably well. However, we urge caution with a detailed comparison of the models and the data. First, the simulations were designed to probe a large parameter space in gas fractions and galaxy masses. Some galaxies were specifically designed to probe relatively extreme conditions (e.g. initial gas fractions $f_g=0.8$, $M_{\text{DM}} \sim 10^{13}M_{\odot}$). Consequently, individual model galaxies can be caught during a brief snapshot with extreme line ratios, and may not exactly map to a particular galaxy from observed galaxy samples in Figure 2.8. Second, the galaxies in the models were not chosen to precisely mimic the relative number of isolated galaxies versus mergers in the GS04a,b samples. Thus, the clustering of simulated points in Figure 2.8 may not exactly match those in the observations. Third, the L_{IR} in the models was calculated using a linear mapping from the SFR. While we do not consider AGN contribution

to L_{IR} in the simulations, there is some in the observations. This is likely to be the reason why the observations extend to brighter L_{IR} ($> 10^{12.5} L_{\odot}$) compared to the simulations, which seem to reach a ceiling at $L_{IR} \sim 10^{12.2} L_{\odot}$.

2.5 Possible Chemistry Effects

It has been suggested that the radiation field associated with an AGN influences the abundance of HCN with respect to other molecules. For example, emitted X-rays could cause X-ray dominated regions (XDRs) which have different properties than regular photon dominated regions (PDRs) found around star-forming regions. Previous authors claim that conditions existing in these XDRs affect molecular gas abundance (Lintott & Viti, 2006; Aalto et al., 2007; Krips, 2007).

On the other hand, Baan et al. (2008) used multiple molecular line ratios to distinguish between XDR and PDR conditions, and found that most of the (U)LIRGs in their sample are dominated by PDRs. They used tracers sensitive to column density (N_H) to distinguish between an elevated HCN/CO intensity ratio resulting from a high- N_H PDR or from a low- N_H XDR, and found the former to be more likely.

Below we present optical spectral diagnostics associated with ISM metallicity and ionization parameter (Figure 2.9). The emission-line ratio $[\text{N II}] \lambda 6584 / [\text{O III}] \lambda 3727$ has been shown to correlate with the gas-phase oxygen abundance $12 + \log(O/H)$ while being less affected by the presence of an AGN than other metallicity diagnostics (Kewley & Dopita, 2002; Kewley & Ellison, 2008). Meanwhile, the emission-line ratio $O_{32} \equiv \log([\text{O III}] \lambda 5007 / [\text{O III}] \lambda 3727)$ traces the ionization parameter. The correspondence between the observed ratio and the ionization depends slightly on the metallicity so the two panels of Figure 2.9 should be interpreted in conjunction.

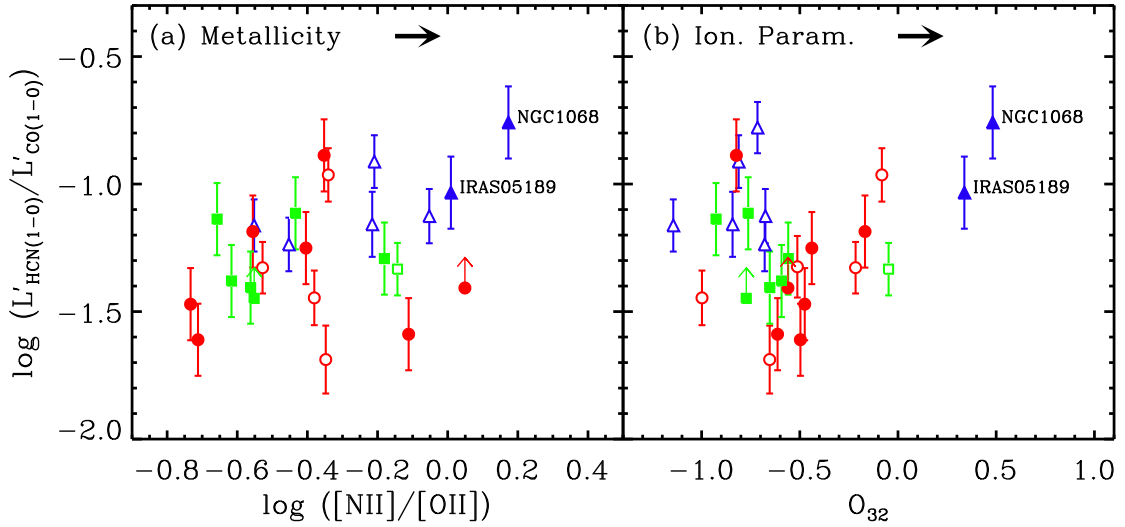


Figure 2.9 HCN(1 – 0)/CO(1 – 0) luminosity ratio as a function of nebular emission-line diagnostics of the diffuse ISM metallicity (*Left*) and ionization parameter (*Right*). There is no obvious trend except for two outliers for which the high HCN(1 – 0)/CO(1 – 0) luminosity ratio could potentially be associated with enhanced metallicity and/or ionization in the ISM. Plotting symbols represent the optical spectral type: star-forming (SF) (*red circles*); AGN (*blue triangles*); and SF/AGN (*green squares*). We use open symbols for galaxies that belong to the GC08 sample and filled symbols otherwise.

Most galaxies are scattered without obvious trends in the $\text{HCN}(1-0)/\text{CO}(1-0)$ - $[\text{N II}] \lambda 6584/[\text{O III}] \lambda 3727$ and $\text{HCN}(1-0)/\text{CO}(1-0)$ - O_{32} planes. The correlations are very weak or non-existent, especially if we exclude the two outliers (IRAS 05189-2524 and the more extreme NGC 1068). In the first panel, the correlation coefficient $r = 0.42$ drops to $r = 0.24$ if we exclude NGC 1068 and down further to $r = 0.15$ if we exclude both outliers mentioned above. In the second panel, the correlation coefficient drops from $r = 0.26$ to $r = -0.09$ if we exclude both outliers. NGC 1068 (and possibly IRAS 05189-2524) may be a special case where unusual ionization or chemistry effects could play a significant role in producing the observed $\text{HCN}(1-0)/\text{CO}(1-0)$ luminosity ratios.

Our result is in agreement with findings of Usero et al. (2004) who conclude that the circumnuclear region of NGC 1068 is effectively a giant XDR. These authors used a combination of single dish and interferometry data of several molecular species to rule out alternative explanations for the observed high HCN/CO ratio (Tacconi et al., 1994). NGC 1068 is also observed to have the largest MIR-excess (it lies 4.5σ from the mean on Figure 2.2), a regime where MIR-pumping can promote $\text{HCN}(1-0)$ emission by exciting a bending mode at $14 \mu\text{m}$ (Aalto et al., 1995).

While the optical emission line ratios used here may give a good indication of the metallicity and ionization state of the diffuse ISM, it is not clear how representative they are of the conditions present in denser molecular gas. Therefore, it may not be surprising that we do not see obvious trends in either panel. This caveat is especially important if young stars (starburst) are the main source of ionization because UV photons do not penetrate deeply into the dense molecular. On the other hand, X-ray photons can penetrate through much larger column densities of material, so it is plausible that the extreme conditions triggered by an AGN

would occur over a large enough volume to effect both the diffuse and dense gas phases. If this were the case, we would expect a larger $\text{HCN}(1-0)/\text{CO}(1-0)$ luminosity ratio to couple with larger values of O_{32} because an increased ionization means more free electrons, which can accelerate the production of HCN molecules (as discussed in §2.1).

Overall, our results indicate that cases with a genuine abundance change in HCN may exist but are the exception rather than the rule.

2.6 Conclusions

Using a sample of 34 nearby infrared luminous galaxies ($10^{10} < L_{IR} < 10^{12.5} L_{\odot}$), we characterized the infrared luminosity dependence of various molecular gas tracers.

- The presence of AGN was assessed using the optical *BPT* diagram. In agreement with previous publications, we find a more frequent occurrence of AGN in more IR-luminous galaxies. This may be related to the availability of larger amounts of dense gas during the mergers of gas-rich galaxies.
- The molecular transitions used, $\text{CO}(1-0)$, $\text{HCO}^+(1-0)$, $\text{HCN}(1-0)$, $\text{HCO}^+(3-2)$ and $\text{HCN}(3-2)$, span 4 orders of magnitude in critical density. We find that the relationship between (F)IR luminosity and molecular line luminosity L_{mol} is shallower for transitions with higher n_{crit} . This trend is in agreement with theoretical models of N08 and KT07 and can be explained by the varying degree of thermalization of the gas giving rise to molecular line emission.
- Trends of molecular line ratios with L_{IR} are consistent with an increased molecular gas density in more IR-bright galaxies. This result agrees with

the picture presented by Gao & Solomon (2004b) and Wu et al. (2005). When comparing high-density and low-density molecular gas tracers, we observe an increase in their luminosity ratio (L_{HD}/L_{LD}) with increasing infrared luminosity. Interestingly, this trend vanishes when comparing two tracers with nearly equal critical density (HCN(1 – 0) and HCO⁺(3 – 2)). We infer that the main driver of the enhanced HD/LD luminosity ratio is the molecular gas density distribution, in agreement with the observations that ULIRGs host large reservoirs of dense molecular gas in their central regions.

- We compare our observed molecular line ratios with theoretical values obtained from a set of galaxy models. We consider SPH simulations of two galaxy mergers as well as individual gas-rich galaxies. With constant Galactic abundances, the models successfully produce an enhanced HD/LD luminosity ratios at brighter infrared luminosity. This provides additional support for a higher molecular gas density in galaxies that are extremely gas-rich or undergoing gas-rich mergers. Indeed, this result suggests that AGN-induced chemistry (or other) effects may not be necessary to reproduce the observations, but rather that AGNs are more likely to reside in galaxies that are very gas-rich and/or experiencing a merger. The simulations also demonstrate important variations in molecular luminosity ratio with the evolutionary stage of the mergers. These variations may be connected with the dynamics of the molecular gas during mergers (inflows, outflows, gas compression, etc.).
- We investigate possible chemistry effects on the well-known HCN(1 – 0)/CO(1 – 0) luminosity ratio using common optical emission line diagnos-

tics of the ISM ionization parameter and metallicity. With the exception of one of two outliers, we do not observe significant correlations between the molecular line ratio and these properties. Decoupling between the dense molecular gas traced by CO(1 – 0) and HCN(1 – 0) and the more diffuse gas that traces the optical nebular line may be responsible for the absence of correlation. However, we note that NGC 1068 shows extreme conditions in the sense of having the largest optically-measured ionization parameter as well as the largest MIR-excess. This outlier is thus more subject to chemistry and/or MIR-pumping effects quoted in the literature. We emphasize that NGC 1068 has properties that are very distinct from the rest of our sample, and thus may not be representative of its class.

- More high-density molecular line observations would be extremely beneficial to confirm the trends outlined in this work. Only half of our combined sample of 34 galaxies have data for all five molecular lines used here. In particular, future observations should target galaxies with fainter IR luminosities to test whether the results presented here extend into the lower luminosity regime. Higher-resolution studies of high-density tracers may complement this work by allowing for a more detailed analysis of the density and excitation structure of the molecular gas within galaxies. Such studies could provide information on the *local* influence of AGN, whereas in this work we probe the *global* influence of AGN.
- Overall, our results support that HCN(1 – 0) is a valid tracer of dense molecular gas in galaxies even in the presence of AGN. We expect scatter in the relationship due to variations in temperature and possible radiative (de-)excitation of this transition. Also, the dense-to-total molecular gas fraction

is expected to differ from galaxy to galaxy, especially in systems undergoing significant mergers.

CHAPTER 3

A NEW DIAGNOSTIC OF ACTIVE GALACTIC NUCLEI: REVEALING
HIGHLY-ABSORBED SYSTEMS AT REDSHIFT > 0.3

We introduce the Mass-Excitation (MEx) diagnostic to identify active galactic nuclei (AGNs) in galaxies at intermediate redshift. In the absence of near-infrared spectroscopy, necessary to use traditional nebular line diagrams at $z > 0.4$, we demonstrate that combining $[\text{O III}] \lambda 5007/\text{H}\beta$ and stellar mass successfully distinguishes between star formation and AGN emission. The MEx classification scheme relies on a novel probabilistic approach splitting galaxies into sub categories with more confidence than alternative high- z diagnostic diagrams. It recognizes that galaxies near empirical boundaries on traditional diagrams have an uncertain classification and thus a non-zero probability of belonging to more than one category. An outcome of this work is a system of statistical weights that can be used to compute global properties of galaxy samples. We apply the MEx diagram to 2,812 galaxies at $0.3 < z < 1$ in the Great Observatories Origins Deep Survey North and Extended Groth Strip fields, and compare it to an independent X-ray classification scheme. We identify Compton-thick AGN candidates with large X-ray absorption, which we infer from the luminosity ratio between hard X-ray emission and $[\text{O III}] \lambda 5007$, a nearly isotropic tracer of AGN. X-ray stacking of sources that were not detected individually supports the validity of the MEx diagram and yields a very flat spectral slope for the Compton-thick candidates ($\Gamma \approx 0.4$, unambiguously indicating absorbed AGN). We present evidence that composite galaxies, which are difficult to identify with alternative high-redshift diagrams, host the majority of the highly-absorbed AGN. Our findings suggest that the interstellar medium of the host galaxy provides significant absorption in

addition to the torus invoked in AGN unified models.

3.1 Introduction

A complete understanding of galaxy evolution requires the study of both galaxy stellar content and nuclear activity. However, differentiating the powering source – star formation versus AGN – poses an appreciable challenge. While there are several independent tracers of AGN, all suffer from limitations. Because the caveats of one tracer can be overcome by the strength of another, it has become clear that multi-wavelength methods are required to assess the ubiquity of AGNs. For example, X-ray emission has been used extensively to uncover and study large populations of AGNs (Bade et al., 1995; Boyle et al., 1993; Brandt et al., 2001). However, even the most sensitive X-ray surveys still miss heavily absorbed systems. These absorbed AGNs were inferred by the unresolved portion of the cosmic X-ray background, which shows a flat X-ray spectral slope highly suggestive of X-ray absorption (Comastri et al., 1995; Mushotzky et al., 2000; Alexander et al., 2003; Bauer et al., 2004; Treister & Urry, 2005).

This scenario is supported by the existence of Compton-thick systems in the nearby universe that would not be detected in the most sensitive X-ray surveys if they were at higher redshift, e.g., NGC 1068. This galaxy was also shown to have X-ray absorbers on a scale of the order of ~ 1 pc (Guainazzi et al., 2000).

Even if X-ray photons are absorbed or scattered by material on a compact scale such as the torus component described in the *unified model* (Antonucci, 1993), emission originating from larger scales may reach the observer regardless of the line of sight. Such isotropic tracers include emission lines from the narrow line regions, which are exterior to the torus. Commonly used lines include [O III] $\lambda 5007$ in the optical (Baldwin et al., 1981; Busko & Steiner, 1988) and [O IV] $\lambda 25.9\mu\text{m}$ or

[Ne v] $\lambda 14\mu\text{m}$ in the infrared regime (Sturm et al., 2002; Armus et al., 2004, 2007; Diamond-Stanic et al., 2009; Rigby et al., 2009; LaMassa et al., 2010). Another such tracer is mid-infrared continuum emission originating from hot dust heated by the AGN (e.g., Lacy et al., 2004; Stern et al., 2005; Donley et al., 2007). This method works especially well for intrinsically luminous AGN that are deeply enshrouded, but does not select the less-luminous systems which may still be absorbed. Mid-infrared aromatic features can also be used to diagnose the powering source in galaxies (Genzel et al., 1998; Lutz et al., 1998; Pope et al., 2008).

On the one hand, some of the distinctions between the classes of AGNs and the selection methods listed above are thought to arise from their orientation with respect to the observer's line of sight. On the other hand, some AGN classes seem to comprise physically distinct phases of activity (i.e., low versus high accretion rate, beginning or end of an active phase). The latter are more interesting from the point-of-view of galaxy evolution as they may provide a handle on the importance of AGN phases, their duty cycle, and the interplay between AGNs and their host galaxies.

One example of physically-distinct AGN phases are Seyferts and low ionization nuclear emission line regions (LINERs). These two categories emerged from optical spectroscopy studies where emission lines with different excitation properties were used as probes of the radiation exciting the interstellar gas (Seyfert, 1943; Heckman, 1980). In addition to exhibiting specific spectral signatures, Seyfert and LINER nuclei were found to reside in distinct host galaxies compared to star-forming galaxies and also relative to one another. Kauffmann et al. (2003) showed that galaxies hosting an AGN tend to have a larger stellar mass compared to star-forming galaxies that lack optical AGN signatures. Galaxies with a Seyfert nucleus (or Seyferts for short) often have a young or intermediate-age component in

their stellar population whereas galaxies with LINER emission have, on average, an older stellar population as well as a larger stellar mass than Seyferts (e.g. Kewley et al., 2006). Putting this evidence together with the observations that AGNs seem to follow a decreasing sequence in accretion rate from Seyferts to LINERs to composite galaxies (Ho, 2008) suggests an evolutionary picture where LINERs may be older, dying, AGNs relative to Seyferts.

Whether this emerging picture is supported by higher-redshift observations is unclear. At larger distances, it is generally more difficult to get a complete census of galaxies with AGNs, let alone to classify them in different AGN categories/phases. Gathering complete samples of galaxies for which we know the powering source, and whether the central black hole is actively accreting, is especially challenging at $z > 0.4$. Beyond that redshift, optical emission lines needed for AGN classification such as $H\alpha$ and $[\text{N II}] \lambda 6584$ are shifted into the near-infrared, preventing the application of well-calibrated, traditional diagnostics (Baldwin et al., 1981; Veilleux & Osterbrock, 1987; Kewley et al., 2001a; Kauffmann et al., 2003; Kewley et al., 2006; Stasińska et al., 2006).

In this paper, we present the Mass-Excitation (MEx) diagnostic diagram, based in part on optical nebular lines that can readily be observed out to $z \sim 1$. Following a similar method as Weiner et al. (2007), who replaced the $[\text{N II}] \lambda 6584/H\alpha$ line flux ratio used in the BPT diagram (Baldwin et al., 1981) with absolute H -band magnitude, we adopt stellar mass as a substitute for $[\text{N II}] \lambda 6584/H\alpha$. We will show that a better census of AGN can be obtained by finding both intrinsically weak AGNs as well as absorbed systems that are undetected in X-ray observations. Our classification scheme relies on a novel probabilistic approach and allows us to split the galaxies into the following categories: purely star-forming galaxies, Seyfert 2s, LINERs or composite systems (i.e., with both star-formation

and AGN). Galaxies near the empirical boundaries on traditional diagnostic diagrams have a less certain classification and are thus assigned a non-zero probability of belonging to more than one category. As a result, the MEx diagnostic also outputs statistical weights that can be utilized to compute global properties (e.g., stellar mass, metallicity, etc.) in statistical samples of galaxies belonging to any of the categories listed above.

Using a sample of low-redshift galaxies described in §3.2, we calibrate our diagnostic in §3.3.1. We briefly analyze the occurrence of low-ionization nuclear emission-line regions (LINERs) in §3.3.2 before introducing a novel approach to galaxy spectral classification based on the probability of each spectral class (e.g., star-forming or AGN, §3.3.3). We describe our $0.3 < z < 1$ galaxy sample in §3.4, and the application of our new Mass-Excitation (MEx) diagram in §3.5. We find an excellent agreement between the MEx diagram and the X-ray classification (§3.5.1). We examine the different optical and X-ray classes more closely with an X-ray stacking analysis (§3.5.2). Combining hard X-ray emission and optical emission lines allow us to probe the X-ray absorption leading to the discovery of Compton-thick AGNs among our intermediate-redshift sample §3.6. We compare the MEx diagram with alternative AGN diagnostic diagrams in §3.7.1 and we describe how the new method contributes to achieving a more complete census of AGNs (§3.7.2). We discuss the fraction of AGNs that suffer from X-ray absorption (§3.7.4) and possible evolution effects on emission-line AGN diagnostics in §3.7.5 before summarizing our main conclusions in §3.8. We assume a flat cosmology with $\Omega_m = 0.3$, $\Omega_\Lambda = 0.7$, and $h = 0.7$ throughout.

3.2 Low-Redshift Galaxy Sample

Our low-redshift calibration sample comes from the Sloan Digital Sky Survey (SDSS; York et al., 2000). The limiting magnitude of the spectroscopic sample is $r < 17.7$. Our analysis is based on data products from Data Release 4 (Adelman-McCarthy et al., 2006), namely the value-added galaxy catalogs¹ from the Max-Planck Institute for Astronomy (Garching) and John Hopkins University. In these catalogs, the stellar masses are calculated as described in Kauffmann et al. (2003) assuming a Kroupa (2001) initial mass function (IMF), while emission line measurements follow the procedures from Tremonti et al. (2004).

In order to avoid strong aperture bias due to SDSS fiber size, we constrain the redshift range to $0.05 < z < 0.2$. This lower limit corresponds to a minimum covering fraction $\sim 30\%$. Kewley & Ellison (2008) found that using a covering fraction down to 20% ($z \sim 0.04$) is not sufficient to obtain global emission line properties for massive galaxies (with $M_* > 10^{10} M_\odot$). That is why we adopt a stricter requirement here.

Imposing a signal-to-noise ratio cut $S/N > 3$ on all emission lines to be used in the diagnostic diagrams ([O III] $\lambda 3727$, $H\beta$, [O III] $\lambda 5007$, $H\alpha$, [N II] $\lambda 6584$ and [S II] $\lambda\lambda 6717, 6731$; §3.3.1), we obtain a sample of 110,205 emission-line galaxies.

3.3 Emission-line Diagnostic Diagrams

Here we aim to create a modified version of the BPT² diagram, involving [N II] $\lambda 6584 / H\alpha$ and [O III] $\lambda 5007 / H\beta$, by replacing the ratio of the redder emission lines ([N II] $\lambda 6584 / H\alpha$) because they shift into the near-infrared at $z > 0.4$. To that purpose, we introduce the Mass-Excitation (MEx) diagram below, which we

¹<http://www.mpa-garching.mpg.de/SDSS/DR4/>

²Named after the last names of the three authors who introduced it: Baldwin-Phillips-Terlevich (Baldwin et al., 1981)

will subsequently apply to intermediate redshift galaxies ($0.3 < z < 1$) in §3.5.

3.3.1 Calibration Using $z \sim 0.1$ SDSS Galaxies

In this section, we introduce and calibrate the Mass-Excitation diagram and compare it to one of the original BPT diagrams. The emission line ratios used in the best-known version of this diagram ($[\text{N II}] \lambda 6584/\text{H}\alpha$ and $[\text{O III}] \lambda 5007/\text{H}\beta$) probe a combination of the ionization parameter and the gas-phase metal abundance within galaxies. As shown in Figure 3.1(a), SDSS galaxies form a well-defined excitation sequence on the lower-left of the BPT diagram (below the semi-empirical dividing curve from Kauffmann et al., 2003, solid line), while the galaxies containing AGN form a plume extending to the top right part of the diagram. The higher ionization parameter and/or harder ionizing radiation that occur only in the presence of AGN cause the line ratios to lie above and to the right of the maximum starburst curve (dashed line) developed by Kewley et al. (2001a). Galaxies that are located between both curves are believed to host a mixture of star-formation and AGN and are sometimes called composites. We adopt this nomenclature in the remainder of this work.

While the BPT diagram shown in Figure 3.1(a) is used extensively to identify the source of ionization in galaxies, the $[\text{N II}]$ and $\text{H}\alpha$ emission lines become unavailable in optical spectra at $z > 0.4$. What would be a good substitute for $[\text{N II}]/\text{H}\alpha$? The $[\text{N II}]/\text{H}\alpha$ line ratio provides an indication of the gas-phase metallicity in star-forming galaxies (Kewley & Ellison, 2008). The empirical mass-metallicity relation (e.g., Tremonti et al., 2004; Savaglio et al., 2005) suggests a physical connection between that line ratio and the stellar mass, as displayed in Figure 3.1(b). While the $M_\star - Z$ relation applies to star-forming galaxies without AGNs, there is another effect that makes stellar mass a good choice. The $[\text{N II}]/\text{H}\alpha$ ratio saturates at high values for normal star-forming galaxies and

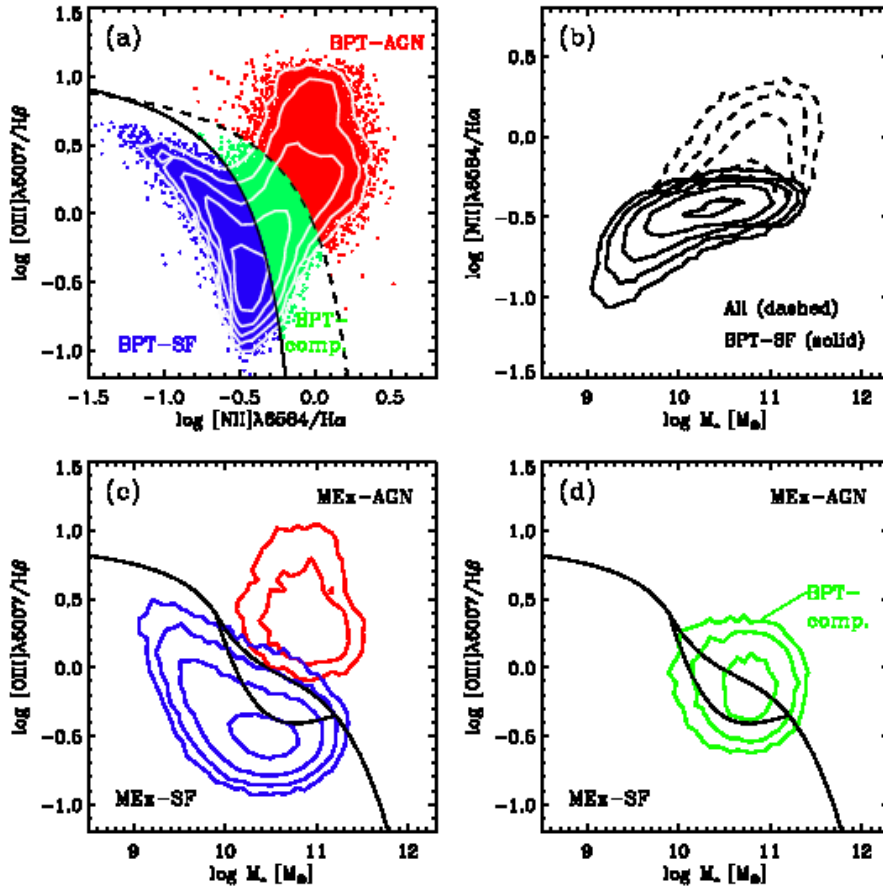


Figure 3.1 Emission line diagnostic diagrams: (a) BPT diagram: purely star-forming galaxies (SF, shown in blue) form a sequence below the solid line adapted from Kauffmann et al. (2003) whereas galaxies hosting an AGN (red) tend to occupy the area above and to the right of the dashed curve (Kewley et al., 2001a). Galaxies located between the two curves are composites, i.e., having mixed SF and AGN contributions (BPT-comp., green). (b) Stellar mass as a function of the line ratio $[\text{N II}]\lambda 6584/\text{H}\alpha$. For star-forming galaxies the trend is analogous to the $M_* - Z$ relation (solid contours).

Figure 3.1 *continued*. For the total sample including composites and AGNs, there is a stronger increase in $[\text{N II}]/\text{H}\alpha$ compared to stellar mass but AGNs reside in galaxies with both a high value of $[\text{N II}]/\text{H}\alpha$ and a high stellar mass. These two features indicate that stellar mass is a viable substitute when $[\text{N II}] \lambda 6584$ or $\text{H}\alpha$ are not available. The modified diagnostic diagram is shown in (c) for the galaxies classified as SF or AGN on the BPT diagram (blue and red contours, respectively) and in (d) for those classified as composites (green contours). The MEx-intermediate region, located between the two empirical curves on the MEx diagram, contains a mix of composites (BPT-comp.) and star-forming (BPT-SF) galaxies. In all panels, the contours indicate the density of points (in bins of $0.075 \text{ dex} \times 0.075 \text{ dex}$) and are logarithmic (0.5 dex apart, with the outermost contour set to 10 galaxies per bin).

only more extreme conditions such as those encountered in the presence of an AGN can yield larger values (Kewley et al., 2006; Stasińska et al., 2006). Because AGNs tend to be found in hosts with high stellar mass (Kauffmann et al., 2003), these systems have both larger $[\text{N II}]/\text{H}\alpha$ and M_* values. This feature puts them in a location of the parameter space of the modified diagram that is analogous to their original location on the BPT diagram with respect to purely star-forming galaxies (i.e., higher and to the right). Consequently, the new AGN diagnostic is obtained by substituting stellar mass for the redder emission line ratio.

Indeed, we find that the BPT-SF and BPT-AGN classes are well separated on the new Mass-Excitation (MEx) diagram (Figure 3.1(c)). We define two empirical dividing lines that maximize the separation between galaxy classes, especially between the BPT-AGN class (above and to the right of the lines) and the purely star-forming BPT-SF class (below and to the left of the dividing lines). We note

that the location of the BPT-composite galaxies on the MEx diagram overlap with galaxies belonging to the other classes as shown in Figure 3.1(d). Their locus peaks in the region between the two empirical curves, which we dub the MEx-intermediate region. We note that 48% of the galaxies in this region are BPT-composites.

The number of galaxies of each BPT-class are reported in Table 3.1 for the three regions of the MEx diagram, and the main empirical division (top curve) is defined as follows:

$$y = \begin{cases} 0.37/(x - 10.5) + 1. & \text{if } x \leq 9.9 \\ a_0 + a_1x + a_2x^2 + a_3x^3 & \text{otherwise,} \end{cases} \quad (3.1)$$

where $y \equiv \log([\text{O III}] \lambda 5007/\text{H}\beta)$ and $x \equiv \log(M_*)$. The coefficients are the following: $\{a_0, a_1, a_2, a_3\} = \{594.753, -167.074, 15.6748, -0.491215\}$. Similarly, the lower curve defined as:

$$y = 800.492 - 217.328x + 19.6431x^2 - 0.591349x^3, \quad (3.2)$$

and is used over the range $9.9 < x < 11.2$.

Using the BPT classes as our reference, we compute the completeness and contamination fractions of the MEx selection for both the AGN and SF classes, separated using Eq. 3.1. The fractions are displayed in Figure 3.2. For the MEx-AGN class, we find that the completeness is very high in terms of BPT-AGNs (i.e., above the Kewley et al. (2001a) line), reaching close to 100% at high stellar mass (see the red diamonds in the top panel of Figure 3.2). The fraction of BPT-composite galaxies that are selected in the MEx-AGN side rises more slowly with stellar mass: from $\sim 20\%$ at $M_* < 10^{10} M_\odot$ to 95% at $M_* > 10^{11.5} M_\odot$ (black triangles). In the top panel, the contamination fraction is defined as the fraction of BPT-SF galaxies (below the Kauffmann et al. (2003) line) in the MEx-AGN side.

Table 3.1. Demographics of the MEx Diagram

BPT type	MEx-AGN	(%)	MEx-Interm. ^a	(%)	MEx-SF	(%)
BPT-SF	1465	6.0	9153	51.7	64243	94.4
BPT-composite	9782	40.0	8468	47.8	3760	5.5
BPT-AGN	13212	54.0	90	0.5	31	0.04
All	24459	100	17711	100	68034	100

(a) MEx-intermediate region: between the two curves defined by Equations 3.1 and 3.2.

The contamination fraction peaks at 10-20% for galaxies with $M_\star \sim 10^{10} M_\odot$, but it mostly stays well below 10%, with an overall fraction around 6% (blue asterisks). Global completeness and contamination values, calculated for the entire SDSS sample (all stellar masses), are shown with the larger plotting symbols on the right hand side of the figure.

Similarly, the completeness for the MEx-SF selection is defined as the fraction of the BPT-SF galaxies that are correctly identified. The completeness is close to 100% (blue asterisks in Figure 3.2[b]) over a wide range of stellar masses with a drop off at $M_\star > 10^{11} M_\odot$. We note that at such high masses, there are very few purely star-forming galaxies (~ 200 and < 10 in the last two bins) whereas there are of the order of 10^4 galaxies per bin at lower mass (Figure 3.2[c]). The contamination with the BPT-AGN class is extremely low (red diamonds), on the order of 0.3%. However, the contamination fraction for BPT-composite goes up to $\sim 30\%$ at $M_\star > 10^{11} M_\odot$. These galaxies lie mostly in the intermediate region

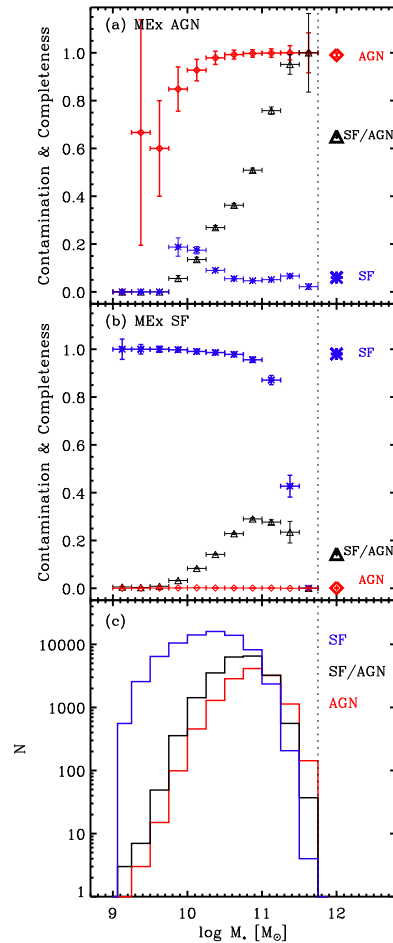


Figure 3.2 Completeness and contamination rates in bins of stellar mass (0.25 dex bins). *Top:* For the MEx-AGN selection, the AGN completeness is defined as the percentage of BPT-AGNs (above the Kewley line in the BPT diagram) that are above the MEx diagram dividing line (red diamonds). The definition is similar for the BPT-composite galaxies (black triangles). The contamination rate corresponds to the percentage of galaxies in the AGN side of the MEx diagram that would be purely star-forming galaxies according to the BPT diagram (blue asterisks). The overall values for the entire stellar mass range are shown on the right hand side of the figure.

Figure 3.2 *continued. Middle* For the MEx-SF selection, the completeness is defined as the percentage of BPT-SF galaxies (below the Kauffmann line) that are correctly identified in the star-forming side. The contamination rates are computed separately for the BPT-AGNs (red diamonds) and BPT composites (black triangles) and correspond to percentage of the number of galaxies in the star-forming side of the MEx diagram. Error bars are Poissonian. *Bottom* Distribution of stellar masses for galaxies that are classified as star-forming (blue), AGN (red), or composite (black).

of the MEx diagram. Whether they should be included with the star-forming sample or rejected will depend on the specific science goal.

We report the numbers for the MEx-intermediate class (i.e., between the lines defined by Eq. 3.1 and 3.2) separately in Table 3.1. Even though the AGN contamination of the MEx-SF class appears to be more substantial at high stellar mass, the effect is exaggerated by the small number of purely star-forming galaxies with $M_\star > 10^{11} M_\odot$. In fact, the AGN completeness peaks at the same mass range where the MEx-SF class appears the most contaminated, indicating that overall, the majority of the most massive galaxies harbor an AGN. Conversely, very few AGNs reside in low- M_\star hosts.

The scarcity of BPT-AGNs in host galaxies with $M_\star < 10^{10} M_\odot$ was previously noted by Kauffmann et al. (2003). These authors found that adding the emission from low-luminosity AGNs (with $10^5 < L_{[\text{O III}] \lambda 5007} < 10^6 L_\odot$) to low- M_\star star-forming galaxies would significantly alter their line ratios and move the corresponding points into the composite or AGN regions of the BPT diagram (in 93% of the cases with low-luminosity AGNs, and >99% for high-luminosity AGNs, i.e., with $L_{[\text{O III}] \lambda 5007} > 10^7 L_\odot$).

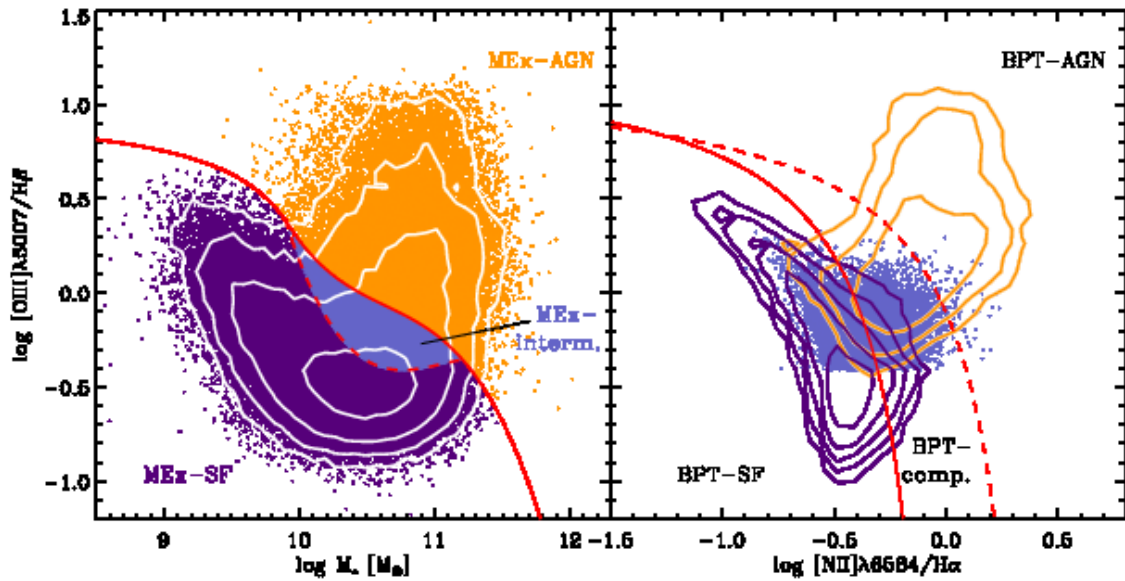


Figure 3.3 (left) Distribution of SDSS galaxies on the MEx diagram with our empirical divisions. Galaxies above the lines as classified as MEx-AGN (orange) whereas the galaxies below the lines are classified as star-forming (MEx-SF, in violet) and galaxies between the lines are MEx-intermediate (MEx-interm., in light purple). Using the same color-coding, we show these galaxies on the standard BPT diagram (right). Here, galaxies that are in the MEx-intermediate region are shown with dots while the MEx-SF and MEx-AGN subsamples are overplotted with contours (violet and orange, respectively). The contours indicate the density of points (in bins of $0.075 \text{ dex} \times 0.075 \text{ dex}$) and are logarithmic (0.5 dex apart, with the outermost contour set to 10 galaxies per bin).

So far, we have used the BPT spectral types (SF, AGN, composites) as references to quantify the completeness and contamination rates of the MEx selection. Now, we turn the situation around and we show a graphical comparison of the MEx diagram selection (eq. 1) mapped back onto the usual BPT diagram. Figure 3.3(a) shows the classification on the MEx diagram with MEx-AGN and MEx-SF galaxies colored in orange and purple, respectively. The contours show the density of points on a logarithmic scale. As can be seen in panel (b), our new AGN selection (orange contours) picks all the AGNs from the BPT diagram (above the dashed line in panel (b)) as well as a fair number of BPT-composites (mostly at higher $[\text{O III}] \lambda 5007/\text{H}\beta$ ratio), whereas our new MEx-SF selection (purple contours) captures the BPT star-forming sequence extremely well, with an extension into the BPT-composite region between the two dividing lines, especially in the region close to the Kauffmann et al. (2003) solid line. Galaxies in the MEx-intermediate region (light purple dots) are distributed over the BPT-comp. and BPT-SF regions.

3.3.2 A closer look at LINERs

The nature of LINERs remains controversial. Historically, they have been identified by the unusual strength of their narrow optical emission lines with low-ionization potential (Heckman, 1980). While most studies consider that LINERs are accretion-powered (Ho, 1999; Kewley et al., 2006), there are also claims that, in some cases, the powering source could be entirely stellar (e.g., from post AGB stars and/or white dwarfs, Binette et al., 1994; Stasińska et al., 2008) or a combination of processes including shocks (Heckman, 1980). Eracleous et al. (2010) argue that AGN activity does not provide enough energy to produce the LINER emission in half of their X-ray-selected sample of 35 LINERs. Such a deficit had been suggested previously (e.g., Ho et al., 1993), and could be compensated by

either obscuration of UV photons from the AGN, or by contributions from alternative sources such as post-AGB stars.

Chandra X-ray observations have been used to look for X-ray cores within LINERs. The detection fraction is typically high, ranging from 50% to 70% (see the review by Ho, 2008, and references therein). Employing *Spitzer* spectroscopy, Dudik et al. (2009) searched for high-ionization lines associated with AGN activity ([Ne V] 14 and $24\ \mu\text{m}$). They find that 39% of their sample of 67 LINERs have such detections and that many of these cases lack AGN signatures at optical and X-ray wavelengths. They also show that the optical identification (from, e.g., broad $H\alpha$ lines) is more subject to fail at higher infrared luminosities, suggesting that some AGNs may be missed due to dust obscuration. Their AGN fraction in LINERs goes up to 74% after combining diagnostics in all three wavelength ranges (X-ray, optical, mid-IR).

The BPT diagram that includes $[\text{O III}] \lambda 5007 / H\beta$ against $[\text{S II}] \lambda\lambda 6717, 6731 / H\alpha$, hereafter the [S II] diagram, can be used to tell apart the LINERs from the Seyfert 2 (Sy2) galaxies (e.g., Kewley et al., 2006). We apply this diagram to our SDSS sample in Figure 3.4. Panel (a) shows the [S II] diagram with dividing lines between star-forming, Seyfert, and LINER populations as labeled. Seyfert 2 (in red) and LINER (in orange) galaxies as defined in the [S II] diagram overlap slightly on the [N II] (panel b) and MEx (panels c,d) diagrams. BPT-composites (between the lines on the BPT [N II] diagram) fall closer to the LINER than to the Sy2 distribution.

Composite galaxies stand out more in their $[\text{N II}] / H\alpha$ than in their $[\text{S II}] / H\alpha$ ratio. Consequently, the star-forming selection (blue contours) extends into the composite and AGN regions of the BPT and MEx diagrams [Figure 3.4(b) and (c)]. As mentioned previously, the $[\text{S II}] / H\alpha$ ratio has the advantage of splitting

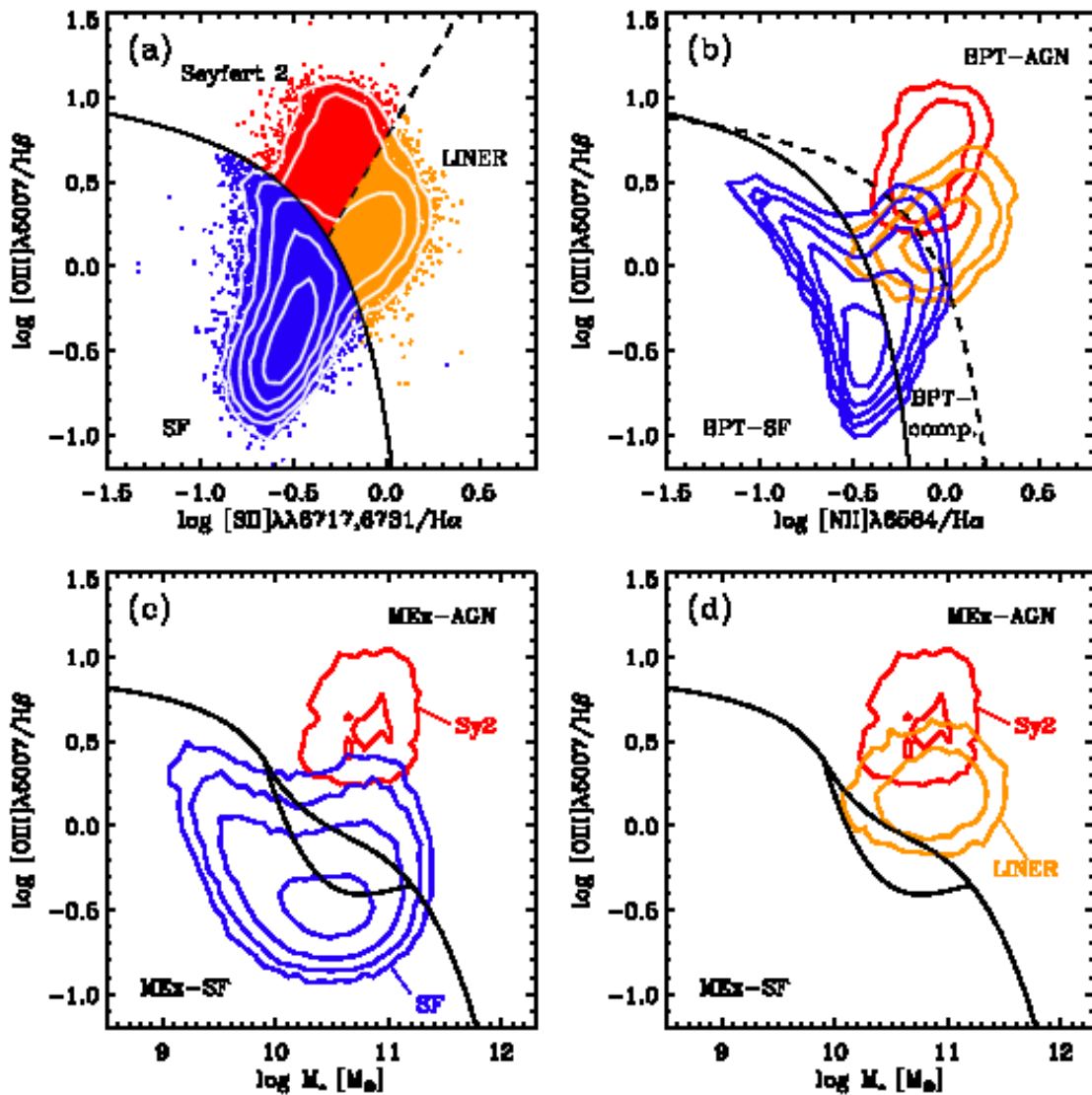


Figure 3.4 (a) The [S II] diagram. SDSS galaxies are color-coded according to their classification as SF (blue), Seyfert 2 (red) or LINER (orange). The dividing lines are taken from Kewley et al. (2006). All three classes are shown on the BPT diagram (b) with the same color scheme. The [S II] diagram is not very sensitive to composite galaxies (BPT-comp.) as most of them are classified as SF (blue contours). Similarly, the three [S II] diagram classes are shown on the MEx diagram (panel (c) for the SF and Seyfert 2 galaxies, and panel (d) for the LINERs relative to the Seyfert 2's).

Figure 3.4 *continued*. The upper empirical line on the MEx diagram selects all Sy2's and LINERs on the AGN side (above the lines), with some overlap between the two classes. In all panels, contours indicate the density of points (in bins of $0.075 \text{ dex} \times 0.075 \text{ dex}$) and are logarithmic (0.5 dex apart, with the outermost contour set to 10 galaxies per bin).

the LINERs from the Seyfert AGNs [dashed line from Kewley et al. (2006)]. This allows us to see that the MEx diagram selects both of these types of AGNs, and that the SDSS sample used here contains more LINERs than Seyfert 2's.

In the remainder of our analysis, we will use a scheme that combines the most trusted features of each diagram (i.e., the [N II] and the [S II] diagrams), which we introduce in the next section.

3.3.3 A Probabilistic Approach to Galaxy Classification

As was shown previously, some galaxy spectral classes overlap on the MEx diagram [Fig. 3.1(b,c); 3.3 and 3.4(c,d)]. Namely the MEx-intermediate region contains BPT-SF and BPT-composites, and there is also overlap between the BPT-LINERs and other AGN subclasses. To better assess the classification in such cases we present a scheme based on the probability of each spectral class given a galaxy's position on the MEx diagram. This approach is useful to discriminate between star-forming galaxies, composite galaxies, LINERs and Seyfert 2's.

In order to quantify the probabilities, we use a low-redshift³ SDSS sample as a calibration set. All of the BPT diagnostic emission lines are available for these galaxies and we can place them on the MEx diagram with prior knowledge of their source of ionization. The source of ionization is assigned according to a

³ $0.05 < z < 0.1$; The upper bound of the redshift range is chosen to remain complete in all categories including LINERs, whose detection rate decreases beyond $z \sim 0.1$ (Kewley et al., 2006).

hybrid classification based on both the [N II] and [S II] BPT diagrams with the following rules:

1. Star-Forming (SF): galaxies below the Kauffmann et al. (2003) line on the [N II] diagram irrespectively of their class on the [S II] diagram.
2. LINER: galaxies that are classified as AGN in the [N II] diagram (above the line from Kewley et al., 2001a) or in the [S II] diagram and that are below and to the right of the Seyfert/LINER dividing line on the [S II] diagram (Eq. 13 of Kewley et al. (2006)).
3. Seyfert 2 (Sy2): galaxies that are classified as AGN in the [N II] diagram (above the line from Kewley et al., 2001a) or in the [S II] diagram and that are above and to the left of the Seyfert/LINER dividing line on the [S II] diagram (Eq. 13 of Kewley et al. (2006)).
4. Composite (comp): composite galaxies from the [N II] diagram (between the (Kauffmann et al., 2003) and (Kewley et al., 2001a) curves) that were not included in the LINER and Sy2 classes described above.

The resulting spectroscopically-classified sample is the *SDSS prior sample*, which we assume is representative of galaxies out to $z = 1$ (see §3.7.5 for a discussion of possible evolutionary effects).

Relative to the previous diagrams, the combined classification method yields a slightly greater number of AGNs than each of the [N II] and [S II] diagram taken separately (because we use the union of the two AGN subsamples). Correspondingly, the composite class is slightly less numerous because some composite galaxies from the [N II] diagram are selected as AGN based on the [S II] diagram (mostly in the LINER region). Another distinction is that the LINERs

from the [S II] diagram that extend into the star-forming side of the [N II] diagram are now in the star-forming category. The latter category is identical to the original [N II] star-forming selection.

We now have a spectral classification scheme that exploits the strengths of both the [N II] and [S II] diagrams, and contains four mutually exclusive categories: star-forming (SF), composite (comp), LINER and Seyfert 2. We employ the distribution of the SDSS galaxies on the MEx diagram with *a priori* knowledge of their BPT classification to compute the fraction of galaxies of each category across the MEx plane.

For galaxies at higher redshift for which only [O III] $\lambda 5007/H\beta$ and stellar mass (M_*) are available, we use the rectangular region on the MEx diagram defined by the one-sigma uncertainties on these two measurements. We compute the number of *SDSS prior* galaxies in each category (star-forming, composite, LINER, and Seyfert 2) and we normalize by the total number of *SDSS prior* galaxies within the rectangular box. The fractions are converted to percentages. Given that the four classes described above are mutually exclusive, the sum $P(SF) + P(comp) + P(LINER) + P(Sy2) = 100\%$. For example, if a region surrounding given values of [O III] $\lambda 5007/H\beta$ and M_* (defined by the one-sigma error bars) contains 20,000 SF galaxies; 10,000 composites; 10,000 LINERs and no Seyfert 2s in the SDSS prior sample, the assigned probabilities would be $P(SF) = 50\%$, $P(comp) = 25\%$, $P(LINER) = 25\%$, and $P(Sy2) = 0\%$. Thus, this probabilistic AGN classification scheme has a built-in uncertainty. This is a useful feature compared to alternative diagrams where there is often no knowledge of the reliability of a certain classification. With this new approach, we know whether a given galaxy is near a dividing line or whether it is located far into the AGN or star-forming locus. In this paper, we assume that composites, LINERs,

and Seyfert 2's all host an active nucleus and often use: $P(AGN) = 1 - P(SF)$ (equivalent to $P(AGN) = P(comp) + P(LINER) + P(Sy2)$).

The empirical division on the MEx diagram introduced earlier (§ 3.3.1) traces well the observed transition between SDSS galaxies that host AGN activity of any category (composite, LINER, or Seyfert 2) and galaxies that are most likely star-forming [Figure 3.5(a,b)]. Figure 3.5 shows the probabilities $P(SF)$ and $P(AGN)$ as a function of position on the MEx diagram. The lower dividing curve delineates the separation between a *cleaner* star-forming galaxy sample (below) and the MEx region where $P(AGN) > 30\%$ (above). The region between the two curves contains a mixed BPT-SF/BPT-composite population. We adopt the term MEx-intermediate to describe this region of the MEx diagram and the galaxies that are located within it.

An alternative diagnostic diagram, developed in parallel to the MEx diagram, involves the same emission-line ratio on the vertical axis but makes use of rest-frame $U - B$ color rather than stellar mass (Yan et al., 2011, hereafter Y11). We display the AGN and star-forming fractions on this color-excitation diagram from Y11 in a similar fashion as for the MEx diagram [Figure 3.5(c,d)]. The original dividing lines are adapted from Y11 (straight lines) and the definition is included here for completeness:

$$\log([\text{O III}] \lambda 5007/\text{H}\beta) = \max\{1.4 - 1.2(U - B), -0.1\}. \quad (3.3)$$

In this paper, we add a curve on the diagram from Y11 that follows the transition where the AGN probability is $P(AGN) > 30\%$. The new region between this curve and the straight lines is analogous to the MEx-intermediate region of the MEx diagram and contains $> 50\%$ of BPT-composite galaxies. The lower curve in Figure 3.5(c,d) is defined by:

$$y = 12.3914 - 27.0954x + 18.5122x^2 - 4.02369x^3, \quad (3.4)$$

where $y \equiv \log([\text{O III}] \lambda 5007/\text{H}\beta)$ and $x \equiv (U - B)_0$. As in Y11, we calculate the rest-frame $U - B$ color, expressed in AB magnitudes, by using the *k-correct* v4.1.4 code from Blanton & Roweis (2007).

The bivariate distributions of galaxies on both the mass-excitation (MEx) and the color-excitation (CEX) diagrams are examined in more detail in Appendix B.

The SDSS subsample used here has been implemented as a reference to provide probabilities of each class as a function of the location on the MEx (or CEx) diagram. Given a stellar mass and $[\text{O III}] \lambda 5007/\text{H}\beta$ ratio, our publicly available IDL⁴ routines⁵ return a probability that the input galaxy belongs to the SF, composite, LINER, and Seyfert 2 categories. The MEx diagram is well motivated from the successes at separating and quantifying the overlap of BPT-classes for a large SDSS sample of galaxies. We will apply this new diagnostic to a sample of galaxies at $0.3 < z < 1$ in the following sections.

3.4 Intermediate-Redshift Galaxy Sample

Our intermediate-redshift galaxy sample is based on observations from the Great Observatories Origins Deep Survey⁶ (GOODS) and the All-wavelength Extended Groth strip International Survey⁷ (AEGIS). Most of the analysis is performed on galaxies at $0.3 < z < 1$, although we extend the range to slightly lower values when we use redder emission lines (such as in §3.5.1).

Optical spectra are drawn from the Team Keck Redshift Survey⁸ (TKRS Wirth et al., 2004) for galaxies in the GOODS-North (GOODS-N) field, and from the DEEP2 Galaxy Redshift Survey (hereafter DEEP2; Davis et al., 2003, 2007) for

⁴Interactive Data Language.

⁵<http://monkey.as.arizona.edu/~sjuneau/AGN-Galaxy-Classification.html>

⁶<http://www.stsci.edu/science/goods/>

⁷<http://aegis.ucolick.org/>

⁸<http://tkserver.keck.hawaii.edu/tksurvey/>

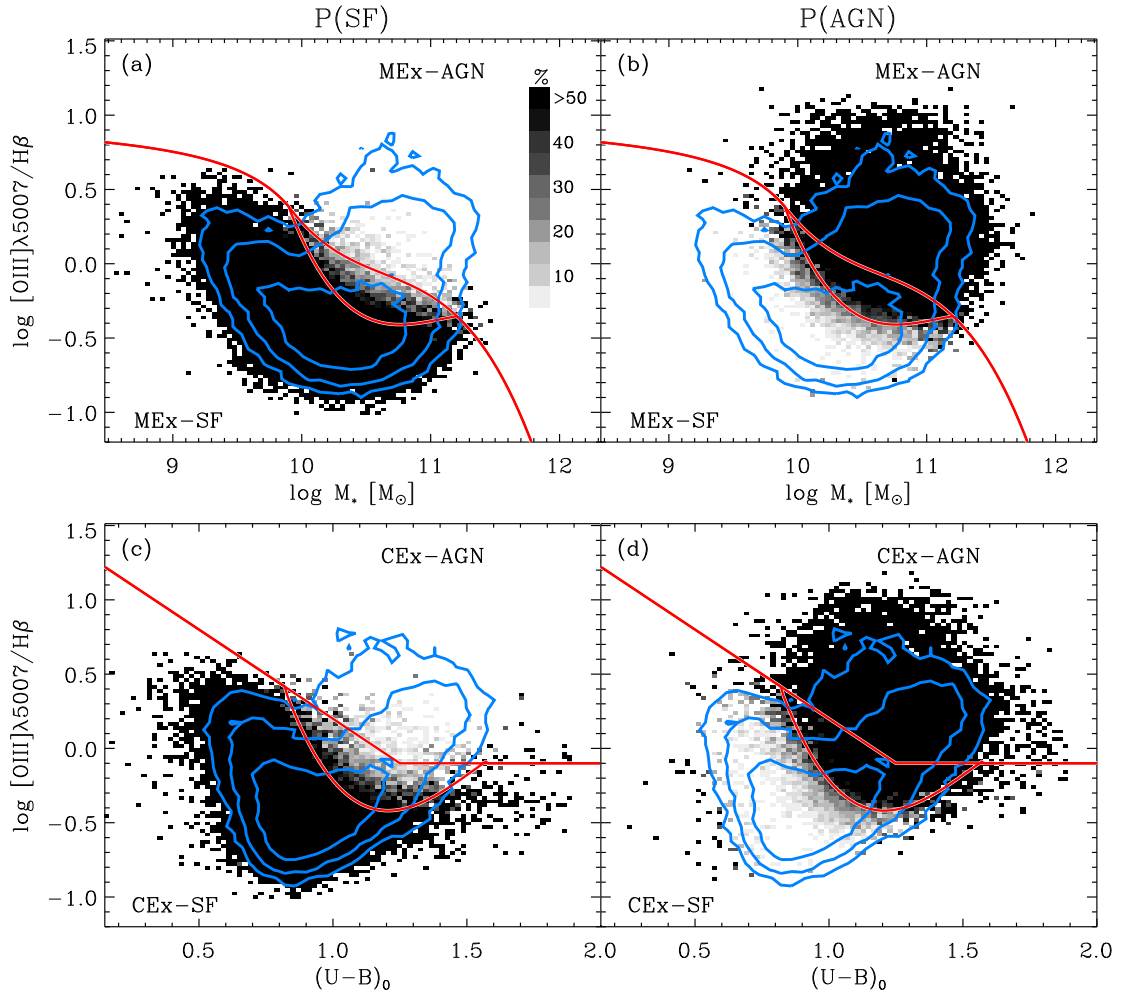


Figure 3.5 Percentages of galaxies classified as star-forming or AGN (all sub-categories) as a function of location on the MEx and CEx diagrams (top and bottom row, respectively). The left-hand side shows the number of SF galaxies divided by total number galaxies, or $P(SF)$, in each bin ($0.04 \text{ dex} \times 0.04 \text{ dex}$) for the MEx (a) and CEx (c) diagrams. The AGN percentages $P(AGN)$ are displayed on the right hand side, where panel (b) is the MEx diagram and panel (d) the CEx diagram developed by Y11. $(U-B)_0$ denotes the rest-frame $U-B$ color expressed in AB magnitudes.

Figure 3.5 *continued*. In all panels, the upper lines mark the main division between AGN and star-forming galaxies, whereas the lower lines approximately correspond to a transition from $P(\text{AGN}) < 30\%$ (below) to $P(\text{AGN}) > 30\%$ (above). Galaxies between both sets of lines are a mixed SF/composite population, which we call MEx-intermediate galaxies (or CEx-intermediate in panels c,d). The bivariate distribution of the SDSS sample combining all galaxy classes is shown with logarithmic contours.

galaxies in the Extended Groth Strip (EGS) field. These two spectroscopic surveys have similar limiting magnitudes of $R_{AB} = 24.3$ and 24.1 , respectively. The former lies within GOODS-N ($10' \times 16'$) and includes redshifts for 1440 galaxies (1044 galaxies with confident redshifts $0.3 < z < 1$). From the DEEP2 survey, we only use the pointing in the Extended Groth Strip (centered at $14\ 17, +52\ 30$) covering $120' \times 15'$. There are 6,588 DEEP2 galaxies with confident redshifts $0.3 < z < 1$ in this pointing.

Both sets of observations were obtained with the DEIMOS spectrograph (Faber et al., 2003) at the Keck Observatory and reduced with the pipeline⁹ developed by the DEEP2 team at the University of California-Berkeley. However, their spectral resolution and spectral range differ due to the use of different gratings (600 line mm^{-1} for TKRS and 1200 line mm^{-1} for DEEP2). The TKRS resolution is 4\AA full-width-half-maximum (FWHM) over the wavelength range $5500\text{--}9800\text{\AA}$, whereas DEEP2 spectra have a resolution of 2\AA FWHM with a wavelength coverage of $6500\text{--}9100\text{\AA}$. These different spectral ranges mean that emission lines of interest are accessible over somewhat different redshift ranges for the two samples. $\text{H}\beta$ and $[\text{O III}] \lambda 5007$ can be observed out to $z \sim 1$ with TKRS spectra but

⁹<http://astro.berkeley.edu/~cooper/deep/spec2d/>

only out to $z \sim 0.8$ with DEEP2 spectra.

A wealth of multiwavelength data is available in both GOODS-N and EGS. In this paper, we utilize ancillary *Chandra* X-ray data, *Spitzer* IRAC data, and ground-based optical imaging (§3.4.2). *Spitzer*/IRAC photometry is available in all four channels (available through the *Spitzer* Science Center, also see Barmby et al., 2008, for EGS). In what follows, IRAC photometry is used to estimate the rest-frame *K*-band magnitude (§3.4.2). We take advantage of the fact that the *Chandra* X-ray coverage is very deep: 2 Msec in GOODS-N (Alexander et al., 2003) and 200 ksec in EGS (Laird et al., 2009; Nandra et al., 2005). This provides us with an independent AGN/star-forming classification scheme (§3.5). The sensitivity of the shallower data is adequate to ensure the detection of luminous X-ray sources ($L_{2-10\text{keV}} > 10^{42} \text{ erg s}^{-1}$, a nominal luminosity threshold for AGN) out to $z \sim 1$. Furthermore, we can detect fainter X-ray galaxies (including starbursts) at all redshifts in GOODS-N.

3.4.1 Emission Line Fluxes

Emission line fluxes from the TKRS and DEEP2 spectra were measured using automated IDL routines. For each emission line, we fit the continuum with a linear relation over 30 \AA windows on either side of the line with a biweighting scheme. This technique efficiently rejects outliers and is thus robust against pixels with large errors (e.g., due to large sky subtraction residuals). If the flux density at the line peak is greater than three times the standard deviation of the continuum, the line is fitted with a Gaussian function. In such cases, we calculate emission line fluxes in two ways. First, we integrate the resulting Gaussian fit over a wavelength range corresponding to $\pm 2.5\sigma$, where σ is the Gaussian width parameter (= FWHM/2.35). Secondly, we directly integrate the continuum-subtracted spectra over the same wavelength range.

In most cases, we use the fluxes obtained from integrating the data directly. However, some potentially problematic cases were flagged for visual inspection. Among 509 TKRS galaxies for which both the $H\beta$ and $[\text{O III}] \lambda 5007$ emission lines passed the signal-to-noise and quality criteria, 61 were flagged as uncertain. Similarly, 245 among 2,536 DEEP2 galaxies were flagged for visual inspection. This generally occurs when the data are corrupted nearby the targeted emission line, or when the Gaussian fit is inadequate. These objects are examined on a case-by-case basis, and the flux measurement is adjusted accordingly. Among a total of 306 galaxies that were examined, 184 were validated whereas 122 were flagged as uncertain and not used in subsequent analysis.

We correct for underlying stellar absorption at $H\beta$ and $H\alpha$. TKRS spectra with a median signal-to-noise ratio (S/N) per pixel greater than three were fit individually using Bruzual & Charlot (2003, hereafter BC03) spectral synthesis models. Utilizing IDL *simplefit* routines (C. Tremonti, private communication), we fit the continuum of the galaxies with a linear combination of ten representative stellar population templates, leaving dust obscuration as a free parameter. We subtract the continuum to correct Balmer lines for underlying stellar absorption. The median corrections (\pm half of $84^{\text{th}} - 16^{\text{th}}$ percentile range), expressed in terms of equivalent widths (EWs), are $2.8(\pm 0.9) \text{ \AA}$ at $H\beta$ and $1.4(\pm 0.7) \text{ \AA}$ at $H\alpha$. These values were applied to spectra that were not fit individually due to low signal-to-noise ratio or uncertain spectrophotometry. We note that applying the median correction to $H\beta$ ($H\alpha$) for spectra with an individual fit changes their line fluxes by 0.08 (0.03) dex r.m.s.

In addition to using line ratios, we will use $[\text{O III}] \lambda 5007$ luminosities to quantify the strength of AGN activity (e.g., in §3.6). For that purpose, the slit loss corrections are obtained by calculating synthetic photometry from the spectra in

the band nearest to the observed wavelength of [O III] $\lambda 5007$ (usually ACS $F775w$ or $F814w$ for GOODS-N and EGS observations, respectively) and comparing to the true observed photometry. The synthetic photometry is obtained by applying the filter curve and integrating over the wavelength range of interest in the observed band. The ratio between the total flux from observed photometry and the synthetic photometry is used as a multiplicative correction factor. The median slit loss correction is a factor of two.

3.4.2 Stellar Masses

The stellar masses of our intermediate-redshift sample were calculated by fitting stellar population synthesis models to spectral energy distributions (SEDs) measured by galaxy photometry. The procedure is described in Salim et al. (2007). For galaxies in EGS, the following photometric bandpasses are used: FUV, NUV (GALEX), $ugriz$ (CFHTLS), and K (Palomar) (see Salim et al., 2009; Gwyn, 2008, 2011; Bundy et al., 2006). For galaxies outside of the Canada-France-Hawaii Telescope Legacy Survey (CFHTLS) field-of-view, we use CFHT 12k BRI photometry from Coil et al. (2004). For GOODS-N, the constraints are provided by the following photometry: $UBVRiz$ taken from Capak et al. (2004) and JK obtained with the Flamingos camera on the Mayall 4 m NOAO telescope. In GOODS-N, the SED fitting is performed for galaxies with $K < 20.5$ (Vega) (as in Daddi et al., 2007, but extending to lower redshifts).

The calculations assumed a Chabrier IMF (Chabrier, 2003), and output a probability distribution function (PDF) for the stellar mass. We assume the average of the PDF as the stellar mass, and estimate errors from the 2.5th and 97.5th percentiles [= $(97.5PL - 2.5PL)/3.92$]. Note that this fitting method is highly uncertain for systems with a Type 1 AGN (identified by broad emission lines arising from the broad-line region) for which the central engine may contribute enough

photons to affect the broad-band photometry and alter the SED fitting results. However, these broad-line AGNs are easily identified and are not the object of this study, which targets narrow-line objects (Type 2 AGNs, LINERs, and star-forming galaxies).

We note that, for SDSS galaxies, the method used by Salim and collaborators to derive stellar masses was tested against the results from Kauffmann et al. (2003). Salim et al. (2005) found a very good agreement between the two distinct methods and calculated the scatter of the difference to be 0.11 dex (without 3σ outliers, see their Fig. 1), which is smaller than the typical uncertainties for our galaxy sample. Thus, we do not anticipate strong systematic differences to be associated with the methods used to derive stellar masses for the low-redshift and intermediate-redshift samples that we use.

In general, we find that the values of stellar mass correlate well with the absolute rest-frame K -band magnitudes (M_K). The latter are obtained by applying a k -correction to the observed IRAC $3.6\mu\text{m}$ photometry. We calibrate the relation between M_\star and M_K (see Appendix C) for galaxies with both of these estimates in order to estimate a stellar mass for galaxies lacking SED fitting calculations.

Starting from 2,561 galaxies with a valid stellar mass from SED fitting ($\chi^2 < 7$) and satisfying our emission-line selection, we augment our sample with 251 stellar masses estimated from M_K . The added galaxies had either missing photometry or an unacceptable SED fit ($\chi^2 > 7$). We obtain a total sample size of 2,812 galaxies at $0.3 < z < 1$ with stellar mass estimates and valid [O III] $\lambda 5007$ and $\text{H}\beta$ emission line fluxes.

3.4.3 X-ray Luminosity and Classification

We convert X-ray fluxes in the hard band (2 – 8 keV; rest-frame 2.6 – 16.0 keV at $z = 0.3 - 1$) to rest-frame 2 – 10 keV luminosities, assuming a power-law spec-

trum with photon index as calculated in Alexander et al. (2003) to perform the k -correction. The fluxes are corrected for Galactic extinction but not for absorption intrinsic to each galaxy.

Our X-ray classification is based on two criteria: (i) $L_{2-10\text{keV}} > 10^{42} \text{ erg s}^{-1}$; (ii) hardness ratio¹⁰ $HR > -0.1$ (which corresponds to photon index $\Gamma < 1$). X-ray sources are classified as AGN if they satisfy *at least one* of these criteria. Otherwise, they are classified as X-ray starbursts. We cannot rule out that some AGNs may fail both the luminosity and hardness criteria due to X-ray absorption or intrinsically weak emission. Those objects are especially interesting in the framework of this study given the difficulty in identifying them using solely X-ray observations. We keep this possibility in mind as we will look for AGN signatures at other wavelengths besides X-rays.

Some galaxies lack a detection in the hard band (2 – 8 keV) but are detected in the full band (0.5 – 8 keV). In these cases, we k -correct the full band fluxes to obtain rest-frame 2 – 10 keV luminosities assuming an index $\Gamma = 1.9$. These galaxies will be marked with different plotting symbols when using their inferred $L_{2-10 \text{ keV}}$ since those values may be limits.

Formally, our classification scheme differs from that described in Bauer et al. (2004). Those authors used a different X-ray luminosity threshold ($L_{0.5-8 \text{ keV}} > 3 \times 10^{42} \text{ erg s}^{-1}$) and also included criteria based on inferred Hydrogen column density and the presence of broad ($> 1000 \text{ km s}^{-1}$) or high-ionization emission lines in the optical spectrum. Here, we aim for a classification based only on X-rays, independent from optical spectroscopy. Nevertheless, we note that the resulting classification is very similar for galaxies that overlap between the sample from Bauer et al. (2004) and that presented here.

¹⁰Hardness ratio $\equiv (H-S)/(H+S)$, where H and S are the number of X-ray counts in the hard (2-8 keV) and soft (0.5-2 keV) bands.

We consider X-ray detections for most of our analysis but we also calculated X-ray upper limits for GOODS-N galaxies that were selected based on their [O III] luminosity. The X-ray upper limits were calculated following §3.4.1 of Alexander et al. (2003) and assuming $\Gamma = 1.9$.

3.5 Diagnostics at Redshift 0.3 – 1

Now that we have calibrated the MEx diagram at low-redshift with SDSS galaxies, we apply it to a sample of intermediate redshift galaxies. Our sample, described in §3.4, contains 2,812 galaxies at $0.3 < z < 1$ from the GOODS-N and EGS fields with valid $H\beta$ and [O III] $\lambda 5007$ measurements.

3.5.1 Comparison with X-ray Classification

The validity of the MEx diagram was demonstrated by showing a good correspondence with the BPT classification in §3.3.1. Here we show another line of support based on the comparison of the MEx classification with a completely independent scheme based on X-ray observations. As can be seen in Figure 3.6(a), 85% (34/40) of the X-ray AGNs with valid emission line measurements (S/N > 3) are classified as MEx-AGN (26/40) or MEx-intermediate (8/40) on the MEx diagram. Thus the MEx diagram has a high success rate for recovering X-ray identified AGNs.

As for the X-ray starbursts, 50% (8/16) are classified as SF on our new diagram, while 19% (3/16) are in the intermediate region and the remaining 31% (5/16) reside in the AGN region. However, low-luminosity AGNs and some heavily absorbed AGNs may appear as faint as X-ray starbursts so this class of objects likely includes these different systems in addition to genuine starbursting galaxies. Indeed, the two X-ray starbursts that are in the AGN region of the MEx diagram but that lie at sufficiently low redshift to be placed on the BPT diagram

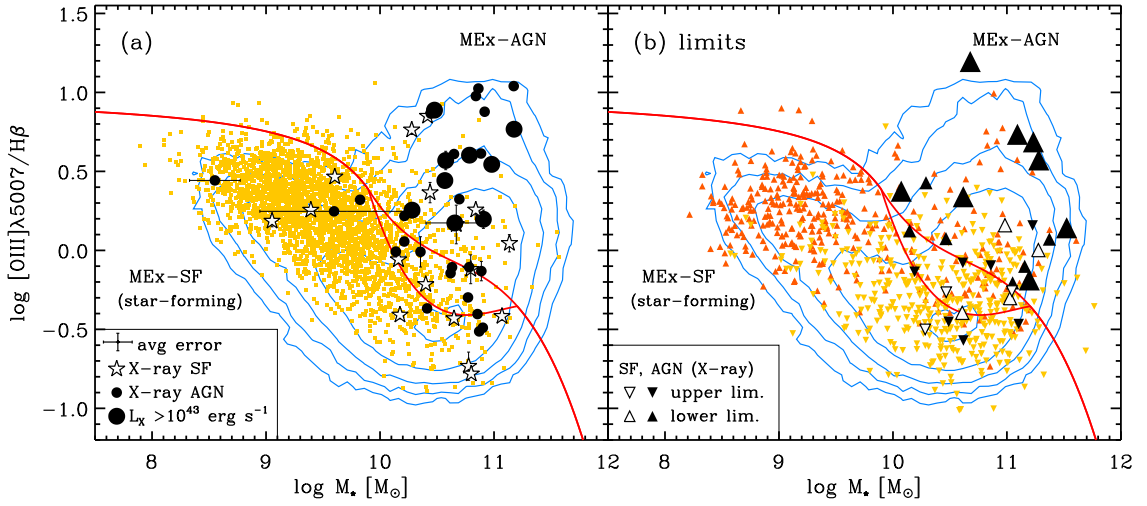


Figure 3.6 Application of the MEx diagnostic to identify the presence of active nuclear activity within galaxies at $0.3 < z < 1$. Contours show the SDSS low- z sample (evenly spaced on a logarithmic scale). (a) Our intermediate redshift sample is superimposed (filled squares) and, when available, the X-ray classification is marked with larger symbols [star symbols for X-ray starbursts; small (large) filled circles for X-ray AGNs with $L_X < 10^{43} \text{ erg s}^{-1}$ ($L_X > 10^{43} \text{ erg s}^{-1}$)]. We also show galaxies with only one emission line detection and one upper limit (b). The resulting $[\text{O III}]/\text{H}\beta$ ratios are upper limits when only $\text{H}\beta$ is detected (yellow downward triangles) or lower limits when only $[\text{O III}] \lambda 5007$ is detected (orange upward triangles). The X-ray classification is marked with open triangles for X-ray starburst, and solid black triangles for X-ray AGNs [small (large) for X-ray AGNs with $L_X < 10^{43} \text{ erg s}^{-1}$ ($L_X > 10^{43} \text{ erg s}^{-1}$)]. The empirical lines on the MEx diagram are described in the text (see §§3.3.1, 3.3.3). The error bar shown in the legend represents the typical uncertainty although we plot individual error bars for objects whose uncertainty are significantly larger. This diagram is applicable out to $z \sim 1$ and yields spectral classes that are very consistent with the independent X-ray classification shown here.

($z < 0.5$) stand out in the BPT-AGN region (Figure 3.7), further confirming the presence of actively accreting black holes in these galaxies. The optical diagnostics are thus especially useful when the X-ray signal alone is ambiguous (e.g., too faint to securely identify AGNs). Additional support for the presence of AGN in the X-ray starburst class is provided for at least one galaxy for which we have a clear detection of the [Ne V] $\lambda 3425$ emission line (Figure 3.8). This transition is an unambiguous tracer of AGN activity because of its high ionization potential (97.1 eV).

Next, we use the MEx classification probability method described in §3.3.3. We calculate $P(\text{AGN})$ by adding the probabilities of any AGN category (composite, LINER and Seyfert 2). We will show in §3.5.2 that $P(\text{AGN}) > 30\%$ is a useful threshold to distinguish AGNs from purely star-forming galaxies. When X-ray AGNs, X-ray starbursts, and non-X-ray detections are considered separately, we find that 29 among 35 X-AGNs (83%) galaxies have $P(\text{AGN}) > 30\%$, with an average AGN classification probability of 77%. For the X-ray starbursts, which all have a low hard X-ray luminosity ($L_{2-10\text{keV}} < 10^{42} \text{ erg s}^{-1}$), we find that 11 among 17 X-SBs (65%) have $P(\text{AGN}) > 30\%$ (average $P(\text{AGN}) = 52\%$). This suggests that some of them host an X-ray absorbed or X-ray weak AGN. Lastly, we note that some of the galaxies lacking an X-ray detection lie well into the AGN region with $P(\text{AGN})$ up to 100%. These X-ray faint AGN candidates are studied in more detail in §3.5.2. Like the X-ray starburst class, they may in fact include weak or heavily absorbed AGNs.

Not all of the X-ray detected sources have valid emission line measurements. X-ray galaxies for which only one of $H\beta$ or [O III] $\lambda 5007$ is measured and the other line has an upper limit are shown in Figure 3.6(b). In these cases, the [O III]/ $H\beta$ line ratio is either an upper or lower limit. We find that most X-ray classified

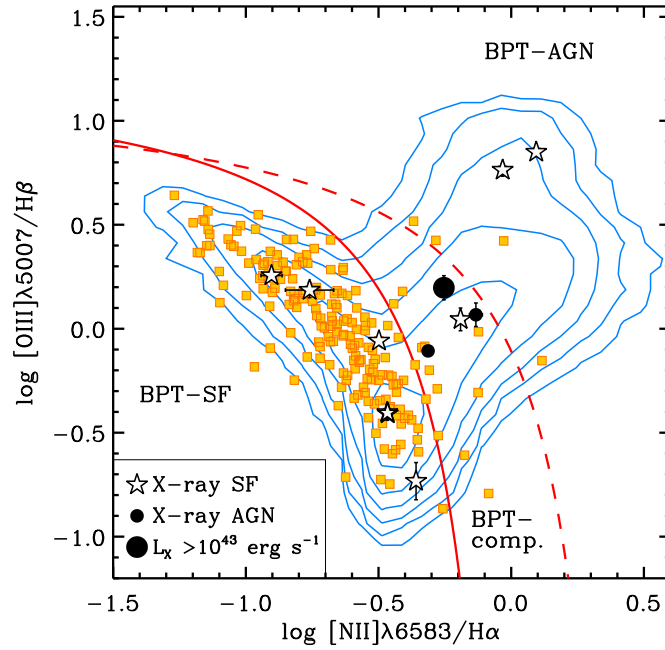


Figure 3.7 The BPT diagram, where BPT-AGNs are found above the dashed line (adapted from Kewley et al., 2001a), star-forming (BPT-SF) galaxies below the solid line (adapted from Kauffmann et al., 2003), and composites (BPT-comp.) between the two lines. Contours show the SDSS low- z sample (evenly spaced on a logarithmic scale). The $z \sim 0.35$ galaxies for which we have all four diagnostic lines from TKRS ($0.2 < z < 0.5$) and DEEP2 ($0.3 < z < 0.4$) are mostly distributed along the star-forming sequence, with a few galaxies extending along the AGN plume (filled squares). We identify galaxies with a *Chandra* detection as a function of their X-ray classification [star symbols for X-ray starbursts; small (large) filled circles for X-ray AGNs with $L_X < 10^{43} \text{ erg s}^{-1}$ ($L_X > 10^{43} \text{ erg s}^{-1}$)]. While all the X-ray identified AGNs lie above the Kauffmann line (solid line), there are also two galaxies nominally classified as X-ray starbursts that lie in the region where AGNs are prominent. These systems also lie in the MEx-AGN region [Figure 3.6(a)] and they may be X-ray weak or X-ray absorbed AGNs. In either case, the optical diagnostic is a useful complement to X-ray observations alone.

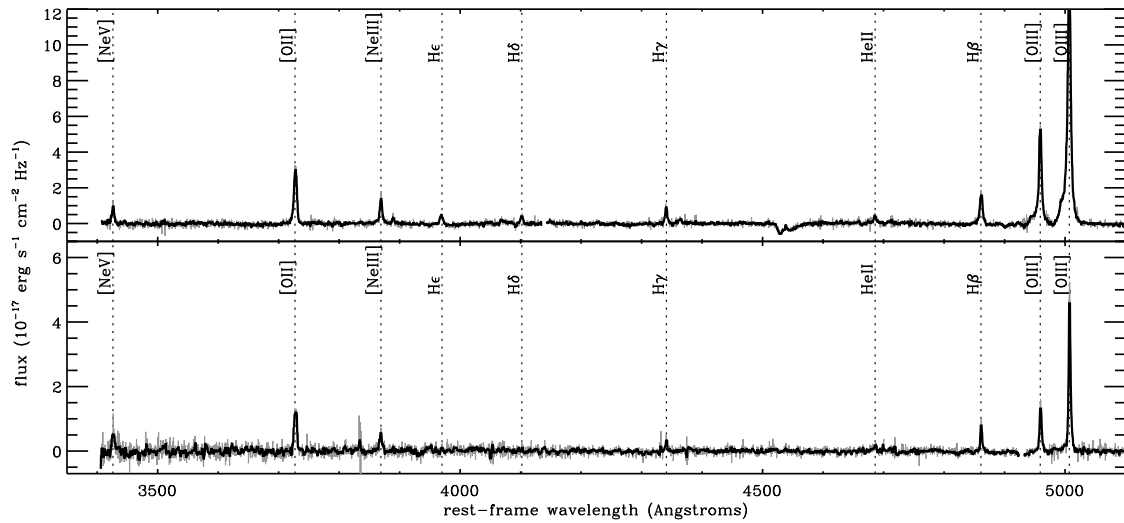


Figure 3.8 Two example TKRS spectra with the most obvious [Ne V] $\lambda 3425$ detections. While the top spectrum is for a galaxy that was also identified as AGN in the X-rays (J123608.13+621036.2, $z=0.679$), the bottom one is for a galaxy that was classified as X-ray starburst (J123645.40+621901.3, $z=0.455$). The spectra are continuum-subtracted (grey line) and smoothed with a running median (thicker black line). Typical emission lines are marked with vertical dotted lines and labeled.

AGNs appear consistent with their optical classification given their limits on the MEx diagram. X-ray galaxies for which no lines could be measured due to insufficient data quality or intrinsic weakness of the emission lines are considered in §3.5.3.

We note that the locus of our intermediate-redshift star-forming galaxies may be offset slightly from the SDSS contours. A more careful analysis of the selection effects would be required to determine whether such a shift is real or simply results from selection biases. We discuss possible evolutionary effects in §3.7.5.

Overall, the MEx diagram is a new tool that can be used on galaxies with [O III] $\lambda 5007$ and $H\beta$ line fluxes as well as stellar mass. It is thus possible to apply a robust AGN diagnostic to optical spectroscopic samples out to $z \sim 1$, provided the galaxies also have photometry allowing a stellar mass estimate. An independent X-ray classification scheme supports the validity of our diagram. This means that surveys with optical spectroscopy but lacking X-ray coverage can still benefit from a reliable AGN diagnostic.

In order to complete the comparison between the optical MEx diagram AGN classification, and the X-ray based classification, we perform two experiments. First, we use X-ray stacking to search for AGN signatures in galaxies that are undetected in the X-ray observations (§3.5.2). Second, we calculate the demographics of all X-ray AGNs regardless of the presence of optical emission lines (§3.5.3). This exercise highlights the complementarity of the optical and X-ray selection techniques.

3.5.2 X-ray Stacking

Stacking the X-ray observations allows us to probe X-ray emission to fainter flux levels and, in the case of significant detections in more than one energy band, to estimate the X-ray spectral slope. The X-ray spectral slope (or photon index

Γ) can be used to distinguish between different source types. While unabsorbed AGNs and low-mass X-ray binaries (LMXBs) exhibit a large index ($\Gamma > 1.3$ and > 1.7 , respectively), high-mass X-ray binaries (HMXBs) can yield flatter slopes with indices down to ($\Gamma > 0.5$) and absorbed AGNs have still flatter slopes with ($-1 < \Gamma < 1$). These ranges are illustrated on Figure 2 of Alexander et al. (2005, see references therein).

In the case of X-ray absorbed AGNs, the flattening is caused by the photoelectric absorption of soft X-ray photons by heavy atoms in neutral gas along the line of sight. Because softer photons are preferentially absorbed relative to harder ones, Compton-thick AGNs (with $N_H > 10^{24} \text{ cm}^{-2}$) should exhibit a flat slope with $\Gamma < 1$. However there are at least two situations where Compton-thick AGNs instead have a steep X-ray slope at energies $< 10 \text{ keV}$. First, the shape of the X-ray spectrum varies greatly when the X-ray emission is dominated by reflection rather than direct transmission. In this case, the slope of the spectrum does not truly reflect the hardness of the radiation and one must use other indicators to estimate X-ray absorption (e.g., the equivalent width of the Fe $K\alpha$ line). Second, the photon index at energies $0.5 - 10 \text{ keV}$ can be significantly altered when soft emission from starburst activity is coincident with the harder emission from an absorbed AGN. We keep these possibilities in mind when we interpret the results of X-ray stacks.

In this paper, we perform two different X-ray stacking analyses. The first analysis is a proof-of-concept of the MEx diagram. In this case, the goal is to stack the X-ray signal for subsamples defined from the MEx classification. A more detailed description and the results are provided in this section. For the second analysis (described below in §3.6.3), we apply additional criteria to target specifically X-ray absorbed AGN candidates.

In this section, we are interested in galaxies that are not detected individually in the deep 2 Msec *Chandra* observations in GOODS-N but that have the required emission line measurements for the MEx diagram. Employing a stellar mass cut-off at $10^{10} M_{\odot}$ and requiring $H\beta$ and $[O III] \lambda 5007$ emission line detections ($S/N > 3$), there are 69 such galaxies at $0.3 < z < 1$.

For the X-ray stacking we adopt a similar approach to Worsley et al. (2005), who stacked sources and calculated the significance of the stacked result using 10,000 Monte Carlo trials. In all cases, we limit the X-ray stacking to sources within 6 arcmin of the *Chandra* aim point to maximize sensitivity and we stack the sources in the soft and hard bands. Sources that lie within a factor of 2 of the 90% encircled energy radius of another X-ray detected source are excluded. We only consider the stacked signal as a significant detection when the number of detected counts in a given band exceed the background count rate determined from the Monte Carlo trials by $\geq 3 \sigma$.

Following the criteria outlined above there are 47 (out of 69) X-ray undetected galaxies in GOODS-N for which we can stack the *Chandra* data. We select subsamples of the X-ray undetected galaxies to stack based on the probabilities $P(AGN)$ & $P(SF)$. Here we use $P(AGN)$ as the total probability for the composite, LINER and Seyfert subclasses. We divide the sample at $P(AGN) > 50\%$ and also at $P(AGN) > 30\%$ in order to include the MEX-intermediate region.

In the former case, we find significant detections in *Chandra*'s soft band and marginal detections in the hard band for these $P(AGN) > 50\%$ and $P(SF) > 50\%$ subsamples of 25 and 22 galaxies, respectively. The X-ray spectral slopes are respectively flat ($\Gamma \sim 0.8$) and slightly steeper ($\Gamma \sim 1.2$; Table 3.2). A flat X-ray spectral slope of $\Gamma \sim 0.8$ unambiguously indicates the presence of absorbed AGN activity (see Fig. 2 of Alexander et al., 2005; Maiolino et al., 1998) in the

$P(\text{AGN}) > 50\%$ subsample. The stacked signal of the complementary subsample may correspond to a mixture of star-forming galaxies and some absorbed AGNs. However, the difference in Γ between the $P(\text{AGN}) > 50\%$ and $P(\text{SF}) > 50\%$ subsamples is not statistically significant so there is a fair likelihood that some absorbed AGNs are present. This result suggests that $P(\text{AGN}) > 50\%$ may not be sufficient to recover all of the AGNs.

Imposing a lower cutoff at $P(\text{AGN}) > 30\%$ yields 34 objects to stack. Stacking these sources gives significant detections in the soft and hard bands corresponding to a flat X-ray spectral slope of $\Gamma \sim 0.8$, again unambiguously indicating the presence of absorbed AGN activity. We then stacked the remaining 13 systems, with $P(\text{SF}) > 70\%$. In this case, we only find a significant detection in the soft band. The steep X-ray spectral slope ($\Gamma \sim 1.7$) is consistent with the X-ray emission of these galaxies being dominated by star formation processes. These analyses are summarized in Table 3.2 and provide good first-order confirmation that the combination of the MEx diagram and our probabilistic approach provides a comparatively clean selection of star-forming galaxies and AGNs.

Our results suggest that using $P(\text{AGN}) > 30\%$ as a threshold for nuclear activity leads to a cleaner separation between AGNs and star-forming galaxies than using $P(\text{AGN}) > 50\%$. We examine the objects with intermediate AGN likelihood separately by stacking the 12 galaxies with $30\% < P(\text{AGN}) < 50\%$. As expected, galaxies in this subset are likely composite systems. We calculate $P(\text{comp})$, $P(\text{LINER})$, $P(\text{Sy2})$ separately and, on average, the composite class is 5.5 times more likely than the LINER and Seyfert 2 classes taken together. We find a flat spectral slope of $\Gamma \sim 0.6$, statistically indistinguishable from the $P(\text{AGN}) > 50\%$ subsample. This result indicates that some galaxies with $30\% < P(\text{AGN}) < 50\%$ host an X-ray absorbed AGNs, therefore are an impor-

Table 3.2. X-ray Stacking of Non-Detections

Sample	N ^a	$\langle z \rangle$	Soft ^b	Soft σ	Hard ^b	Hard σ	HR ^c	Γ^d	Comment
(i) MEx Diagram Selection (see §3.5.2)									
P(AGN) \geq 50%	22	0.70 ± 0.18	1.61 ± 0.54	4.6	1.61 ± 0.81	2.9	0.00	0.8	Many absorbed AGNs
P(SF) $>$ 50%	25	0.60 ± 0.19	2.20 ± 0.54	6.3	1.49 ± 0.81	2.7	-0.19	1.2	Star-forming galaxies and some absorbed AGNs
P(AGN) \geq 30%	34	0.72 ± 0.17	1.31 ± 0.45	4.4	1.67 ± 0.69	3.6	0.12	0.8	Many absorbed AGNs
P(SF) $>$ 70%	13	0.54 ± 0.15	2.78 ± 0.77	5.8	1.03 ± 1.10	1.4	-0.46	1.7	Mostly star-forming galaxies
$30\% \leq P(\text{AGN}) < 50\%$	12	0.77 ± 0.14	1.56 ± 0.77	3.1	2.1 ± 1.2	2.6	0.15	0.6	Many absorbed AGNs
(ii) Absorbed AGN Selection (based on $T \equiv L_{2-10\text{keV}}/L_{[\text{O III}] \lambda 5007}$, see §3.6.3)									
$\log(T) < 0.25^e$	13	0.71 ± 0.19	1.72 ± 0.68	3.9	2.7 ± 1.0	4.0	0.22	0.4	Very absorbed AGNs

(a) Number of galaxies in the X-ray stack.

(b) Count rate in units of 10^{-6} count s^{-1} .

(c) Hardness Ratio $\equiv (H-S)/(H+S)$, where H and S are the X-ray count rates in the hard (2-8 keV) and soft (0.5-2 keV) bands.

(d) Effective Photon Index.

(e) Also required $P(\text{AGN}) > 30\%$ and $\log(M_\star [M_\odot]) > 10.2$ as selection criteria.

tant population to search for Compton-thick AGNs and to take into account for a complete census of AGNs.

We have demonstrated that the MEx diagnostic diagram works well at intermediate redshift ($0.3 < z < 1$) given that the majority of the X-ray AGNs lie in the MEx-intermediate and MEx-AGN regions rather than the MEx-SF region. The X-ray stacking analyses presented in this section consolidate this result. Furthermore, there are unidentified AGNs within the X-SB class (nominally X-ray starburst although some sources with faint luminosities are more difficult to classify unambiguously) and within an X-ray undetected population. These can be identified using the MEx diagram.

3.5.3 Demographics of X-Ray Selected AGNs

So far, we have compared the X-ray and MEx classification schemes for galaxies with valid emission line measurements ($S/N > 3$ for $H\beta$ and/or $[O\ III] \lambda 5007$). Here, we also consider X-ray detected sources that have sufficient spectral coverage for both emission lines but nonetheless lack detections. We use the X-ray AGN classification described in §3.4.3 to keep only secure X-ray AGNs (i.e., with $L_{2-10keV} > 10^{42} \text{ erg s}^{-1}$ or hardness ratio $HR > 0.1$).

Combining GOODS-N and EGS subsamples, there are 101 X-ray detected AGNs with $H\beta$ and $[O\ III] \lambda 5007$ within the spectroscopic wavelength coverage. We require $S/N > 3$ for either $H\beta$ or $[O\ III] \lambda 5007$ in order to perform the MEx classification. Based on this criterion, 33% of the X-ray selected AGNs lack optical emission line signatures. Performing the MEx classification for the remaining 68 objects with emission line measurements shows that 60 are in the MEx-AGN or MEx-intermediate region, and the remaining 8 lie in the MEx-SF region. To summarize the demographics, 59% are in the MEx-AGN or MEx-intermediate regions (48% and 11%, respectively), 8% are in the star-forming region, and 33%

lack a classification because their emission lines are either too weak or corrupted.

As a comparison, Y11 used an X-ray selected sample in EGS that is a superset of the EGS sample studied here. They combined DEEP2 spectra and MMT spectra that were obtained specifically to target X-ray sources that were not part of the DEEP2 slit masks (Coil et al., 2009). For their X-ray selected sample, they found that 51% met their AGN class based on the color-excitation diagram, 22% were in the star-forming region of their diagram and 25% lacked emission lines. Yan and collaborators refer to the latter as X-ray bright, optically-normal galaxies (XBONGs), which they study in more detail (also see Rigby et al., 2006; Trump et al., 2009).

A distinction between the present work and the results presented in Y11 is their lower signal-to-noise cutoff for emission line measurements ($S/N > 2$). We prefer to use a more conservative selection by imposing $S/N > 3$ based on the visual inspection of the spectra and the large residuals often present near the lines with $S/N < 3$. Allowing for a lower S/N is likely responsible for the apparent smaller fraction of galaxies lacking emission line measurements in Y11 although the difference between the two analyses is not statistically significant ($\sim 1\sigma$). We stress that using the intermediate region – where composite and star-forming galaxies overlap – helps to recover a larger fraction of the X-ray detected AGNs, indicating the importance of composite systems in achieving a global AGN census.

In summary, we find that X-ray selected AGNs cover the full range of optical spectroscopic classes (AGN, SF, no or weak emission lines). Our results are similar to previous work. Also, we have shown that the MEx and X-ray AGN selection methods remain complementary. Some AGNs lack X-ray detection (or are X-ray faint) and we found evidence for absorption among that population. Given

the importance of X-ray absorbed AGNs, and the possibility to start identifying this missing population, we will now focus on this topic.

3.6 Compton-Thick AGN Candidates

While soft (0.5–2 keV) X-ray emission may be produced by star-formation activity, a large amount of hard (e.g., 2–10 keV) radiation is considered to be an obvious signature of AGN activity. However, large column densities ($N_H > 10^{24} \text{ cm}^{-2}$) can cause severe absorption even for hard X-rays, making it challenging to identify Compton-thick AGNs even with sensitive *Chandra* observations such as those used in this work.

In the event that photons with energies between 2–10 keV are absorbed by intervening material, it is possible to estimate the intrinsic luminosity of an AGN by looking at emission originating from larger scales than the source of absorption (e.g., Mulchaey et al., 1994; Bassani et al., 1999). Because [O III] $\lambda 5007$ emission arises in the narrow-line region, which extends several hundred parsecs beyond the active nucleus, it is not subject to the same small-scale nuclear absorption as hard (2-10 keV) radiation. This type of compact absorption is expected for geometries involving an obscuring torus as suggested in AGN unification models (Antonucci, 1993). Thus, the ratio of X-ray (2-10 keV) to intrinsic (dust corrected) [O III] luminosities can serve as a Compton-thickness parameter $T [\equiv L(2-10 \text{ keV})/L([\text{O III}] \lambda 5007)]$ (Bassani et al., 1999). This quantity has two main caveats.

The first caveat is the uncertain obscuration of [O III] $\lambda 5007$ by dust in the host galaxy (external to the narrow line regions, Maiolino & Rieke, 1995). For example, LaMassa et al. (2009) found a median correction of 1.0 mag (0.5 to 2.3 mag) at [O III] $\lambda 5007$ based on the Balmer decrement using a SDSS-selected sample of 17

Seyfert 2 galaxies that are [O III]-luminous. Given the uncertain dust obscuration corrections for [O III], we conservatively choose to use the observed luminosities in our analysis while keeping in mind that a typical correction of 1.0 mag would shift the values of the Compton-thickness parameter down by ~ 0.4 dex.

The second caveat is the possible contribution of stellar photoionization to the [O III] luminosity. Kauffmann et al. (2003) calculated the fractional contributions to emission line luminosities in galaxies hosting both star formation and AGN activity. For metal-rich galaxies with AGN, they found that only around 7% of [O III] $\lambda 5007$ luminosity is due to star formation (the remaining 93% originates from AGN-excited gas). This is in contrast with other lines such as $H\beta$ and [O III] $\lambda 3727$ for which a larger contribution can be expected to come from H II regions rather than the narrow line region photoionised by the AGN (up to 45%–70%).

However, the stellar contribution to $L_{[\text{O III}]}$ can be much more significant in low-metallicity galaxies since oxygen becomes one of the main coolants and changes in line blanketing produce a harder ionization field (Kewley et al., 2006). To alleviate this source of contamination to the [O III] luminosity, we restrict the Compton-thickness analysis to high stellar mass (and presumably high-metallicity) galaxies, with $M_* > 10^{10.2} M_\odot$.

3.6.1 X-Ray Absorption Versus Observed AGN Power

In order to compare the X-ray absorption to the observed AGN power, we plot the Compton-thickness parameter T as a function of the observed (i.e., not corrected for absorption) hard X-ray luminosity (Figure 3.9).

Heckman et al. (2005) found that the average values of $\log(T)$ are 1.59 ± 0.48 dex and 0.57 ± 1.06 dex for Type 1 and Type 2 AGNs, respectively. Type 1s are less absorbed and show a tighter correlation while Type 2s include a much broader

range of X-ray absorption (going down to smaller values of T). We reproduce this result in Figure 3.9(a) where we combine samples of Seyferts from Heckman et al. (2005) and Bassani et al. (1999). We also see a clear trend between the location of nearby Seyfert 2's on Figure 3.9(a) and their inferred column density N_H from Bassani et al. (1999). As expected, the Compton-thick galaxies, with $N_H > 10^{24} \text{ cm}^{-2}$, tend to lie at low values of T [$\log(T) \lesssim 0.25$ for observed X/[O III] ratios, and $\log(T) < -0.3$ after correcting $L_{[\text{O III}]}$ for dust obscuration].

Turning our attention to the sample of $0.3 < z < 1$ galaxies, we find a similar trend in X-ray absorption versus hard X-ray luminosity as found for the nearby galaxies. There is an apparent transition at $L_X \approx 10^{42} \text{ erg s}^{-1}$ (vertical dotted line). X-ray AGNs above that luminosity threshold span a restricted range in their X-to-[O III] luminosity ratio ($1 < \log(T) < 3$) compared to fainter hard X-ray sources. Galaxies that likely host an AGN based on the MEx diagram lie along the lower envelope of the distribution, consistent with their large [O III]/H β ratios being driven by luminous [O III] emission. Galaxies that are likely star forming according to the MEx diagram have lower X-ray luminosities on average, and occupy the mid-range of the Compton-thickness parameter values.

While some of the X-ray starbursts (open star symbols) were also classed as SF from the MEx diagram, there are a few objects with a conflicting spectral class. These X-ray-SB but MEx-AGN galaxies (open stars around red circles) are clustered around $\log(T) = 0$, the nominal value for Compton-thick AGNs. Given the predicted offset due to using uncorrected [O III] $\lambda 5007$ luminosities, and the location of known nearby Compton-thick AGNs on Fig. 3.9(a), we will adopt $\log(T) < 0.25$ as a criterion for identifying Compton-thick AGN candidates in the next sections. In cases with low values of $\log(T)$ the [O III] $\lambda 5007$ line luminosity may be a better indicator of the bolometric AGN luminosity. We investigate this

next.

3.6.2 X-Ray Absorption Versus Intrinsic AGN Power

In the previous section, we considered candidate absorbed AGNs with a detection in the X-rays, at least in the full band. In this section, we will expand by including cases with upper limits in X-rays. Limits were derived for observations in GOODS-N as described in §3.4.3.

We again utilize the Compton-thickness parameter in Figure 3.10. Here, we use $L_{[\text{O III}]}$ on the horizontal axis to probe the intrinsic AGN power. Nearby [O III]-selected Seyfert 1's from Heckman et al. (2005) occupy the bright (elevated $L_{[\text{O III}]}$) and unabsorbed ($\log(T) > 1$) region of Figure 3.10(a). Seyfert 2's span a broad range of X-ray absorption and intrinsic AGN power.

In our intermediate-redshift sample (panel b), we note that star-forming galaxies seem to occupy a region contiguous with the Compton-thick candidates, which have $\log(L_{2-10\text{keV}})/\log(L_{[\text{O III}]}) < 0.25$. To discard these systems and keep absorbed AGN candidates, we select galaxies below the $L_X/L_{[\text{O III}]}$ threshold (red line) that also have a significant probability of hosting an AGN according to the MEx diagram. We adopt $P(\text{AGN}) > 30\%$ and stack the *Chandra* observations to search for hidden AGN signal in §3.6.3.

Figure 3.10 shows that the Compton-thick AGN candidates, with $\log(T) < 0.25$, span a similar range in [O III] $\lambda 5007$ luminosity as the unabsorbed AGNs, with $\log(T) > 1$. At high [O III] $\lambda 5007$ luminosities (e.g., $L_{[\text{O III}] \lambda 5007} > 10^{41} \text{erg s}^{-1}$) the distribution of Compton-thickness values appears to be bimodal, with the AGNs being either largely unabsorbed ($\log(T) > 1$) or heavily absorbed ($\log(T) < 0.25$). We note that this possible bimodality is seen in both the nearby and the intermediate-redshift galaxy samples. Our sample is mostly complete at the bright

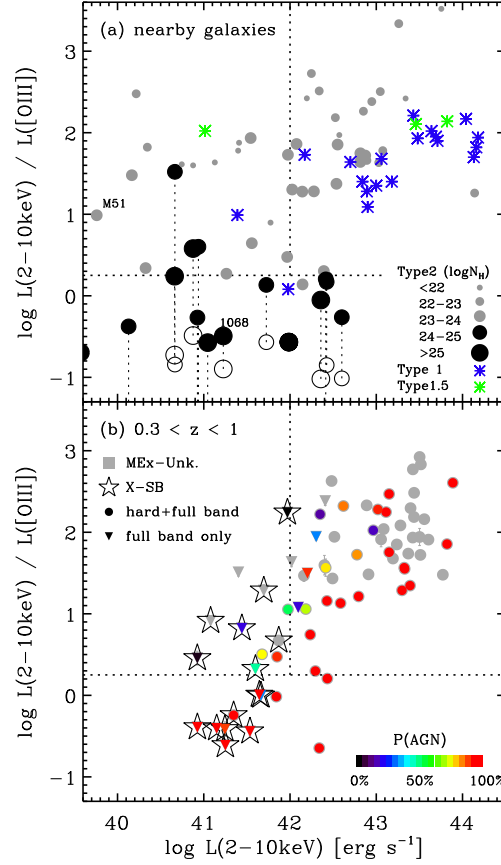


Figure 3.9 Compton-thickness parameter $T \equiv L_{2-10\text{keV}}/L_{[\text{O III}]}$ as a function of hard X-ray luminosity ($L_{2-10\text{keV}}$) for (a) nearby galaxies and (b) intermediate-redshift galaxies. In panel (a), the [O III]-selected type 1 AGN sample from Heckman et al. (2005) is shown with blue asterisks. Type 1.5 and type 2 AGNs (green asterisks and filled circles, respectively) are taken from Bassani et al. (1999). The symbols are keyed to the column density N_H in the case of type 2 AGNs (see legend). Dust-corrected [O III] values are shown with open circles for galaxies with $N_H > 10^{24} \text{ cm}^{-2}$. The intermediate-redshift sample (b) is selected to have $\log(M_\star[M_\odot]) > 10.2$, and is color-coded according to the probability to host an AGN from the MEx diagram (see color bar).

Figure 3.9 *continued*. The very likely AGNs (orange and red) tend to follow the bottom envelope of the points, and reveal some Compton-thick AGN candidates in galaxies that were otherwise classified as X-ray starbursts (star symbols; see §3.4.3). Most X-ray AGNs (points lacking star symbols) are characterized by $\log(L_X/L_{[\text{O III}]}) > 1$. Galaxies that were not identified on the MEx diagram (grey points) fail the emission-line quality flag for $\text{H}\beta$.

$[\text{O III}]$ end¹¹ so we do not believe that this trend can be attributed to selection effects. However, the number statistics are too small to investigate it further.

Unsurprisingly given the fairly small volume probed, we mostly detect AGNs with Seyfert-like luminosities and below [$\log(L_{[\text{O III}]}) < 42.5 \text{ erg s}^{-1}$]. However, we note two possible AGNs with intrinsic luminosity in the quasar regime [with $\log(L_{[\text{O III}]}) > 42.5 \text{ erg s}^{-1}$], both of which appear to suffer from large X-ray absorption. These systems may be important testbeds for evolutionary scenarios where quasars are born in a deeply enshrouded environment (presumably following a major galaxy merger) before a blowout phase where the surrounding material is ejected revealing the optically and X-ray bright central engine (Sanders & Mirabel, 1996; Di Matteo et al., 2005; Hopkins et al., 2005). We leave this analysis for future work.

In this section we have investigated the presence of X-ray absorbed AGNs by using both X-ray detected and X-ray undetected $[\text{O III}]$ -selected objects. We find that the range of intrinsic luminosities probed by $L_{[\text{O III}]}$ are comparable for Compton-thick candidates and X-ray unabsorbed systems. The presence of X-ray absorption is inferred from the X-to- $[\text{O III}]$ luminosity ratio (T) and we utilize X-ray stacking analyses in the following section to further justify the presence of

¹¹We detect galaxies with $L_{[\text{O III}] \lambda 5007} > 10^{41} \text{ erg s}^{-1}$ out to $z = 0.95$

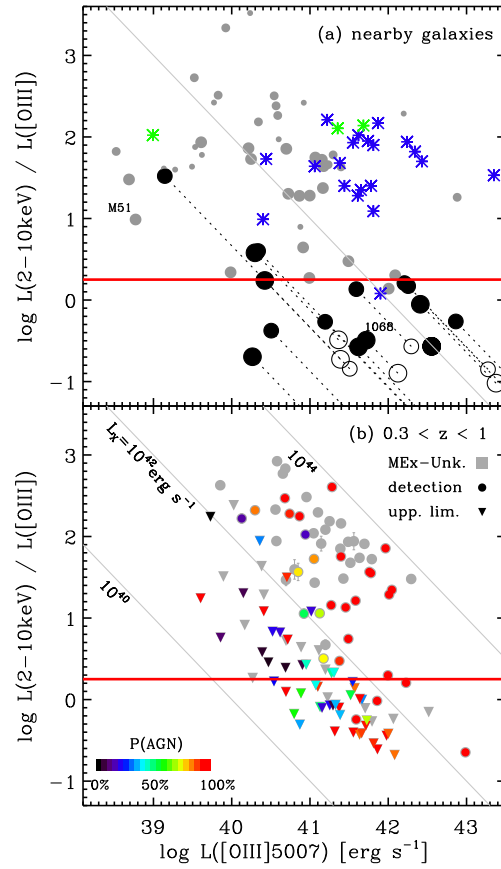


Figure 3.10 Compton-thickness parameter $T \equiv L_{2-10\text{keV}}/L_{[\text{O III}]\lambda 5007}$ as a function of $[\text{O III}]\lambda 5007$ luminosity. Both panels are shown on the same scale. Nearby galaxies are plotted in panel (a) and the symbols are as described in Fig. 3.9. The intermediate-redshift sample is shown in panel (b). The diagonal lines correspond to fixed hard X-ray ($2 - 10$ keV) luminosities of 10^{40} , 10^{42} , 10^{44} erg s^{-1} as labeled. We note that $L_{2-10\text{keV}} = 10^{42}$ erg s^{-1} is the nominal division that we adopt to separate X-ray AGNs from the X-ray starbursts although there are some X-AGNs below that luminosity threshold (recognized by their hardness ratio $HR > -0.1$). In addition to the X-ray classification, the MEX AGN probabilities are indicated with the color coding. $P(\text{AGN})$ includes all AGN classes, such that $P(\text{AGN})+P(\text{SF})=100\%$.

Figure 3.10 *continued*. Galaxies that were not identified on the MEx diagram (grey points) fail the emission-line quality flag for $H\beta$. This figure shows that star-forming/starburst galaxies occupy a contiguous region with the absorbed AGN candidates, stressing the importance of the MEx diagram in selecting likely AGNs. Based on the observed position of the known Compton-thick galaxies in panel (a), we adopt $\log(L_X/L_{[\text{O III}]})=0.25$ as a criterion for Compton-thick candidates (horizontal line).

absorption in these systems.

3.6.3 X-ray Stacking of Highly-Absorbed AGNs

Here we search for X-ray signatures in the X-ray undetected absorbed AGNs with low X-ray/[O III] ratios identified in the previous section (§3.6.2). There are 33 galaxies that are part of our candidate Compton-thick AGN selection¹² (see Fig. 3.10b). Sixteen are X-ray detected and are examined on a case-by-case basis below. Of the 17 X-ray undetected objects, 13 lie sufficiently close to the *Chandra* aim point without lying too close to X-ray bright sources to allow for X-ray stacking analyses. We employ the same X-ray stacking method described in §3.5.2. However, while in §3.5.2 we were concerned with stacking the X-ray data for galaxies selected solely from the MEx classification scheme, galaxies in this section are selected as potential Compton-thick AGNs by requiring $\log(T) < 0.25$.

Of the 16 X-ray detected sources, six are bright at X-ray energies ($F_{0.5-8keV} > 3 \times 10^{-16} \text{ erg s}^{-1} \text{ cm}^{-2}$) and ten are faint ($F_{0.5-8keV} < 3 \times 10^{-16} \text{ erg s}^{-1} \text{ cm}^{-2}$). The galaxies with bright X-ray fluxes tend to lie at lower redshift and have steep spectral slopes ($\Gamma \approx 1.3-2.0$). Two of the six X-ray bright sources have a clear [Ne V] $\lambda 3425$ detection (Fig. 3.8), an unambiguous tracer of AGN, and reside in

¹² $\log(L_{2-10keV})/\log(L_{[\text{O III}]}) < 0.25$, $P(\text{AGN}) > 30\%$ and $\log(M_\star [M_\odot]) > 10.2$.

the Seyfert 2 region of the BPT diagram. However, only one of them is clearly identified as an X-ray AGN ($L_X > 10^{42}$ erg s $^{-1}$; J123608.13+621036.2 in Fig. 3.8). This object is strongly absorbed ($\Gamma \sim 0.2$) and is a potential Compton-thick AGN. The remaining five X-ray bright sources fail both the luminosity and hardness criteria to be clearly identified as X-ray AGNs.

As for the X-ray faint galaxies, one is detected in the hard band and has a flat X-ray spectral slope ($\Gamma \approx 0.7$), indicating that it hosts a heavily absorbed AGN. The other nine objects are too faint to provide significant constraints on their X-ray spectral slopes. However, from stacking the *Chandra* data of these nine X-ray faint galaxies we find a comparatively steep X-ray spectral slope ($\Gamma \approx 1.4$), consistent with that found for the X-ray bright galaxies.

We stacked the *Chandra* data for the 13 X-ray undetected Compton-thick AGN candidates, which we treat separately from the individual detections. While the individually detected galaxies show steep X-ray indices, for the stacked objects we find a very flat photon index of $\Gamma \approx 0.4$ (see Table 2). The flatter slope found here strongly suggests the presence of X-ray absorbed AGN activity in at least a fraction of the objects that were stacked. The combined low X-ray photon index and small values of the thickness parameter make these systems robust Compton-thick AGN candidates.

Except for two objects, the results from the case-by-case analyses of the spectral slope are less obvious. The low X-ray-to-[O III] luminosity ratio and their position on the MEx diagram suggests that these X-ray detected objects host X-ray absorbed AGN activity, which may appear to be in conflict with the steep X-ray spectral slopes found for the majority of these systems. However, the steep X-ray spectral slopes do not preclude the possibility that all of these objects are heavily absorbed or Compton-thick AGN because the soft X-ray emis-

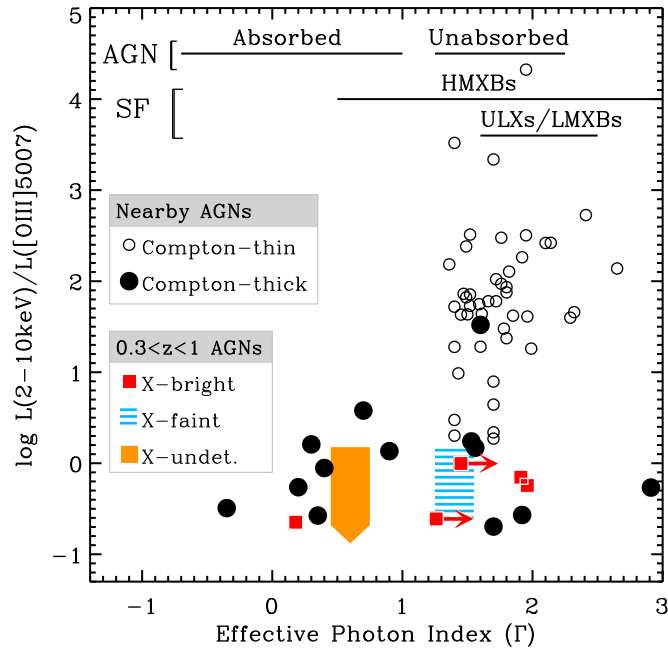


Figure 3.11 Compton-thickness parameter $T \equiv L_{2-10\text{keV}}/L_{[\text{O III}]}$ as a function of the effective photon index (Γ) calculated as described in Bassani et al. (1999) and Alexander et al. (2003) for nearby and intermediate-redshift galaxies, respectively. The expected ranges of Γ are shown for various sources of X-ray emission at the top of the figure (taken from Alexander et al., 2005, and references therein). While Compton-thin galaxies have $\Gamma > 1$ as expected (open circles), Compton-thick AGNs can have either a flat or a steep index (filled circles; see text for details). We compare the locus of these nearby AGNs (open and filled circles) with the $0.3 < z < 1$ systems that we identified as Compton-thick AGN candidates based on the following criteria: $\log(T) < 0.25$, $P(\text{AGN}) > 30\%$ and $\log(M_*[M_\odot]) > 10.2$. The intermediate-redshift galaxies with bright X-ray fluxes (red squares) span a range of photon indices. One galaxy has an obviously flat slope ($\Gamma \sim 0.2$) and the remaining four have steeper slopes ($\Gamma > 1$) but are consistent with the range of values spanned by known, nearby Compton-thick AGNs (solid circles, from Bassani et al., 1999).

Figure 3.11 *continued*. We furthermore show the results from X-ray stacking of candidate Compton-thick AGNs that are either X-ray weak (light blue hatched region) or X-ray undetected (orange shaded region). The height of the shaded regions illustrates the range of values for the individual galaxies used in the stack (upper limits in the case of the non-detections). The sample of X-ray non-detections clearly includes absorbed AGNs.

sion could be dominated by either scattered nuclear emission or star formation (e.g., Matt et al., 2000). Indeed, known Compton-thick AGNs span a range of spectral slopes from very flat to very steep (Figure 3.11), encompassing the range that we observe in our intermediate-redshift sample. The nearby galaxies in Figure 3.11 are taken from Bassani et al. (1999) and divided between Compton-thin and Compton-thick at $N_H = 10^{24} \text{ cm}^{-2}$ (also see Figures 3.9 and 3.10). Overall, it is therefore possible that all of our Compton-thick AGN candidates are genuinely absorbed by Compton-thick material (colored symbols on Fig. 3.11); however, some of them cannot be unambiguously identified as such based on the X-ray slope alone. Higher energy observations ($>10 \text{ keV}$) may help to confirm the presence of Compton-thick AGNs in galaxies with a steep X-ray slope.

3.6.4 Linking AGN Absorption and Optical Classification

Next, we show the X-ray absorbed AGN candidates on the MEx diagram in Figure 3.12(a). Interestingly, their location differs from that of the X-ray unabsorbed systems [Figure 3.12(b)]. The latter are distributed evenly in the main MEx-AGN region with a possible bias toward high stellar mass. In contrast, the absorbed AGN candidates cluster in the MEx-intermediate region with a few exceptions along the low-mass and outermost contour of the AGN plume. As a reminder, the MEx-intermediate region is populated by BPT-composites and BPT-SF galaxies.

This suggests that the X-ray absorbed AGN candidates are more likely composite systems than Seyferts or LINERs.

While we consider all objects (X-ray detections and non-detections) together, we highlight the subset of 13 galaxies that were not individually detected but yielded a very flat X-ray spectral slope of $\Gamma \sim 0.4$ (see green squares on Fig. 3.12). The flat slope makes these systems robust Compton-thick AGN candidates. They occupy the MEx-intermediate region and the lower part of the AGN region where different AGN sub-classes overlap. The average probabilistic classification is $P(\text{AGN}) = 58\%$ with the AGNs three times more likely to belong to the composite sub-class than the Seyfert 2 and LINER sub-classes. This result strengthens our conclusion that composite galaxies, hosting both star formation and AGN, are a very important population to search for highly-absorbed AGNs. We further discuss these findings and their implications in §3.7.3.

3.7 Discussion

Several previous studies have presented AGN diagnostic diagrams as alternatives to the BPT diagram. Because the $[\text{N II}] \lambda 6584 / \text{H}\alpha$ line ratio is only available in optical spectra out to redshift ~ 0.4 , it needs to be replaced in order for the diagnostic to be applicable at higher redshift while avoiding the need to obtain near-infrared spectra. In this section, we first compare the MEx diagram with a few other AGN diagnostics from the literature (§3.7.1). We then discuss how the MEx diagram contributes toward a more complete census of AGNs (§3.7.2). We follow with a discussion of the importance of composite systems in this regard (§3.7.3) and we compare the fraction of absorbed AGNs from our work to results from the literature (§3.7.4). Finally, we mention possible evolutionary effects that are relevant to all nebular line diagnostic diagrams (§3.7.5).

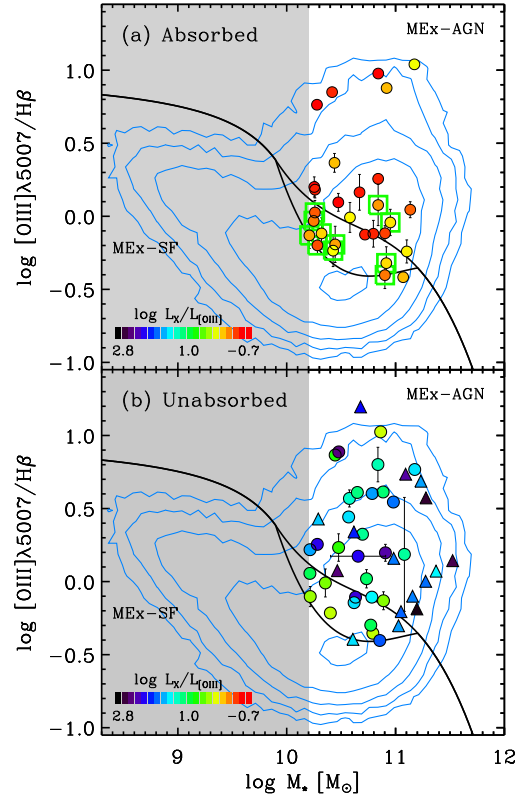


Figure 3.12 Systems with $P(\text{AGN}) > 30\%$ and $\log(M_* [M_\odot]) > 10.2$ shown on the MEx diagram. The points are color-coded according to the Compton-thickness parameter T shown in Figure 3.10. Red corresponds to the most absorbed systems, with $\log(T) \approx -0.7$ and the color changes gradually toward violet for the largest values of $\log(T)$ (≈ 2.8). Galaxies where both H β and [O III] $\lambda 5007$ lines are robust detections ($S/N > 3$; filled circles) are shown in panels (a) and (b) depending if they are absorbed [$\log(T) \leq 0.25$] or largely unabsorbed [$\log(T) > 0.25$]. We also show galaxies with detected [O III] $\lambda 5007$ lines and H β upper limits (triangles in panel b). In these cases, the [O III] $\lambda 5007$ /H β ratio is a lower limit. The green squares in panel (a) mark the X-ray undetected galaxies that yielded a flat spectral slope when stacked. Those tend to lie in the MEx-intermediate region indicating that some galaxies with a buried AGN are also undergoing an episode of active star formation.

3.7.1 Comparison with existing diagnostics

Lamareille et al. (2004) developed an AGN diagnostic diagram that, like the MEx diagram, is designed to be applicable to optical spectra of galaxies out to $z \sim 1$. In this case, the BPT diagram was modified by replacing the $[\text{N II}] \lambda 6584/\text{H}\alpha$ ratio with $[\text{O III}] \lambda 3727/\text{H}\beta$. Because of the greater wavelength separation between $[\text{O III}] \lambda 3727$ and $\text{H}\beta$, their flux ratio is very sensitive to dust obscuration. Thus, the authors opted for an equivalent width ratio to mitigate against that effect. The dividing lines on that diagram were recently revised (Lamareille, 2010).

The so-called blue diagram (because it includes only blue lines compared to $\text{H}\alpha$) has the advantage of splitting the LINERs from the Seyfert 2s. However, it suffers from confusion between other classes of galaxies (SF, Sy2, and composites, see Lamareille et al 2004; Lamareille 2010; and Appendix C). The MEx diagram has a notably cleaner separation between SF and Sy2 galaxies, is more sensitive to BPT-composite galaxies, and includes virtually all AGNs selected in the blue diagram.

In the case of the intermediate-redshift sample used here, a lot of galaxies with DEEP2 spectra have an insufficient wavelength coverage and do not contain all the lines required for the blue diagram. As a consequence, the number of galaxies for which we can use this diagram is much smaller than for the MEx diagram. The modest wavelength range required for the spectra makes the latter more versatile than the blue diagram, which requires $\Delta\lambda_{rest} > 2900 \text{ \AA}$.

For the galaxies that have all the required observations, we find that the X-ray AGN selection has a much better agreement with the MEx diagram (Appendix C). This seems to be partially due to the mixing between BPT-SF and BPT-Sy2 galaxies in one of the regions of the blue diagram, and the mixing between BPT-SF and BPT-composites in another region.

The approach most similar to the MEx diagram was developed by Weiner et al. (2007); in fact, those authors used datasets that overlap with the present study. They combined TKRS and DEEP2 spectra in order to benefit from both the larger wavelength coverage of TKRS and the larger number of galaxies in the DEEP2 survey. They investigated the trends between $[\text{N II}]/\text{H}\alpha$ and $[\text{O III}]/\text{H}\beta$ as a function of absolute H -band magnitude (M_H), and found that $[\text{N II}]/\text{H}\alpha$ was sufficiently correlated with M_H for the latter to be a helpful parameter when only the $[\text{O III}]$ and $\text{H}\beta$ lines are available. Weiner and collaborators did not go as far as developing a diagnostic line, but showed a division between the red and blue galaxies on those plots in the sense that the red galaxies are predominantly occupying the region where AGNs are expected to lie. This suggests that optical color may be another useful discriminant between star-forming and AGN galaxies when combined with $[\text{O III}]/\text{H}\beta$. Indeed, this approach was used recently by Yan et al. (2011).

Yan and collaborators designed a similar diagram as presented here, except for using rest-frame $U - B$ color in lieu of stellar mass. Their diagnostic produces comparable results to the MEx diagram when classifying the bulk of SDSS galaxies into AGN or star-forming. In detail, they chose to avoid targeting the composite galaxies that lie beyond the distribution of the more obvious AGNs (i.e., above the Kewley line in the BPT diagram). This implies that the galaxies on the star-forming side suffer from more frequent contamination by AGNs. Thus, we identified the region where the composite galaxies have an important overlap with star-forming galaxies (region between Eq. 3 and Eq. 4). The motivation is twofold. First, it provides a means to obtain a cleaner sample of star-forming galaxies. Secondly, we have shown that composite galaxies are an important population to look for highly-absorbed AGNs that are co-existing with star formation

in their host galaxies. More detailed comparisons between the MEx diagram and the CEx diagram developed in Y11 are presented in §3.3.3 and Appendix B.

Another alternative diagram, called the DEW diagram, was developed by Stasińska et al. (2006). It includes a separation based on the 4000Å-break and equivalent width of [Ne III] λ 3869 or [O III] λ 3727 (whichever is greater). In this case, the AGN hosts tend to have a larger $D_n(4000)$ with respect to normal star-forming galaxies. Unfortunately, the 4000Å-break is located near, or directly over, the detector gap for most of the DEEP2 spectra at the redshift of interest (peaking near $z = 0.7$), so we are unable to apply this diagram for the bulk of our sample. The authors presented evidence that the DEW diagram has a better correspondence with the BPT diagram compared to the blue diagram (at least prior to its revision in 2010).

One notable difference between the MEx diagram and the original BPT diagram (or blue diagram) is that the former is not scale-free. The inclusion of stellar mass as a parameter imposes an absolute physical scale to the problem (whereas emission line ratios do not). This aspect raises questions about possible redshift evolution effects that could systematically affect the locus of the galaxies on diagnostic diagrams. We discuss such possibilities below (§3.7.5).

3.7.2 A More Complete Census of AGNs

Understanding active galactic nuclei and their role in galaxy evolution requires a robust AGN classification scheme. A complete sample should include both intrinsically weak and intrinsically bright but absorbed AGNs. Weak AGNs are interesting to study and learn more about the low accretion phase and whether the AGN unified model needs to be revised (Ho, 2008; Trump et al., 2009). Absorbed AGNs are sought to explain the unresolved portion of the cosmic X-ray background, and to quantify their contribution to mid- and far-infrared emission

seen in infrared-luminous galaxies. They are also of interest to test evolutionary scenarios where galaxy major mergers are invoked as a mechanism to form quasars, through a deeply-embedded and absorbed phase (Sanders et al., 1988; Fabian, 1999; Hopkins et al., 2005).

The MEx diagram introduced in this paper is a tool to uncover AGNs that are weak in X-ray observations, presumably due to either intrinsic weakness or X-ray absorption. Both of these AGN phases – weak or absorbed – may be found in galaxies that are simultaneously undergoing episodes of star formation, potentially masking AGN signatures. One important feature that allows us to find these systems is our probabilistic approach.

As shown in §3.5.2, using $P(\text{AGN}) > 30\%$ as a threshold provides a more complete census of AGN than using $P(\text{AGN}) > 50\%$. We found that both high-probability AGNs ($P(\text{AGN}) > 50\%$) and medium-probability AGNs ($30\% < P(\text{AGN}) < 50\%$) that are not individually detected in the *Chandra* data show signs of X-ray absorption when we stacked their X-ray emission (from the resulting flat X-ray spectral slope; see Table 3.2). The galaxies with $30 < P(\text{AGN}) < 50\%$ are likely composite systems (see §3.5.2), and occupy a region of the diagram that overlaps with other classes, making them more challenging to identify without the probability approach. Thus, identifying those AGNs is a step toward a more complete census of active galactic nuclei.

Our finding that the X-ray undetected galaxies identified using the MEx diagram are likely absorbed AGNs prompted us to make a more systematic search for X-ray absorbed systems. We probed X-ray absorption using the Compton-thickness parameter T as described in §3.6.3 (see references therein). We again found a significant detection in *Chandra's* hard band and a still flatter spectral slope ($\Gamma \approx 0.4$) for galaxies that were not detected individually. This result

supports the idea that the X-ray-to-[O III] luminosity ratio does select absorbed AGNs as expected. We also note some galaxies with a steep spectral slope ($\Gamma > 1$) and a low value of T . These systems are also consistent with X-ray absorption given that they are within the range of values of Γ and T spanned by known Compton-thick AGNs that are nearby and easier to study in more detail (see Fig. 3.11). In these cases, the soft X-ray emission may arise from a scattered AGN spectrum or from contamination by a superimposed starburst component.

To summarize the absorbed AGN samples, we first found signs of X-ray absorption in MEx-AGNs that were not detected at X-ray wavelengths. These samples were selected with no *a priori* knowledge of X-ray absorption and the results are tabulated in §3.5.2 (Table 3.2). We then specifically targeted X-ray absorbed AGN candidates by imposing $\log(L_{2-10\text{keV}}/L_{[\text{O III}] \lambda 5007}) < 0.25$ (§3.6.3). This yielded a sample of 33 absorbed AGN candidates: six have bright X-ray fluxes (and mostly a steep spectral slope, see red squares on Fig. 3.11); ten have faint X-ray fluxes and the stacked signal is characterized by a slightly steep slope (blue shaded region on Fig. 3.11), and of the remaining 17 that lack detections, 13 could be stacked and yielded a very flat spectral slope. So we have a sample of 33 candidates with heavy absorption of their X-ray emission, including a subsample of 15 more robust candidates (the 13 non-detections that were stacked plus the two individual detections that have a flat X-ray spectral slope).

3.7.3 Notes on Composite Galaxies

The separation between BPT-composites and BPT-AGNs is likely not as sharp as illustrated on the BPT diagram (Figure 3.1(a)) and may instead be a continuum of fractional AGN contribution to the spectral emission lines used in the diagnostic. This was suggested by, e.g., Kewley et al. (2006), who introduced a parameter to measure the distance from the star-forming sequence on the BPT diagram (also

see Yuan et al., 2010). The AGN branches defined in Kewley et al. (2006) start from the metal-rich end of the star-forming sequence and follow mixing sequences toward larger values of $[\text{S II}] \lambda\lambda 6717, 6731/\text{H}\alpha$ or $[\text{O I}] \lambda 6300/\text{H}\alpha$ depending on the diagram used. The idea is that there is a continuous transition from star-forming toward AGN with an increasing AGN contribution.

Like composites, which host both star formation and AGN, galaxies classified as BPT-AGNs (above the Kewley line) may also have a significant star formation rate (SFR), up to $\sim 10 M_{\odot}\text{yr}^{-1}$ (Salim et al., 2007). On average their SFRs will be less than that in the population of composite galaxies (Salim et al., 2007). One consequence is that the emission lines of the BPT-composites are characterized by a smaller fractional contribution from AGN relative to star formation, which makes the line ratios more ambiguous. These results also imply a continuity (or mixing sequence) between star-formation and AGN-dominated systems. The so-called composites may be in the midst of a transition between the two types.

We might expect that some X-ray absorbed AGNs would reside in BPT composite galaxies because large amounts of gas can provide fuel for star formation and act as absorbing material that attenuate X-ray signatures. In this case the X-ray absorption could come from the host galaxy's ISM in addition to torus-scale absorption. In addition, if the gas is also mixed with dust, or if the galaxy is viewed through a dust lane, AGN emission-line signatures such as $[\text{O III}] \lambda 5007$ can be weakened and further diluted with emission from peripheral star formation (Maiolino & Rieke, 1995; Malkan et al., 1998; Goulding & Alexander, 2009), causing the global signal to exhibit composite signatures.

The degree to which the host galaxy ISM absorbs X-ray and $[\text{O III}]$ emission may vary depending on the detailed geometry of the emitting and absorbing regions. The X-ray emission arises on the very small scales of the accretion disk,

while [O III] is emitted on the larger scale of the narrow line regions (reaching several hundred parsecs to kiloparsecs from the nucleus). If the absorption from the host galaxy ISM were approximated as a uniform screen with an extent that covers both the X-ray and narrow line emitting regions and with a Milky Way-like dust-to-gas ratio, then we would expect optical AGN signatures (such as [O III] $\lambda 5007$) to be obscured more than the X-ray emission. An extinction of $A_V = 10$ mag would fully obscure [O III] emission from the narrow line regions, but would correspond to a gas column density of $N_H = 1.6 \times 10^{22} \text{ cm}^{-2}$, causing only modest absorption of the X-ray emission. This would suppress the $L_{[\text{O III}]} / L_{2-10\text{keV}}$ ratio, leading to the opposite effect of the preferential X-ray absorption that we observe in some systems.

However, if the foreground ISM is clumpy, then it is possible for a dense cloud with large N_H to obscure the compact X-ray emitting region, while the average absorption to the larger [O III]-emitting narrow line regions could be much less. There will be lines of sight to the extended narrow line regions with more modest obscuration which will dominate the global emission line signal (relative to more heavily obscured lines of sight). As a result, we may in this case expect a preferential absorption of the X-ray emission relative to the optical ([O III] $\lambda 5007$) emission.

The preferential extinction of the small-scale X-ray emission when compared to the larger scale [O III] emission could also be caused by a physical connection between the gas at galaxy scales and the gas on the scales of the AGN torus. For example, in the simulations of Hopkins & Quataert (2010), an overall larger gas fraction on kpc scale can result in more gas funneling to the inner sub-pc region of the systems. These simulations predict that the transport of gas toward the central region depends most strongly on the disk-to-bulge ratio and on the gas

fractions on 100 – 300 pc scales. We note that these authors did not specifically model a torus. However, the presence of instabilities on small scales increases the gas flow to the inner regions and suggests that the torus, often thought to be an extension of the accretion disk, could contain more obscuring material (or have a larger filling factor). If this scenario were true, it would imply that a higher gas fraction on galaxy scales could lead to both a larger SFR and a more gas-rich accretion disk (and potentially torus), thus creating preferential absorption of small scale emission (hard X-rays) relative to larger scale emission ([O III] λ 5007).

Based on these scenarios, and on our observations of a hard X-ray signal by stacking only 12 likely composite galaxies (with $30 < P(\text{AGN}) < 50\%$, §3.6.3) that were not detected with very sensitive *Chandra* observations, we propose that not all BPT-composite galaxies have intrinsically weak *transition* AGNs. Instead, a fraction of them have powerful but absorbed AGNs whose light is diluted with that of their host galaxies (regardless of whether the host galaxy ISM provides additional AGN absorption or not).

In addition, the composite galaxy populations may differ with redshift. In general, star-forming galaxies had a higher specific star formation rate ($SSFR \equiv SFR/M_*$) at earlier times (Noeske et al., 2007; Elbaz et al., 2007). The larger amount of star formation at higher redshift is also linked to larger reservoirs of molecular gas (e.g., Daddi et al., 2010; Tacconi et al., 2010). As mentioned before, large amounts of gas contribute to increase the column density along the line of sight thus X-ray absorption. The more sizable gas reservoirs in isolated galaxies at higher redshift may be a way to obtain more absorbed AGNs without major mergers.

There is also evidence for a larger infrared-to-X-ray luminosity ratio with increasing redshift (Mullaney et al., 2010), further suggesting a larger SSFR in the

host galaxies of higher-redshift AGNs relative to the current epoch. The enhanced star formation may affect the line ratios in the sense that more galaxies will be classified as BPT-composites at higher redshift. While we do not study star formation rates in this work, we remind the reader that the composite galaxy population plays an important role in the search for X-ray absorbed AGNs and as such should be identifiable at high-redshift. Thus, the MEx diagram and the probabilistic classification scheme introduced in this Paper are expected to fulfill this need and to contribute to a significant improvement in identifying the population of missing Compton-thick AGNs.

3.7.4 Absorbed AGN Fractions

Next, we examine the absorbed AGN fraction in terms of the number of galaxies identified as well as fractional contribution to $L_{[\text{O III}]}$. Galaxies with $\log(L_X/L_{[\text{O III}]}) > 1$ are considered as unabsorbed while galaxies with $\log(L_X/L_{[\text{O III}]}) < 0.25$ are considered absorbed and likely Compton-thick and galaxies in between are likely absorbed but Compton-thin with $22 < \log(N_H[\text{cm}^{-2}]) < 24$ [Figure 3.9(a)].

For galaxies in EGS, we compute X-ray upper limits using sensitivity and exposure time maps¹³. We convert the count rates in the hard band to fluxes assuming the conversion factor used by Laird et al. (2009). The X-ray detection limit is highly variable across the EGS field. For the [O III]-selected samples that we consider here, it varies from 6.6×10^{-16} to 1.2×10^{-14} $\text{erg s}^{-1} \text{cm}^{-2}$. The average value is 2.5×10^{-15} erg s^{-1} , similar to the flux limit at which the survey is complete over 50% of the area (2×10^{-15} $\text{erg s}^{-1} \text{cm}^{-2}$; Laird et al., 2009). We discard the X-ray upper limits of 10% (7/70) of [O III]-selected galaxies with $L_{[\text{O III}] \lambda 5007} > 10^{41}$ erg s^{-1} because they lie in very shallow regions of the X-ray data (with upper limits that are $> 5 \times 10^{-15}$ $\text{erg s}^{-1} \text{cm}^{-2}$).

¹³Data products from <http://astro.ic.ac.uk/content/chandra-data-products>

However, we note that a typical upper limit value of $2.5 \times 10^{-15} \text{ erg s}^{-1} \text{ cm}^{-2}$ does not constrain the absorption very tightly, especially at $\log(L_{[\text{O III}]}) < 41.5$ where a lot of upper limits correspond to $\log(T) > 1$. Thus, we derive lower and upper limits to the absorbed AGN fraction by assuming that these galaxies are respectively all unabsorbed (i.e., they actually lie at $\log(T) > 1$) or all absorbed (i.e., they lie at $\log(T) < 1$). We furthermore weigh the galaxies with the probability that they host an AGN according to the MEx diagnostic. The fractional number and [O III] luminosity contribution of absorbed AGNs are respectively defined as follows:

$$f_{\text{absorbed}} = \frac{\sum_{i=1}^{N_{\text{absorbed}}} P(\text{AGN})_i}{\sum_{j=1}^{N_{\text{total}}} P(\text{AGN})_j} \quad (3.5)$$

$$f([\text{O III}]_{\text{absorbed}}) = \frac{\sum_{i=1}^{N_{\text{absorbed}}} P(\text{AGN})_i \times L([\text{O III}])_i}{\sum_{j=1}^{N_{\text{total}}} P(\text{AGN})_j \times L([\text{O III}])_j} \quad (3.6)$$

where $P(\text{AGN})$ is the fractional probability of hosting an AGN varying from 0 to 1, N_{absorbed} is the number of X-ray absorbed AGNs, and N_{total} is the total number of AGNs (absorbed and unabsorbed). At $\log(L_{[\text{O III}]}) > 41$, the absorbed (Compton-thick) fractions are poorly constrained: we find $f_{\text{absorbed}} = 25 - 81\%$ ($f_{\text{Compton-thick}} = 12 - 81\%$). Using equation 3.6, the fractional contribution of absorbed (Compton-thick) AGNs to the [O III] luminosity of all AGNs with $\log(L_{[\text{O III}]}) > 41$ is $f([\text{O III}]_{\text{absorbed}}) = 54 - 82\%$ ($31 - 82\%$).

The constraints are slightly better with a higher [O III] luminosity threshold. Restricting our analysis to the 34 galaxies at $0.5 < z < 0.8$ with $\log(L_{[\text{O III}]}) > 41.5$, we find an absorbed (Compton-thick) fraction ranging from 45% to 68% (17% to 68%) in number of galaxies, and a contribution to $L_{[\text{O III}]}$ between 70–81% (39–81%). Similarly, Y11 estimated an absorbed AGN fraction by calculating the X-ray detection probability assuming a constant intrinsic X-ray/[O III] $\lambda 5007$ ratio and measured [O III] luminosities, and by comparing the expected number of X-

ray detections to the actual number of detections at the EGS depth. Attributing the non-detections to X-ray absorption, they find an X-ray absorbed fraction of $\sim 50\text{--}60\%$ at the same [O III] luminosity threshold used here, in agreement with our estimate for EGS and GOODS-N combined ($45\text{--}68\%$).

Using only GOODS-N galaxies provides stronger constraints on X-ray absorption given the high sensitivity of the *Chandra* observations in that field, but is subject to smaller number statistics. In this case, restricting our analysis to the 29 galaxies at $0.3 < z < 0.8$ with $\log(L_{[\text{O III}]}) > 40.5$ yields an absorbed (Compton-thick) fraction of $75 \pm 18\%$ ($54\text{--}64\%$). For $\log(L_{[\text{O III}]}) > 40.5$, Y11 calculated that 70.5% of AGN fail to be detected at the EGS depth, suggesting an absorbed fraction ($70.5 \pm 4.1\%$) that agrees with our calculations for GOODS-N galaxies (75%). Our results are also consistent with Akylas & Georgantopoulos (2009), who studied 38 nearby (< 70 Mpc) Seyferts and found an absorbed fraction $55 \pm 12\%$. Considering only sources with $L_{2-10\text{keV}} > 10^{41} \text{erg s}^{-1}$, they find that $75 \pm 19\%$ of 21 galaxies are absorbed ($N_H > 10^{22} \text{cm}^{-2}$) and $15\text{--}20\%$ are Compton-thick.

At quasar-like luminosities, Vignali et al. (2010) found that 68% of SDSS Type 2 quasars at $0.3 < z < 0.8$ are Compton-thick according to [O III] versus X-ray criteria. As they discuss, an [O III]-selection may bias the numbers toward a larger absorption fraction. Our estimates do not allow us to predict whether the absorbed AGN fraction rises or declines with [O III] luminosity. Larger samples with very sensitive X-ray observations would help to address that question.

3.7.5 Possible evolutionary effects

As noted in §3.5, there is some evidence that the intermediate-redshift galaxies may be offset in the MEx diagram relative to the lower-redshift SDSS sample. Other authors have reported similar shifts in the BPT diagram, i.e., higher- z

galaxies appear displaced toward larger values of $[\text{O III}]/\text{H}\beta$ and/or $[\text{N II}]/\text{H}\alpha$. Some attributed this trend to varying HII region conditions (Liu et al., 2008; Brinchmann et al., 2008; Hainline et al., 2009) while others claim that additional AGN contribution may be the driving factor (Groves et al., 2006; Wright et al., 2010).

In particular, Wright et al. (2010) presented a detailed study of one BPT-composite galaxy at $z \sim 1.6$. Using adaptive optics combined with integrated field spectroscopy, they were able to separate the AGN from the host galaxy emission and found that the central region (inner $0.''2 \times 0.''2$) occupies the AGN part of the BPT diagram, while the integrated measurements place this galaxy in the BPT-composite region and the host galaxy alone shares the locus of the normal star-forming galaxies (i.e., not shifted from the low- z sequence). This suggests that diluted AGN contribution may explain the offset in at least some cases.

What would be the consequences of such offsets on the MEx diagram? If more galaxies have diluted AGN contributions, they will be selected as MEx-AGNs because the offset would tend to move the galaxies over the dividing line. A fraction of the higher-mass galaxies are already subject to be BPT-composite ($\sim 20 - 30\%$) so in this case, moving them over the AGN line would actually increase the completeness. On the other hand, if galaxies had different physical conditions in their HII regions in the past, in the sense of having larger $[\text{O III}]/\text{H}\beta$ ratios compared to galaxies today, then some purely star-forming galaxies could be moved over the AGN dividing line. However, the differences out to $z \sim 1$ are probably small since the empirical offset is around 0.2 dex in $\log([\text{O III}]/\text{H}\beta)$.

Given that the situation is still under debate, and that selection effects are not well constrained, we do not implement an offset at this point. However, we note that the very good agreement between the X-ray and the MEx selection even out

to redshift ~ 1 supports the conclusion that the empirical division works well over the redshift range considered here. Future work would be required to test whether it holds to even higher redshift.

3.8 Summary

In this paper, we provide a new tool to gather a more complete census of actively accreting black holes in galaxies. We argue that intrinsically weak AGNs, as well as heavily absorbed AGNs, are important to understand the connection between supermassive black holes and their host galaxies. We successfully find systems that belong to these observationally-challenging AGN classes.

Using 110,205 emission-line galaxies from the SDSS, we calibrate a new excitation diagram to identify galaxy nuclear activity. By combining the observed [O III] $\lambda 5007/H\beta$ emission line ratio with stellar mass, we obtain a diagnostic applicable to galaxies out to $z \sim 1$. Here we summarize a few properties of the Mass-Excitation (MEx) diagram:

1. The simplest version splits galaxies into three classes: MEx-AGN, MEx-SF and MEx-intermediate. The latter is found in a region where BPT-composite galaxies have significant overlap with star-forming galaxies. The classification has an excellent correspondence to that from the BPT diagram based on [O III] $\lambda 5007/H\beta$ and [N II] $\lambda 6584/H\alpha$.
2. The classification scheme is refined using a novel probabilistic approach to predict the location of high-redshift galaxies on standard BPT diagrams based on their [O III] $\lambda 5007/H\beta$ ratio and stellar mass (§3.3.3). Utilizing SDSS priors, we calculate the probability of four mutually exclusive spectral classes (star-forming, composite, LINER, or Seyfert 2) as a function of position on the MEx diagram for each galaxy.

3. The MEx diagram offers a more complete AGN selection than alternatives such as the blue diagram (Lamareille, 2010). It is comparable to the Color-Excitation (CEX) diagram developed by Yan et al. (2011) but may be particularly useful for dusty, strongly reddened galaxies which may have unusual colors. Furthermore, we add a dividing line to the CEx diagram to identify composite galaxies, an important population to search for absorbed AGNs.
4. We provide publicly available IDL routines to calculate the probabilities of different galaxy spectral classes based on the MEx and CEx diagrams.

Another outcome of a nearly complete AGN selection is that the complementary selection results in a very clean star-forming galaxy sample. Indeed, with our probability scheme, one can weight galaxies as a function of $P(\text{SF})$ when computing average properties such as the stellar mass-metallicity relation or the global star formation rate and thus mitigate against AGN contamination. We anticipate that a wide variety of applications will benefit from our approach to galaxy spectral classification.

We successfully classify AGN and star forming galaxies at $0.3 < z < 1$ using our new diagnostic. The sample is drawn from the AEGIS and GOODS-N surveys. Our main findings are as follows:

- An independent X-ray classification scheme shows that the MEx diagram selects around 82% of the X-ray AGNs with detected emission lines ($S/N > 3$ for $H\beta$ and $[O\ III] \lambda 5007$). When considering all X-ray AGNs, we find that 59% are in the MEx-AGN or MEx-intermediate regions, 8% are in the star-forming region, and 33% lack a classification (they fail the $S/N > 3$ requirement for valid emission line detections).

- The MEx diagram reveals X-ray absorbed AGN candidates, which were missed or mis-identified in X-rays while having robust signatures in their optical spectra. We combine support from three lines of evidence:
 1. The subset of these galaxies with a low enough redshift to be placed on the BPT diagram lie in the BPT-composite or BPT-AGN regions (Fig. 3.7). In addition, one galaxy has a clear detection of [Ne V] $\lambda 3425$ in emission, a secure AGN tracer (§3.5.1).
 2. Stacking *Chandra* data of galaxies that were not individually detected in GOODS-N reveals a hard signal and a flat X-ray spectral slope for galaxies that have $P(\text{AGN}) > 30\%$. This suggests that at least some of the 32 galaxies that were stacked do host an actively accreting black hole (§3.5.2).
 3. By combining [O III] $\lambda 5007$ and hard X-ray luminosities, we calculate a Compton-thickness parameter ($T \equiv L_{2-10\text{keV}}/L_{[\text{O III}] \lambda 5007}$). We identify 33 highly-absorbed AGN candidates. The presence of AGN in at least some of the candidates is supported by the hard X-ray signal ($\Gamma \sim 0.4$) obtained from stacking 13 galaxies that were not detected individually (§3.6.3). We note that some X-ray galaxies have a steep spectral slope despite a low value of T . These objects are also consistent with the range of values expected from a comparison with known, nearby Compton-thick AGNs (Fig. 3.11).
- Many absorbed AGNs in the intermediate redshift sample are composite systems, with both star formation and active black hole accretion. The increase in the SF:AGN ratio – and hence a decrease in [O III] $\lambda 5007/\text{H}\beta$ – may be related to the global rise in the specific star formation rate with redshift.

However, the details of such a connection remain open questions (does the host galaxy ISM provide additional AGN absorption? is there a link between host galaxy and torus properties?). The identification of these composites poses a considerable challenge on the observational point-of-view. The MEx probabilistic approach proved to be key in this respect.

On-going and future near-infrared multi-object spectroscopy surveys will shed more light by allowing us to observe all the traditional emission lines directly. The MEx diagram will nevertheless be useful to fill in gaps where $H\alpha$ and/or $[\text{N II}] \lambda 6584$ fall in especially noisy regions of the spectra or where $[\text{N II}] \lambda 6584$ fails to be detected (as it is typically fainter than $H\alpha$). In principle, the MEx diagram could be applied out to $z \sim 4$ using near-infrared spectroscopy, thus pushing the limits beyond what will be achievable when relying on $H\alpha$ and $[\text{N II}] \lambda 6584$ detections (since the latter redshift out of the K -band at $z \sim 2.5$).

CHAPTER 4

ON THE UBIQUITY OF ACTIVE GALACTIC NUCLEI AMONG FAR-INFRARED
SELECTED GALAXIES

We characterize the incidence of active galactic nuclei (AGN) in galaxies that are luminous in the infrared regime and we test the AGN influence on their mid-to-far infrared color. Multi-wavelength AGN diagnostics (X-ray, optical, mid-infrared) are applied to a sample of $0.3 < z < 1$ galaxies selected at $70\text{-}\mu\text{m}$ from the Far-Infrared Deep Extragalactic Legacy survey (FIDEL). We find a high occurrence of AGN – at least 37% – among FIR-selected galaxies. This AGN fraction is over twice as high as that reported in the literature for galaxies in the same infrared luminosity and redshift range but is in good agreement with that of nearby ($0.05 < z < 0.1$) FIR-selected galaxies. The more elevated AGN fraction compared to other high-redshift studies is attributed to a more complete census of AGN thanks to the recently developed Mass-Excitation (MEx) diagnostic diagram. This optical diagnostic is also sensitive to X-ray weak AGN and X-ray absorbed AGN, and reveals that AGN in infrared-bright hosts tend to be much more X-ray absorbed relative to those in infrared-faint galaxies. This connection may have considerable implications on our understanding of the main mode of AGN growth in galaxies.

4.1 Introduction

It has become increasingly clear that we need to reconcile the growth of stars in galaxies with the growth of the supermassive black hole at their centers for a complete picture of galaxy evolution. These topics have been studied separately for decades but there is a growing effort to compile all the findings in one coherent

picture.

On the stellar assembly side, there is now a very clear indication for a decline in the cosmic star formation history since redshift $z > 1$ (e.g., Lilly et al., 1996; Madau et al., 1996; Hopkins, 2004). Furthermore, analyses of the infrared (IR) luminosity function demonstrate that the bulk of star formation took place in increasingly more IR-luminous galaxies at higher redshift (Le Flocc'h et al., 2005; Magnelli et al., 2009). These studies suggest that the star formation rates (SFRs) in individual galaxies have declined over the last ~ 8 billion years and demonstrate the importance of IR studies at intermediate and high redshifts. Additional trends were reported when galaxy populations are split by stellar mass. In the cosmic-averaged sense, it was found that higher mass galaxies were more actively forming stars at earlier times and that the stellar mass scale for active star formation shifts down as the universe evolves (Heavens et al., 2004; Juneau et al., 2005), a phenomenon dubbed downsizing from the original suggestion by Cowie et al. (1996).

While this may be true for the global galaxy populations, constraining the analysis to star-forming galaxies shows a correlation between SFR and stellar mass in a given redshift range (Noeske et al., 2007; Elbaz et al., 2007), sometimes called a star formation *main sequence*. Furthermore, there is now mounting evidence suggesting two star formation regimes within galaxies. Recent studies of Schmidt-Kennicutt (Schmidt, 1959; Kennicutt, 1998) relations – between the SFR surface density and that of molecular gas – found that known gas-rich galaxy mergers follow a distinct relation from normal star-forming disk galaxies both at low and high redshift (Daddi et al., 2010; Tacconi et al., 2010; Genzel et al., 2010). The former have a more elevated SFR for a given molecular gas mass. This is interpreted as evidence for a higher star formation efficiency and attributed to,

e.g., compression of molecular gas complexes (resulting in a higher molecular gas density as observed (Gao & Solomon, 2004; Juneau et al., 2009) and predicted by merger simulations (Narayanan et al., 2008)). A closer examination of the $\text{SFR}-M_*$ relation presented additional evidence supporting distinct regimes of star formation Elbaz et al. (2011). The higher specific SFR ($\text{SSFR} \equiv \text{SFR}/M_*$) on the starburst sequence, presumed to be driven by galaxy mergers, is associated with more compact emission region (Rujopakarn et al., 2011; Elbaz et al., 2011). This results in different dust emission properties as also found in nearby ultraluminous galaxies (da Cunha et al., 2010). What do these modes of star formation imply about the growth of the central black holes (or vice versa)?

Similarly to star formation history studies, analyses of supermassive black hole (SMBH) accretion rates also infer a decline of the global SMBH accretion rate with time (e.g., Barger et al., 2001). Also analogous to SFRs, there are indications for downsizing in the sense that in recent epochs, active SMBH grow at a rate closer to their Eddington limit in systems with lower SMBH mass (Marconi et al., 2004; Gallo et al., 2010). Together with the well-known Magorrian relation (Magorrian et al., 1998; Ferrarese & Merritt, 2000; Tremaine et al., 2002), this is highly suggestive of an overall co-evolution between galaxy stellar content and central SMBH. The interplay between star formation (SF) and AGN activity may be due to positive or negative feedback from the AGN (e.g. Fabian, 1999).

Different modes of SMBH growth have been proposed, including major galaxy mergers (Sanders et al., 1988; Di Matteo et al., 2005; Hopkins et al., 2006), large-scale disk instabilities (Bournaud et al., 2011), and a secular growth where SMBH growth is unrelated to the SFR of galaxies (Shao et al., 2010; Cisternas et al., 2011; Mullaney et al., 2011b). Some of these studies favor hybrid models where the high-luminosity end (quasar regime, with $L_{\text{AGN}} > 10^{44} \text{ erg s}^{-1}$) is dictated by

major galaxy mergers while the lower-luminosity AGN follow a secular evolution (e.g., Shao et al., 2010; Lutz et al., 2010). However, the role of AGN and their underlying physical connection with host galaxies remain uncertain. For instance, most studies of the high-redshift (> 0.5) connection between AGN and host galaxy morphology (to distinguish between, e.g., major merger and secular growth) rely on X-ray selected samples of AGN (Cisternas et al., 2011; Schawinski et al., 2011; Mullaney et al., 2011b). The main drawback of this approach as a test of the major merger hypothesis is the insensitivity to a key phase of AGN growth – when the SMBH is expected to be deeply buried in the gas-rich center of the merging system (Sanders et al., 1988). During that buried phase, X-ray emission from the AGN will be very absorbed by intervening material with high column densities and is likely to be undetected in even the deepest X-ray surveys currently available. Merger models predict that the AGN X-rays become X-ray visible at later stages, after some of the surrounding gas has been either consumed by star formation or evacuated through feedback (from AGN, supernovae, or both). Thus, a real test of this connection and of the AGN content of actively star-forming galaxies require the identification of both absorbed and unabsorbed AGN.

Observationally, the detection of active nuclei at multiple wavelengths can reveal more information about the existence and also the nature of distinct AGN phases. AGN phases may differ by their mass accretion rates (thus output power) as well as by their levels of obscuration, both from within the AGN region itself (e.g., obscuring torus in AGN unified models, Antonucci, 1993) or possibly from their host galaxies. X-ray identification is often a favored method due its reliability (few contaminants) and accessibility to fairly high redshift in the deep surveys such as those conducted with the XMM-Newton and *Chandra* observatories.

However, this method suffers from incompleteness of the absorbed AGN phases, as mentioned previously. Nebular emission lines tracing the narrow line regions (NLRs) surrounding AGN are not subject to the same small-scale obscuration as X-rays owing to their much larger physical extent (100's of pc to a few kpc scale). The [O III] λ 5007 luminosity can be combined with hard (2–10 keV) X-ray luminosity as a Compton-thickness parameter in order to infer the X-ray absorption (Mulchaey et al., 1994; Bassani et al., 1999; Heckman et al., 2005; Juneau et al., 2011). AGN identified at optical wavelengths tend to either have a direct view of the nuclear region with low-level obscuration by dust in the host galaxy (type 1 AGN, recognized by broad emission lines) or a large obscuration of the nuclear region along the line-of-sight combined with a lesser obscuration of the narrow-line regions (type 2 AGN, lacking broad emission lines¹). However, it is conceivable that extreme dust obscuration with large covering fraction within the host galaxy could attenuate the emission lines from the narrow-line regions thereby suppressing all signatures in optical spectra.

In cases where both X-ray emission and optical line emission are completely obscured, infrared light may provide clues by showing emission of high-ionization potential lines in the mid-IR region (e.g., Lutz et al., 1998; Armus et al., 2004; Rigby et al., 2009), less subject to extinction than shorter wavelengths (Draine, 2003). Alternatively, one can probe reprocessed thermal emission from AGN-heated dust grains. The more energetic radiation field from an AGN heats the dust to higher temperatures, adding a hot dust component with thermal emission at shorter MIR wavelengths (Elvis et al., 1994; Lacy et al., 2004; Stern et al., 2005; Mullaney et al., 2011a). This extra hot dust may alter the mid-IR spectral

¹Additionally, some type 2 (narrow lines only) AGN may be radiatively inefficient and simply lack broad line regions (Trump et al., 2011) but these systems are intrinsically weaker and presumably have less effect on their host galaxies.

energy distribution (SED) by producing an excess between the usual stellar bump at $\sim 1.6\mu\text{m}$ and the normal (non-AGN heated) dust emission. Broad-band MIR observations such as those from *Spitzer*/IRAC can probe that feature (Lacy et al., 2004; Stern et al., 2005; Donley et al., 2007). Not all AGN will exhibit MIR signatures because of the required geometry and dust content. Also, intrinsically weaker AGN occurring alongside star formation tend not to dominate the IR SED of their host galaxies (Barmby et al., 2006).

Overall, it is clear that no single diagnostic can achieve a complete census of AGN for all galaxies. As such, combining selections at multiple wavelengths may be the key to achieving both a better sampling and a better understanding of AGN and their connection with star formation activity.

In this paper, we characterize the incidence of AGN in FIR-selected galaxies, which are major contributors to the global SFR at intermediate redshift ($0.3 < z < 1$). We further identify various AGN phases by utilizing a combination of X-ray, optical nebular emission-line, and MIR diagnostics. The galaxy sample is described in Section 4.2. The AGN diagnostics are introduced and applied in Section 4.3. The recently developed MEx diagnostic diagram (Juneau et al., 2011, hereafter J11) is of crucial importance to identify AGN with various degrees of X-ray absorption. Section 4.4 contains the results regarding the AGN fraction among FIR-selected galaxies (Section 4.4.1). We show how the occurrence of AGN behaves as a function of both stellar mass and SFR for low-redshift comparison galaxy samples, and for intermediate-redshift FIR-selected galaxies (Section 4.4.2). We test for the influence of AGN emission on mid-to-far infrared color, probing the dust temperature on the warm side of the SED (Section 4.4.3). The AGN content is broken down between X-ray selected AGN, X-ray absorbed AGN, and weak AGN. X-ray absorbed systems are discussed in further detail

in Section 4.5.1 before we list possible physical interpretations of the triggering mechanisms of AGN in Section 4.5.2, and discuss the caveats in Section 4.5.3. Lastly, we summarize our findings in Section 4.6. We assume a flat cosmology with $\Omega_m = 0.3$, $\Omega_\Lambda = 0.7$, and $h = 0.7$ throughout, and a Chabrier (2003) IMF when deriving stellar masses and SFRs.

4.2 Galaxy Samples

The primary intermediate-redshift galaxy sample is based on observations from the Great Observatories Origins Deep Survey² (GOODS) and the All-wavelength Extended Groth strip International Survey³ (AEGIS), specifically in the GOODS-North and the Extended Growth Strip (EGS) fields. The multiwavelength datasets and sample selection criteria are described in Sections 4.2.1 and 4.2.2, respectively. There is substantial overlap with the methodology described in J11, which we summarize when necessary. In addition, we characterize the total infrared luminosities in Section 4.2.3 and the mid-to-far infrared colors in Section 4.2.4. Lastly, we cull comparison samples at low redshift from the literature (Section 4.2.5).

4.2.1 Multiwavelength Dataset

A wealth of multiwavelength data are available in both the GOODS-N and EGS fields, which are the focus of this paper. Most relevant for this study are *Spitzer* MIPS and IRAC data, Keck/DEIMOS optical spectra, and deep *Chandra* X-ray observations.

4.2.1.1 Infrared Photometry

Both fields were observed during the Far-Infrared Deep Extragalactic Legacy survey (FIDEL; Dickinson & FIDEL team, 2007), yielding sensitive *Spitzer* observa-

²<http://www.stsci.edu/science/goods/>

³<http://aegis.ucolick.org/>

tions at $24\mu\text{m}$ and $70\mu\text{m}$ (respective 3σ limiting fluxes of $\sim 20\mu\text{Jy}$ and 2 mJy). MIPS photometry was obtained using a guided extraction method, where images at shorter wavelength, less subject to confusion, are used to build a set of prior positions to fit for the same sources at longer wavelengths. In this case, IRAC images were used to select priors which were then fit simultaneously at $24\mu\text{m}$. Next, sources with a $24\mu\text{m}$ detection were fit at $70\mu\text{m}$. The data and method are described in more detail in Magnelli et al. (2009, 2011). This guided extraction method can effectively deblend sources that are at least $0.5 \times \text{FWHM}$ apart ($\sim 9''$ for MIPS $70\mu\text{m}$). Systematic uncertainties were quantified using Monte Carlo simulations to calculate the difference between the extracted flux of simulated sources to the real input flux (Magnelli et al., 2009). The latest catalogs in GOODS (Magnelli et al., 2011) include two estimates of the uncertainties: the systematic uncertainties quantified from the Monte Carlo simulations, as well as local background noise uncertainties (from the residual maps). We use the maximum of the two values for each galaxy.

Spitzer/IRAC photometry is available in all four channels (3.6, 4.5, 5.8 and $8.0\mu\text{m}$) (available through the *Spitzer* Science Center for GOODS-N Barmby et al., 2008, for EGS). In what follows, IRAC photometry is used to calculate rest-frame K-band magnitudes, which are in turn used to estimate stellar masses when they are not available through SED fitting. In addition, IRAC photometry is used for mid-infrared color-color AGN diagnostics (§4.3.3).

4.2.1.2 Optical Spectra

As in J11, the GOODS-N optical spectra are drawn from the Team Keck Redshift Survey⁴ (TKRS Wirth et al., 2004), whereas the EGS spectra come from the DEEP2 Galaxy Redshift Survey (hereafter DEEP2; Davis et al., 2003, 2007). However, we

⁴<http://tkserver.keck.hawaii.edu/tksurvey/>

augment the sample with spectra obtained during the DEEP3 campaign (Newman et al, in prep.), including galaxies in GOODS-N (Cooper et al., 2011) and EGS.

All sets of observations were reduced with the same pipeline⁵. However, their spectral resolution and spectral range differ due to the use of different gratings (600 line mm^{-1} for TKRS and DEEP3, and 1200 line mm^{-1} for DEEP2). The TKRS and DEEP3 resolution is 4\AA FWHM over the wavelength range 5500–9800 \AA , while DEEP2 spectra have a resolution of 2\AA FWHM with a wavelength coverage of 6500–9100 \AA .

Emission line fluxes are measured as described in J11, by fitting a Gaussian curve to each line individually and integrating the flux over $\pm 2.5\sigma$, where σ is the Gaussian width. Through this paper, we are only concerned with the $\text{H}\beta/[\text{O III}] \lambda 5007$ flux ratio and with the $[\text{O III}] \lambda 5007$ luminosity. The $\text{H}\beta$ fluxes are corrected for underlying Balmer absorption either by using a population synthesis model fit to the continuum (with Bruzual & Charlot (2003) models when the median S/N per pixel is greater than 3), or by applying the median value of $2.8 \pm 0.9\text{\AA}$ for spectra with low S/N.

4.2.1.3 X-ray Data

We take advantage of the fact that the Chandra X-ray coverage is very deep: 2Msec in GOODS-N (Alexander et al., 2003) and 200 ksec in the EGS (Laird et al., 2009; Nandra et al., 2005). The shallower EGS data are sufficient to detect moderate luminosity X-ray AGN ($L_{2-10\text{keV}} > 10^{42} \text{ erg s}^{-1}$) out to $z \sim 1$. Furthermore, we can detect fainter X-ray galaxies (mostly starbursts) in GOODS-N.

X-ray observations are primarily used for AGN identification (Section 4.3.1).

⁵<http://astro.berkeley.edu/cooper/deep/spec2d/>, developed by the DEEP2 team at the University of California-Berkeley

Furthermore, they are used to infer X-ray absorption by comparing the hard X-ray luminosity ($L_{2-10keV}$, calculated as in J11) to the [O III] $\lambda 5007$ narrow-line region luminosity ($L_{[O III]}$), a more isotropic tracer of the intrinsic AGN luminosity than X-rays. For that purpose, we derive X-ray upper limits for [O III]-selected AGN. Upper limits were derived as described in Alexander et al. (2003) in the GOODS-N field, and estimated from the sensitivity maps in the EGS as described in J11.

4.2.2 Sample Selection

In this section, we describe the intermediate redshift galaxy sample. We start from a parent sample of spectroscopically selected galaxies in the range $0.3 < z < 1$. The upper bound of this range is set in order to detect $H\beta$ and [O III] $\lambda 5007$ within the spectral coverage of the optical spectra⁶. The FIR-selected subsample is defined to have a MIPS $70\mu\text{m}$ detection with $S/N > 3$, yielding a sample of 324 galaxies at $0.3 < z < 1$ (59 in GOODS-N; 265 in EGS). All of these galaxies have a robust $24\mu\text{m}$ detection.

We sometimes put the FIR-selected sample in context by making comparisons with the parent spectroscopic sample and with a $24\mu\text{m}$ -selected sample. However, most of the analysis concerns the FIR-selected sample. We note that $70\mu\text{m}$ corresponds to a rest-frame wavelength of $45\mu\text{m}$ at $z \sim 0.56$, the median redshift of our sample. For context with recent and upcoming galaxy studies with the *Herschel* space telescope, this rest-frame wavelength is sampled by *Herschel* PACS $100\mu\text{m}$ observations of $z \sim 1.2$ galaxies or PACS $160\mu\text{m}$ observations of $z \sim 2.5$ galaxies.

⁶In detail, there is some variation in the wavelength range of individual spectra due to the instrumental set-up (as described in Section 4.2.1.2) and due to the exact position of the slits on the mask.

4.2.3 Infrared Luminosities

We describe some properties of the galaxy sample below, namely the infrared luminosities and mid-to-far infrared colors. Given the sensitivity of the FIDEL survey at $70\mu\text{m}$, the majority of the $70\mu\text{m}$ -selected galaxies are luminous IR galaxies (LIRGs; with $L_{IR}(8 - 1000\mu\text{m}) > 10^{11} L_{\odot}$). These objects are responsible for a large fraction of the global SFR density at $z \sim 1$ (Le Floch et al., 2005; Magnelli et al., 2009) thus represent a relevant sample to study the concurrence of AGN and star formation in galaxies.

Total infrared luminosities ($8 < \lambda < 1000\mu\text{m}$) were obtained by fitting the $70\mu\text{m}$ flux density and redshift with templates from Chary & Elbaz (2001, hereafter CE01) and are shown in Figure 4.1. Even when used with only data at much shorter wavelengths than the peak of typical infrared SEDs ($>100\mu\text{m}$), these templates have been shown to give consistent results with integrating over the longer wavelength *Herschel* bands that directly measure the FIR SED in galaxies out to $z \sim 1.5$ (Elbaz et al., 2010).

The $\text{H}\beta$ and $[\text{O III}] \lambda 5007$ emission lines, which will be used to identify the presence of AGN, are available in the spectra of 265 among the 324 FIR galaxies at $0.3 < z < 1$ (filled black circles on Figure 4.1). Of these 265 galaxies, 143 (54%) have a valid emission line measurements with a 3σ detection for both the $\text{H}\beta$ and $[\text{O III}] \lambda 5007$ lines, while 59 (18%) galaxies have one detection and one upper limit. This results in 202 galaxies (76%) with a potential constraint on their $[\text{O III}] \lambda 5007/\text{H}\beta$ flux ratios. The targeted emission lines shift beyond the wavelength range of DEEP2 spectra by $z \sim 0.8$. This explains the smaller fraction of galaxies with available emission line measurements at $0.8 < z < 1$.

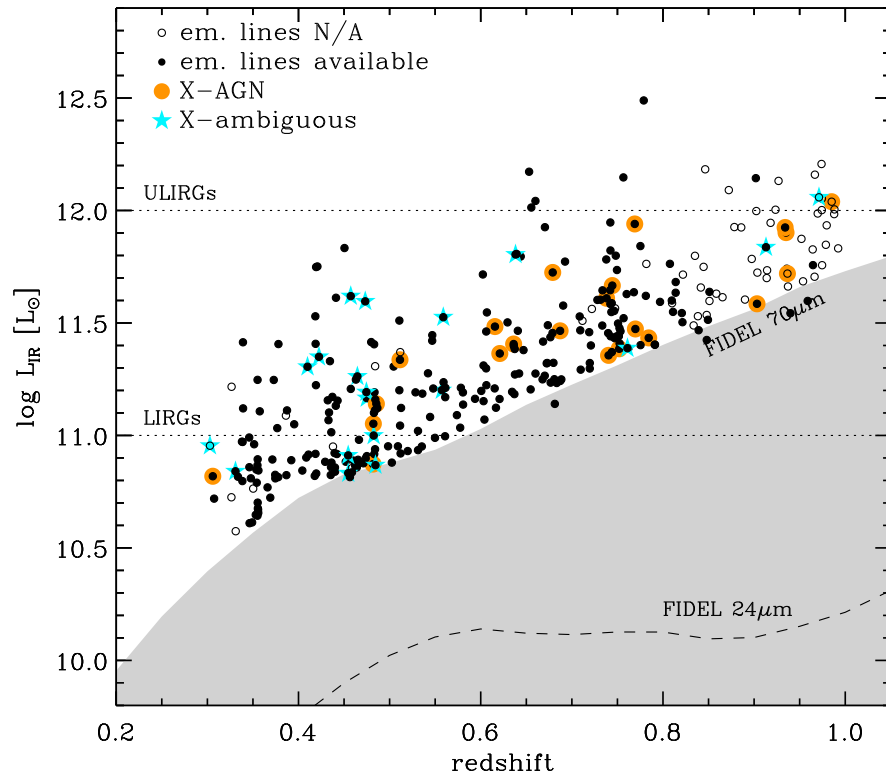


Figure 4.1 Total infrared luminosity as a function of redshift for galaxies in GOODS-N and the EGS. Galaxies with spectral coverage of both the $H\beta$ and $[\text{O III}] \lambda 5007$ emission lines are shown with black filled circles. The X-ray classification indicates which galaxies are robust X-ray AGN (large orange circles) or ambiguous and possibly X-ray starbursts (small cyan circles). For comparison, we also show the 3σ sensitivity limit of the $24\mu\text{m}$ data of FIDEL (dashed line on Figure 4.1), also derived with the CE01 templates.

4.2.4 Mid-to-Far Infrared Color

The observed 24-to-70 μm flux ratios of the intermediate galaxy sample span a broad range of values (Figure 4.2), extending beyond the range of the IR SED templates from Dale & Helou (grey lines 2002, hereafter DH02), especially at lower redshift. We use one of the DH02 templates as a redshift-dependent dividing line between what we will refer to as high S_{24}/S_{70} (blue squares) and low S_{24}/S_{70} (red triangles) galaxies. We select the template empirically to split the sample in roughly equal numbers on either side. The chosen template has parameter $\alpha = 1.85$ (α is the index of the power-law relating the mass of dust heated to the intensity of the interstellar radiation field responsible for the heating, see Equation 1 of Dale & Helou (2002)). According to the method described in Marcillac et al. (2006), this SED corresponds to a total infrared luminosity of $10^{11} L_{\odot}$.

X-ray identified AGN (black filled circles) tend to reside above the line with the high S_{24}/S_{70} galaxies, reaching the largest values. This is not surprising because it is known that AGN can contribute a hot dust component to the IR SED peaking in the mid-IR, thus boosting the mid- to far-IR ratio of their host galaxy. For comparison, we show tracks corresponding to redshifted 24-to-70 μm ratios for three different AGN: NGC 1068 (Seyfert 2), Mrk 231 (Seyfert 1) and UGC 5101 (obscured AGN). We will study the role of AGN on mid-to-far infrared color more explicitly in Section 4.4.3.

4.2.5 Low-Redshift Comparison Samples

Two main comparison samples are built from the Sloan Digital Sky Survey (SDSS). First, we use the same emission-line sample as in J11, i.e., selected to be at redshift $0.05 < z < 0.1$ and to have emission line detections with $S/N > 3$ for all features used in the spectral classification from J11 ($H\beta$, $[\text{O III}] \lambda 5007$, $H\alpha$, $[\text{N II}] \lambda 6584$, and $[\text{S II}] \lambda\lambda 6717, 6731$). This sample comprises 110,205 galaxies.

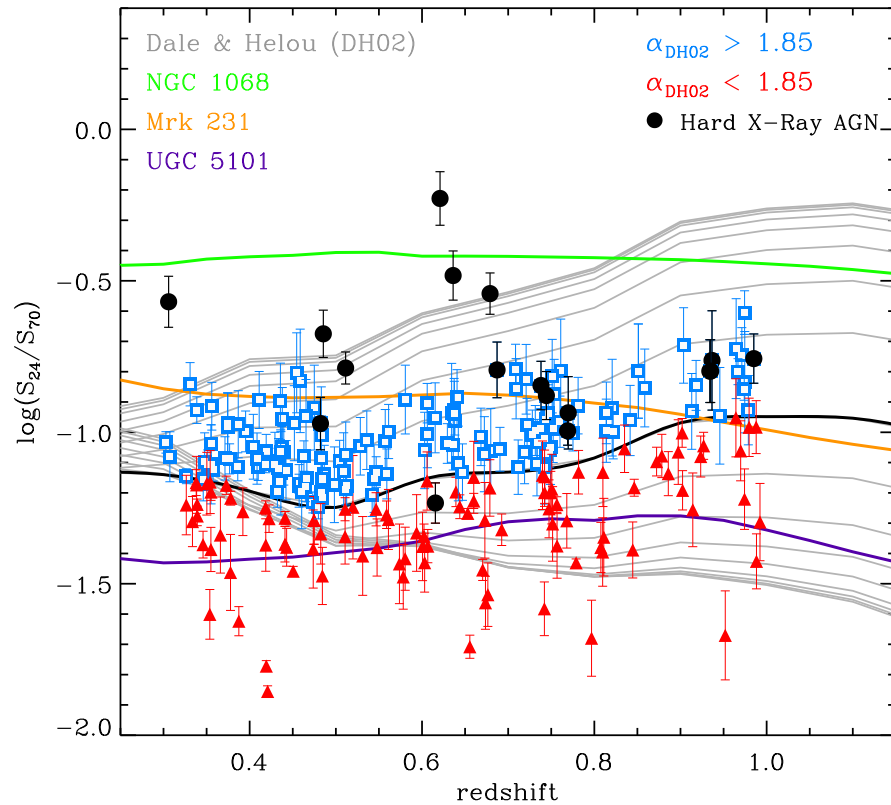


Figure 4.2 Observed 24-to-70 μm flux density ratio as a function of redshift for galaxies in GOODS-N and EGS. The observed values are compared directly to redshifted model templates from Dale & Helou (2002), applicable to star-forming galaxies (gray lines). The black line shows the DH02 template chosen to split our sample between high S_{24}/S_{70} (blue squares) and low S_{24}/S_{70} ratios (red triangles). X-ray AGN are marked with filled black circles. For visual comparison, we also include redshifted tracks for three nearby AGN: NGC 1068 (Seyfert 2, in green), Mrk 231 (Seyfert 1, in orange), and UGC 5101 (obscured or buried AGN, in purple).

Second, we use a FIR-selected sample of SDSS galaxies. The selection was based on the detection in the IRAS $60\mu\text{m}$ or AKARI $90\mu\text{m}$ bands (Hwang et al., 2010a,b). We further impose a redshift selection $0.05 < z < 0.1$ and the availability of a SDSS spectrum with measurable emission lines ($S/N > 3$)⁷, yielding a sample of 4034 galaxies. The emission line fluxes, stellar masses, and star formation rates needed for the current analysis were obtained from the Value Added Catalogs developed by the Max-Planck Institute for Astronomy (Garching) and John Hopkins University (MPA/JHU)⁸. The methodology for measurements of emission line fluxes and SFRs is described in Tremonti et al. (2004) and Brinchmann et al. (2004), respectively, with a few modifications between DR4 and DR7 for the SFRs as described in the value added catalog documentation. Stellar masses were derived following Kauffmann et al. (2003) in DR4 and by fitting the photometry similarly to Kauffmann et al. (2003) and Salim et al. (2007) in DR7.

We adopt the AGN classification based on the BPT [N II]- and [S II]-diagrams, as described in Juneau et al. (2011) but we note that using the classification scheme from Kewley et al. (2006) does not alter our results. We additionally retrieve some AGN that were not included in the MPA catalogs due to extreme linewidths ($> 700 \text{ km s}^{-1}$) by including galaxies with *spclass*= 3 in the SDSS database, assigned to QSOs. The number of such objects is 64, corresponding to only 1.5% of the 4034 galaxies.

We also compare with the IR-selected samples used in Yuan et al. (2010), which include the IRAS Bright Galaxy Survey (Veilleux et al., 1995, BGS), the IRAS 1 Jy ULIRGs sample (Kim & Sanders, 1998; Veilleux et al., 2002), and the

⁷The S/N requirement was relaxed for galaxies with SDSS flag *spclass* = 3 in order to retrieve broad-line AGN. Among 64 *spclass* = 3 objects, 40 have $S/N > 3$ in the catalog and the remaining 24 either had a lower S/N or were not measured in the MPA/JHU catalog due to the breadth of the lines.

⁸Available for DR4: <http://www.mpa-garching.mpg.de/SDSS/DR4/>; and for DR7: <http://www.mpa-garching.mpg.de/SDSS/DR7/>

Southern Warm Infrared Galaxy sample (Kewley et al., 2001b, SW01). For our purposes, we combine all three samples in order to calculate the overall AGN fraction as a function of L_{IR} with better number statistics in Section 4.4.1.2. We consider as AGN any spectral type other than purely star-forming according to the adopted classification in Yuan et al. (2010, see their Tables 1, 2 and 3). We note that this approach selects the same AGN as the J11 spectral classification (a combination of composites, LINERs, and Seyferts) and that these IR-selected samples have been reported to contain very few LINERs (Yuan et al., 2010).

4.3 Multiwavelength AGN Diagnostics

In this section, we apply several AGN diagnostics in order to increase the completeness of the AGN census among FIR-selected galaxies, but also to learn more about the AGN properties such as accretion rate and obscuration, which we discuss in Sections 4.4.2 and 4.5.1.

4.3.1 X-ray Diagnostic

The X-ray identification of AGN is based on two criteria: (1) hard X-ray luminosity $L_{2-10\text{keV}} > 10^{42} \text{ egs s}^{-1}$, and (2) hardness ratio⁹ $HR > 0.1$. An object is classified as X-ray AGN if either of these two criteria is satisfied. We note that several other studies also adopt such a luminosity criterion when selecting samples of AGN from deep X-ray surveys (e.g., Cisternas et al., 2011; Schawinski et al., 2011; Mullaney et al., 2011b). The addition of a hardness criterion in the current study allows us to include weaker and/or more absorbed AGN, although only one among 19 X-ray AGN has $L_{2-10\text{keV}} < 10^{42} \text{ egs s}^{-1}$.

While the bright emission of hard (2–10 keV) X-rays is a fairly reliable and

⁹Hardness Ratio $\equiv (H - S)/(H + S)$, where H and S are the X-ray count rates in the hard (2 – 8 keV) and soft (0.5 – 2 keV) bands, respectively.

commonly used method for finding AGN, it is subject to incompleteness due to X-ray absorption by intervening gas along the line of sight. Complementary approaches include even higher energy observations (>10 keV), which have thus far been limited to only very modest redshift or rare luminous objects due to low sensitivity, or alternative wavelength AGN tracers. Next, we consider an optically-based diagnostic, which traces the narrow-line regions around AGN. Those spatially-extended regions are not subject to the same absorption as the X-rays, which originate in a small volume around the central engine although the larger-scale ISM of the host galaxy may extinct the NLR in some cases.

4.3.2 MEx Diagnostic

The second AGN identification method is the MEx diagnostic diagram, introduced in J11¹⁰. The MEx diagram plots stellar mass versus the $[\text{O III}] \lambda 5007/\text{H}\beta$ flux ratio (Figure 4.3). Empirical dividing lines indicate spectrally distinct regions of the MEx diagram: optically-identified AGN tend to lie above the lines, purely star-forming galaxies below the lines and the MEx-intermediate region (between the lines) contains a sharp transition from star-forming to AGN galaxies. More than 50% of galaxies in the MEx-intermediate region are AGN/SF composites according to the SDSS calibration sample used in J11. The main strengths of this diagram are its applicability to higher redshift relative to traditional BPT diagrams¹¹ and the use of a probabilistic approach to retrieve composite galaxies and to assess the uncertainty of a given spectral class.

The FIR-selected sample is shown on the MEx diagram in Figure 4.3 with two different plotting schemes. The X-ray AGN classification is illustrated on the left

¹⁰See <https://sites.google.com/site/agndiagnostics/home/mex> for software to compute the MEx AGN classification.

¹¹BPT diagrams require $\text{H}\alpha$ and other fairly red emission lines ($[\text{N II}] \lambda 6584$, $[\text{S II}] \lambda\lambda 6717, 6731$, or $[\text{O I}] \lambda 6300$), which redshift out of the optical window at $z > 0.4$.

panel. Most of the X-ray detected galaxies lie in the MEx-AGN and intermediate regions, as expected. The secure X-ray AGN all have a high stellar mass $M_* > 10^{10.7} M_\odot$, and seem to be more massive on average than the global AGN population. However, the statistics are poor with only 12 X-ray AGN on the MEx diagram. When comparing the stellar masses of FIR-selected hosts and all X-ray AGN, Mullaney et al. (2011b) found a small difference with the FIR-selected hosts having a marginally higher mass (by ~ 0.1 dex, a $\sim 1\sigma$ difference). More significantly, they found that the mean stellar mass of X-ray selected AGN does not evolve with redshift between $0.5 < z < 3$. This provides additional support for the validity of the MEx diagram at higher redshift.

The right panel of Figure 4.3 shows the FIR-selected galaxies coded as a function of their mid-to-far infrared color. Galaxies with a low S_{24}/S_{70} (red triangles) occupy predominantly the star-forming and intermediate regions whereas galaxies with a high S_{24}/S_{70} (blue squares) are distributed across the full range of $[\text{O III}] \lambda 5007/\text{H}\beta$ values, with the most extreme cases (filled black squares) exclusively classified as AGN.

4.3.3 IRAC Single-Color and Two-Color Diagnostics

The next AGN identification method relies on probing AGN-heated dust. In the presence of the energetic photons emitted around the AGN, a larger amount of small dust grains can reach high temperatures compared to other dust heating mechanisms like in individual star-forming regions. This dust heating results in reprocessed emission in the mid-infrared region. The advantage of using dust emission as a marker for AGN is the complementarity to X-ray and optical AGN signatures, which can be attenuated by intervening material much more severely than mid-infrared emission.

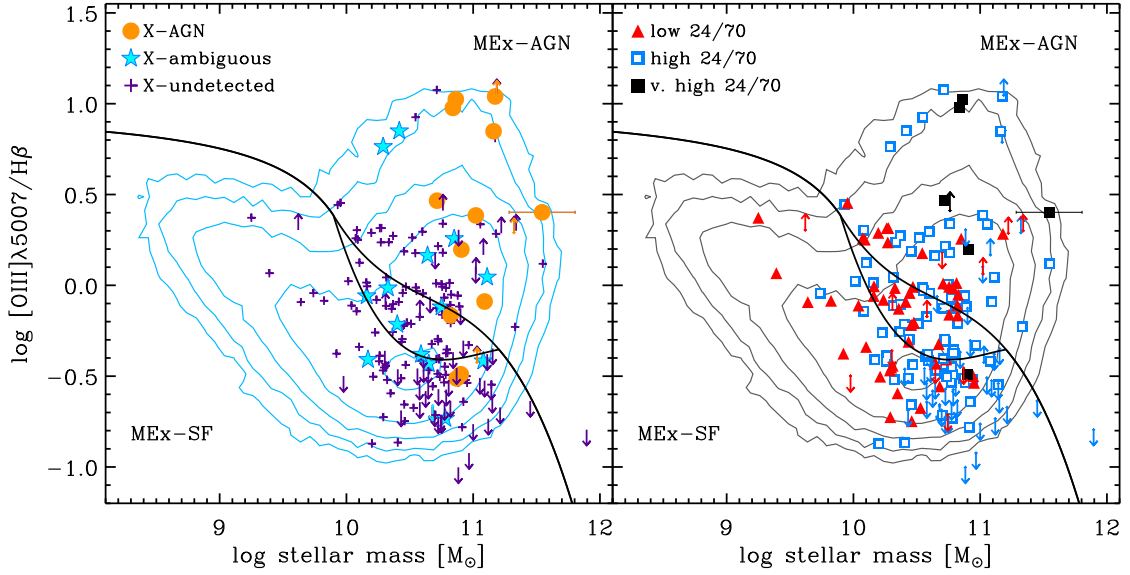


Figure 4.3 The MEx AGN diagnostic diagram. The empirical curves (solid lines) split the diagrams into galaxy spectral types as labeled, with a MEx-intermediate region between the MEx-AGN and MEx-SF classes. Contours show the SDSS low- z sample (evenly spaced logarithmically), and the $70\mu\text{m}$ sample is superimposed with larger symbols keyed to an independent X-ray classification (left panel, see legend). X-ray AGN (large filled circles) are only unambiguously identified in high-mass galaxies ($M_{\star} > 10^{10.7} M_{\odot}$). (right) Plotting symbols are keyed to the mid-to-far-infrared color S_{24}/S_{70} . Objects with low values of S_{24}/S_{70} (red triangles) tend to be centrally distributed on the MEx diagram while the location of the high- S_{24}/S_{70} galaxies (blue squares) extends to both extremes of the $[\text{O III}]/\text{H}\beta$ range. Galaxies with very high S_{24}/S_{70} (black squares) are exclusively on the AGN tail of the distribution toward high values of $[\text{O III}]/\text{H}\beta$.

Lacy et al. (2004) reported that their combination of IRAC colors selects both obscured and unobscured luminous AGN (roughly half of their low- z AGN sample was diagnosed as obscured quasars or luminous Seyfert 2 galaxies that were missed in the optical SDSS data). Similarly, Stern et al. (2005) found that using IRAC colors could identify over 90% (40%) of the broad-line (narrow-line) AGN in their sample drawn from the IRAC Shallow Survey, and state that 17% of their IRAC-selected AGN were not spectroscopically identified (presumably due to dust obscuration of the optical signatures). On the other hand, Barmby et al. (2006) found that these MIR diagnostics miss a larger fraction of X-ray selected AGN when applied to more sensitive IRAC data and that they furthermore suffer from more contamination from non-AGN galaxies. The latter is caused by the deeper observations probing to higher redshift and making the IRAC colors of starburst and normal star-forming galaxies appear redder and moving into the AGN selection box.

Here, we adopt the IRAC color-color diagram developed by Stern et al. (2005) because it was shown to suffer from less star-forming galaxy contamination when applied to higher-redshift and to more sensitive IRAC observations (Donley et al., 2007). The diagram is shown in Figure 4.4, where AGN nominally lie in the upper boxed region. We note that the diagram was calibrated with shallower data than are used here and that systematic differences can play a role in the AGN selection. Namely, purely star-forming galaxies may enter the AGN selection region at $z > 1$ (Donley et al., 2007). We show some tracks of expected mid-infrared colors for various galaxy templates in panel (a) of Figure 4.4. We do not expect strong contamination by star-forming galaxies at $z < 1$, but we note that some well-known AGN are located outside of the AGN region when their colors are redshifted.

Panels (b) and (c) show a comparison with the X-ray and optical MEx classifications, respectively. The optically-selected AGN (green to red color on panel (c)) display a similar distribution as the X-ray AGN shown in (b) although a few of the absorbed AGN candidates (undetected in X-rays) have a valid AGN classification in the optical diagnostic. Combining both the X-ray and MEx classification selects 83% (10/12) of the galaxies within the IRAC selection box. The remaining two IRAC AGN candidates are either genuine (but obscured) AGN or star-forming contaminants. We distinguish between these two possibilities by employing a single IRAC color as a function of redshift, as described below.

For this exercise, we utilize the entire parent sample of $0.3 < z < 1$ galaxies regardless of their emission-line measurements and FIR detection. Because IRAC color-color diagrams do not include information about the redshift of the galaxies, there are degeneracies in observed colors from overlapping redshift tracks of different galaxy populations (see, e.g., Donley et al., 2007). To remove such degeneracies, we look at the IRAC [3.6]-[8.0] color as a function of redshift. As shown in Figure 4.5, infrared-selected star-forming galaxies (yellow lines) occupy a distinct region from nearby AGN (black lines), especially at $z > 0.5$. The example nearby AGN shown are Mrk 231, UGC 5101, Mrk 273, and known compton-thick AGN NGC 6240. The AGN templates were constructed from gathering photometry from the NASA Extragalactic Database and interpolating with templates (R. Chary, private communication (2008)). The star-forming galaxy templates are taken from Rieke et al. (2009) and are constructed from observations of nearby galaxies. The outermost template shown in cyan is for IRAS 12112+0305, which we use to separate the IRAC star-forming galaxies (below the cyan curve) from the IRAC AGN candidates (above the cyan curve). The change in IRAC [3.6]-[8.0] color with redshift of the infrared selected star-forming galaxies (yellow curves)

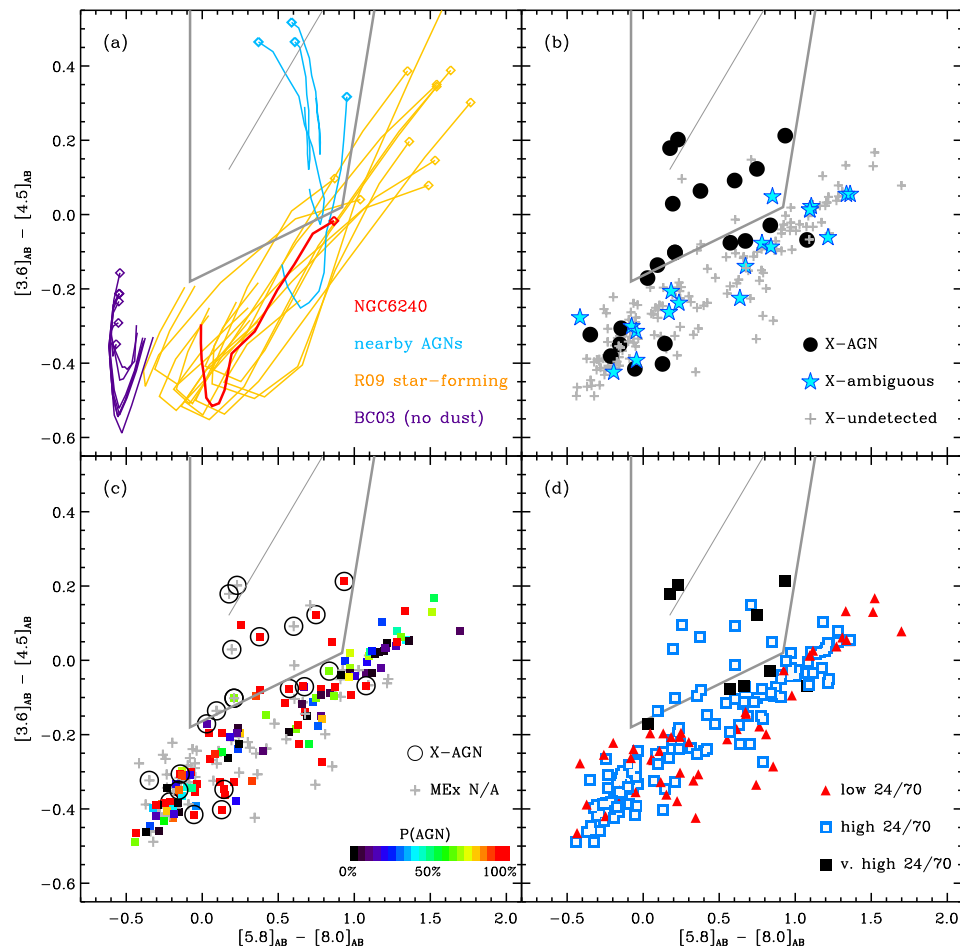


Figure 4.4 IRAC color-color diagram from Stern et al. (2005). The AGN selection box (thick solid line) and the power-law locus (thin solid line) are the same on all panels. In Panel (a), IRAC colors are computed for various templates as a function of redshift from $z = 0.3$ (open diamonds) to $z = 1$. Namely, we display the expected colors of nearby star-forming LIRGs and ULIRGs from the templates in Rieke et al. (2009, in yellow), and highlight a nearby Compton-thick double AGN, NGC 6240, in red. The IRAC AGN selection is compared to the X-ray classification in Panel (b) where X-ray starbursts/ambiguous systems (AGN) are plotted with star symbols (filled circles). Panel (c) shows a comparison with optically-

Figure 4.4 *continued*. selected AGN (color bar) from the MEx diagram. Most IRAC AGN candidates in our sample are also recognized as such from the X-ray or MEx selection methods (or both). Panel (d) displays the location of galaxies as a function of S_{24}/S_{70} . Galaxies with the highest S_{24}/S_{70} are located within or nearby the boundaries of the AGN region, as expected if there were a $24\mu\text{m}$ excess caused by AGN-heated dust emission.

is due in part to the aromatic features at rest-frame wavelengths $6.2 - 8.6 \mu\text{m}$ gradually shifting outside of the [8.0] band (between $0 < z < 0.4$) and entering the [3.6] band at $0.7 < z < 1.2$.

When AGN-heated dust dominates the mid-IR emission, the near power-law shape of the continuum causes a flatter [3.6]-[8.0] color evolution with redshift, as exemplified by Mrk 231 and UGC 5101. Lastly, dust-free stellar populations templates (Bruzual & Charlot, 2003) follow the lower envelope of the observations. As expected, some of the non-FIR galaxies detected with IRAC are not very dusty and the IRAC color instead correspond to stellar photospheres in these cases.

Unsurprisingly, the FIR-selected galaxies mostly follow the tracks of the nearby infrared galaxies. It is worth noting that FIR-galaxies that host X-ray AGN (black circles) span the whole range of IRAC colors covered by the FIR-sample (non-AGN and up to the most extreme AGN-like color). The X-ray AGN that are indistinguishable from star-forming galaxies are likely systems where star formation dominates at infrared wavelengths even in the presence of nuclear activity (e.g. Rujopakarn et al., 2011). Alternatively, the AGN-heated dust emission may be preferentially absorbed compared to dust emission from stellar heating. This would only occur in extremely dense and dusty environments where the medium is optically thick even at mid-IR wavelengths, which is rare and unlikely to be the

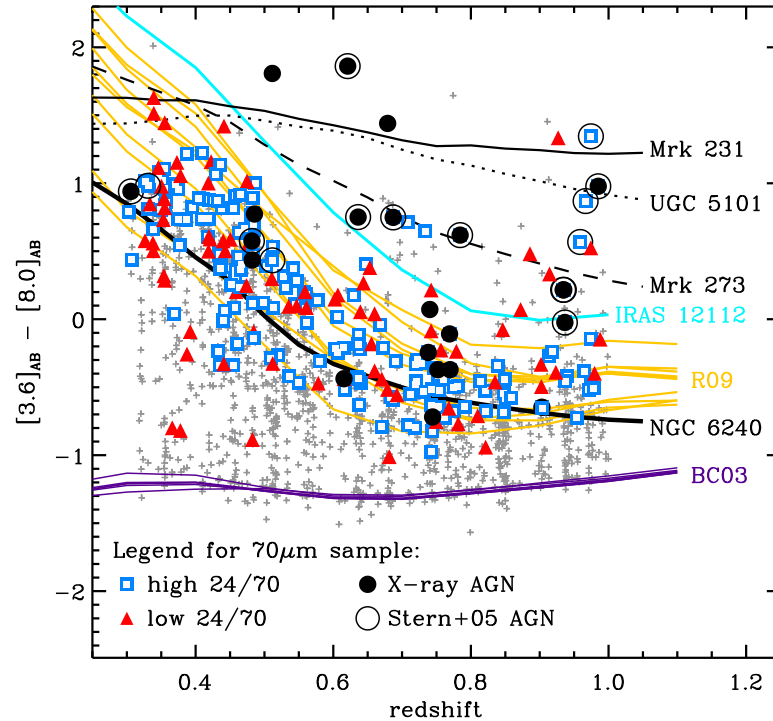


Figure 4.5 IRAC color between observed channels 1 and 4 as a function of redshift. EGS and GOODS-N $70\mu\text{m}$ galaxies with low (red triangles) or high (blue squares) values of S_{24}/S_{70} are distributed similarly. The cyan curve, which corresponds to the redshift track of IRAS 12112+0305, is the star-forming galaxy template showing the most extreme IRAC colors. The remainder of the star-forming galaxy templates from Rieke et al. (2009) (yellow tracks) span a fairly restricted range in color. Galaxies above that range are suspected to host AGN activity. This picture is further supported by the projected colors of a few nearby AGN [black lines: Mrk 231 (solid); UGC 5101 (dot-dashed); IRAS 05189-2524 (dotted line); and Mrk 273 (dashed line)]. However, X-AGN span the entire range of IRAC colors. We highlight a nearby Compton-thick AGN (NGC 6240) with a thicker

Figure 4.5 *continued*. black line. FIR-selected galaxies that were also selected by the IRAC color-color diagnostic from Stern et al. (2005) are marked with open black circles. Lastly, dust-free stellar population models from Bruzual & Charlot (2003) define the lower envelope of the parent sample of galaxies (grey crosses). Systems near these tracks are likely dust poor and their color resemble that of stellar photospheres rather than dust emission.

case in most systems. Lastly, we note additional AGN candidates that were not selected by the X-ray method (filled black circles) nor by the IRAC color-color diagram used earlier in this section (open black circles). In the remainder of this paper, IRAC-selected AGN (or simply IRAC-AGN) refer to AGN identified from either the color-color or the single-color (versus redshift) method.

4.4 Results

In what follows, we study the occurrence of AGN as a function of stellar mass and SFR of their host galaxies (Section 4.4.1). We present an analysis of these dependencies in low-redshift ($0.05 < z < 0.1$) galaxy samples derived from SDSS in Section 4.4.1.1. The AGN fractions are then reported for the intermediate-redshift emission-line subsample as well as for the global FIR-selected sample in Sections 4.4.1.2 and 4.4.2, respectively. We find a good agreement between the low- and intermediate-redshift FIR-selected samples, and a strong indication for a high fraction of X-ray absorbed AGN in infrared luminous galaxies.

Next, we will examine the behavior of the $70\mu\text{m}$ -selected galaxies as a function of their mid- to far-IR flux density ratio. In general, this quantity provides us with an indication of the average temperature of the warm dust component. In particular, we will compare the 24-to- $70\mu\text{m}$ color of galaxies with and without

AGN (Section 4.4.3). Lastly, we will compare the luminosities from star formation and AGN emission in Section 4.4.4.

4.4.1 AGN Fraction as a Function of Stellar Mass and SFR

In this section, we restrict the analysis to emission line galaxy samples as well as emission line AGN identification for homogeneity. We use the standard BPT classification but the results do not change when using the MEx classification (Section 4.4.1.2). We then expand the analysis to multiwavelength diagnostics and overall FIR-selected samples in Section 4.4.2, where we quantify the global AGN fraction in FIR galaxies. Here, AGN fraction refers to the number of galaxies that host an AGN and not to the fractional contribution of AGN to the luminosity or energy output although we will divide moderate-luminosity AGN from weak AGN in Section 4.4.2.

4.4.1.1 Low-Redshift Galaxies

In order to interpret the AGN triggering in galaxies, we first characterize the dependence of the AGN fraction on stellar mass and SFR in low-redshift samples derived from SDSS. While the AGN occurrence was already reported to increase strongly with stellar mass (e.g., Kauffmann et al., 2003), the behavior with SFR is not as well studied. We use two $0.05 < z < 0.1$ comparison samples: (1) emission-line selected SDSS galaxies, and (2) FIR-selected SDSS galaxies, as described in Section 4.2.5.

In the case of the FIR-selected sample, we also compute SFRs from the infrared luminosities using the relation from Kennicutt (1998) and applying a factor of 0.66 to account for the difference in IMF (to convert from Salpeter (1955) to Chabrier (2003) IMF):

$$\text{SFR}[M_{\odot} \text{ yr}^{-1}] = 1.14 \times 10^{-10} \times L_{IR}[L_{\odot}] \quad (4.1)$$

where $L_{IR} = L(8 - 1000 \mu\text{m})$. We will use the notation $\text{SFR}(L_{IR})$ to distinguish between SFRs obtained using the infrared luminosity and the values from the SDSS value added catalogs, simply denoted SFR.

We show the AGN fraction on the $\text{SFR}-M_*$ plane on Figure 4.6. The contours show the bivariate distribution of the emission-line SDSS galaxies (left panel). The correlation is similar to that shown in Brinchmann et al. (2004) except that these authors used only galaxies without AGN and reported that the distribution of SFRs becomes broader for stellar masses greater than $10^{10} M_\odot$ and that the correlation breaks down at large stellar masses ($> 10^{10-10.5} M_\odot$ from their Figure 17). We do not find evidence for such a break down here as we include galaxies with AGN, which tend to dominate the high-mass range. However, there is a tail of galaxies extending to low SFRs at all masses. We fit a linear relation to the tight sequence between $\log(\text{SFR})$ and $\log(M_*)$ with the IDL¹² LINFIT routine. Restricting the fit to galaxies within the innermost two contours, we obtain a slope of 0.61 (shown with a dashed line). The effect of the emission line selection criteria (i.e., $S/N > 3$) is investigated in Appendix E, where we take into account all SDSS galaxies – with and without emission lines – to obtain a lower limit to $P(\text{AGN})$ on the $\text{SFR}-M_*$ plane.

For both the emission-line and FIR samples, there is a strong increase of $P(\text{AGN})$ with stellar mass, as has been previously observed. However, the AGN fraction tends to decrease with increasing SFR at fixed stellar mass. We note that the gradient is steeper as a function of stellar mass than with SFR (the slope of the sharp AGN transition region (in yellow color) is around 1.55), suggesting that the former is a better tracer of the underlying cause governing black hole growth. The situation is somewhat different for the FIR-selected SDSS sample (right-hand side

¹²Interactive Data Language

of Figure 4.6). In this case, the trend with SFR observed on the left-hand panel is not maintained at masses $> 10^{10.5} M_{\odot}$. There is in fact a reversal of the relation, as shown more clearly on Figure 4.7, comparing the AGN incidence as a function of SFR for the same range of stellar masses.

While the AGN fraction in massive ($10^{10.5-11.1} M_{\odot}$) galaxies drops with increasing SFR in the emission-line selected galaxy population, it turns over around $\text{SFR} \sim 10 M_{\odot} \text{ yr}^{-1}$ and increases with SFR for FIR-selected galaxies with similar stellar masses. The high-SFR galaxies that are not selected in the FIR display systematically lower values of the $\text{H}\alpha/\text{H}\beta$ Balmer decrement and are thus much less extinguished than the FIR-selected counterparts (by 0.6 to 0.8 mag in visual extinction A_V depending on the extinction curve adopted). Thus, it appears that the FIR-selection is important in selecting galaxies with AGN in a given range of stellar masses and SFRs.

We postulate that this reversal in AGN fraction with SFR in FIR-luminous systems is due to galaxy mergers, which are ubiquitous among nearby galaxies in this luminosity range ($L_{\text{IR}} > 10^{11-12} L_{\odot}$, Sanders & Mirabel, 1996; Veilleux et al., 2002; Hwang et al., 2010a; Nardini et al., 2010), and have been postulated to act as AGN triggering mechanism (Sanders et al., 1988; Veilleux et al., 1995). Mergers could also explain the IR emission due to the compactness of the induced starburst, which could potentially lead to more dust extinction (and IR emission), a high SFR as well as AGN fueling. In this scenario, galaxies with an equally high SFR but with less dust extinction could have star formation spread over a large disk and lack the mechanism driving enhanced dust emission and AGN fueling. This picture is well-supported here, where there is a stark contrast with respect to the global emission-line SDSS population. For the latter, the decreasing incidence of AGN with high SFRs may be related to AGN shutting off the star formation in

their host galaxies, as postulated by studies of post-starburst galaxies (e.g., Yan et al., 2006) and AGN host galaxy colors (e.g., Smolčić, 2009; Schawinski et al., 2009).

The connection between mergers and AGN triggering has been tested more directly by Yuan et al. (2010), who quantified the AGN incidence as a function of both L_{IR} and merger stage for ~ 500 nearby infrared-selected galaxies. They found that the AGN incidence increases with L_{IR} , and that the relative AGN contribution increases with merger stage in ULIRGs. Similarly, Hwang et al. (2010a) reported an increasing AGN fraction with L_{IR} in their much larger sample of 11,964 low-redshift FIR-selected galaxies.

Regardless of the interpretation, the trends established with the low-redshift galaxy samples will be useful benchmarks against which to compare the intermediate redshift sample, which we evaluate next.

4.4.1.2 Intermediate-Redshift Galaxies

We consider the subsample of FIR-luminous galaxies with available $H\beta$ and $[O\ III]\ \lambda 5007$ emission lines. The AGN fraction is shown as a function of infrared luminosity, tracing the SFR (Figure 4.8) and as a function of stellar mass (Figure 4.9). The AGN fraction shown in this section is strictly based on emission line properties and the MEx diagram AGN probabilities:

$$\text{AGN fraction} = \frac{1}{N} \sum_{i=1}^N P_{MEx}(AGN)_i \quad (4.2)$$

where the AGN probability $P_{MEx}(AGN)$ varies from 0 to 1 and is summed over the number of galaxies N that belong to a given bin (or either L_{IR} or M_* values depending on what is examined).

We augment our intermediate-redshift sample of galaxies in EGS and GOODS-N (the FIDEL sample) with MIPS70 μ m galaxies selected in the COSMOS field for

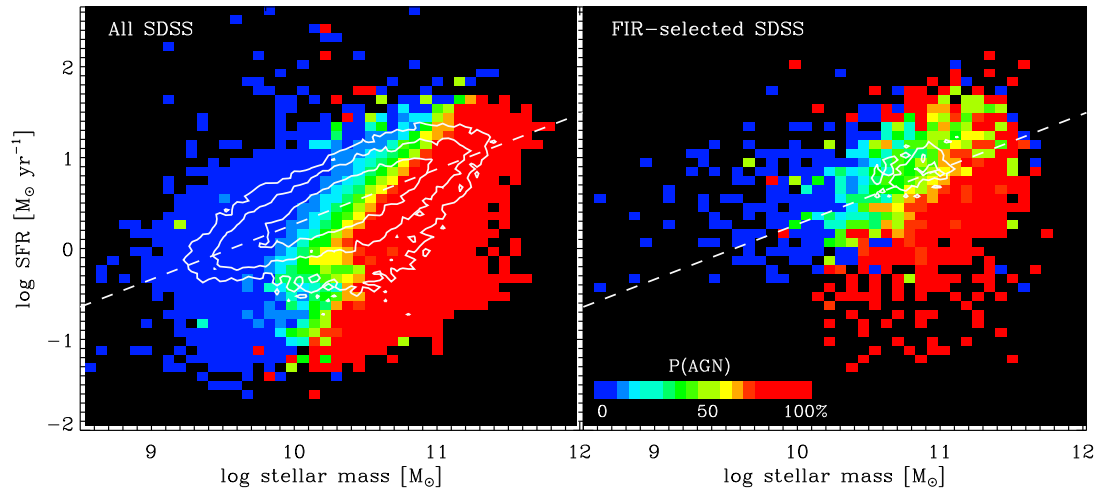


Figure 4.6 Probability of presence of AGN as a function of SFR and stellar mass (color scale). (Left) In the emission-line selected SDSS sample, the AGN probability rises toward higher values stellar mass with a sharp transition region. At a given stellar mass, the AGN probability (or AGN fraction) is either flat or decreasing (toward blue) with increasing SFR. The overall bivariate distribution is shown with logarithmic contours (with the outermost contour delineating 10 galaxies per bin, and a spacing of 0.5 dex between contours). The slope of the SFR- M_* sequence (0.61, dashed line) is shallower than that of the AGN transition region (green/yellow color). (Right) The FIR-selected SDSS sample shows a very similar behavior of the AGN probability with stellar mass although it spans a smaller range in both stellar masses and SFRs. There is however a notable excess of high-AGN fraction at higher SFR (red colored bins at $\log(M_*) > 10.5$ and $\log(\text{SFR}) > 1.3 - 1.5$). The trend between P(AGN) and SFR is investigated further in Figure 4.7.

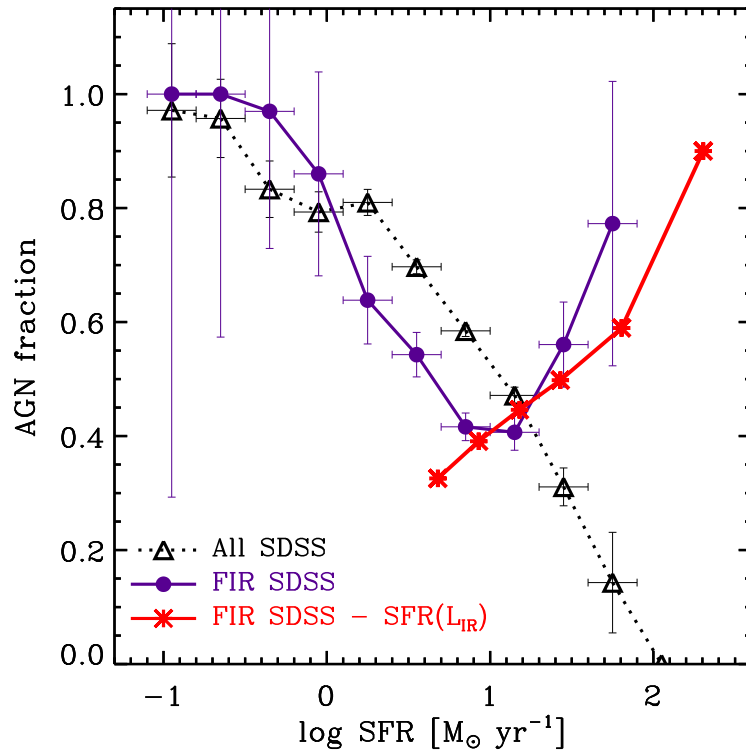


Figure 4.7 AGN fraction as a function of SFR. The emission-line selected SDSS sample (triangles) exhibits a declining AGN fraction with increasing SFR. In contrast, the FIR-selected SDSS sample (filled circles) shows a reversal where the AGN fraction first decreases up to a $\text{SFR} \sim 10$ before rising with increasing SFR. These two samples are restricted to the same mass range: $10.5 < \log(M_{\star}[M_{\odot}]) < 11.1$, which corresponds to the range from the 16th to the 84th percentile of the FIR-SDSS sample stellar mass distribution. The SFR estimates used in this figure were derived from stellar population fitting, and we compare directly to the trend for L_{IR} -derived SFRs for the total FIR SDSS subsample (red asterisks).

which there are $H\beta$ and [O III] emission lines measurements. The parent sample of 500 galaxies is described in Kartaltepe et al. (2010a) and Kartaltepe et al. (2010b), and the emission line properties will be detailed in a forthcoming paper (Kartaltepe et al., in preparation). The larger area of the COSMOS field results in better statistics for high infrared luminosity systems. For brevity, we refer to the GOODS-N, EGS, and COSMOS combined sample simply as the *combined* sample in the remainder of this section.

We find that the AGN fraction increases steadily with L_{IR} and that both the increase and the magnitude of the AGN fraction are consistent with the values obtained for the low-redshift FIR-selected SDSS sample (Figure 4.8). The overall AGN fractions are $50\pm 7\%$ and $45\pm 3\%$ for the FIDEL and combined samples, respectively. FIR-selected galaxies may be expected to be strongly star-forming and dusty, which may result in both dilution and extinction of the AGN signal. If we missed AGN due to star formation dilution, our AGN census would be more incomplete at the bright end. However, we already observe a larger AGN fraction in more IR-bright systems, which is opposite to the effect of dilution.

The increase in AGN fraction appears to be a stronger function of stellar mass (Figure 4.9). For the FIDEL sample, the AGN fraction rises by $48\pm 12\%$ over 1 dex of stellar mass increase, whereas the corresponding increase for the L_{IR} trend is $38\pm 21\%$. Similar values are found for the combined sample ($52\pm 5\%$ /dex of stellar mass and $36\pm 10\%$ /dex of L_{IR}), confirming the result with smaller uncertainties due to improved statistics.

Overall, the AGN fraction behaves similarly to that of the low-redshift FIR-selected samples. In the case of the host galaxy L_{IR} , this is in contrast with the trends with SFR observed for the bulk of the emission-line galaxy population at low-redshift. The stellar mass dependence of the intermediate-redshift sample is

undistinguishable from both the emission-line and the FIR-selected low-redshift comparison samples even though the latter are significantly different from one another at the high mass range (see black dashed line and solid red lines in Figure 4.9). As a reminder, these conclusions apply to the $70\mu\text{m}$ -detected galaxies that also have measurable $\text{H}\beta$ and $[\text{O III}] \lambda 5007$ emission lines. Next, we will examine the AGN content of the global $70\mu\text{m}$ -detected galaxy sample, including the objects lacking emission line flux measurements.

4.4.2 Global AGN Fraction in Intermediate-Redshift Infrared Galaxies

Here, we combine all the AGN identification methods introduced earlier in this paper, namely: the MEx diagnostic diagram, the X-ray classification, and the IRAC single-color and two-color diagrams. In the case of the MEx classification, we maintain the same weighting scheme as before, i.e., the $P(\text{AGN})$ values are used to count the number of AGN, except with the following modification: AGN identified from any alternative method (X-ray or IR colors) are set to have $P(\text{AGN}) = 1$. Furthermore, we keep track of EGS galaxies that were identified as AGN in Yan et al. (2011) based on the AGN diagnostic diagram introduced by these authors. Adopting this procedure, the global AGN fraction in $0.3 < z < 1$ FIR-selected galaxies is 37% (42%) with (without) including the Yan et al. (2011) classification. The discrepancy between the latter classification scheme and the one used in this paper arises from the lower S/N threshold used for emission line detection in Yan et al. (2011), who adopted $S/N > 2$ instead of $S/N > 3$.

Furthermore, we divide the AGN population into three categories: (1) X-ray identified AGN, (2) X-ray absorbed but intrinsically luminous AGN, and (3) intrinsically weak AGN. The first category corresponds to X-ray identified AGN (as described in Section 4.3.1) with the exclusion of two systems which have the highest expected X-ray absorption according to their low $[\text{O III}]$ -to-hard X-ray

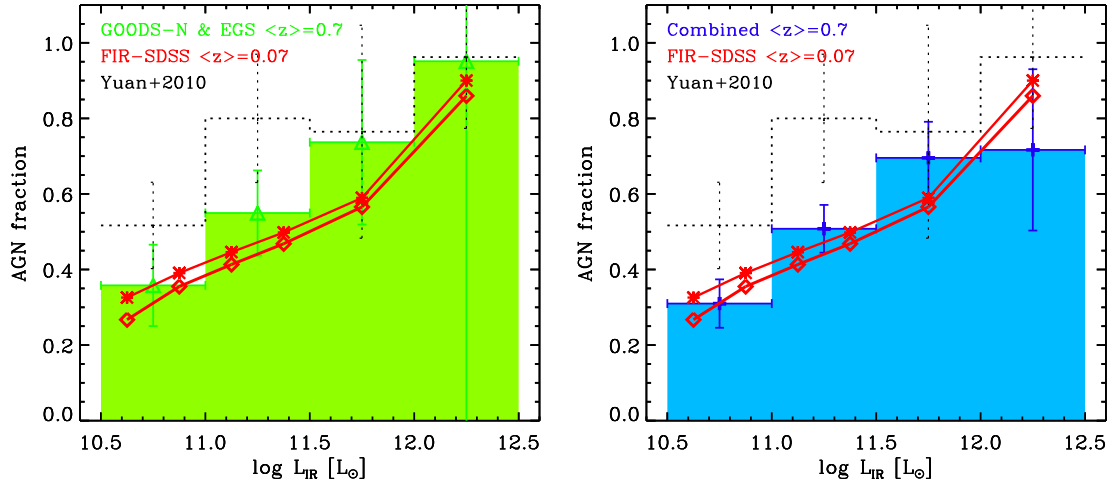


Figure 4.8 AGN fraction as a function of L_{IR} for the FIDEL sample (left) and combined sample (right) of intermediate-redshift FIR-selected galaxies. The AGN fraction rises with increasing L_{IR} in agreement with the trend observed for low-redshift ($0.05 < z < 0.1$) FIR-selected SDSS galaxies from Hwang et al. (2010a, shown in red). The AGN fraction for the latter are calculated using both the BPT-based classification described in J11 (red asterisks) and the MEx-based classification (red diamonds). Only the MEx-based classification is available for most of the intermediate-redshift sample (histograms). We also show values obtained for the nearby IR-selected samples from Yuan et al. (2010) with dotted black lines. Error bars are Poissonian. They are omitted for the FIR-SDSS sample for clarity but see Figure 4.10, where they are included.

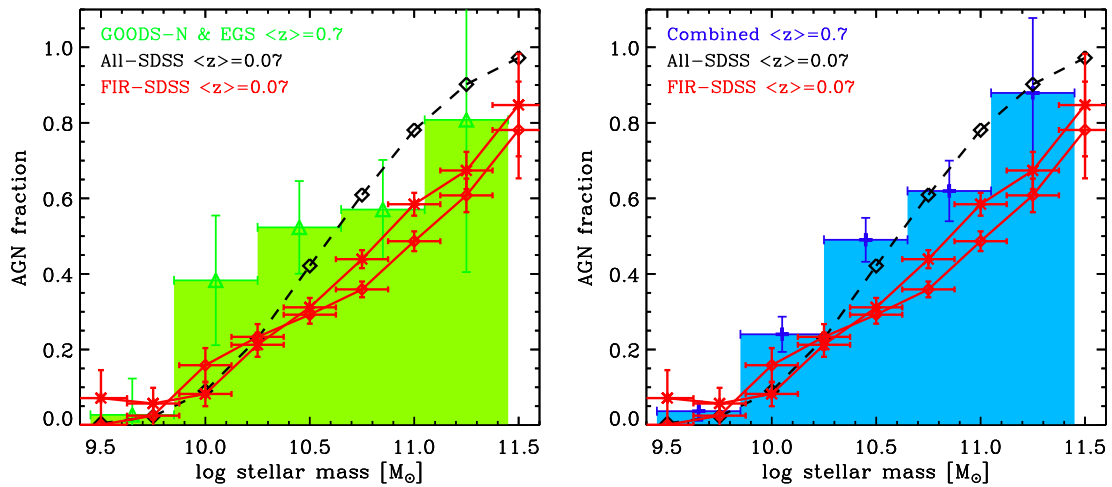


Figure 4.9 AGN fraction as a function of stellar mass for the FIDEL sample (left) and combined sample (right) of intermediate-redshift FIR-selected galaxies. Both panels show an increased AGN fraction at higher stellar masses, with a sharper increase relative to that with L_{IR} . The intermediate-redshift trends (histograms) on both panels are more consistent with that of the full emission-line SDSS sample (open diamonds with dashed line) than for the FIR-selected SDSS subsample (red asterisks and diamonds with solid lines), although the difference between the latter are modest ($\sim \sigma$). Error bars are Poissonian.

luminosity ratio (< 2 while the average is ≈ 40 for nearby unobscured (type 1) AGN, Heckman et al., 2005). The remainder may contain moderately absorbed AGN as we do not take into account the absorbing column density from X-rays, which is highly uncertain due to low number of counts in some galaxies. The second category corresponds to AGN that are not identified in X-rays (except for the two cases mentioned above), but which are either identified with one of the IRAC methods or which have $L_{[\text{O III}] \lambda 5007} > 10^7 L_{\odot}$. The third category refers to the remaining AGN, which are not identified in the X-rays and which have a faint (or unavailable) $[\text{O III}] \lambda 5007$ luminosity. We refer to these three categories as: X-ray, absorbed, and weak AGN.

When we infer the intrinsic AGN luminosity based on $L_{[\text{O III}]}$, which traces the emission from the narrow-line regions, we find that the absorbed class of AGN spans a very similar range ($10^{6.6-8.4} L_{\odot}$, with median $10^{7.4} L_{\odot}$) as the X-ray selected sample of AGN ($10^{6.5-8.7} L_{\odot}$, with median $10^{7.7} L_{\odot}$). We consider the AGN with $L_{[\text{O III}]} < 10^{6.5-7} L_{\odot}$ to be intrinsically weak. For reference, assuming the average ratio for unabsorbed AGN reported in Heckman et al. (2005), $L_X > 10^{42} \text{ erg s}^{-1}$ corresponds to $L_{[\text{O III}]} > 10^{40.4} \text{ erg s}^{-1} = 10^{6.8} L_{\odot}$. Some of the weak AGN may represent a distinct AGN regime with possibly radiatively inefficient accretion Trump et al. (2011) rather than a simple extension of the same accretion process down to lower luminosity.

We plot the global AGN fraction in Figure 4.10, and divide the AGN content into the three categories described above with an additional grouping for AGN with lower S/N in their emission lines fluxes that were identified as AGN by Yan et al. (2011, gray shaded portion of the histograms). While the global AGN fraction increases with stellar mass and with L_{IR} , the AGN fractions are systematically lower than those found for the emission-line subsample presented in Sec-

tion 4.4.1.2 (cyan triangles, which represent the histogram for the FIDEL sample shown in Figures 4.8 and 4.9). This may be due to a combination of a truly lower AGN fraction (see Section 4.4.2) and AGN incompleteness because emission line diagnostics are in general more sensitive to the presence of AGN excitation than the X-ray or mid-IR color methods used in work.

For the sample considered here, the stellar mass distributions of the weak and absorbed AGN samples are similar to one another while the mass distribution of X-ray AGN is skewed toward higher stellar masses. This suggests that X-ray selected AGN will tend to be more easily identified in more massive hosts. Indeed a recent study by Mullaney et al. (2011b) found that X-ray selected AGN always lie in high stellar mass hosts ($\langle M_\star \rangle = 10^{10.7-10.8} M_\odot$), across a broad range of redshift (up to $z \sim 3$). This may be due to the presence of more massive black holes in these systems although the authors only found a weak correlation between stellar mass and X-ray luminosity over the $10^{42} - 10^{44} \text{ erg s}^{-1}$ range ($M_\star \propto L_X^{(1/7)}$).

4.4.3 Effect of AGN on Mid-to-Far Infrared Color

Potential AGN contribution to dust heating is expected to peak at shorter wavelengths ($\sim 10 - 20 \mu\text{m}$) compared to dust heated by star formation processes, and hence produce an enhanced mid- to far-IR ratio. The average AGN SED template of Elvis et al. (1994) suggests this feature (see also Mullaney et al., 2011a, for the intrinsic AGN IR SED of more moderate luminosity AGN). Using IRAS 25-to-60 μm color, Veilleux et al. (2002) found that the spectra of nearby ULIRGs with warmer color ($f_{25}/f_{60} > 0.2$) are quasar-like whereas the spectral features of cooler ULIRGs are similar to LINER or purely star-forming galaxies. Similarly, we observe that the galaxies with the highest S_{24}/S_{70} values were selected as X-ray AGN (Figure 4.2), MEx-AGN (Figure 4.3) and mostly also as IRAC AGN

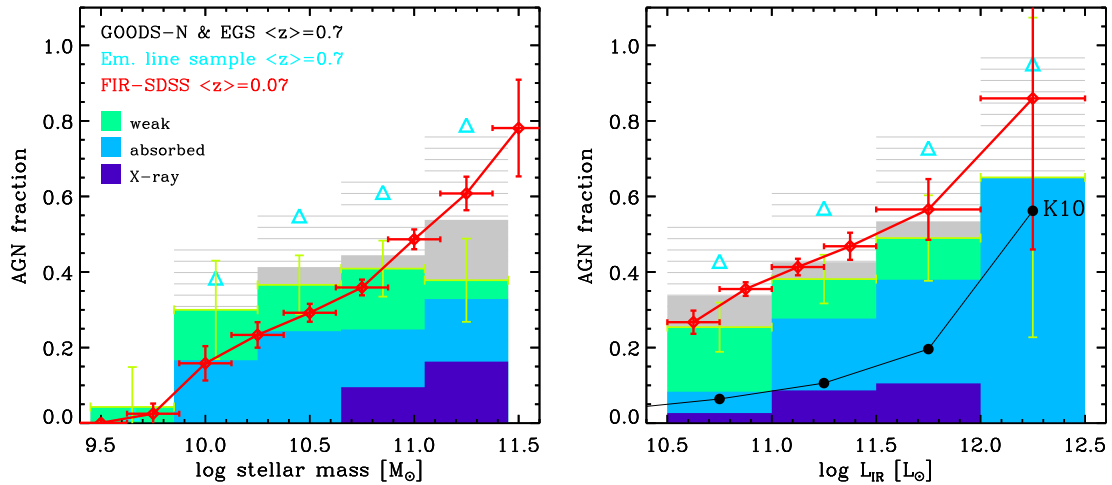


Figure 4.10 AGN fraction of the primary FIR-selected sample ($0.3 < z < 1$) as a function of stellar mass (left) and infrared luminosity (right). The AGN population is divided between the following categories: (1) X-ray AGN, (2) absorbed (but intrinsically luminous) AGN, (3) weak AGN, and (4) low S/N identification with emission lines (grey shaded portion). The global AGN fractions rise with stellar mass and with increasing luminosity, but they are systematically lower than the emission line FIR subsamples at both low redshift (red diamonds) and intermediate redshift (cyan triangles, from Figures 4.8 and 4.9). We also show the AGN fraction found for a $70 \mu\text{m}$ selected sample in the COSMOS field (Kartaltepe et al., 2010a, labeled K10) with filled black circles. Our larger AGN fractions indicate that the AGN selection is more complete, thanks to the identification of X-ray absorbed and X-ray weak AGN. Error bars are Poissonian (and are omitted for the cyan triangles for clarity, but we refer the reader to the error bars on the original figures in this case: Figs 4.8 and 4.9).

(Figure 4.4). The expectations appear to hold well for these few extreme systems. Is there also a trend for the more normal, less extreme AGN?

We present another diagnostic by combining the $[\text{O III}] \lambda 5007/\text{H}\beta$ and S_{24}/S_{70} ratios (Figure 4.11). There are 202 galaxies in our sample with all required measurements, including galaxies with an upper limit for either $[\text{O III}] \lambda 5007$ or $\text{H}\beta$ (but not both). The bulk of the sample tends to occupy the bottom left part of the plot with several outliers toward the upper right, which are the more extreme and easily identified AGN (according to at least one of (typically both) the X-ray and the MEx classification schemes). We define an empirical curve to divide the region dominated by X-ray AGN from the rest of the sample:

$$\log([\text{O III}]/\text{H}\beta) = \frac{0.6}{\log(S_{24}/S_{70}) + 0.28} + 1.2 \quad (4.3)$$

We further add a dividing line at fixed $[\text{O III}]/\text{H}\beta$ ratio ($\log([\text{O III}]/\text{H}\beta) = -0.15$) to separate the optically selected AGN (green to red colored symbols) from the star-forming galaxies (purple to blue colored symbols). Given the range of $[\text{O III}]/\text{H}\beta$ values and the fact that the galaxies between the lines are not detected in hard X-rays, we posit that they are mostly composite SF/AGN galaxies and possibly LINERs. Interestingly, the composite/LINERs and SF galaxies appear to have a very similar distribution in their 24-to-70 μm colors. These systems may have a weak AGN whose contribution to the IR SED is small, or a more luminous AGN concurrent with an elevated SFR and thus also resulting in a small relative contribution. Alternatively, the IR SED shape might have a more complicated dependence on AGN heating owing to, e.g., the geometry of the system. More generally, this result implies that factors other than the presence of AGN should be taken into account in order to explain the spread in S_{24}/S_{70} values.

This analysis is analogous to that presented in Kewley et al. (2001b), where the authors derived a mixing line going from low values of IRAS 25/60 μm flux ratio

and $[\text{O III}]/\text{H}\beta$ ratio toward higher values as the AGN fraction increases. Furthermore, they find AGN fractions of 73% and 77% in galaxies with $\log(S_{25}/S_{60}) > -0.6$ and -0.5 , respectively. Although probing slightly different rest-frame wavelengths, our results are also consistent with the same general picture, as all galaxies with $S_{24}/S_{70} > -0.6$ satisfy our AGN selection criteria. The results of increasing incidence of AGN in systems with warmer mid-to-far infrared colors from Kewley et al. (2001b) and Veilleux et al. (2002) were derived for nearby galaxies. With Figure 4.11, we now provide a higher-redshift analog.

There are two galaxies with an ambiguous X-ray classifications above our empirical strong AGN curve (star symbols). These two X-ray ambiguous sources are optically-identified as AGN with the MEx diagram. A closer look at their optical spectra confirms that they host significant AGN activity. One of them is within GOODS-N and its optical spectrum shows a clear $[\text{Ne V}] \lambda 3425$ emission line (13σ detection) as well as an elevated $[\text{Ne III}] \lambda 3869/[\text{O III}] \lambda 3727$ line flux ratio ($= 0.50 \pm 0.02$), both signs of a very high-ionization powering source (see Figure 8 in J11). The other X-ray ambiguous source lies within the EGS field, and has $[\text{O III}]/\text{H}\beta$ and $[\text{N II}]/\text{H}\alpha$ line ratios that place it clearly in the AGN-dominated region of the BPT diagram (i.e., above the Kewley et al. (2001a) dividing line). Intriguingly, they both lack a detection in the hard X-ray band of Chandra (2-8 keV) and both have a low X-ray luminosity ($\leq 1.5 \times 10^{41} \text{ erg s}^{-1}$). These systems are among the Compton-thick AGN candidates studied in J11. We discuss heavily absorbed AGN further in Section 4.5.1.

The overall trend between the presence of AGN and the mid-to-far-IR color S_{24}/S_{70} is shown in Figure 4.12, where the AGN fractions are calculated using the same methodology as in Section 4.4.2. We find an increasing AGN fraction with warmer S_{24}/S_{70} values, with the extreme range on the warm color side driven

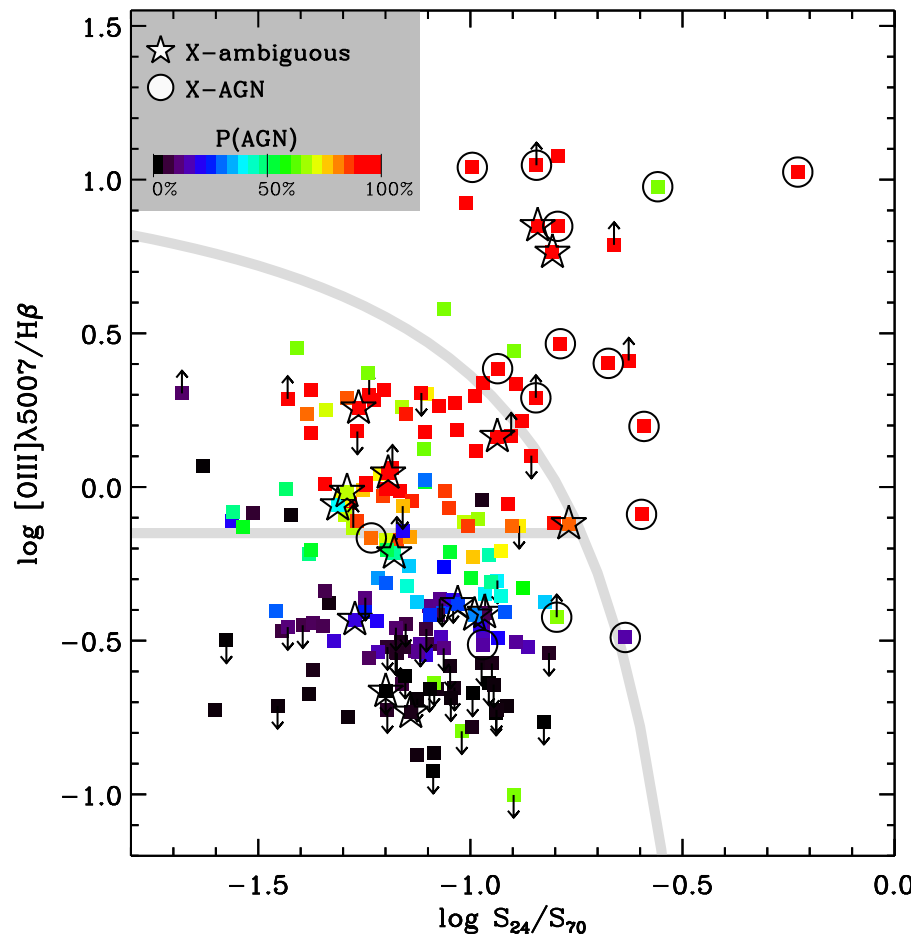


Figure 4.11 Combined optical/IR diagram showing the $[O\ III] \lambda 5007 / H\beta$ emission-line flux ratio as a function of a mid- to far-IR color (24-to-70 μm). The 70 μm galaxy sample was classified based on the MEx diagram (color keyed to P(AGN) as shown on color bar) as well as from their X-ray properties (star symbols for X-ray starbursts/ambiguous systems, and black circles for X-ray AGN). The lines represent an empirical division between the most extreme AGN (top right), the more common AGN (middle) and star-forming galaxies (bottom left).

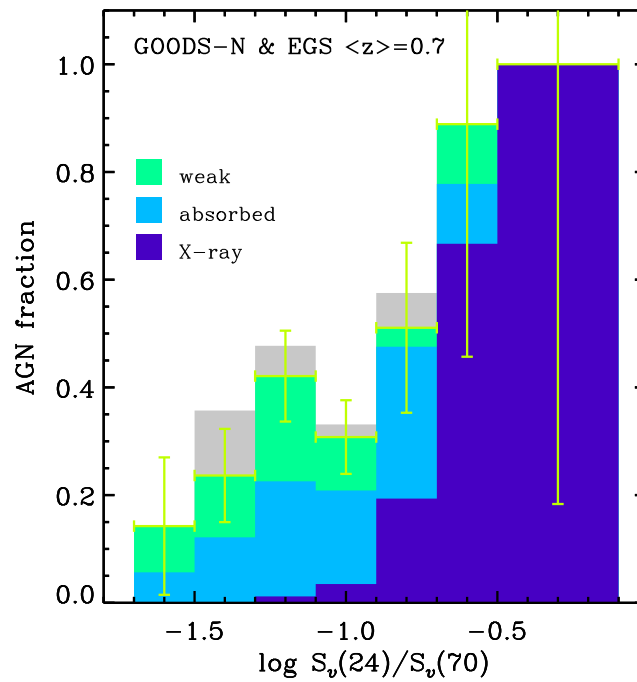


Figure 4.12 AGN fraction as a function of mid- to far-IR color (24-to-70 μ m). The FIDEL 70 μ m galaxy sample was classified as AGN based on all of the AGN diagnostics used in this paper: X-rays, MEx diagram, and IRAC colors. The split into AGN sub-categories is described in Section 4.4.2 and is identical to Figure 4.10.

by X-ray detected AGN. Removing these objects lessens the linear Pearson coefficient from 0.94 to 0.32.

4.4.4 Star Formation Rates and AGN Luminosities

In this section, we compare the energy contributed by star formation and by AGN emission. If we assumed that [O III] $\lambda 5007$ emission comes mostly from gas excited by AGN and not by star formation, whereas $H\beta$ emission traces more closely star formation, we should find that they do not behave the same way as a function of infrared luminosity unless SFRs and SMBH accretion rates correlate. For luminous infrared galaxies, L_{IR} is generally believed to trace the SFR (from the bolometer approximation, see Kennicutt, 1998, for a review). While AGN heated dust emission also contributes to the total L_{IR} , it rarely dominates in the luminosity regime that we are probing here. Furthermore, by selecting at FIR wavelengths, the light is less subject to AGN contamination than MIR wavelengths, where the AGN-heated dust SED peaks. Among others, (Nardini et al., 2008) report that the AGN contribution may dominate in the mid-IR range while remaining a small fraction of the total infrared light, typically less than 25%.

Figure 4.13 shows L_{IR} versus $L_{[O\ III]\ \lambda 5007}$ and versus $L_{H\beta}$. It appears that L_{IR} and $L_{H\beta}$ trace one another pretty well probably resulting from both quantities linearly tracing the SFR¹³, as expected. On the other hand, the AGN seem offset from the SF galaxies in the sense of having a larger $L_{[O\ III]}$ at a given L_{IR} . L_{IR} and $L_{[O\ III]}$ do not follow linear correlations (diagonal lines on Figure 4.13) which is in agreement with published results that the AGN luminosity is largely independent of the host galaxy's SFR in moderate luminosity systems (e.g., Mullaney et al., 2011b). Instead, many of the high-P(AGN) points are displaced toward

¹³With the caveat that $H\beta$ has not been corrected for dust extinction given the large uncertainty in doing so.

larger $L_{[\text{O III}]}$, suggesting excess emission from AGN but also departing from a linear correlation. In fact, a lot of these high-P(AGN) objects are beyond the strong AGN cut $L_{[\text{O III}]} > 10^7 L_{\odot}$ adopted by, e.g., Kauffmann et al. (2003). Here, strong AGN correspond to what we have been calling moderate-luminosity systems, and would have $L_{2-10 \text{ keV}} > 10^{42} \text{ erg s}^{-1}$ if unabsorbed in the X-rays.

Thus, we find that the trends observed are consistent with $L_{[\text{O III}]}$ tracing primarily AGN emission when present, whereas $\text{H}\beta$ shows a better correspondence with L_{IR} and presumably with the SFR. Based on this interpretation, we do not find that SMBH accretion rates correlate with SFRs of the host galaxies.

4.5 Discussion

In this section, we discuss the identification of X-ray absorbed AGN and their ubiquity in FIR-selected galaxies (Section 4.5.1). Then, we list physical interpretations of the high AGN fractions (both absorbed and unabsorbed) in Section 4.5.2 before discussing the main caveats in Section 4.5.3.

4.5.1 X-ray Absorbed AGN

As we showed in Section 4.4.2, X-ray absorbed AGN more common in FIR-selected galaxies (18%) than X-ray unabsorbed systems (7%). In this section, we further examine the X-ray absorption in the FIR-selected sample in comparison with fainter infrared galaxies, and on an individual galaxy basis. The $24\mu\text{m}$ comparison sample is drawn from FIDEL in the GOODS-N and EGS fields, with a much lower ($\sim 10\times$) L_{IR} sensitivity limit than the $70\mu\text{m}$ sample (Figure 4.1).

First, we compare the distributions of the Compton-thickness parameter ($\equiv \log(L_{2-10\text{keV}}/L_{[\text{O III}]})$) between the FIR-selected sample, the MIR-selected ($24\mu\text{m}$) sample and the parent spectroscopic sample (top panel of Figure 4.14). The FIR-selected sample tend to host more absorbed AGN compared to both comparison

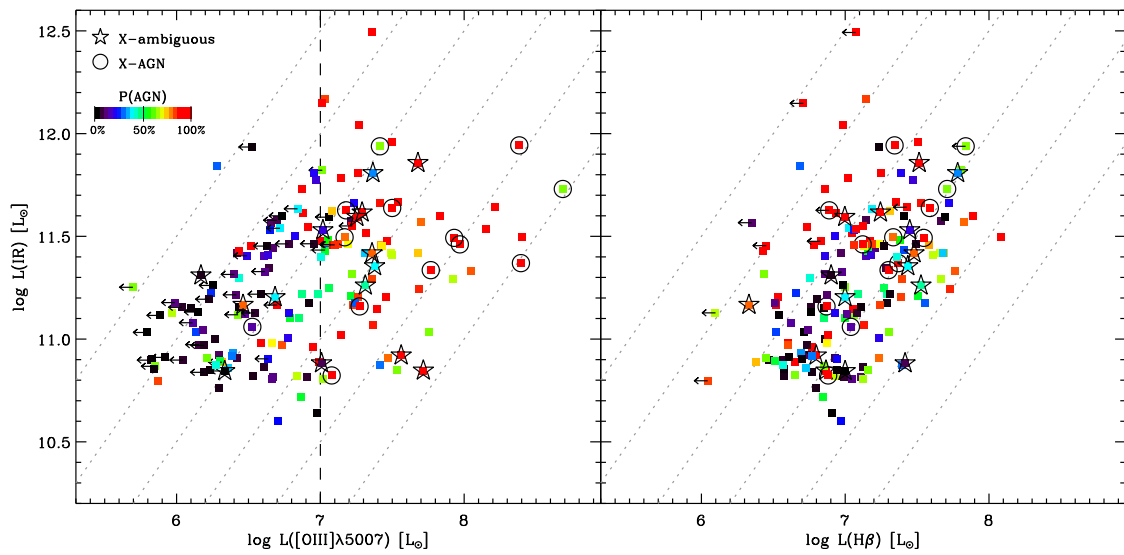


Figure 4.13 Total infrared luminosity versus $[\text{O III}] \lambda 5007$ luminosity (left) and $\text{H}\beta$ luminosity (right). The plotting symbols are colored according to the probability of hosting an AGN from the MEx diagram (see color bar on the left-hand panel). X-ray AGN are further marked with open circles. The diagonal lines correspond to a linear relations between the IR and emission line luminosities with various normalizations. The vertical dashed line on the left panel indicates the threshold used in the literature for strong AGN (e.g., Kauffmann et al., 2003).

samples, with a more striking difference in distribution with the parent spectroscopic sample (effectively X-ray and [O III]-selected as both quantities need to be detected in order to be included in the histogram). The distributions of the FIR (light gray) and the remainder of the spectroscopic (black line) samples have a probability of 0.6% of being drawn from the same parent population according to a KS test, whereas that probability is 7.4% between the FIR- and MIR-selected samples (when excluding the $70\mu\text{m}$ detections from the $24\mu\text{m}$ sample). The distribution of the latter is intermediate between the IR-faint (undetected at $24\mu\text{m}$) and IR-luminous (detected at $70\mu\text{m}$) samples. Clearly, the majority of the most absorbed systems (with Compton-thickness < 0.3) tend to be infrared-luminous given their high detection rate at $70\mu\text{m}$.

The bottom panel displays the individual values of infrared luminosities and Compton-thickness parameters. In this case, we also show upper or lower limits on $\log(L_{2-10\text{keV}}/L_{[\text{O III}]})$ when the hard X-ray or the [O III] $\lambda 5007$ luminosity is an upper limit, respectively. However, we restrict the sample to galaxies $70\mu\text{m}$ and/or $24\mu\text{m}$ detections in order to compute L_{IR} . Again, there is a trend for the most absorbed AGN to be more infrared luminous, but there is not a strict anti-correlation between the two quantities (the linear Pearson correlation coefficient $r = -0.2$ excluding points that are upper or lower limits).

FIR-selected galaxies, which undergo significant levels of star formation (by selection), are more likely to host heavily absorbed AGN than their less IR-luminous counterparts. It seems unlikely for this effect to be caused by geometry or alignment with respect to the line of sight because far-IR emission is mostly isotropic (only absorbed in extreme conditions) and thus should not depend on the orientation of the host galaxy. However, FIR-selected galaxies are more likely to be disks (or irregular/interacting galaxies) than spheroids, and may have a more

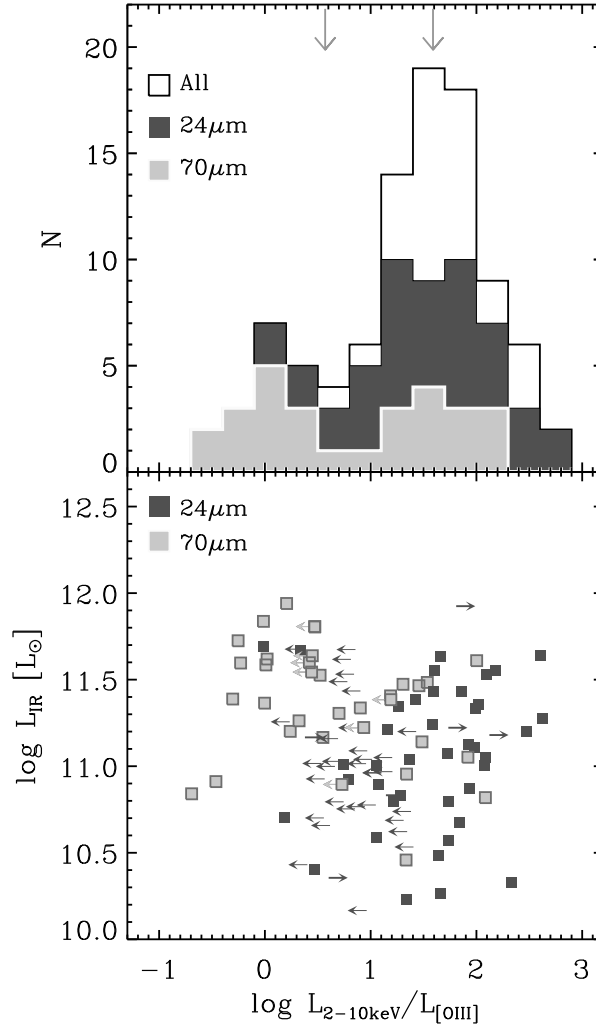


Figure 4.14 [Top] Distribution of the Compton-thickness parameter $T \equiv L_{2-10\text{keV}}/L_{[\text{O III}] \lambda 5007}$ for X-ray and [O III]-selected sample (black line). The corresponding distributions for the subsamples of galaxies detected at 24 μm and at 70 μm are overplotted in dark and light gray, respectively. The most absorbed systems (with lower values of T) are preferentially detected at 70 μm . This subsample displays a much broader distribution of thickness parameter and a larger relative number of absorbed AGN compared to both the 24 μm and the parent X-ray and [O III]-selected sample.

Figure 4.14 [Bottom] Compton-thickness parameter $T \equiv L_{2-10\text{keV}}/L_{[\text{O III}] \lambda 5007}$ versus total infrared luminosity derived from $24 \mu\text{m}$ (dark squares) and, when available, $70 \mu\text{m}$ fluxes (light gray squares) using the CE01 templates. Upper and lower limits on the Compton-thickness parameter respectively correspond to upper limits on X-ray and $[\text{O III}] \lambda 5007$ luminosities. Galaxies that are not detected at $24 \mu\text{m}$ are omitted from this panel.

significant column density when seen edge-on compared to lower L_{IR} galaxies. As a result, random orientation may be more likely to cause large AGN absorption from the IR-luminous host galaxies than from the average X-ray AGN host galaxies, which are less IR-luminous. Another possibility is for the small-scale obscuring material (e.g., the torus invoked in AGN unified models) to be more plentiful in FIR-bright galaxies. We cannot distinguish between these possibilities with the current observations, but it is also plausible that the gas reservoir available to sustain the elevated SFR also acts as an important absorber for the central AGN. We consider a few physical scenarios below (Section 4.5.2).

4.5.2 Physical Origin of High AGN Fractions

Next, we interpret the higher AGN fraction (37%) that we find in this study relative to results from the literature. Combining multiwavelength diagnostics from X-ray to radio, Kartaltepe et al. (2010a) found that the AGN fraction rises steeply with IR luminosity and/or redshift (see the filled black circles on the right panel of Figure 4.10), but their values are lower than ours with an overall fraction $\sim 10 - 20\%$ over the redshift and luminosity ranges of interest in this paper. Similarly, Symeonidis et al. (2010) studied the occurrence of AGN in $70\mu\text{m}$ galaxies over a similar redshift range and found an AGN fraction around $\sim 13\%$. The main difference between these previous investigations and the current work is

the use of the MEx diagnostic diagram, which unveils the majority of the AGN including absorbed and weak systems. We note that some absorbed AGN were successfully selected by previous authors with, e.g., mid-IR color diagnostics, but that the latter are not as complete nor as sensitive to the presence of AGN as the MEx method.

What are the physical causes of such a frequent occurrence of AGN? Is there a connection between the AGN and the elevated SFR in their host galaxies? or between the AGN absorption and their host galaxies? The results from this work imply that active SMBH growth occurs in parallel with active star formation. The elevated SFRs are probed by the FIR emission and there is a connection between the infrared luminosity and both the occurrence and absorption of AGN. One interpretation that fits all of these observational trends is the major merger scenario (e.g., Sanders et al., 1988). Major mergers of gas-rich galaxies are expected to fuel both starbursts and AGN, with the AGN originally deeply buried in large amounts of gas before emerging as X-ray detected AGN. Qualitatively, this scenario can be supported by our observations, which would be in contrast with recent studies of moderate luminosity X-ray AGN in intermediate redshift galaxies (Cisternas et al., 2011; Schawinski et al., 2011; Mullaney et al., 2011b). The latter used X-ray selected samples of AGN and so would miss a large number of the X-ray absorbed systems, which may be more closely linked to major merger signatures. Future studies of the connection between AGN and their host galaxies should include both absorbed and unabsorbed AGN to provide us with a more conclusive test.

However, we note that major galaxy mergers may not be required to explain our results. For instance, an alternative way to obtain elevated star formation, a high incidence of AGN and also a high incidence of AGN absorption could be

large-scale disk instabilities in gas-rich galaxies, as exemplified by high-redshift clumpy galaxies (Elmegreen et al., 2007). These systems are more common at higher redshift ($z \gtrsim 2$) and may be explained by simulations (Agertz et al., 2009) in the context of cold stream accretion cosmological models (e.g., Dekel et al., 2009). Clumpy galaxies persist down to intermediate redshift in more intermediate mass galaxies (Elmegreen et al., 2009). Unstable (or clumpy) disk galaxies are predicted to efficiently fuel AGN, including a high likelihood of absorption of the X-rays from the central engine (Bournaud et al., 2011).

While we cannot distinguish between major galaxy mergers and large-scale violent disk instabilities without additional observations, it is clear that a complete picture of the growth of galaxies and their central SMBHs must include a gas-rich phase with concurrent SF and AGN, where the central AGN is often absorbed even for moderate-luminosity AGN (i.e., below the quasar regime). This connection furthermore suggests that either the host galaxy's ISM absorbs X-ray emission from the AGN (i.e., galaxy-scale obscuration instead of – or in addition to – small-scale torus-like absorption) or the properties of the obscuring torus are dictated by galaxy scale properties. Recent observations suggest some (at least small degree) alignment of AGN and their host galaxies (Lagos et al., 2011), and a correlation between AGN X-ray absorption and ~ 100 pc scale starburst in nearby Seyferts (Diamond-Stanic & Rieke, 2011). Both of these possibilities are interesting as they differ from the typical AGN unified models where the very central region is assumed to be somewhat decoupled from its large-scale surroundings.

Lastly, while the AGN *fraction* of the intermediate-redshift FIR-selected sample is similar to that in nearby FIR-selected galaxies, we note that the *number* of IR-luminous galaxies is much larger at higher redshift. A greater availability of gas at earlier epochs may be responsible for the more common occurrence of

highly star-forming (thus IR-bright) galaxies. The high fraction of AGN, even if consistent with that at low-redshift, means that a much larger population of AGN – and especially X-ray absorbed AGN – in IR-luminous hosts exists at higher redshift. We may be starting to uncover the missing AGN population that has been inferred from cosmic X-ray background studies (Comastri et al., 1995; Mushotzky et al., 2000; Alexander et al., 2003; Bauer et al., 2004).

4.5.3 Caveats

In this section we discuss the three main caveats of this analysis even though none of them is expected to significantly alter our results. The first caveat is that total infrared luminosities, which we interpret loosely as measures of SFRs, contain mixed contributions from dust heated by both stars and AGN. While longer wavelengths ($> 70\mu\text{m}$) are less subject to AGN contamination than, say, $24\mu\text{m}$, it may not be completely immune to AGN emission. The rest-frame wavelengths probed by MIPS70 are $54 - 35\mu\text{m}$ at redshift $0.3 < z < 1$ (with most galaxies at $z < 0.8$ corresponding to $\lambda_{rest} > 39\mu\text{m}$). Recent *Herschel* studies have shown that the FIR colors of galaxies with an AGN do not differ from those of purely star-forming galaxies (Hatziminaoglou et al., 2010; Elbaz et al., 2010), indicating that on average AGN contamination does not dominate at $\lambda(\text{observed}) > 70\mu\text{m}$. The lower the redshift, the more robust the SFR estimate.

The possible flux boosting at $24\mu\text{m}$ from AGN contamination would lead to an overestimate of L_{IR} . Some objects in the $24\mu\text{m}$ comparison sample used in Figure 4.14 may be subject to this effect. If the actual L_{IR} values were lower, it would move these galaxies (which host, on average, less absorbed AGN than the $70\mu\text{m}$ sample) toward lower infrared luminosities. This would either strengthen our conclusion that more absorbed AGN tend to reside in more infrared-luminous galaxies or not affect the result significantly depending on the magnitude of this

possible offset.

The second caveat concerns the overall completeness of the AGN selection methods used in this work. As mentioned in Section 4.4.2, some objects have an unknown classification because of the low S/N of their emission lines. As a consequence, the AGN fraction that we derive for the overall FIR-selected sample (i.e., with and without emission line measurements) may be underestimated as we consider these systems are purely star-forming by default. Taken into account that some of the unknown class are AGN would strengthen our conclusion that AGN are ubiquitous among FIR-selected galaxies given that we already find a large AGN fraction. We computed a maximum AGN fraction assuming that all of the unknown class galaxies host an AGN, also providing us with an upper limit to AGN incompleteness. The AGN fraction would rise from 37% to 62%, but this scenario is unlikely given that the unknown galaxies do not fulfill the emission line criteria and that emission-line galaxies were shown to have a higher incidence of AGN than their non emission-line counterparts (e.g. Yan et al., 2006). We test this trend with our own sample by comparing the X-ray and IRAC AGN fractions for the global FIR sample and the emission-line FIR sample. These methods suggest a $1.5\times$ higher AGN fraction in emission-line galaxies. There are $11\pm 3\%$ (15/136) X-AGN and IRAC-AGN in the emission-line subsample, but only $7\pm 3\%$ (8/111) in the non emission-line sample, resulting in a global fraction of 9% (23/247) when considering all FIR-selected galaxies regardless of the detection of emission lines.

The third caveat concerns the use of [O III] $\lambda 5007$ as an indicator of intrinsic AGN luminosity. On the one hand, [O III] emission could include a contribution from star formation yielding to an overestimate of the total AGN power. However, this is only a concern for low-metallicity galaxies, which also have a

low stellar mass (Tremonti et al., 2004). Given that all the FIR-selected galaxies are fairly massive, they most likely have a very small contribution from star formation. Indeed, Kauffmann et al. (2003) found that the [O III] $\lambda 5007$ line is the least contaminated of the strong emission lines found in optical spectra, with a flux fraction of 7% from star formation (and the remaining 93% from AGN induced emission) in high-metallicity (thus high stellar mass) galaxies. As an extra precaution, we restricted the AGN absorption analysis to galaxies that have $\log(M_\star > 10^{10} M_\odot)$ and $P(\text{AGN}) > 30\%$ ¹⁴ in Section 4.5.1.

On the other hand, [O III] $\lambda 5007$ emission may be affected by dust obscuration. Even though we use [O III] $\lambda 5007$ as a more isotropic tracer than 2–10 keV, it is not in fact perfectly isotropic (e.g. Diamond-Stanic et al., 2009). Dust obscuration would have the opposite effect, and would yield to an underestimate of the intrinsic AGN luminosity when not applying a correction for extinction. We conservatively choose not to correct for dust obscuration, which means that the X-ray absorption may be underestimated and similarly, the number of absorbed AGN may be a lower limit. Given that we already find a high incidence of absorbed AGN among FIR-selected galaxies, our result would only be strengthened if we indeed underestimated the number of absorbed AGN.

4.6 Summary

In this paper, we investigate the incidence of AGN among FIR-selected galaxies at intermediate redshift ($0.3 < z < 1$). More specifically, we quantify the AGN fraction and characterize the nature of the AGN phase (X-ray bright, X-ray absorbed, weak accretion) as a function of host galaxy properties. AGN are identified based on four diagnostics: MEx diagram (Juneau et al., 2011), X-ray criteria, IRAC color-

¹⁴The $P(\text{AGN})$ criterion is waived if the source is selected as an X-ray AGN.

color (Stern et al., 2005) or IRAC [3.6]-[8.0] color versus redshift. The last two are similar but not identical. Our main findings are:

1. The fraction of FIR-selected galaxies hosting AGN increases as a function of stellar mass and as a function of L_{IR} . For the FIR subsample with emission line detections (both $H\beta$ and [O III]), the AGN fractions are very similar to that in nearby ($0.05 < z < 0.1$) FIR-selected galaxies but opposite to the bulk to the SDSS emission-line galaxies at high SFRs (probed by L_{IR} at intermediate redshift).
2. Combining all AGN diagnostics, the global AGN fraction is 37% in the $70\mu\text{m}$ selected galaxy population, a factor of > 2 greater than previous results in similar infrared luminosity and redshift ranges.
3. The differences between the higher fraction presented here and in previous studies may be accounted for by (i) heavily absorbed AGN, and (ii) intrinsically weaker AGN that are difficult to detect – but which we select thanks to the increased sensitivity of the MEx diagnostic.
4. The systems with the most X-ray absorption are Compton-thick AGN candidates. They tend to reside in IR-luminous galaxies, suggesting a potential connection between the host galaxy's gas content and absorption of the central engine. The latter can be achieved either through absorption of the AGN X-rays by the host galaxy's ISM or by a physical link between the host galaxy's gas content and the obscuring torus properties.
5. AGN radiation is likely responsible for the highest 24-to-70 μm flux ratios in the most extreme cases, which tend to be X-ray detected AGN. However, other parameters are required to explain the spread of that mid-to-far IR

color among star-forming galaxies and galaxies with a weak or absorbed AGN.

CHAPTER 5

CONCLUSIONS

Overall, this thesis addresses the physical connection between supermassive black holes and their host galaxies at redshift < 1 . The main goals are to (1) provide a new AGN diagnostic that yields a more complete census of AGN; (2) use the new diagnostic along with complementary methods to calculate a more realistic AGN fraction in infrared-luminous galaxies; (3) relate AGN X-ray absorption with host galaxy properties; (4) understand the underlying physical processes driving the growth of both the stellar content and the supermassive black holes in galaxies. The main findings are summarized separately for each Chapter below.

5.1 Enhanced molecular gas density in nearby (U)LIRGs

It was suggested that an AGN may play a role by changing the chemistry of its surroundings, and enhancing HCN abundance and thus the HCN(1-0) luminosity for a given amount of dense gas. If true, this implies that the use of HCN(1-0) as a probe of dense gas is no longer valid in galaxies hosting an AGN. We present radiative transfer calculations (Naranayan et al., 2008) which reproduce a larger HCN (1-0)/CO(1-0) intensity ratio for galaxies with a higher IR-luminosity without chemistry effects (the AGN is artificially switched off in the simulations). Although we do not rule out the occurrence of chemistry effects, we present evidence that it is possible to obtain considerably higher HCN/CO intensity ratios in very gas-rich mergers. Our favored interpretation is that AGN will occur in an environment where the dense gas fraction is already higher. In other words, it is possible that the AGN is the result rather than the cause of a higher dense-to-total gas fraction observed in nearby ULIRGs.

5.2 New AGN diagnostic: Toward a more complete AGN census

The MEx diagnostic diagram allows us to identify the presence of AGN using optical spectra out to $z \sim 1$. This extends the availability of AGN sensitive BPT diagrams to higher redshift. The traditional versions of the BPT diagrams include $H\alpha$ and other fairly red emission lines, which shift beyond the optical band at $z > 0.4$. The MEx diagram relies on shorter wavelength lines ($H\beta$ and $[O\ III] \lambda 5007$) and stellar mass. It was calibrated using $\sim 110,000$ SDSS galaxies and can be utilized as a system of statistical weights thanks to a novel probabilistic approach to galaxy classification.

The X-ray classification is mostly in agreement that of the MEx diagram. Furthermore, we find evidence for X-ray obscured (possibly Compton-thick) AGN, which have an obvious signature in their optical spectra but not in the X-rays.

X-ray image stacking was used for galaxies that are not individually detected in the X-ray. Galaxies were binned according to the MEx diagnostic diagram described above. We found signatures of X-ray absorbed AGN in galaxies that were not detected individually but that were correctly identified as AGN according to the MEx diagram. A more targeted investigation of X-ray absorption (based on $L_X/L_{[O\ III]}$) suggests the presence of Compton-thick AGN at redshift 0.6-0.7, a range where they are predicted to be in large number from cosmic X-ray background studies (despite the small number of successful identifications so far).

5.3 Occurrence of AGN among intermediate-redshift FIR-selected galaxies

We selected ~ 300 galaxies at $0.3 < z < 1$ from the Far Infrared Deep Extragalactic Legacy (FIDEL) survey. These galaxies are mostly in the LIRG regime ($L_{IR} = 10^{11} - 10^{12} L_{\odot}$). A small fraction of the sample shows AGN activity according to their X-ray properties ($< 10\%$). However, using the MEx diagram in

combination with X-ray and IRAC color diagnostics reveals an AGN fraction of 37% (as high as 50% when considering only emission-line galaxies). This value is much higher than the results from previous studies of 70- μm selected samples (e.g., Symeonidis et al. 2009, Kartaltepe et al. 2010), who find an overall AGN fraction of 10 – 20%. We attribute the difference to being more complete in terms of highly-absorbed AGN and intrinsically weaker AGN.

Furthermore, we find that absorbed AGN hosts tend to be infrared-luminous, suggesting a high star formation rate. We posit two scenarios to explain this trend: (1) the host galaxy's ISM provides substantial absorption of the AGN X-rays, and/or (2) there is a physical connection between the host galaxy gas content (or gas dynamics) and the small-scale AGN obscuring medium (e.g., torus invoked in AGN unification models).

Future work is required to understand the consequences of the presence of (absorbed) AGN on the gas within galaxies, and the energy balance between these phenomena out to intermediate and high redshifts. For instance, the presence of major mergers should be investigated using quantitative and qualitative morphology measurements. While the former are more reproducible and objective, they suffer from limitations such as lack of sensitivity to low surface brightness features and to later merger stages (at or after coalescence). Thus, the visual morphology information should be supplemented with additional insight on the physical state of the system by, e.g., measuring the stellar or gas dynamics, or by measuring the starburstiness with respect to the main sequence of SFR vs. stellar mass (Elbaz et al., 2011). Galaxies undergoing a starburst phase tend to have an elevated SFR given their stellar mass (and redshift) compared to the bulk of galaxies at the same mass and redshift. They also have a more compact region of stellar heated dust emission (Rujopakarn et al., 2011; Elbaz et al., 2011).

If galaxy mergers were indeed responsible for driving the bulk of SMBH growth and if this growth predominantly occurred during X-ray absorbed phases, we would expect the X-ray absorbed (but intrinsically luminous systems) to exhibit merger signatures in their morphology and to have a high starburstiness value ($\text{SFR}/M_\star > 2 \times (\text{SFR}/M_\star)_{MS}$). Exceptions may occur if there is a sufficiently long delay between the onset of the starburst and that of the AGN. Such time delays have already been implemented in some semi-empirical models (e.g., Somerville et al., in preparation) but they are poorly constrained on the observational point of view. Thus some constraints could be placed by comparing the number of X-ray absorbed AGN, X-ray unabsorbed AGN, and weak or absent AGN in galaxy mergers identified via morphology and/or starburstiness.

Another avenue for future work would be multi-object near-infrared spectroscopy allowing us to directly measure the emission lines traditionally used on BPT diagrams. A direct comparison between intermediate- and high-redshift galaxies on the BPT and MEx diagrams would be beneficial to define a MEx prior sample directly at intermediate redshifts and thus to quantify evolutionary effects, if any. The diagnostic power of emission lines and stellar mass across cosmic time could be put in context with physical trends like the $M_\star - Z$ relation. Furthermore, such experiments could reveal the underlying cause for the observed offset on BPT diagrams between nearby ($z \sim 0.1$) and high-redshift (up to $z = 2 - 3$) galaxies, the nature of which is much debated in the literature (see Discussion in Chapter 3). As a result, we could learn whether it is a more common occurrence of AGN or changing H II region conditions that dominate the offset or whether selection effects induce an artificial trend (by only selecting more rare luminous systems at higher redshift that may not be representative of the average population).

APPENDIX A

OBSERVED HCN(3-2) SPECTRA

The Heinrich Hertz Submillimeter Telescope (HHT) HCN(3 – 2) spectra from the survey presented in Bussmann et al. (2008) are displayed in Figure A.1.

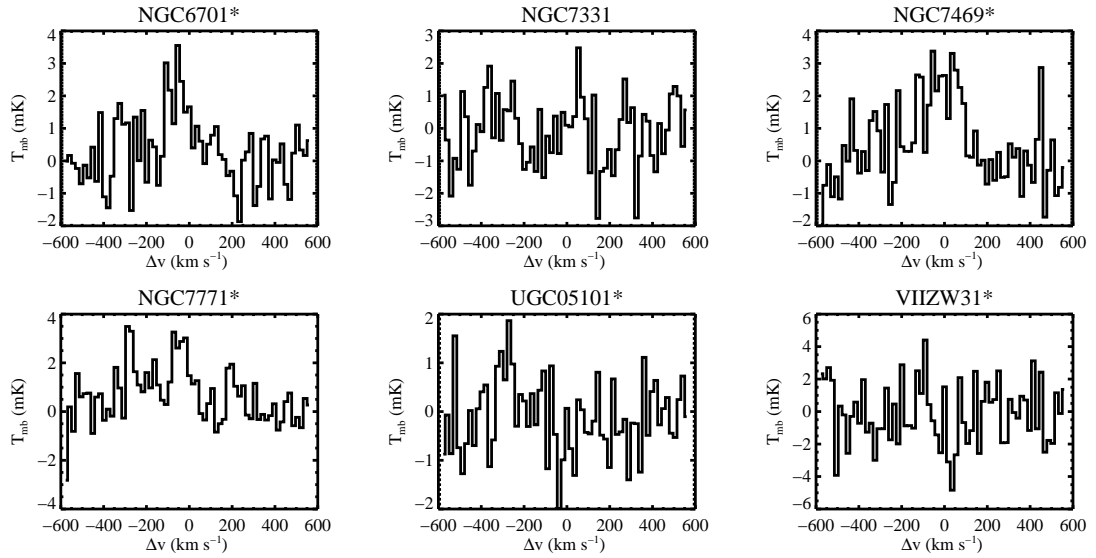


Figure A.1 HCN(3-2) spectra for all galaxies observed in B08. The 23 galaxies overlapping with this sample are marked with an asterisk. One galaxy was mapped (NGC 253, plus symbol). These observations were combined with the HCN(3-2) data presented in Graciá-Carpio et al. (2008) as described in §4.2.

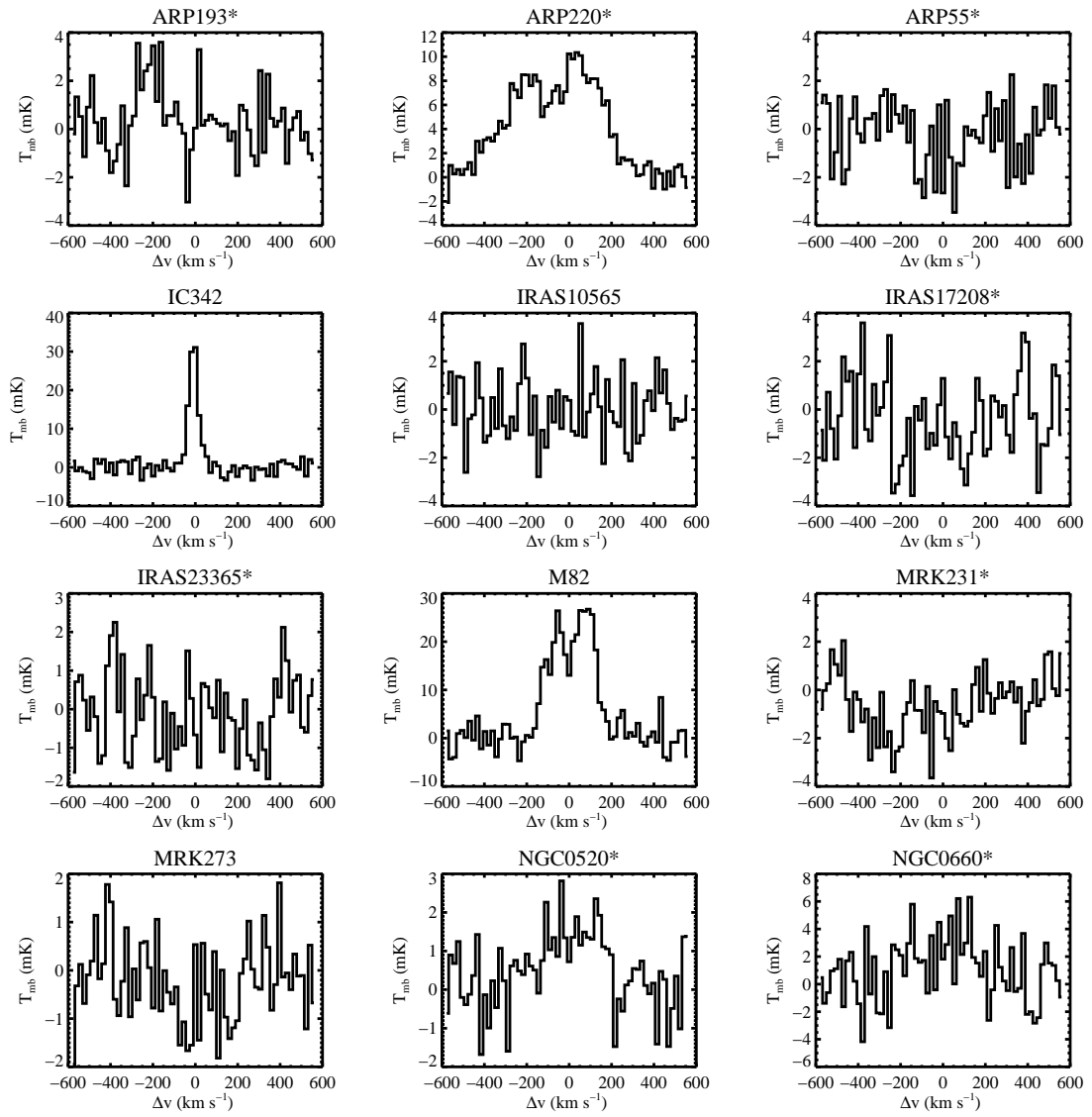


Figure A.1 Continued.

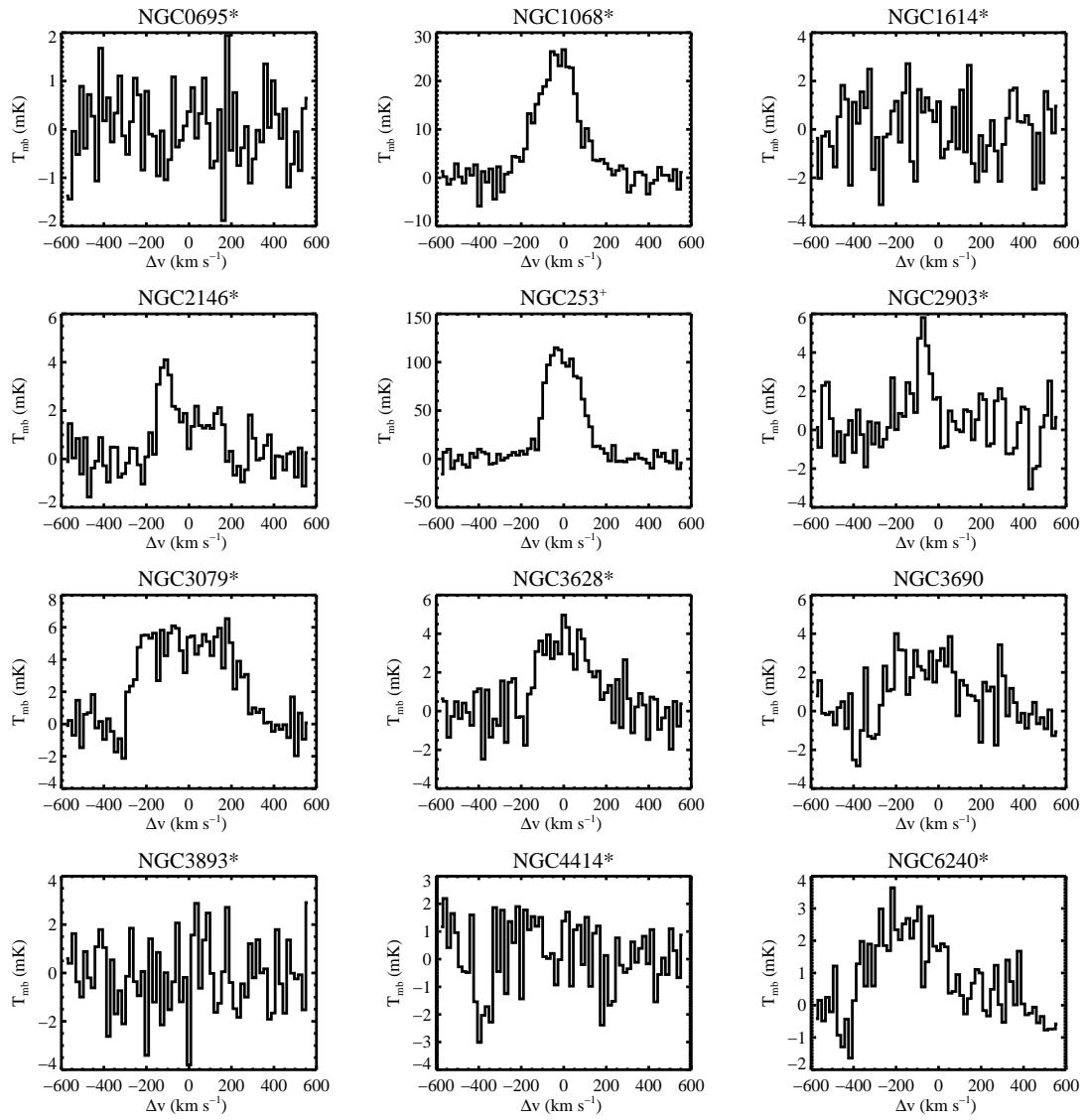


Figure A.1 Continued.

APPENDIX B

COMPARING THE MEX AND CEX DIAGRAMS

The mass-excitation (MEx) and color-excitation (CEX) diagrams are two useful alternatives when the emission lines typically used for AGN diagnostics such as the BPT diagram are not available. The former is developed in this paper (§3.3.1) and involves using stellar mass as a discriminant between predominantly star-forming galaxies and those hosting an AGN. The CEx diagram was developed by Yan et al. (submitted) and involves using rest-frame $U - B$ color rather than stellar mass. Galaxies hosting an AGN tend to be both massive and redder in $U - B$ so it is not surprising that both these approaches give similar results for many galaxies.

We compared the fraction of galaxies hosting AGN to the purely star-forming galaxies according to the BPT diagram in §3.3.3. We defined an additional line on the CEx diagram to provide a means to identify a region where star-forming galaxies are mixed with composite galaxies, analogous to our method with the MEx diagram. Here we look at the bivariate distributions of galaxies split into the four categories defined in §3.3.3. Figure B.1 shows that both diagrams are generally comparable. The main dividing lines (upper lines) make a division between the LINERs and Seyfert 2's on the upper side and the star-forming galaxies on the lower side. By design, the MEx diagram selects a larger fraction of the composites in the AGN side. This decision was motivated by our goal to provide an increased completeness of AGN candidates including intrinsically weak as well as absorbed systems that may be undergoing star formation simultaneously with an AGN phase. We have shown the strong potential to find X-ray absorbed candidates among such a population of galaxies (§§3.5.2,3.6).

On the CEx diagram, we note a few galaxies in the star-forming category that seem to be outliers with very red $U - B$ colors (also see Figure 3.5). These may be especially dusty. Their number is small relative to the bulk of the star-forming population in the SDSS sample but they may be interesting targets in a different context. For instance, we may expect more star formation and active galactic nuclei to take place in dusty, infrared-luminous galaxies at higher redshift (Le Floc'h et al., 2005; Magnelli et al., 2009).

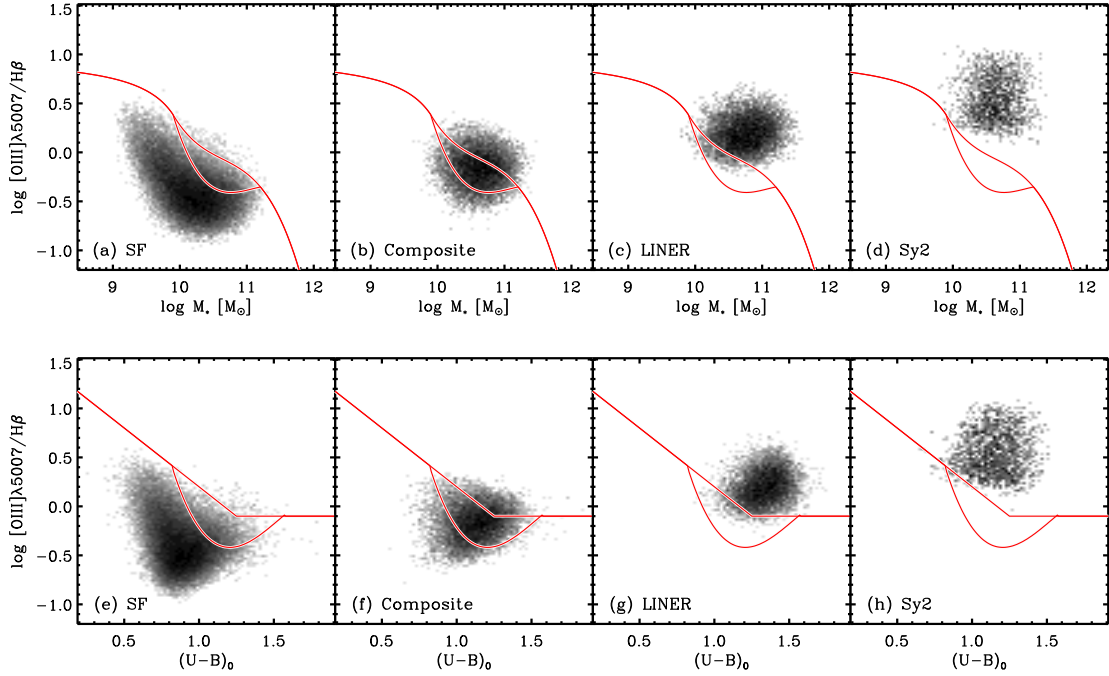


Figure B.1 Bivariate distributions of the SDSS galaxies on the MEx diagram (top row) and CEx diagram developed by Y11 (bottom row). Galaxies are plotted separately for each classification: (a) star-forming, (b) composite, (c) LINER, and (d) Seyfert 2. The same order is followed in panels (e)-(h) for the CEx diagram. The lower dividing lines were added to mark the region with significant overlap between BPT star-forming and BPT-composite galaxies (the fraction of composites is greater than 40–50% between the lines).

APPENDIX C

STELLAR MASS ESTIMATION

There are 3174 galaxies with both a stellar mass estimate from SED fitting and absolute rest-frame K -band magnitude from observed IRAC photometry. Here, we use EGS galaxies with a SED fit to the FUV, NUV, $ugriz$, and K photometry and GOODS-N galaxies with a SED fit to $UBVRIZJK$ bands (§3.4.2).

The relation between stellar masses derived from SED fitting and rest-frame K -band absolute magnitudes is displayed in Figure C.1. The broken power-law relation is expressed as:

$$\log M_{\star} = -0.398 \times M_K + 1.357; \quad \text{for } M_K > -20.5 \text{ AB} \quad (\text{C.1})$$

$$= -0.519 \times M_K - 1.128; \quad \text{for } M_K < -20.5 \text{ AB} \quad (\text{C.2})$$

Writing the relation as $M_{\star} \propto L_K^{\alpha}$, the slopes found in Eq. B1 & B2 imply power-law indices $\alpha = 0.99$ at $M_K > -20.5 \text{ AB}$ and $\alpha = 1.3$ at $M_K < -20.5 \text{ AB}$. This relation is linear at the faint end but slightly steeper at the bright end. The steepening of the slope is presumably due to the fact that more massive galaxies are redder owing to the older average age of their stellar populations, and thus have higher mass-to-light ratios.

The residuals of the broken power-law fit (bottom of Figure C.1) have a constant scatter with luminosity. The dispersion of the overall sample is 0.18 dex, around the mean (median) of 0.004 (0.009) dex.

Errors on the stellar masses calculated using Eq. B1 & B2 are estimated by combining the average error on $\log(M_{\star})$ from galaxies with SED fitting (0.12 dex) and the dispersion on the $\log(M_{\star}) - M_K$ residuals (0.18 dex). Adding these two

contributions in quadrature yields 0.22 dex, which we use for all galaxies lacking a SED fit.

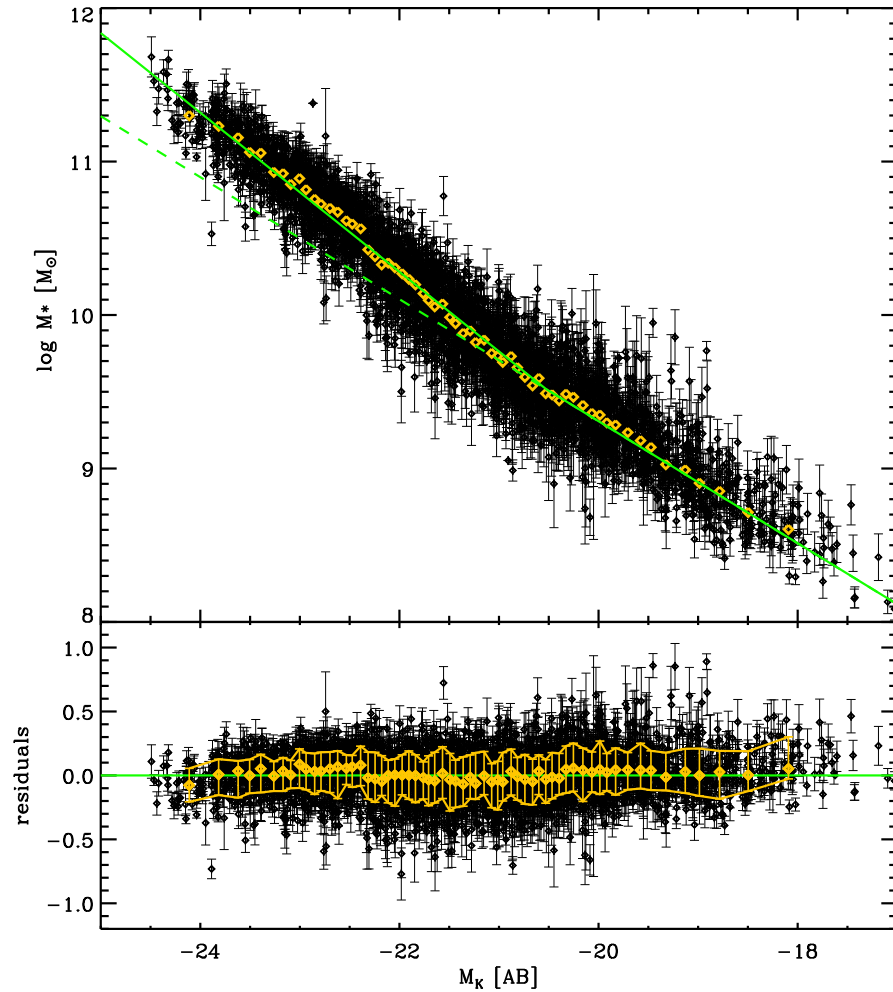


Figure C.1 [Top] Stellar mass obtained from SED fitting as a function of absolute rest-frame K -band magnitude (M_K , in AB magnitudes). We fit two mass-luminosity power laws for the bright and faint ends, which intersect at $M_K = -20.5$ AB (green lines). The dashed line is the extension of the fit at the faint end, with a linear slope between mass and luminosity. For reference, the yellow diamonds show the median $\log(M_*)$ in M_K bins (every 51 points). [Bottom] Residuals of the top panel as a function of M_K . Yellow diamonds and error bars show the median and the 16th to 84th percentile range. There is no obvious trend in the residuals (median=0.009 dex), and the overall dispersion ($\approx (84PL - 16PL)/2$) is 0.18 dex.

APPENDIX D

COMPARISON WITH THE *Blue* DIAGRAM

The blue diagram discussed in §3.7.1 was developed in Lamareille et al. (2004) and recently improved in Lamareille (2010). The diagnostic employs lines at blue rest-frame wavelengths, from [O III] $\lambda 3727$ to [O III] $\lambda 5007$, in order to facilitate its use out to $z \sim 1$. This motivation is similar to that which guides the design of our MEx diagram, although our results differ significantly.

In this diagnostic, the abscissa is an equivalent width ratio because the spectral separation between the [O III] $\lambda 3727$ and $H\beta$ lines is significant and their line flux ratio would thus be very sensitive to dust attenuation. Note the inability to distinguish between SF and Seyfert 2 galaxies in the region marked as SF/Sy2. We show that this ambiguity is completely removed with our new diagram.

We examine the selection functions built in the blue diagram against the three other diagnostics introduced earlier. On Figure D.1, the blue points represent the star-forming galaxies (panel (a); note that there is a known overlap with the composite galaxy population as discussed in Lamareille, 2010). The pale blue points mark the ambiguous region where SF and Seyfert 2 galaxies are indistinguishable (SF/Sy2) whereas the black dots indicate the AGNs (encompassing both Seyfert 2's and LINERs). Panels (b)-(d) show the location of the same galaxies over the other diagnostic diagrams.

The main features are that **(i)** the ambiguous SF/Sy2 region (pale blue points) is resolved in the other diagrams, which all break the degeneracy observed in the [O III] $\lambda 3727/H\beta$ EW ratio of low- M_* SF galaxies and Seyfert 2s; **(ii)** the blue diagram AGNs (black dots and black contours) include some BPT-composites: more so than the [S II]-diagram shown in (c), but less so than the BPT (b) and

MEx (d) diagrams; and **(iii)** a large fraction of SF galaxies on the blue diagram are in fact composites or AGNs according to the BPT diagram (b).

The MEx diagram (Figure 3.6) is applicable to 2,812 galaxies out to $z \sim 1$, whereas the emission lines in the blue diagram (Figure D.2) are only available for 826 galaxies (29%). While 423 out of 531 (80%) GOODS-N galaxies with $H\beta$ and $[\text{O III}] \lambda 5007$ also have a valid measurement of the $[\text{O III}] \lambda 3727$ line, the situation is very different for EGS galaxies. The DEEP2 spectra used for these galaxies span a more restricted range in wavelength and so only 403 among 2,536 objects (16%) with valid $[\text{O III}] \lambda 5007$ and $H\beta$ also have a valid $[\text{O III}] \lambda 3727$ line flux.

The star-forming region of the blue diagram (Figure D.2) accounts for 10/13 (77%) of the X-ray starbursts but also for 6/11 (55%) of the X-ray AGNs. The Seyfert 2 region only accounts for 3/11 (27%) of the X-ray AGNs. The smaller number of galaxies on the blue diagram hinder a quantitative comparison with the MEx diagram. Nevertheless, it appears that the former is less reliable at selecting X-ray AGNs.

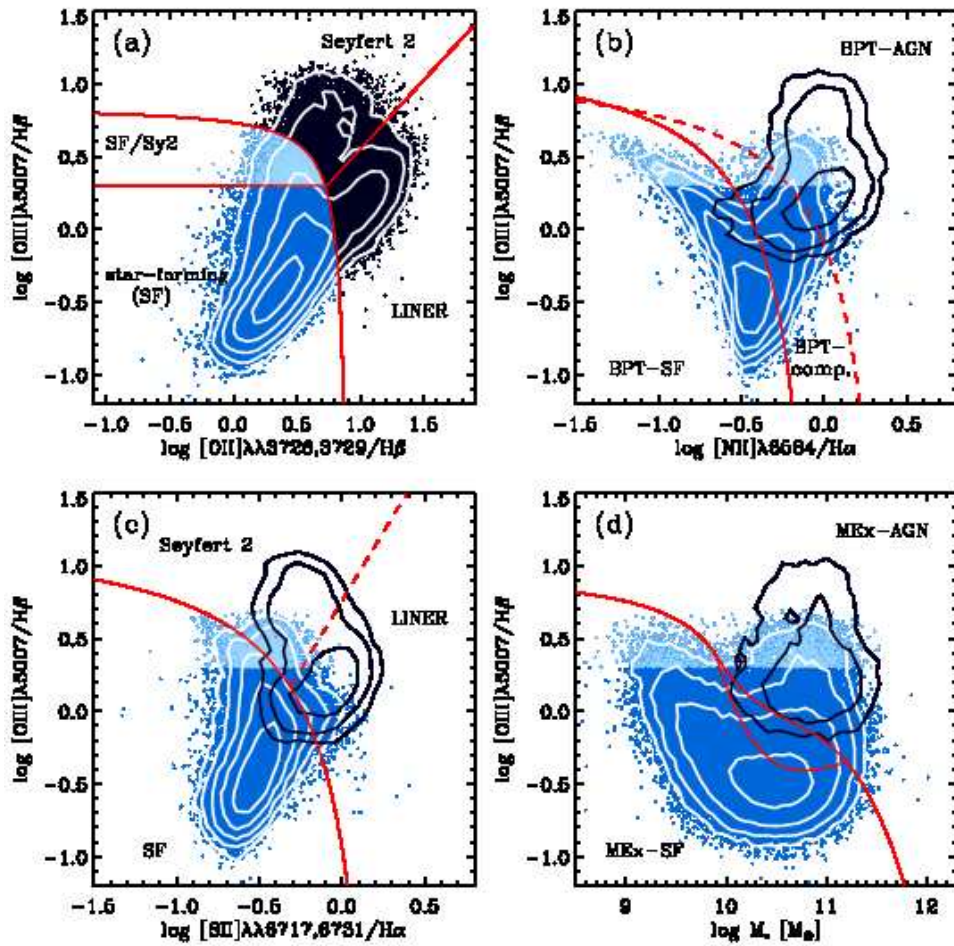


Figure D.1 Distribution of SDSS galaxies on the blue diagram: $[\text{O III}] \lambda 5007/\text{H}\beta$ line flux ratio against $[\text{O III}] \lambda 3727/\text{H}\beta$ equivalent width ratio. This diagram and dividing lines are adapted from Lamareille (2010). Most star-forming galaxies (SF) occupy the bottom left of the plot (blue dots) but include a number of composite galaxies. The black dots correspond to AGNs (Seyfert 2s and LINERs), and the light blue points mark the galaxies in the region where SF and Sy2 classes overlap. These classifications are compared to other diagnostics: (b) [N II] BPT diagram, (c) [S II] BPT diagram, and (d) MEx diagram. The blue diagram star-forming galaxies include a number of composite galaxies as shown on the

Figure D.1 *continued*. BPT diagram (b), as well as AGNs that are mostly LINERs according to panel (c). The ambiguous SF/Sy2 galaxies (light blue) are well separated on the other panels, especially (b) and (d). In all panels, the contours indicate the density of points (in bins of $0.075 \text{ dex} \times 0.075 \text{ dex}$) and are logarithmic (0.5 dex apart, with the outermost contour set to 10 galaxies per bin).

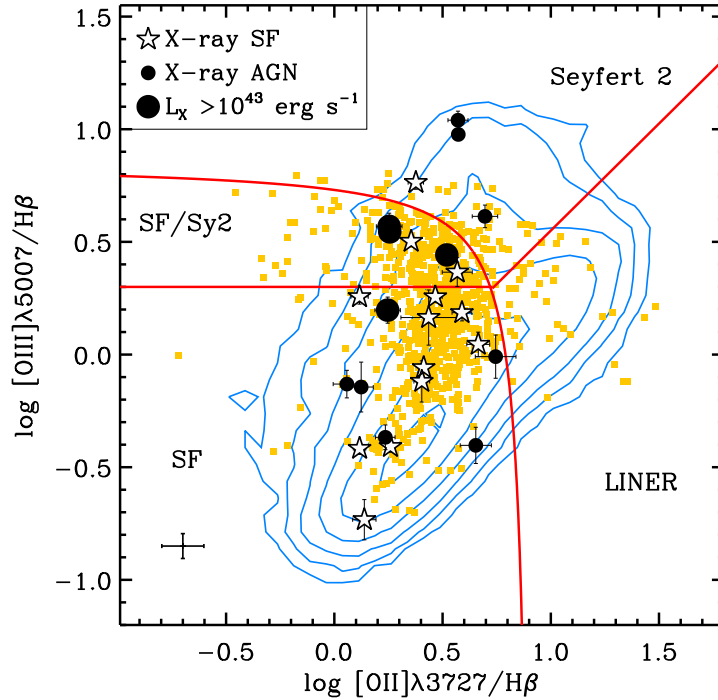


Figure D.2 The blue diagram, where AGNs are found above the solid curve and further separated between Seyfert 2 and LINER classes, as labeled. Star-forming (SF) galaxies lie below the curve including a region where they are indistinguishable from Seyfert 2 galaxies (labeled as SF/Sy2). In principle, this diagram is applicable out to $z \sim 1$. However, the DEEP2 spectra used in this work span a narrow wavelength range and very few cover all three lines required in this diagram. While performing well at selecting the X-ray starbursts (star symbols), this diagram misses the majority of X-ray AGNs (filled black circles) including the brighter ones (larger circles). Contours show the SDSS low- z sample (evenly spaced on a logarithmic scale). Our intermediate redshift sample is superimposed (orange points) and, when available, the X-ray classification is marked with larger symbols [star symbols for X-ray starbursts; small (large) filled circles for X-ray AGNs with $L_X < 10^{43} \text{ erg s}^{-1}$ ($L_X > 10^{43} \text{ erg s}^{-1}$)].

APPENDIX E

AGN FRACTION ON THE SFR-MASS PLANE

In this Appendix, we investigate the effect of the emission line selection criterion on the resulting AGN fraction on the SFR- M_* plane shown in Figure 4.6. As discussed in Section 4.4.1.1, we find that for emission-line selected galaxies (i.e., with $S/N > 3$), $P(\text{AGN})$ rises with increasing stellar mass. However, at the high-mass end, $P(\text{AGN})$ increases with *decreasing* SFR. Why is there such a high AGN fraction in low SFR galaxies? Is this effect driven by requiring $S/N > 3$ in the emission lines? In galaxies with low SFR, emission lines are expected to be faint. In this case the presence of AGN may boost the flux just enough to meet the signal-to-noise ratio threshold. If this were the case, the AGN fraction would be lower when considering all SDSS galaxies with measurable SFR and stellar mass.

We test this possibility by calculating a lower limit to the AGN fraction on the SFR- M_* plane, which we obtained by dividing the number of AGN (identified in emission-line galaxies) by the total number of SDSS galaxies (i.e., dropping the S/N criterion). This corresponds to making the assumption that any galaxy that fails the $S/N > 3$ criterion for *at least one* of the required emission lines does not host an AGN. This assumption is unlikely to be true but it provides us with a lower limit on $P(\text{AGN})$, displayed in Figure E.1. For reference, we also show the fraction of SDSS galaxies that meet the $S/N > 3$ requirement on the same SFR- M_* plane (right panel of Figure E.1). At a given stellar mass, the emission-line detection fraction is higher in galaxies with higher SFR. It is also fairly high in the lowest mass galaxies. This may be due to a combination of their proximity (they tend to lie at lower redshift and so intrinsically fainter lines can be detected) and their lower metallicity which may result in brighter emission lines (e.g., oxygen

becomes one of the main coolants so [O III] $\lambda 5007$ is luminous).

We can place slightly tighter constraints on P(AGN) lower limits and obtain higher emission line detection fractions if we relax the S/N criterion to $S/N > 2$. The results are shown in Figure E.2 and are largely similar to the $S/N > 3$ except for recovering more AGN and probing slightly lower on the SFR- M_* sequence.

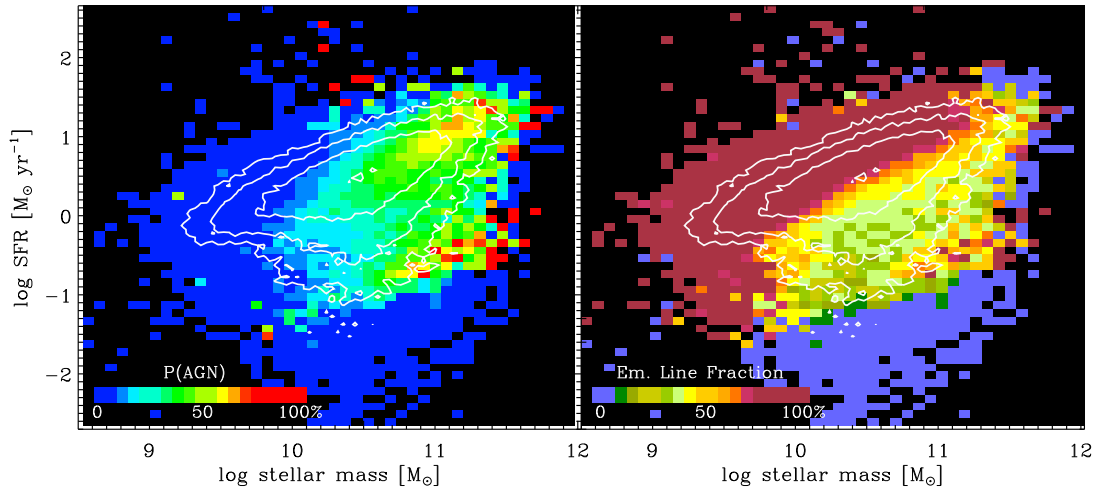


Figure E.1 (Left) Lower limit on the probability of presence of AGN as a function of SFR and stellar mass (color scale). The overall bivariate distribution of SDSS galaxies (including galaxies that fail the $S/N > 3$ criterion for at least one emission line) is shown with logarithmic contours (with the outermost contour delineating 10 galaxies per bin, and a spacing of 0.5 dex between contours). (Right) Fraction of galaxies that meet the $S/N > 3$ detection criterion for all emission lines ($H\beta$, [O III] $\lambda 5007$, $H\alpha$, [N II] $\lambda 6584$, [S II] $\lambda\lambda 6717, 6731$). The color scale is shown on the figure.

While the normalization of P(AGN) is lower in the versions presented in this Appendix compared to the emission-line subsample (Figure 4.6), it shows a similar qualitative behavior in the sense that the transition region from $P(\text{AGN})=0$

to $P(\text{AGN}) > 0$ is located at the same place in both Figures E.1(left) and 4.6(left). In addition, we still find a high AGN fraction in low-SFR galaxies with high stellar masses ($10^{10.5} - 10^{11.5} M_{\odot}$). However, the rise in $P(\text{AGN})$ with decreasing SFR (at fixed mass) is not clearly monotonic when considering the lower limit on $P(\text{AGN})$. It appears to be perhaps bimodal in Figures E.1 and reffig:SNR2, with higher $P(\text{AGN})$ along the main sequence and then again below it in the high-mass portion of the *green valley*. It is not clear whether this trend is real or whether it is due to a lower sampling fraction of galaxies along the bottom ridge of the main sequence (see right-hand panels of Figures E.1 and reffig:SNR2). If real, it would support previous work that find AGN host galaxies preferentially in the *green valley* on color-magnitude diagrams (Silverman et al., 2008; Schawinski et al., 2009) and in post-starburst galaxies (Yan et al., 2006), which have a low current SFR but show signatures of recent starbursts. AGN hosts were also reported to have intermediate SFRs between non-AGN hosts and quiescent (red sequence) galaxies (Salim et al., 2007).

We note a cutoff at $\text{SFR} < 0.1 M_{\odot} \text{ yr}^{-1}$ below which galaxies fail to be detected in their emission lines and so we are unable to constrain $P(\text{AGN})$ in that regime. These passive galaxies may be part of the so-called red sequence on the color-magnitude diagram and perhaps other AGN selection methods like radio emission would be more appropriate to search for AGN. However, this is beyond the scope of this work as we are mostly interested in actively star-forming galaxy populations.

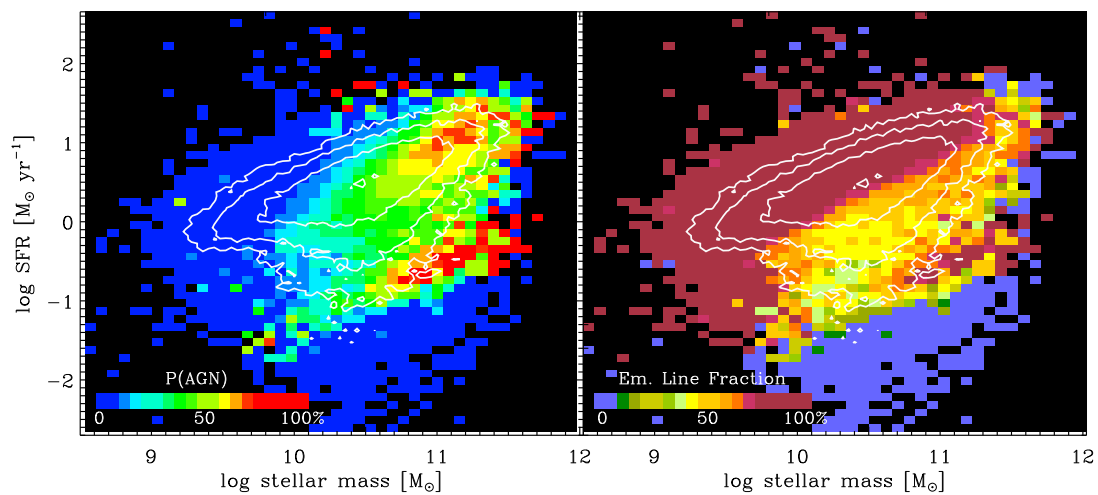


Figure E.2 Identical to Figure E.1 except for using $S/N > 2$ (instead of $S/N > 3$) to identify AGN (Left) and to calculate the emission line detection fraction (Right).

REFERENCES

- Aalto, S., Booth, R. S., Black, J. H., & Johansson, L. E. B. 1995, *A&A*, 300, 369
- Aalto, S., Spaans, M., Wiedner, M. C., & Hüttemeister, S. 2007, *A&A*, 464, 193
- Abazajian, K. N., Adelman-McCarthy, J. K., Agüeros, M. A., et al. 2009, *ApJS*, 182, 543
- Adelman-McCarthy, J. K., Agüeros, M. A., Allam, S. S., et al. 2006, *ApJS*, 162, 38
- Agertz, O., Teyssier, R., & Moore, B. 2009, *MNRAS*, 397, L64
- Akylas, A. & Georgantopoulos, I. 2009, *A&A*, 500, 999
- Alexander, D. M., Bauer, F. E., Brandt, W. N., et al. 2003, *AJ*, 126, 539
- Alexander, D. M., Bauer, F. E., Chapman, S. C., Smail, I., Blain, A. W., Brandt, W. N., & Ivison, R. J. 2005, *ApJ*, 632, 736
- Antonucci, R. 1993, *ARA&A*, 31, 473
- Armus, L., Charmandaris, V., Spoon, H. W. W., et al. 2004, *ApJS*, 154, 178
- Armus, L., Charmandaris, V., Bernard-Salas, J., et al. 2007, *ApJ*, 656, 148
- Baan, W. A., Henkel, C., Loenen, A. F., Baudry, A., & Wiklind, T. 2008, *A&A*, 477, 747
- Bade, N., Fink, H. H., Engels, D., Voges, W., Hagen, H., Wisotzki, L., & Reimers, D. 1995, *A&AS*, 110, 469
- Baldwin, J. A., Phillips, M. M., & Terlevich, R. 1981, *PASP*, 93, 5

- Barger, A. J., Cowie, L. L., Bautz, M. W., Brandt, W. N., Garmire, G. P., Hornschemeier, A. E., Ivison, R. J., & Owen, F. N. 2001, *AJ*, 122, 2177
- Barmby, P., Alonso-Herrero, A., Donley, J. L., et al. 2006, *ApJ*, 642, 126
- Barmby, P., Huang, J.-S., Ashby, M. L. N., Eisenhardt, P. R. M., Fazio, G. G., Willner, S. P., & Wright, E. L. 2008, *ApJS*, 177, 431
- Bassani, L., Dadina, M., Maiolino, R., Salvati, M., Risaliti, G., della Ceca, R., Matt, G., & Zamorani, G. 1999, *ApJS*, 121, 473
- Bauer, F. E., Alexander, D. M., Brandt, W. N., Schneider, D. P., Treister, E., Hornschemeier, A. E., & Garmire, G. P. 2004, *AJ*, 128, 2048
- Bell, E. F. 2003, *ApJ*, 586, 794
- Bennert, N., Canalizo, G., Jungwiert, B., Stockton, A., Schweizer, F., Peng, C. Y., & Lacy, M. 2008, *ApJ*, 677, 846
- Binette, L., Magris, C. G., Stasińska, G., & Bruzual, A. G. 1994, *A&A*, 292, 13
- Blanton, M. R. & Roweis, S. 2007, *AJ*, 133, 734
- Blitz, L. & Rosolowsky, E. 2006, *ApJ*, 650, 933
- Bournaud, F., Dekel, A., Teyssier, R., Cacciato, M., Daddi, E., Juneau, S., & Shankar, F. 2011, *ArXiv e-prints*
- Boyle, B. J., Griffiths, R. E., Shanks, T., Stewart, G. C., & Georgantopoulos, I. 1993, *MNRAS*, 260, 49
- Brandt, W. N., Alexander, D. M., Hornschemeier, A. E., et al. 2001, *AJ*, 122, 2810

- Brinchmann, J., Charlot, S., White, S. D. M., Tremonti, C., Kauffmann, G., Heckman, T., & Brinkmann, J. 2004, *MNRAS*, 351, 1151
- Brinchmann, J., Pettini, M., & Charlot, S. 2008, *MNRAS*, 385, 769
- Bruzual, G. & Charlot, S. 2003, *MNRAS*, 344, 1000
- Bundy, K., Ellis, R. S., Conselice, C. J., et al. 2006, *ApJ*, 651, 120
- Busko, I. C. & Steiner, J. E. 1988, *MNRAS*, 232, 525
- Bussmann, R. S., Narayanan, D., Shirley, Y. L., Juneau, S., Wu, J., Solomon, P. M., Vanden Bout, P. A., Moustakas, J., & Walker, C. K. 2008, *ApJL*, 681, L73
- Canalizo, G., Bennert, N., Jungwiert, B., Stockton, A., Schweizer, F., Lacy, M., & Peng, C. 2007, *ApJ*, 669, 801
- Capak, P., Cowie, L. L., Hu, E. M., et al. 2004, *AJ*, 127, 180
- Chabrier, G. 2003, *PASP*, 115, 763
- Chary, R. & Elbaz, D. 2001, *ApJ*, 556, 562
- Cisternas, M., Jahnke, K., Inskip, K. J., et al. 2011, *ApJ*, 726, 57
- Coil, A. L., Newman, J. A., Kaiser, N., Davis, M., Ma, C., Kocevski, D. D., & Koo, D. C. 2004, *ApJ*, 617, 765
- Coil, A. L., Georgakakis, A., Newman, J. A., et al. 2009, *ApJ*, 701, 1484
- Comastri, A., Setti, G., Zamorani, G., & Hasinger, G. 1995, *A&A*, 296, 1
- Condon, J. J., Huang, Z.-P., Yin, Q. F., & Thuan, T. X. 1991, *ApJ*, 378, 65
- Cooper, M. C., Aird, J. A., Coil, et al. 2011, *ApJS*, 193, 14

- Cowie, L. L., Songaila, A., Hu, E. M., & Cohen, J. G. 1996, *AJ*, 112, 839
- Croton, D. J., Springel, V., White, S. D. M., et al. 2006, *MNRAS*, 365, 11
- da Cunha, E., Charmandaris, V., Díaz-Santos, T., Armus, L., Marshall, J. A., & Elbaz, D. 2010, *A&A*, 523, A78+
- Daddi, E., Dickinson, M., Morrison, G., et al. 2007, *ApJ*, 670, 156
- Daddi, E., Bournaud, F., Walter, F., et al. 2010, *ApJ*, 713, 686
- Dale, D. A. & Helou, G. 2002, *ApJ*, 576, 159
- Davis, M., Faber, S. M., Newman, J., et al. 2003, in Presented at the Society of Photo-Optical Instrumentation Engineers (SPIE) Conference, Vol. 4834, Society of Photo-Optical Instrumentation Engineers (SPIE) Conference Series, ed. P. Guhathakurta, 161–172
- Davis, M., Guhathakurta, P., Konidaris, N. P., et al. 2007, *ApJL*, 660, L1
- Dekel, A., Sari, R., & Ceverino, D. 2009, *ApJ*, 703, 785
- Di Matteo, T., Springel, V., & Hernquist, L. 2005, *Nature*, 433, 604
- Diamond-Stanic, A. M. & Rieke, G. H. 2011, ArXiv e-prints
- Diamond-Stanic, A. M., Rieke, G. H., & Rigby, J. R. 2009, *ApJ*, 698, 623
- Dickinson, M. & FIDEL team. 2007, in Bulletin of the American Astronomical Society, Vol. 38, Bulletin of the American Astronomical Society, 822–+
- Donley, J. L., Rieke, G. H., Pérez-González, P. G., Rigby, J. R., & Alonso-Herrero, A. 2007, *ApJ*, 660, 167
- Draine, B. T. 2003, *ARA&A*, 41, 241

- Dudik, R. P., Satyapal, S., & Marcu, D. 2009, *ApJ*, 691, 1501
- Elbaz, D., Daddi, E., Le Borgne, D., et al. 2007, *A&A*, 468, 33
- Elbaz, D., Hwang, H. S., Magnelli, B., et al. 2010, *A&A*, 518, L29+
- Elbaz, D., Dickinson, M., Hwang, H. S., et al. 2011, *ArXiv e-prints*
- Elmegreen, D. M., Elmegreen, B. G., Ravindranath, S., & Coe, D. A. 2007, *ApJ*, 658, 763
- Elmegreen, D. M., Elmegreen, B. G., Marcus, M. T., Shahinyan, K., Yau, A., & Petersen, M. 2009, *ApJ*, 701, 306
- Elvis, M., Wilkes, B. J., McDowell, J. C., Green, R. F., Bechtold, J., Willner, S. P., Oey, M. S., Polomski, E., & Cutri, R. 1994, *ApJS*, 95, 1
- Eracleous, M., Hwang, J. A., & Flohic, H. M. L. G. 2010, *ApJ*, 711, 796
- Evans, II, N. J. 1999, *ARA&A*, 37, 311
- Faber, S. M., Phillips, A. C., Kibrick, R. I., et al. 2003, in Presented at the Society of Photo-Optical Instrumentation Engineers (SPIE) Conference, Vol. 4841, Society of Photo-Optical Instrumentation Engineers (SPIE) Conference Series, ed. M. Iye & A. F. M. Moorwood, 1657–1669
- Fabian, A. C. 1999, *MNRAS*, 308, L39
- Farrah, D., Afonso, J., Efstathiou, A., Rowan-Robinson, M., Fox, M., & Clements, D. 2003, *MNRAS*, 343, 585
- Farrah, D., Bernard-Salas, J., Spoon, H. W. W., et al. 2007, *ApJ*, 667, 149
- Ferrarese, L. & Merritt, D. 2000, *ApJL*, 539, L9

- Gabor, J. M., Impey, C. D., Jahnke, K., et al. 2009, *ApJ*, 691, 705
- Gallo, E., Treu, T., Marshall, P. J., Woo, J., Leipski, C., & Antonucci, R. 2010, *ApJ*, 714, 25
- Gao, Y. & Solomon, P. M. 2004, *ApJ*, 606, 271
- Gao, Y. & Solomon, P. M. 2004a, *ApJS*, 152, 63
- . 2004b, *ApJ*, 606, 271
- Genzel, R., Lutz, D., Sturm, E., et al. 1998, *ApJ*, 498, 579
- Genzel, R., Tacconi, L. J., Gracia-Carpio, J., et al. 2010, *MNRAS*, 407, 2091
- Gordon, K. D., Clayton, G. C., Witt, A. N., & Misselt, K. A. 2000, *ApJ*, 533, 236
- Goulding, A. D. & Alexander, D. M. 2009, *MNRAS*, 398, 1165
- Graciá-Carpio, J., García-Burillo, S., Planesas, P., & Colina, L. 2006, *ApJL*, 640, L135
- Graciá-Carpio, J., García-Burillo, S., Planesas, P., Fuente, A., & Usero, A. 2008, *A&A*, 479, 703
- Greve, T. R., Papadopoulos, P. P., Gao, Y., & Radford, S. J. E. 2009, *ApJ*, 692, 1432
- Grogin, N. A., Conselice, C. J., Chatzichristou, E., et al. 2005, *ApJL*, 627, L97
- Groves, B. A., Heckman, T. M., & Kauffmann, G. 2006, *MNRAS*, 371, 1559
- Guainazzi, M., Molendi, S., Vignati, P., Matt, G., & Iwasawa, K. 2000, , 5, 235
- Gwyn, S. D. J. 2008, *PASP*, 120, 212
- . 2011, ArXiv e-prints

- Hainline, K. N., Shapley, A. E., Kornei, K. A., Pettini, M., Buckley-Geer, E., Allam, S. S., & Tucker, D. L. 2009, *ApJ*, 701, 52
- Hatziminaoglou, E., Omont, A., Stevens, J. A., et al. 2010, *A&A*, 518, L33+
- Heavens, A., Panter, B., Jimenez, R., & Dunlop, J. 2004, *Nature*, 428, 625
- Heckman, T. M., Armus, L., & Miley, G. K. 1990, *ApJS*, 74, 833
- Heckman, T. M., Lehnert, M. D., Strickland, D. K., & Armus, L. 2000, *ApJS*, 129, 493
- Heckman, T. M., Ptak, A., Hornschemeier, A., & Kauffmann, G. 2005, *ApJ*, 634, 161
- Heckman, T. M. 1980, *A&A*, 87, 152
- Hopkins, P. F. & Quataert, E. 2010, *MNRAS*, 407, 1529
- Hopkins, P. F., Hernquist, L., Cox, T. J., Di Matteo, T., Martini, P., Robertson, B., & Springel, V. 2005, *ApJ*, 630, 705
- Hopkins, P. F., Hernquist, L., Cox, T. J., Di Matteo, T., Robertson, B., & Springel, V. 2006, *ApJS*, 163, 1
- Hopkins, A. M. 2004, *ApJ*, 615, 209
- Ho, L. C., Filippenko, A. V., & Sargent, W. L. W. 1993, *ApJ*, 417, 63
- Ho, L. C. 1999, *Advances in Space Research*, 23, 813
- . 2008, *ARA&A*, 46, 475
- Hwang, H. S., Elbaz, D., Lee, J. C., Jeong, W.-S., Park, C., Lee, M. G., & Lee, H. M. 2010a, *A&A*, 522, A33+

- Hwang, H. S., Elbaz, D., Magdis, G., et al. 2010b, *MNRAS*, 409, 75
- Imanishi, M. 2009, *ApJ*, 694, 751
- Iono, D., Wilson, C. D., Yun, M. S., Baker, A. J., Petitpas, G. R., Peck, A. B., Krips, M., Cox, T. J., Matsushita, S., Mihos, J. C., & Pihlstrom, Y. 2009, *ApJ*, 695, 1537
- Juneau, S., Glazebrook, K., Crampton, D., et al. 2005, *ApJL*, 619, L135
- Juneau, S., Narayanan, D. T., Moustakas, J., Shirley, Y. L., Bussmann, R. S., Kennicutt, Jr., R. C., & Vanden Bout, P. A. 2009, *ApJ*, 707, 1217
- Juneau, S., Dickinson, M., Alexander, D. M., & Salim, S. 2011, *ApJ*, 736, 104
- Kartaltepe, J. S., Sanders, D. B., Le Floch, E., et al. 2010a, *ApJ*, 709, 572
- Kartaltepe, J. S., Sanders, D. B., Le Floch, E., et al. 2010b, *ApJ*, 721, 98
- Kauffmann et al., G. 2003, *MNRAS*, 346, 1055
- Kauffmann, G., Heckman, T. M., White, S. D. M., et al. 2003, *MNRAS*, 341, 33
- Kelly, B. C. 2007, *ApJ*, 665, 1489
- Kennicutt, Jr., R. C. 1989, *ApJ*, 344, 685
- Kennicutt, Jr., R. C. 1998, *ARA&A*, 36, 189
- . 1998, *ApJ*, 498, 541
- Kewley, L. J. & Dopita, M. A. 2002, *ApJS*, 142, 35
- Kewley, L. J. & Ellison, S. L. 2008, *ApJ*, 681, 1183
- Kewley, L. J., Dopita, M. A., Sutherland, R. S., Heisler, C. A., & Trevena, J. 2001a, *ApJ*, 556, 121

- Kewley, L. J., Heisler, C. A., Dopita, M. A., & Lumsden, S. 2001b, *ApJS*, 132, 37
- Kewley, L. J., Groves, B., Kauffmann, G., & Heckman, T. 2006, *MNRAS*, 372, 961
- Kim, D.-C. & Sanders, D. B. 1998, *ApJS*, 119, 41
- Kocevski, D. D., Faber, S. M., Mozena, M., et al. 2011, *ArXiv e-prints*
- Krips, M. e. a. 2007, *A&A*, 468, L63
- Kroupa, P. 2001, *MNRAS*, 322, 231
- Krumholz, M. R. & Thompson, T. A. 2007, *ApJ*, 669, 289
- Lacy, M., Storrie-Lombardi, L. J., Sajina, A., et al. 2004, *ApJS*, 154, 166
- Lagos, C. D. P., Padilla, N. D., Strauss, M. A., Cora, S. A., & Hao, L. 2011, *MNRAS*, 414, 2148
- Lahuis, F., Spoon, H. W. W., Tielens, A. G. G. M., Doty, S. D., Armus, L., Charmandaris, V., Houck, J. R., Stäuber, P., & van Dishoeck, E. F. 2007, *ApJ*, 659, 296
- Laird, E. S., Nandra, K., Georgakakis, A., et al. 2009, *ApJS*, 180, 102
- Lamareille, F., Mouhcine, M., Contini, T., Lewis, I., & Maddox, S. 2004, *MNRAS*, 350, 396
- Lamareille, F. 2010, *A&A*, 509, A53+
- LaMassa, S. M., Heckman, T. M., Ptak, A., Hornschemeier, A., Martins, L., Sonnentrucker, P., & Tremonti, C. 2009, *ApJ*, 705, 568
- LaMassa, S. M., Heckman, T. M., Ptak, A., Martins, L., Wild, V., & Sonnentrucker, P. 2010, *ApJ*, 720, 786

- Le Floch, E., Mirabel, I. F., Laurent, O., Charmandaris, V., Gallais, P., Sauvage, M., Vigroux, L., & Cesarsky, C. 2001, *A&A*, 367, 487
- Le Floch, E., Papovich, C., Dole, H., et al. 2005, *ApJ*, 632, 169
- Levine, E. S., Helfer, T. T., Meijerink, R., & Blitz, L. 2008, *ApJ*, 673, 183
- Lilly, S. J., Le Fevre, O., Hammer, F., & Crampton, D. 1996, *ApJL*, 460, L1+
- Lintott, C. & Viti, S. 2006, *ApJL*, 646, L37
- Liu, X., Shapley, A. E., Coil, A. L., Brinchmann, J., & Ma, C. 2008, *ApJ*, 678, 758
- Lutz, D., Genzel, R., Sternberg, A., et al. 1996, *A&A*, 315, L137
- Lutz, D., Spoon, H. W. W., Rigopoulou, D., Moorwood, A. F. M., & Genzel, R. 1998, *ApJL*, 505, L103
- Lutz, D., Mainieri, V., Rafferty, D., et al. 2010, *ApJ*, 712, 1287
- Madau, P., Ferguson, H. C., Dickinson, M. E., Giavalisco, M., Steidel, C. C., & Fruchter, A. 1996, *MNRAS*, 283, 1388
- Magnelli, B., Elbaz, D., Chary, R. R., Dickinson, M., Le Borgne, D., Frayer, D. T., & Willmer, C. N. A. 2009, *A&A*, 496, 57
- . 2011, *A&A*, 528, A35+
- Magorrian, J., Tremaine, S., Richstone, D., et al. 1998, *AJ*, 115, 2285
- Magorrian, J., Tremaine, S., Richstone, D., et al. 1998, *AJ*, 115, 2285
- Maiolino, R. & Rieke, G. H. 1995, *ApJ*, 454, 95

- Maiolino, R., Salvati, M., Bassani, L., Dadina, M., della Ceca, R., Matt, G., Risaliti, G., & Zamorani, G. 1998, *A&A*, 338, 781
- Malkan, M. A., Gorjian, V., & Tam, R. 1998, *ApJS*, 117, 25
- Marcillac, D., Elbaz, D., Chary, R. R., Dickinson, M., Galliano, F., & Morrison, G. 2006, *A&A*, 451, 57
- Marconi, A., Risaliti, G., Gilli, R., Hunt, L. K., Maiolino, R., & Salvati, M. 2004, *MNRAS*, 351, 169
- Martin, C. L. 2005, *ApJ*, 621, 227
- . 2006, *ApJ*, 647, 222
- Matt, G., Fabian, A. C., Guainazzi, M., Iwasawa, K., Bassani, L., & Malaguti, G. 2000, *MNRAS*, 318, 173
- Mouri, H., Taniguchi, Y., Sato, Y., & Kawara, K. 1998, *A&A*, 334, 482
- Moustakas, J. & Kennicutt, Jr., R. C. 2006, *ApJS*, 164, 81
- Moustakas, J., Kennicutt, Jr., R. C., & Tremonti, C. A. 2006, *ApJ*, 642, 775
- Mo, H. J., Mao, S., & White, S. D. M. 1998, *MNRAS*, 295, 319
- Mulchaey, J. S., Koratkar, A., Ward, M. J., Wilson, A. S., Whittle, M., Antonucci, R. R. J., Kinney, A. L., & Hurt, T. 1994, *ApJ*, 436, 586
- Mullaney, J. R., Alexander, D. M., Huynh, M., Goulding, A. D., & Frayer, D. 2010, *MNRAS*, 401, 995
- Mullaney, J. R., Alexander, D. M., Goulding, A. D., & Hickox, R. C. 2011a, *MNRAS*, 414, 1082

- Mullaney, J. R., Pannella, M., Daddi, E., et al. 2011b, ArXiv e-prints
- Mushotzky, R. F., Cowie, L. L., Barger, A. J., & Arnaud, K. A. 2000, *Nature*, 404, 459
- Nandra, K., Laird, E. S., Adelberger, K., Gardner, J. P., Mushotzky, R. F., Rhodes, J., Steidel, C. C., Teplitz, H. I., & Arnaud, K. A. 2005, *MNRAS*, 356, 568
- Narayanan, D., Groppi, C. E., Kulesa, C. A., & Walker, C. K. 2005, *ApJ*, 630, 269
- Narayanan, D., Cox, T. J., Robertson, B., Davé, R., Di Matteo, T., Hernquist, L., Hopkins, P., Kulesa, C., & Walker, C. K. 2006, *ApJL*, 642, L107
- Narayanan, D., Cox, T. J., Kelly, B., Davé, R., Hernquist, L., Di Matteo, T., Hopkins, P. F., Kulesa, C., Robertson, B., & Walker, C. K. 2008, *ApJS*, 176, 331
- Narayanan, D., Cox, T. J., Kelly, B., Davé, R., Hernquist, L., Di Matteo, T., Hopkins, P. F., Kulesa, C., Robertson, B., & Walker, C. K. 2008a, *ApJS*, 176, 331
- Narayanan, D., Cox, T. J., Shirley, Y., Davé, R., Hernquist, L., & Walker, C. K. 2008b, *ApJ*, 684, 996
- Nardini, E., Risaliti, G., Salvati, M., Sani, E., Imanishi, M., Marconi, A., & Maiolino, R. 2008, *MNRAS*, 385, L130
- Nardini, E., Risaliti, G., Watabe, Y., Salvati, M., & Sani, E. 2010, *MNRAS*, 405, 2505
- Noeske, K. G., Weiner, B. J., Faber, S. M., et al. 2007, *ApJL*, 660, L43
- Osterbrock, D. E. 1989, *Astrophysics of gaseous nebulae and active galactic nuclei* (University Science Books)
- Pope, A., Chary, R., Alexander, D. M., Armus, L., Dickinson, M., Elbaz, D., Frayer, D., Scott, D., & Teplitz, H. 2008, *ApJ*, 675, 1171

- Richstone, D., Ajhar, E. A., Bender, R., et al. 1998, *Nature*, 395, A14+
- Rieke, G. H., Cutri, R. M., Black, J. H., Kailey, W. F., McAlary, C. W., Lebofsky, M. J., & Elston, R. 1985, *ApJ*, 290, 116
- Rieke, G. H., Alonso-Herrero, A., Weiner, B. J., Pérez-González, P. G., Blaylock, M., Donley, J. L., & Marcillac, D. 2009, *ApJ*, 692, 556
- Rigby, J. R., Rieke, G. H., Donley, J. L., Alonso-Herrero, A., & Pérez-González, P. G. 2006, *ApJ*, 645, 115
- Rigby, J. R., Diamond-Stanic, A. M., & Aniano, G. 2009, *ApJ*, 700, 1878
- Rujopakarn, W., Rieke, G. H., Eisenstein, D. J., & Juneau, S. 2011, *ApJ*, 726, 93
- Rupke, D. S., Veilleux, S., & Sanders, D. B. 2005, *ApJS*, 160, 115
- Sakamoto, K., Aalto, S., Wilner, D. J., Black, J. H., Conway, J. E., Costagliola, F., Peck, A. B., Spaans, M., Wang, J., & Wiedner, M. C. 2009, *ApJL*, 700, L104
- Salim, S., Charlot, S., Rich, R. M., et al. 2005, *ApJL*, 619, L39
- Salim, S., Rich, R. M., Charlot, S., et al. 2007, *ApJS*, 173, 267
- Salim, S., Dickinson, M., Michael Rich, R., et al. 2009, *ApJ*, 700, 161
- Salpeter, E. E. 1955, *ApJ*, 121, 161
- Sanders, D. B. & Mirabel, I. F. 1996, *ARA&A*, 34, 749
- Sanders, D. B., Soifer, B. T., Elias, J. H., Madore, B. F., Matthews, K., Neugebauer, G., & Scoville, N. Z. 1988, *ApJ*, 325, 74
- Sanders, D. B., Mazzarella, J. M., Kim, D.-C., Surace, J. A., & Soifer, B. T. 2003, *AJ*, 126, 1607

- Savaglio, S., Glazebrook, K., Le Borgne, D., et al. 2005, *ApJ*, 635, 260
- Schawinski, K., Virani, S., Simmons, B., Urry, C. M., Treister, E., Kaviraj, S., & Kushkuley, B. 2009, *ApJL*, 692, L19
- Schawinski, K., Treister, E., Urry, C. M., Cardamone, C. N., Simmons, B., & Yi, S. K. 2011, *ApJL*, 727, L31+
- Schmidt, M. 1959, *ApJ*, 129, 243
- Schöier, F. L., van der Tak, F. F. S., van Dishoeck, E. F., & Black, J. H. 2005, *A&A*, 432, 369
- Seyfert, C. K. 1943, *ApJ*, 97, 28
- Shao, L., Lutz, D., Nordon, R., et al. 2010, *A&A*, 518, L26+
- Silverman, J. D., Mainieri, V., Lehmer, B. D., et al. 2008, *ApJ*, 675, 1025
- Smolčić, V. 2009, *ApJL*, 699, L43
- Solomon, P. M., Downes, D., & Radford, S. J. E. 1992, *ApJL*, 387, L55
- Solomon, P. M., Downes, D., Radford, S. J. E., & Barrett, J. W. 1997, *ApJ*, 478, 144
- Spoon, H. W. W. & Holt, J. 2009, ArXiv e-prints
- Spoon, H. W. W., Marshall, J. A., Houck, J. R., Elitzur, M., Hao, L., Armus, L., Brandl, B. R., & Charmandaris, V. 2007, *ApJL*, 654, L49
- Springel, V. & Hernquist, L. 2003, *MNRAS*, 339, 289
- Springel, V., Di Matteo, T., & Hernquist, L. 2005, *MNRAS*, 361, 776
- Springel, V. 2005, *MNRAS*, 364, 1105

- Stasińska, G., Cid Fernandes, R., Mateus, A., Sodré, L., & Asari, N. V. 2006, *MNRAS*, 371, 972
- Stasińska, G., Vale Asari, N., Cid Fernandes, R., Gomes, J. M., Schlickmann, M., Mateus, A., Schoenell, W., & Sodré, Jr., L. 2008, *MNRAS*, 391, L29
- Stern, D., Eisenhardt, P., Gorjian, V., et al. 2005, *ApJ*, 631, 163
- Sturm, E., Lutz, D., Verma, A., Netzer, H., Sternberg, A., Moorwood, A. F. M., Oliva, E., & Genzel, R. 2002, *A&A*, 393, 821
- Symeonidis, M., Rosario, D., Georgakakis, A., Harker, J., Laird, E. S., Page, M. J., & Willmer, C. N. A. 2010, *MNRAS*, 403, 1474
- Tacconi, L. J., Genzel, R., Blietz, M., Cameron, M., Harris, A. I., & Madden, S. 1994, *ApJL*, 426, L77+
- Tacconi, L. J., Genzel, R., Neri, R., et al. 2010, *Nature*, 463, 781
- Toomre, A. & Toomre, J. 1972, *ApJ*, 178, 623
- Treister, E. & Urry, C. M. 2005, *ApJ*, 630, 115
- Tremaine, S., Gebhardt, K., Bender, R., et al. 2002, *ApJ*, 574, 740
- Tremonti, C. A., Heckman, T. M., Kauffmann, G., et al. 2004, *ApJ*, 613, 898
- Tremonti, C. A., Moustakas, J., & Diamond-Stanic, A. M. 2007, *ApJL*, 663, L77
- Trump, J. R., Impey, C. D., Taniguchi, Y., et al. 2009, *ApJ*, 706, 797
- Trump, J. R., Impey, C. D., Kelly, B. C., et al. 2011, *ApJ*, 733, 60
- Usero, A., García-Burillo, S., Fuente, A., Martín-Pintado, J., & Rodríguez-Fernández, N. J. 2004, *A&A*, 419, 897

- Vega, O., Clemens, M. S., Bressan, A., Granato, G. L., Silva, L., & Panuzzo, P. 2008, *A&A*, 484, 631
- Veilleux, S. & Osterbrock, D. E. 1987, *ApJS*, 63, 295
- Veilleux, S., Kim, D.-C., Sanders, D. B., Mazzarella, J. M., & Soifer, B. T. 1995, *ApJS*, 98, 171
- Veilleux, S., Kim, D.-C., & Sanders, D. B. 1999, *ApJ*, 522, 113
- Veilleux, S., Kim, D.-C., & Sanders, D. B. 2002, *ApJS*, 143, 315
- Veilleux, S., Cecil, G., & Bland-Hawthorn, J. 2005, *ARA&A*, 43, 769
- Veilleux, S., Rupke, D. S. N., Kim, D.-C., et al. 2009, *ApJS*, 182, 628
- Vignali, C., Alexander, D. M., Gilli, R., & Pozzi, F. 2010, *MNRAS*, 404, 48
- Weiner, B. J., Papovich, C., Bundy, K., et al. 2007, *ApJL*, 660, L39
- Wirth, G. D., Willmer, C. N. A., Amico, P., et al. 2004, *AJ*, 127, 3121
- Worsley, M. A., Fabian, A. C., Bauer, F. E., Alexander, D. M., Hasinger, G., Matteos, S., Brunner, H., Brandt, W. N., & Schneider, D. P. 2005, *MNRAS*, 357, 1281
- Wright, S. A., Larkin, J. E., Graham, J. R., & Ma, C. 2010, *ApJ*, 711, 1291
- Wu, H., Zou, Z. L., Xia, X. Y., & Deng, Z. G. 1998, *A&AS*, 132, 181
- Wu, J., Evans, II, N. J., Gao, Y., Solomon, P. M., Shirley, Y. L., & Vanden Bout, P. A. 2005, *ApJL*, 635, L173
- Yan, R., Newman, J. A., Faber, S. M., Konidaris, N., Koo, D., & Davis, M. 2006, *ApJ*, 648, 281

Yan, R., Ho, L. C., Newman, J. A., et al. 2011, ApJ, 728, 38

York, D. G., Adelman, J., Anderson, Jr., J. E., Anderson, S. F., Annis, J., Bahcall, N. A., Bakken, J. A., Barkhouser, R., & others. 2000, AJ, 120, 1579

Yuan, T., Kewley, L. J., & Sanders, D. B. 2010, ApJ, 709, 884